Trinity College Dublin
Coláiste na Tríonóide, Baile Átha Cliath
The University of Dublin

An exploration of two-dimensional materials for solar energy harvesting

Stefana Anais Colibaba

A thesis presented for the degree of
Doctor of Philosophy

School of Physics
Trinity College Dublin Ireland
September, 2020

Declaration

I declare that this thesis has not been submitted as an exercise for a degree at this or any other university and it is entirely my own work

I was involved in a number of collaborations, and where it is appropriate my collaborators are acknowledged for their contributions.

I agree to deposit this thesis in the University's open access institutional repository or allow the library to do so on my behalf, subject to Irish Copyright Legislation and Trinity College Library conditions of use and acknowledgement.

Signed: ________________________ Date: ________________________

Abstract

The rise in energy demand around the globe can only be met with sustainable and long-term reliance on alternative renewable energy sources. In this context, the goal of this thesis is to conceive a method through which two-dimensional materials and heterostructures thereof can be ranked in terms of their photoabsorption. Firstly we have explored the theoretical limitations of realistic predictions for the photoconversion efficiency obtained with ab-initio methods such as density functional theory. We have studied silicon and methyl ammonium lead iodide and have found that the efficiency is largely affected by the inherent level of disorder in the system. This rendered the efficiency study intractable from an ab-initio perspective. However, the short circuit current density, J_{sc}, has been proven to be reliably determined within our model even in the absence of an empirical treatment. We have designated the short circuit current density at 95% of its maximum saturation value as our ab-initio photovoltaic descriptor, together with the corresponding active layer thickness. This effectively allowed us to rank materials according to their absorption ability.

Next we have looked at the HfS_2/PtS_2 heterostructure, a system with a type II band alignment, in order to identify unique peaks that could be associated with interlayer transitions. We have decomposed the dielectric function into its constituting intra-layer, inter-layer and mixed components. We have found that the inter-layer absorption was much smaller in amplitude than the other components. However, compressing the two layers resulted in the creation of a valence impurity band, which led to the formation of a well-isolated peak at the absorption edge. This new feature of the absorption spectrum was associated with inter-layer transitions.

In the last part of our work, we have studied the process of "band nesting" in transitional metal dichalcogenides and transitional metal halides. We have performed

several classifications of the compounds based on the gradient of the energy difference between the top valence and bottom conduction band mapped onto the irreducible Brillouin zone. We have found similar human discernible patterns in the resulting groups, which justified the emerging groups. Moreover, we investigated the joint density of states in two-dimensional transitional metal dichalcogenides and halides. We have noticed the roughly linear relation between the joint density of states and the imaginary part of the dielectric function spectra, especially for the in-plane component of the imaginary part of the dielectric function, $\varepsilon_2^{||}$. Based on this approximation, we have calculated the absorption coefficient and its integrated value over the energy range of the solar spectrum. We have ranked all materials according to the unapproximated and approximated absorption coefficient integral values and found that the two rankings matched extremely well. We have concluded that the joint density of states is a good descriptor for photovoltaic absorption in transitional metal dichalcogenides and transitional metal halides.

Additional information

The results from Chapter 4 of this thesis have been published in 2019 in *Physical Review Materials*. The article entitled *"Interlayer dielectric function of a type II van der Waals semiconductor: the* HfS_2/PtS_2 *bilayer"* was co-authored with Dr. Sabine Körbel, Dr. Carlo Motta, Professor Fadwa El-Mellouhi and Professor Stefano Sanvito.

Moreover, some of the density functional theory calculations presented in Chapter 5 have been performed by Dr. Rui Dong. I used this data to construct the gradients with respect to the conduction and valence bands of 29 distinct 2D transition metal dichalcogenides. These were employed for the classification of the materials as potential photovoltaic absorbers using a clustering method. Additionally, the electronic structure calculations provided by Dr. Rui Dong were used to further derive the joint density of states spectra for all the investigated 2D compounds. These spectra allowed for a ranking of the materials in terms of the short-circuit current density, an important photovoltaic descriptor.

Acknowledgements

Firstly, I am deeply grateful to **Professor Stefano Sanvito** for his exemplary supervision during the past four years. His ability to generate constructive ideas that lead to novel and realistic tasks has been immensely helpful. Also, his use of critical thinking applied to a wide array of problems, ranging from cutting-edge science to everyday organizational management, has been truly inspiring. Not least importantly, I am genuinely thankful for his consistently balanced and understanding attitude throughout my PhD.

Moreover, I am extremely indebted to Professor **Fadwa El-Mellouhi** for her countless helpful discussions, as well as making my stay in QEERI, Doha a very pleasant and productive one. This project would not have been possible without her effort in providing the necessary funding.

I am also very thankful to **Prof. David O'Regan** and to his group members for all the interesting discussions and encouragements.

My deepest thanks to my two mentors, **Dr. Sabine Körbel** and **Dr. Carlo Motta**. Their continuous support and expertise have contributed a lot to my learning experience. Carlo's rigorous approach and insight has been truly beneficial in my first year of PhD. Also, I offer my sincere gratitude to Sabine for her friendship, as well as for patiently and wisely guiding me throughout most of my work.

I would also like to send my gratitude to **Dr. Heesoo Park** for his deep dedication in teaching me how to use the statistical package R.

My sincere gratitude to my good friend, **Dr. Subhayan Roychoudhury** for offering me help countless times through his extraordinary patience and strong physics knowledge.

I am greatly indebted to **Dr. Stella Skiadopoulou** for her incredibly helpful input regarding my thesis, as well as for her optimism and friendship.

I would also like to thank **Michelangelo Domina** for his very useful help and advice.

I offer my gratitude to **Dr. Rui Dong** for collaborating with me on the 2D materials project and for offering me help and support.

Many thanks to **Dr. Emanuele Bosoni** and to **Dr. Mario Galante** for their constructive advice on several matters.

I am also thankful to **Dr. Rajarshi Tiwari** for offering a lot of support with all types of technical and scientific issues.

I would also like to thank **Stefania Negro** for being such an immensely supportive presence in our group. Her administrative help has facilitated my smooth integration in this group, as well as my participation in very interesting summer schools.

My sincere thanks to the **TCHPC** team. Their patience and technical support has been highly helpful.

Last but not least, I would like to send my deepest gratitude to my **parents**, **sister** and **Jorge** for their continuous support and encouragements. This PhD was to a very large extent achievable thanks to them and to my friends in Dublin, **Gaurav**, **Brian**, **Matteo** and **Romina**.

Contents

1 Introduction

1.1 Global solar power resources

Several research studies have been dedicated over the past years to demonstrate that a significant drop in green-house gas emissions can only be achieved through a supply of carbon-free energy and improvements in energy efficiency [1, 2, 3]. Various renewable resources will be employed to this end, although they are expected to play different roles [3]. For instance, wind power is already close to reach fossil-fuel-based capacity in terms of its competitiveness, despite its particular regional constraints. Compared to wind power, solar-based energy solutions such as photovoltaics (PV) and concentrating solar power (CSP), are more advantageous alternatives thanks to their greater potential, despite their relatively higher generation costs [3]. CSP only employs direct sunlight, *i.e.* solar radiation that travels in a straight line to the surface of the earth. This beam radiation is concentrated by mirrors onto a receiver in which a fluid is heated to produce steam. The produced thermal energy is then converted to electricity in a steam turbine [4]. Hence, CSP is a better solution for thermal energy storage compared to electricity storage. Also, the potential of CSP is limited to arid and semi-arid regions [3, 4]. In contrast, PV make use of the photovoltaic effect emerging in semiconductors, whereby both diffuse and direct solar radiation is absorbed and transformed directly into electricity [3]. PV are more appropriate for use in areas with a larger fraction of diffuse radiation such as those at higher latitudes [3]. In Fig. 1.1, courtesy of Ref. [5], the horizontal solar irradiation as recorded in 2019 is illustrated across the globe. It is clear that the ideal places for deploying solar-based resources are the Southeastern Sahara, the Southwestern USA, the Arabian peninsula, Northern Argentina, Oceania and

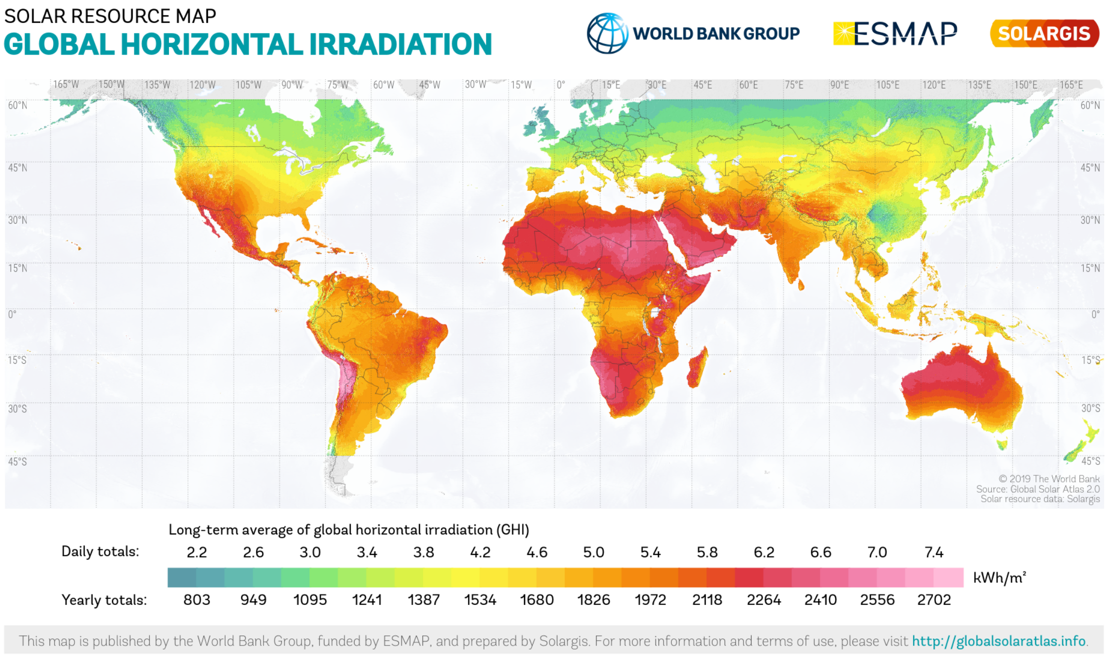

Figure 1.1: Daily and yearly average values of the global horizontal irradiation measured around the world using atmospheric and satellite data with 10, 15, 30-minute time step based on the region. This map and the modelled data herein were produced by Solargis Ref.[5].

Mongolia. Both CSP and PV compete for the same solar resources [3]. However, in terms of cost, CSP is expected to have a higher competitive advantage over PV in the first three locations that exhibit a higher fraction of direct sunlight, while PV will have a higher one in eastern USA, Europe, the Amazon region, Equatorial Africa and monsoon India [3]. Modelling the land use and competition of PV and CSP for the year 2050 under current policies, it is estimated that the combined global CSP and PV potential will be of approximately 135000 TWh/year at a projected cost of around \$0.11/kWh. To put this into perspective, in 2010 the total world power consumption was recorded at approximately 18000 TWh/year. [3].

Throughout this thesis, we focus only on PV technology. In the following, we shall describe the working-principles of a solar cell as well as the different existing types of PV technologies.

1.2 Principles of a solar cell

This section will be loosely based on the chapter "Fundamentals of Solar cell" from the publication entitled "Nanostructured Materials for Solar Energy Conversion" referenced in [6]. The standard architecture of a solar cell consists of a p-n junction, which is an interface of positively (p) and negatively (n) doped semiconductor layers. The latter can be created by adding group-V atoms such as phosphorus to a silicon lattice. P will create covalent bonds with 4 neighboring Si atoms. The fifth electron will be a weakly bound electron and thus, becomes conducting. In this situation, Si is the n-type semiconductor and the impurity atom represented by the negatively-charged phosphorus is called the donor. Conversely, when doping Si with group-III impurity atoms such as boron, the latter forms covalent bonds with the four neighboring atoms. As a result, a conduction hole with positive charge is produced. Then the semiconductor is p-type and the boron impurity atom is an acceptor. Due to the difference in polarity between these two sides of the junction, a nonzero charge concentration gradient emerges, which will in turn produce an electric potential. As a result, electrons will diffuse across the junction into the p-type layer and holes will move across the junction into the n-type layer. These simultaneous migrations leave behind static positive and negative charges, respectively. Due to the electron and hole diffusions, a region that is increasingly depleted of its charge carriers will form [6]. This leads to the depletion region being charged by the ionized donor and acceptor ions, while the regions far from the interface will remain charge neutral as depicted in Fig. 1.2a).

The oppositely charged parts of the depletion layer give rise to an electric field, which opposes the diffusion of charge carriers across the junction. Eventually, the corresponding drift current is offset by the diffusion current across the interface, at which point the Fermi levels of the p- and n-type semiconductor are matched as depicted in Fig. 1.2b). The built-in potential, V_b, is defined as the difference in the electrostatic potential or in the work function between the p-type and n-type

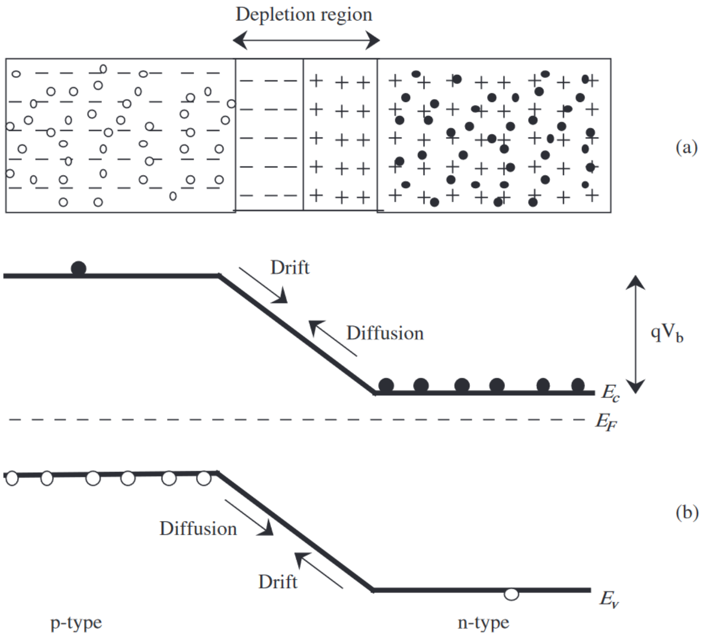

Figure 1.2: a) Pictorial representation of a p-n junction. The dashes and the unfilled circles in the p-part of the junction signify donor atoms and holes, respectively. The crosses and the filled circles in the n-side denote acceptor atoms and electrons. b) The energy band diagrams in thermal equilibrium. This image is originally from Ref. [6].

semiconductors forming the junctions in thermal equilibrium. Its expression is:

$$V_b = \frac{kT}{q} ln \frac{N_A N_D}{n_i^2} \quad , \tag{1.1}$$

where k is Boltzmann's constant, T is temperature of the junction, N_A, N_D are the acceptor and donor concentrations in the p-type and n-type semiconductor, respectively and lastly, n_i is the intrinsic carrier concentration. For an ideal intrinsic semiconductor, n_i is given by the number of holes p in the valence band which is equal to that of electrons n in the conduction band at room temperature *i.e.* n_i=p=n. In a p-type semiconductor at equilibrium, $p \approx N_A$ and similarly, in a n-type semiconductor, $n \approx N_D$. In any case, the charge concentrations are related as $n \cdot p = n_i^2$.

The main process that underpins the operation of any solar PV system is the photovoltaic effect, through which absorbed radiation gets transformed into electricity. This process is not environmentally harmful, since it does not involve any carbon-dioxide emission [7]. When a p-n junction is exposed to solar radiation, photons with energies larger than the band gap excite electrons, thus forming electron-hole pairs called excitons. The light intensity and the number of excitons follow a linear relation [6]. The electric field produced by the ionized impurity atoms in the depletion region causes the excited electrons to drift towards the n-side and the associated holes towards the p-side. As a result, a current starts to flow from the n- to the p-side of the junction when the device is short-circuited as in Fig. 1.3.

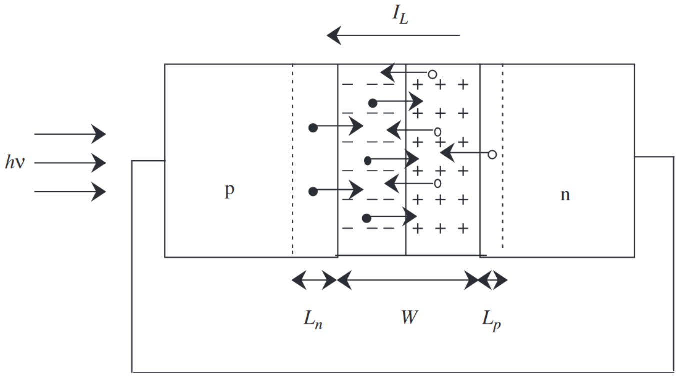

Figure 1.3: Pictorial illustration of current flow in an irradiated p-n junction under short-circuit conditions. Image taken from Ref. [6].

The current is called the short-circuit current, I_{sc}, and it is equivalent to the photogenerated current, I_L, in the case of no resistance. At the same time, the migration of the carriers yields a potential which, under open circuit conditions, is called open circuit potential, V_{oc}. Solar illumination to the junction yields a forward bias or a reverse bias voltage, which reduces or increases, respectively the electrostatic potential in the depletion region. Basically, depending on the polarity of the bias voltage, the drift current is either reduced or increased, which implies that the diffusion of the charge carriers is either increased or suppressed, respectively. The increased diffusion leads to a surplus of carriers called "minority" carriers migrating to the opposite sides of the junction. In other words, electrons are injected on the p-side at a diffusion length, L_n, from the depletion region. Similarly, holes are injected in the n-layer at a length, L_p, from the depletion region. Electron-hole pairs that are within the diffusion length from the edge of the depletion region contribute to the photocurrent too, as seen in Fig. 1.3. The energy band diagrams for the p-n junction short-circuit and open-circuit conditions are shown in Fig. 1.4a) and 1.4b). Certainly the number of processes involving the generation and recombination of carriers in the depletion region is not negligible in a real p-n junction. Electron-hole generation and recombination occur at the energy gap in the reverse and forward

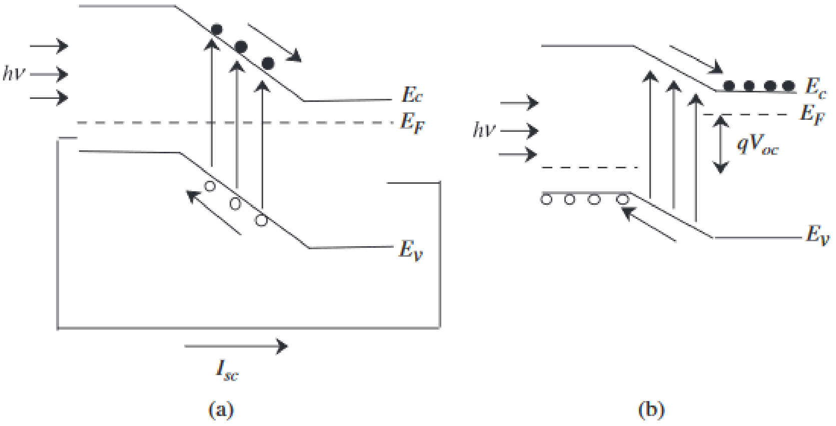

Figure 1.4: a) Energy band diagrams for an irradiated p-n junction where the flowing current is a) short-circuited and b) open-circuited, respectively. Image from Ref. [6].

bias condition, respectively. It can be further shown that the net current under a forward bias, V, is given by

$$I = I_{sc} - I_0(e^{\frac{qV}{kT}} - 1) \quad , \tag{1.2}$$

where I_0 is the reverse saturation current for the case where no voltage is externally applied. I_0 is caused by the diffusion of minority carriers from the neutral regions, where no voltage was externally applied to the depletion one. We shall later provide an exact expression for I_0 in the context of the Shockley-Queisser model. In the case of an open-circuit, there is no net current, which implies that the voltage is:

$$V_{oc} = \frac{kT}{q} ln\Big(\frac{I_{sc}}{I_0} + 1\Big) \quad . \tag{1.3}$$

It can be observed that the higher the recombination current I_0, the lower will be V_{oc}. Hence, V_{oc} is a measure of the recombination occurring in a device. Another useful quantity in solar PV is the fill factor, which is a measure of the quality of a solar cell. It is defined as the maximum output power divided by the open circuit voltage and the short circuit current

$$FF = \frac{V_m I_m}{V_{oc} I_{sc}} \quad , \tag{1.4}$$

where V_m and I_m are the voltage and current that produce the maximum output power. The photoconversion efficiency η or PCE is conventionally defined as the ratio of the maximum generated power to the incident irradiation P_{in}:

$$\eta = \frac{V_m I_m}{P_{in}} = \frac{V_{oc} I_{sc} FF}{P_{in}} \quad . \tag{1.5}$$

The standard measurement conditions to characterize the efficiency of a solar cell are the ASTM G173-03 standard solar photon flux density as tabulated by the American Society for Testing and Materials standard [8]. This standard solar photon flux spectrum is called the air mass (AM) 1.5G and it represents the solar photon flux that illuminates a surface inclined at a 37° tilt towards the equator [8]. Integrating over the solar energy range yields the solar incident power density P_{in} and it is approximately 1000 W/m^2. The other two standard test conditions are a solar cell set at approximately 25°C and a minimum cell area of 1 cm^2 [6, 9].

1.3 Classification of solar cells

The following classification is guided by a systematic PV overview written by Simya et al., which appeared as Chapter 41.1 in Ref.[7]. Solar cells can be broadly categorized into four groups based on the active materials that are employed in their production as well as the generation they belong to. Currently the most commercially accessible and wide-spread PV technology is still composed of first-generation solar cells, namely single and polycristalline silicon cells. The second generation emerged in order to reduce the thickness of the light-absorbing materials, thereby reducing the total thickness to a minimum of a few nanometers. Other directions of research that comprise the third generation include dye-sensitized solar cells (DSSC), organic cells, quantum dots and perovskites. The last generation of solar cells consists of composites [7]. We shall briefly describe some representative device architectures belonging to each generation before we focus on 2D material-based photovoltaics in more detail.

1.3.1 Single-crystalline Si (c-Si) cells

Single crystalline Si (c-Si) cells are composed of a single continuous Si crystal grown along a direction and sliced into wafers. The production cost and the efficiencies of these cells are very high [7]. One of the highest PCE recorded by a single crystalline Si (c-Si) solar cell was recorded at 25% [10]. A Si heterojunction (SHJ) architecture is conventionally adopted in order to reduce the non-radiative recombination at the surface occurring due to the contacts in c-Si cells. This heterostructure is characterized by a thin film of intrinsic hydrogenated amorphous Si (a-Si) sandwiched between the absorber c-Si layer and an either n-doped or p-doped a-Si layer. a-Si is silicon in its non-crystalline form and it is typically arranged in thin layers that have good capability to absorb light [7]. The design of the heterostructure is meant to decouple passivation from charge collection [11]. A drawback of this device is that the gaps between the electrodes can lead to photocurrent loss as light can pass through instead of being reflected back into the layer. Hence, reflective dielectric materials can be used in the gaps. In such a SHJ structure with p- and n- contacts on both sides of the cell, a V_{oc} of 750 mV [12] has been measured. The architecture of the respective device is sketched in Fig.1.5. In general, there is a difference of up to one order of magnitude between the PCE of commercially produced Si wafers and high-quality flat zone c-Si materials that are integrated in this type of architecture. That is due to the intrinsic indirect gap of Si which, in the form used in these commercial devices, cannot be modified. This leads to a low absorption coefficient that can be increased by employing a thicker Si absorption layer. Besides requiring a considerably larger volume of absorbing material than other PV compounds, the long carrier lifetimes imply a higher susceptibility to low levels of defects. [11]. Even taking all these specific features of c-Si into account, the maximum theoretical PCE is 29.4% [13].

1.3.2 Polycrystalline Si cells

An alternative to single-crystalline Si cells that is cheaper to manufacture are polycrystalline Si or multicrystalline Si (mc-Si) [7]. These cells consist of multiple small

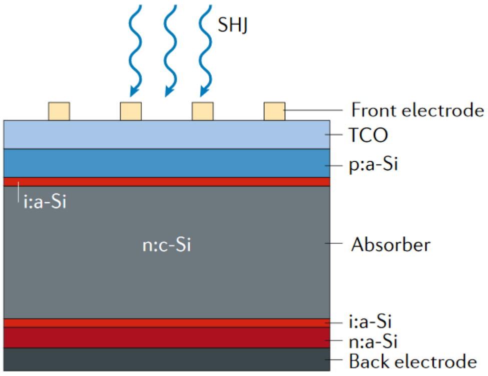

Figure 1.5: Silicon heterojunction (SHJ) cell constituted by a film of intrinsic amorphous Si (a-Si). The p- and n- heterojunctions are embedded near the front and back surfaces, respectively. The transparent conducting oxide layers function as an electrode and as anti-reflective coating. Image taken from [11].

Si crystals which have been recrystallized and therefore, they exhibit grain boundaries and dislocations. Compared to c-Si, this leads to overall smaller values of V_{oc} [11]. Compared to c-Si cells, the efficiency ranges of mc-Si are lower too [7]. Hence, there have been growing efforts in developing high performance mc-Si with a reduced number of structural defects [14]. Certain high performing mc-Si devices have higher minority carriers in the n-part than in the p- one since the most prevalent impurity in Si, namely Fe, acts as an effective electron scattering agent [15]. The best performing mc-Si technology employs a diffused boron front emitter [16] and its PCE is similar to that of c-Si cells and larger than any other polycristalline device. Nevertheless, the losses are greater than those of single-crystal employing technologies [11].

1.3.3 Single-crystalline GaAs cells

The highest PCE ever observed for a single-junction cell was 29.1% for a single-crystalline gallium-arsenide (GaAs) solar cell [17]. The production method is epitaxial lift-off whereby highly reflective back contacts are employed. The highly reflective back contact and the suppression of non-radiative recombination are factors that prevents photons from escaping the cell from the front surface as shown in Fig.1.6. The very sharp absorption onset of GaAs and the almost complete lack of non-radiative recombinations lead to an external radiative efficiency (ERE) close to unity, where ERE is defined as the ratio of the number of charge carriers in the solar cell to the number of photons of a certain energy shining on the solar cell [11].

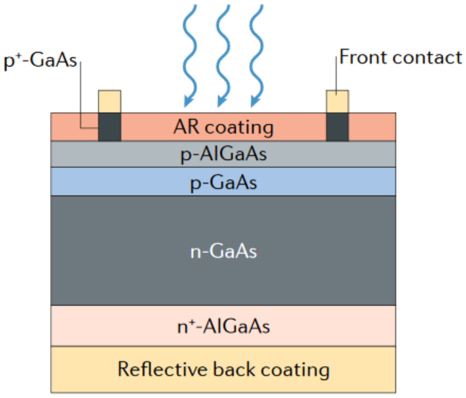

Figure 1.6: Architecture of a single-crystalline GaAs cell consists of of n-type and p-type GaAs, heavily doped n-type and p-type AlGaAs and p-type GaAs. Image taken from Ref. [7].

1.3.4 Thin-film solar cells

The defining feature of this generation of solar cells is that they are produced by depositing heterojunction layers between two contact sheets. The benefit of this architecture is the high absorption coefficient yielded for a layer thickness of about 2.5 μm, compared to Si solar cells that require absorption thickness of up to two orders of magnitude greater [18]. The copper indium gallium selenide (CIGS)-based solar cells is composed of glass, metal and polymer foil. CIGS and cadmium sulfide are the typical p- and n-type semiconductor materials, sandwiched between the molybdenum positive electrical back contact and the negative transparent oxide contact [7].

1.3.5 Dye-sensitized solar cells

This generation of solar cells distinguishes itself from the rest as it does not employ p-n junctions to separate the light generated carriers [7]. A dye-sensitized solar cell is a photochemical system, in which a monolayer of charge-transfer dye is placed between the anode and the electrolyte. The anode is made of nanometer-sized TiO_2 that have been sintered together in order to enable electron conduction [19].

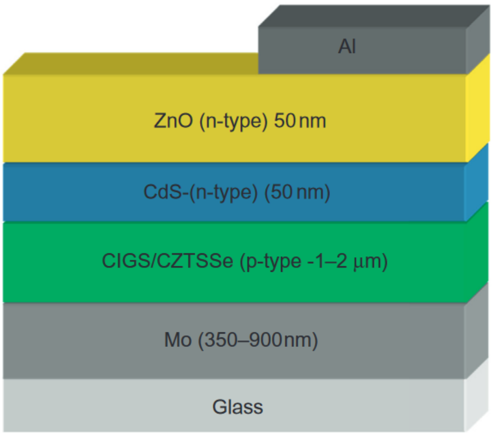

Figure 1.7: Schematic structure of a thin-film solar cell consisting of several layers such as glass, positive and negative contacts composed of molybdenum and zinc oxide and two p- and n-doped semiconductors- CIGS and CdS, respectively. Image from Ref. [7].

This type of oxide has the advantage of being stable and nontoxic [7]. When the dye is excited by incoming light, it releases an electron in the conduction band of TiO_2. Then the dye returns to its original state after receiving an electron from the redox mediator as a result of a redox reaction taking place in its constituting organic solvent. The redox system is in turn replenished at the counter electrode by the electrons passing through the load. The open-circuit voltage in this circuit is dictated by the difference between the redox potential of the electrolyte (or mediator) and the Fermi level of the electrons in the semiconductor TiO_2 film [19]. A diagram depicting the key elements of a dye-sensitized solar cells is shown in Fig.1.8.

1.3.6 Tandem solar cells

The fourth generation solar cells consist of composites made out of polymers mixed with nanoparticles that behave as an absorbing layer. They are convenient as they can be stacked to form a heterostructure that can absorb solar radiation of various wavelengths. Such a device is characterized by an upper and a lower solar cell. In between them, there is a buffer layer through which the photocurrent passes, before the charge carrier are extracted at the electrodes [7]. Stacked cells exceed single cells in terms of their efficiency. [17].

After having reviewed some of the PV technologies that are associated with each

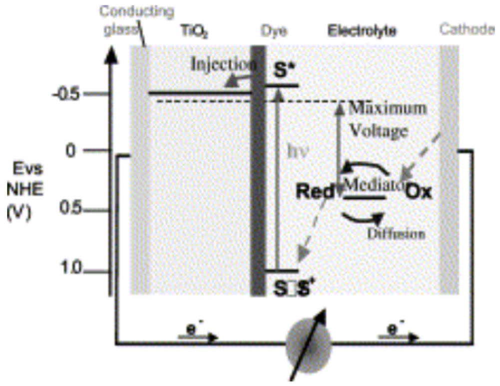

Figure 1.8: Diagram describing the general operation of a dye-sensitized nanocrystalline solar cell. A photon is absorbed by a dye which gets excited from state S to state S*. The electron is released into the conduction band of TiO_2 and then transported through the sintered particles to the contact, while the hole gets injected into the electrolyte. The dye returns to its ground state after receiving electrons from a redox mediator. The oxidated mediator diffuses towards the electrodes. This image is from Ref. [19].

solar cell generation, we present in Fig.1.9 the progress that has been made in the past 27 years in terms of the PCE of single cell devices. The Shockley-Queisser theoretical limit, which we will review in the upcoming sections, is taken as a benchmark.

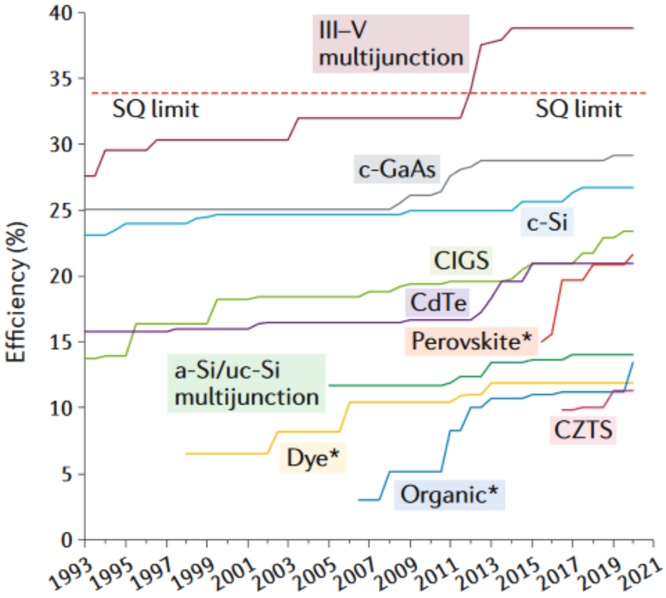

Figure 1.9: The PCE for various technologies over the past 27 years compiled at air mass 1.5G and cell area > 1 cm^2. The efficiencies in this picture were compiled and collated in this diagram by the authors of Ref. [17].

1.4 2D materials in photovoltaics

The herein overview of 2D materials employed in PV technologies will be following the comprehensive review published in 2019 by Das et al. [20].
Two-dimensional atomic sheets are layered crystalline solids of atomic thickness, which exhibit covalent bonds between in-plane atoms and van der Waals bonds between the out-of-plane atoms [21]. Several types of 2D materials have been synthesized and intensely studied. Few notable examples include graphene [22], [23], [24], diatomic hexagonal boron nitride (h-BN) [25] and transition metal dichalcogenides (TMDs) [26], [27]. A comprehensive study of all the different classes of 2D compounds can be found in the work of Miró et al. [28].

We shall provide an overview of the three main uses that 2D materials have in various PV technologies. Firstly, we briefly discuss the role 2D materials play as key elements in the architecture of a solar cell that either has a non-2D compound acting as an absorbing material or which is a mixed heterojunction that is composed of a 2D crystal in conjunction with a non-2D compound.
The motivation behind developing the second generation solar cells was driven by the need to reduce the active absorber thickness of silicon [29, 30, 31, 32]. Despite the existing technological predictions regarding the production of high efficiency Si layers of only 25 μm by 2024, it seems that industrial technological solutions involving the increase of absorption efficiency of thin Si cells are not yet tangible [33]. Nevertheless, due to their intrinsically high conductivity, transparency and flexibility, 2D materials will likely be integrated in the next generation of flexible silicon solar cells as bendable substrates [20]. The potential contribution of 2D crystals to the emerging field of flexible nanoelectronics that comprise smart tablets, smart phones, smart watches and smart fabrics is already highly promising [21]. Moreover, hybrid organic-inorganic perovskites have been drawing a lot of interest as PV materials, since they are cheap light-harvesting materials with low temperature production conditions and with longer carrier diffusion lengths than silicon [35, 36, 37]. This last condition ultimately might be the reason for their superior PCE values [20]. However, their poor stability under normal humidity conditions has proven to be an obstacle in their large-scale production [38]. Having said that, 2D

materials have also been used as stabilizer materials for perovskite solar cells [20]. Furthermore, WS_2 and MoS_2 have each been employed in perovskite PV devices as an electron-extraction layer [39].

Secondly, we will focus on the prospect of 2D materials, with a special emphasis on transition metal dichalcogenides (TMD), as future flexible, light-absorbing media for thin, lightweight solar cells. Their applicability to solar cell devices is attributed to their bandgaps that have energies matching the visible to near-infrared part of the solar spectrum. Fig.1.10, taken from Ref. [40], indicates the large range of band gaps that various 2D semiconductor materials possess, along with the band gap range that each 2D semiconductor can achieve by altering the number of layers, by alloying or straining. The wide array of band gaps, spanning from 0 to 8 eV implies that 2D materials can be employed in a large variety of optoelectronic applications, such as photovoltaics, light-detectors, fiber optics communications and displays [20].

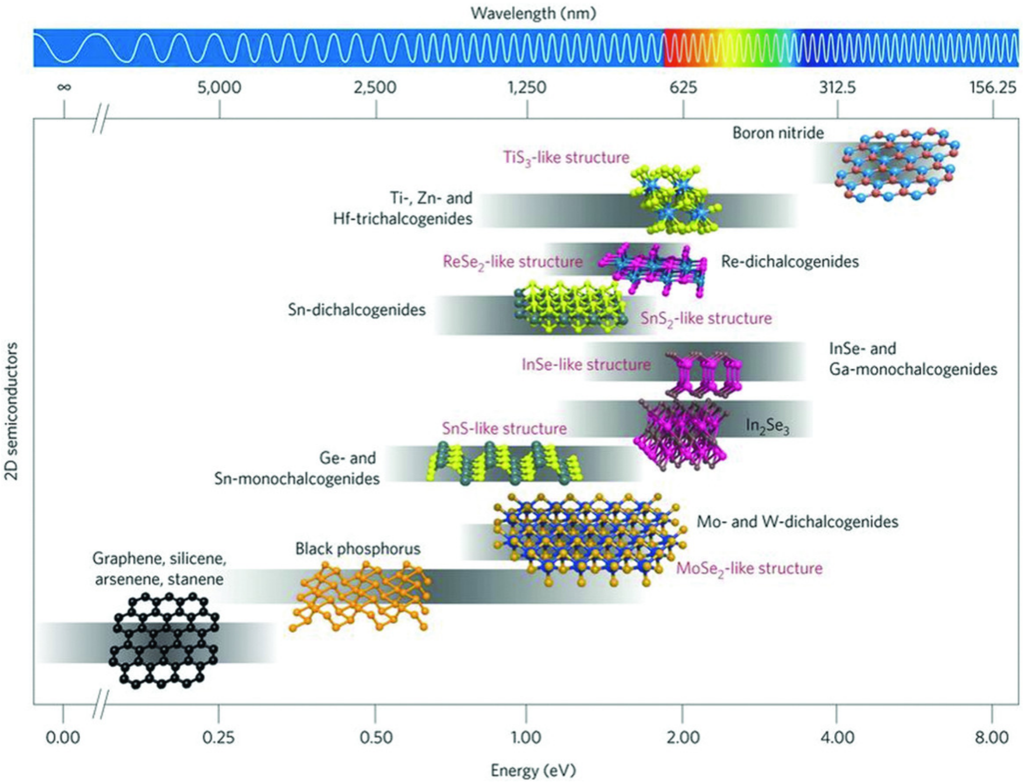

Figure 1.10: Visual representation of the band gap values and crystal structures of various families of 2D materials. The gray bars represent the range of band gap values that can be obtained by altering the number of layers, by alloying or straining. This image is taken from Ref. [40].

It may seem that creating a solar cell only with 2D materials would have low absorption capabilities due to their atomic thickness; however, that is not necessarily the case. In theory, a single TMD monolayer with an active layer of less than 1 nm can absorb as much sunlight as 50 nm of Si or 15 nm GaAs, hence generating electric currents of up to 4.5 mA·cm^{-2} [41]. The absorbance is a physical quantity that indicates the percentage of incident light that is absorbed through a material and it has been recorded for MoS_2, $MoSe_2$, and WS_2, graphene, along with the solar flux, where all monolayers had a layer thickness of L=1 nm. The graph shown in Fig.1.11 together with the compilation of its results were produced by Bernardi et al. [41].

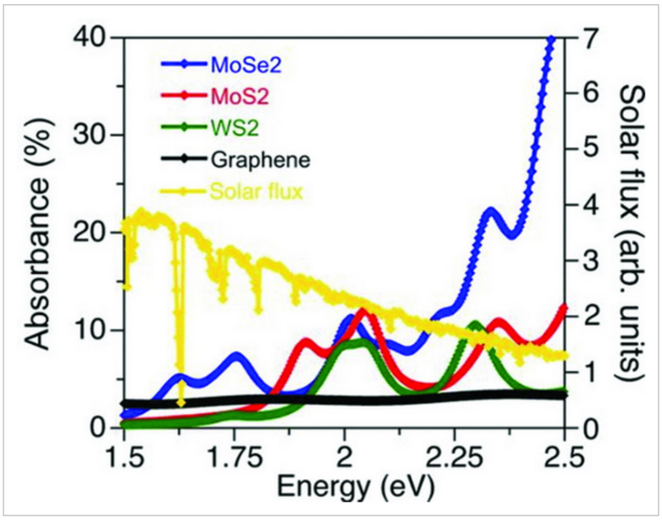

Figure 1.11: Absorbance of three TMD monolayers and graphene, along with the incident AM1.5G solar flux. This picture is the work of Bernardi et al. [41].

Also, in the case of monolayers such as MoS_2 and WS_2, there are close to no nonradiative recombination losses due to their direct band gaps [20]. Nevertheless, despite exhibiting large values of absorption coefficient, a typical monolayer of TMD only absorbs approximately 10% of the solar spectrum [20].

This brings us to the third application of 2D materials, namely as building blocks of heterojunctions commonly referred to as 2D or van der Waals heterostructures [42]. By combining multiple 2D layered materials with distinct bandgaps, the efficiency of the resulting van der Waals heterostructure is thought to be improved compared to that of the constituting individual layers [20]. Hence, developing light-trapping designs [43, 44] as well as exploring the possibilities of producing novel heterogeneous van der Waals cells of only a few layers [45] will lie at the foundation of the emergent field of "all 2D" solar cells. Fig. 1.12a), taken from Ref. [20], pictorially describes a vertical van der Waals heterojunction composed of two sheets of 2D crystals. Such a device is a bilayer van der Waals heterostructure. Fig. 1.12b) depicts a type-II diagram that corresponds to the bilayer heterostructure which enables separation of charges. In this example, excitons with sufficiently long lifetimes can diffuse through the 2D/2D interface and can get dissociated.

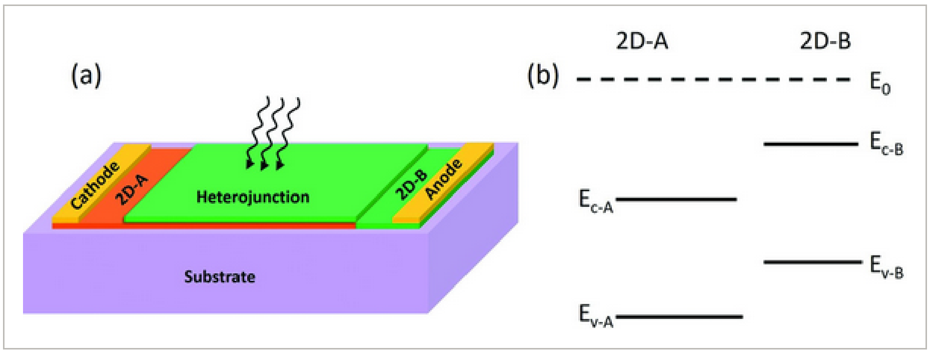

Figure 1.12: a) Illustration of an "all 2D" heterojunction acting as a solar device. b) Diagram of a type II 2D-heterojunction. Here the valence and conductions bands of layers A and B are represented relative to the vacuum level E_0. Image taken from Ref.[20]

.

The probability of electron–hole recombinations in "all 2D" heterostructures is very low since the carriers are separated due to the atomically sharp interfaces and the absence of a depletion region in between the 2D films [20]. Note that despite the low probabilty of interlayer recombination, the overall absorption of photons can be strong as the exciton could be generated in one layer and then it could go through several other processes before recombining between the two layers. Carrier extraction has been thus ensured for several heterogeneous van der Waals cells [46, 47, 48, 49]. Nevertheless, as a cause of the built-in potential across the interface, the probability of interlayer tunnelling recombination is not negligible [47, 48]. Despite the fact that "all 2D" heterostructures exhibit reduced densities of interface trap states [46], the requirement to employ large-area 2D materials, which are scarce, is an inherent limitation [20]. We shall now enumerate notable examples of promising PV "all 2D" heterostructures. Vertically stacking a p-type monolayer WSe_2 and n-type few-layer MoS_2 results in an atomically thin p-n heterojunction that exhibits an open circuit voltage V_{oc} of $\approx$ 0.27 V under a laser illumination of 514 nm and 5 μW [50]. The measured open circuit voltage associated to this few-nanometer thick heterostructure is high considering that one of the most optimized c-Si heterojunctions of approximately 100-μm thickness has attained a V_{oc} of 0.75 V and a PCE of 24.7% [51]. Another interesting example of the great potential that 2D junctions exhibit in terms of PV application is demonstrated by a n- and p-doped, respectively, MoS_2/MoS_2 bilayer junction. Under UV-ozone plasma treatment, it turns out that n-type MoS_2 nanosheets are converted to p-type nanosheets [52]. Moreover, a recent study demonstrated an external radiative efficiency higher than 50% and absorbance exceeding 90% in a 12 nm thick WSe_2/MoS_2 bilayer heterojunction [53]. Despite the promising prospect of combining in a Lego-type fashion all the possible TMDs, the growth of such "all 2D" heterostructures is possible for only a few chalcogenides [20]. However, the idea of building 3D heterostructures using 2D materials for the efficient light collection and charge transfer needed for the photovoltaic effect has been proposed by Novoselov et al. [54]. Constructing heterostructure by stacking one layer at a time typically involves first mechanically and chemically exfoliating the 2D materials from their bulk crystals. These are then manually stacked into vdW heterostructures [55]. The shortcoming of heterostructures produced with these methods is that they can present low quality interfaces that contain trapped chemicals or solvents used during the exfoliation, that are necessary for the transfer [55]. Therefore, an alternative process that can be implemented for large-scale production consists of growing 2D materials. The direct synthesis of 2D heterojunctions results in better optimized interfaces as well as more precise control over the location and number of layers [55]. We will conclude this section dedicated to solar cells by highlighting the outline of the present thesis.

The overarching goal of the project is to screen materials for photovoltaic applications. Therefore, in the remainder of this chapter, we shall discuss three existing theoretical models that were proposed in literature to help determine the photovoltaic efficiency of devices. In Chapter 2 we shall present the theoretical framework *i.e.* density functional theory, which was employed throughout this PhD to obtain the electronic structure of various compounds together with its limitations regarding the determination of the band gap. Then we go on to discuss the details regarding the chosen quantum chemistry code and the exchange-correlation functional that was used most extensively. Moreover, we will briefly indicate the steps involved in the derivation of the central quantity of this thesis, the dielectric function. Lastly, we shall mention the basic principles behind the k-means clustering method and its use for classifying materials.

In Chapter 3 we present our method for obtaining the photoconversion efficiency of standard seminconductors used in solar cells, solely through ab-inio methods. The efficiencies and other relevant descriptors of silicon and methylammonium lead iodide will be shown. Moreover, we shall examine the interplay between the pre-edge absorption spectrum of a material and its photoconversion efficiency. The objective will be to determine whether a full ab-initio treatment of the pre-edge absorption coefficient is attainable. We will introduce a more robust descriptor to describe the performance of photovoltaic materials in terms of their absorption. This quantify defined as 95% of the saturated J_{sc} and its corresponding characteristic material thickness will be used to rank a total of 6 compounds.

Chapter 4 will be dedicated to an investigation of the dielectric function in vertically stacked TMD monolayers. We aim to observe whether the interlayer transitions in heterostructures with type II band alignment can be associated with clear, distinguishable peaks in the dielectric function spectrum. Once we will decompose the total dielectric function into its three constituting terms (intra-layer, inter-layer and mixed components), we will analyze the amplitude of the inter-layer component relative to the intra-layer one. We shall also look into the effects of gradually compressing the two layers together on the band structure and the dielectic function spectra.

In Chapter 5 we plan to study the absorption in 2D materials, in particular in transition metal dichalcogenides, by investigating its relationship to the regions in reciprocal space where band-nesting arises. To this end, we will consider the gradients of the energy difference between the the top valence and bottom conduction bands, *i.e.* $|\nabla_{\boldsymbol{k}}(E_{c1} - E_{v1})|$ mapped onto the irreducible Brillouin zone of 29 compounds. We aim to classify these compounds based on the mentioned quantity, both in their monolayer and bulk form, using statistical algorithms such as "k-means". We plan to also consider the solar flux in the expression of the quantity over which we shall classify the compounds. This will be done in order to study transitions occurring through band-nesting at energies matching with the strong solar flux. Separately, we plan to examine the relationship between the spectrum of the joint density of states and that of the imaginary part of the dielectric function. Assuming an almost linear relation between the two spectra, the goal is to be able to use the joint density of states in order to determine the absorption coefficient and the short-circuit current density. These two macroscopic quantities will serve as the quantitative criteria for ranking the studied 2D compounds and hence, will aid in the screening of potential photovoltaic compounds.

In Chapter 6 we will briefly go through the findings and results of this thesis. The future work and goals will also be mentioned.

As a last note, the physical quantities expressed throughout this thesis are in S.I. units. An exception is made for the expressions of the dielectric function in Chapters 2 and 5 where atomic units were employed instead. This was done in order to simplify the notation.

1.5 Theoretical models for solar cells

Obtaining reliable photoconversion efficiency measurements is an intricate process that needs to account for many factors such as the varying composition of sunlight through the atmosphere, the changing parameters for temperature and light intensity, the correct calibration of the reference device and the exact determination of the cell area [10]. In the face of all these challenges, there have been considerable efforts made over the past 60 years to devise models that accurately predict solar efficiency. Such models are immensely helpful as they guide the selection of the appropriate materials for photovoltaic applications. Thus, photovoltaic models provide a set of physical quantities that define materials as suitable or not for solar cell devices. These key quantities are termed "descriptors" and they can vary from model to model. The most well-established model that has introduced the so-called "radiative efficiency limit" in physics is the Shockley-Queisser (SQ) model [56]. The SQ limit is a benchmark for maximum solar energy conversion efficiency by which new emerging photovoltaic devices are assessed [57]. It stands out as a model that is not material specific but which provides an upper-bound estimate of the number of quantities of interest in any solar device. We will dedicate this section to discussing the assumptions that underlie this important model. To this end, we will provide a broad overview of the physical processes and the descriptors typically used for solar devices. These are the short-circuit current density J_{sc}, the open-circuit voltage V_{oc} and the photoconversion efficiency PCE or equivalently, η. Further on, we will briefly introduce two more recent models: the "multiple parameter" model [58] and the "spectrally limited maximum efficiency" (SLME) model [59]. We will end by discussing the goals of these models and their inherent limitations. The following comparative overview will serve as the foundation for developing our own model that will be presented in Chapter 3.

1.5.1 Shockley-Queisser model

One of the earliest purely theoretical investigations of the maximum efficiency of a solar cell dates back to 1961 and it is attributed to William Shockley and Hans-Joachim Queisser. The upper limit for the efficiency that is derived in this model does not rely on material-dependent values, but rather on the "*nature of atomic processes required by the basic laws of physics*", specifically the principle of detailed balance [56]. We shall base our brief explanations of this model on the original paper by Shockley and Queisser referenced in Ref.[56]. The model examines a typical p-n junction cell from a thermodynamic perspective. The great advantage of this approach is that the efficiency depends on very few parameters. Therefore, the SQ efficiency limit significantly exceeds semiempirically determined ones that are based on experimental parameters such as carrier lifetimes [60]. The far-reaching scope of this model is justified as it sets the upper limit for device efficiency, thus it helps in understanding the room for improvements that can be achieved in real devices. The basic assumptions and quantities mentioned here will prove relevant for our own work presented in Chapters 3 and 5. The analysis is based on the following assumptions:

1. the only recombination between electrons and holes is radiative
2. the absorption is an energy-dependent step-function
3. the solar cell and the sun emit radiation whose spectra can be approximated

by the emission of two black bodies, one with a surface temperature of T_c=300 K and the other with T_s=6000 K, respectively.

The radiative recombination determines the efficiency based on the principle of detailed balance, whereby in equilibrium, each elementary process is balanced by its reverse process [61]. The most important portion of the radiative recombination is assumed to be between free holes and electrons and it is proportional to the product of their densities. Moreover, the fact that radiation energies higher than the band gap energy yield complete absorption is motivated by the goal to study the theoretical photoconversion limit, which entails the complete omission of material specific features besides the band gap. Finally, the thermodynamic framework, in which the absorption and recombination processes are studied, requires the treatment of the solar cell and of the main radiating source (e.g. the sun) as ideal black bodies [56]. In the following, the quantities involved in the SQ model will be illustrated. The photon flux Φ_{sun} is generally defined as the number of sun-generated photons hitting the cell per unit time, area and energy. In the SQ model, the solar photon flux is determined based on the irradiance of a black body that corresponds to the sun surface with a temperature of $T_s = 6000$ K measured at the Sun–Earth distance [9]. Therefore, the maximum photogenerated current density, J_{max}, for an illumination with a photon flux Φ_{sun} is:

$$J_{max} = q\int_0^\infty \Phi_{sun}(E)a(E)dE = q\int_{E_g}^\infty \Phi_{sun}(E)dE \tag{1.6}$$

where E is the photon energy and q is the elementary charge. Here $a(E)$ is the absorbance of the material and in the SQ model it is 0 for energy values lower than the bandgap E_g and unity for those higher. This comes from the second assumption, namely that only the incident photons with energies equal or higher than E_g will get absorbed, and in turn- each of these will generate an electron-hole pair, thus leading to an absorption efficiency that is effectively 100%.

The reverse process has to be considered as well, namely the case where an electron and a hole meet and recombine, emitting a photon and thus reducing the efficiency of the cell. Note once more that in the model here, the steady state is when the cell is in thermal equilibrium with its surrounding black body environment at temperature T_c.

In this case, Kirchhoff's law of thermal radiation, a particular case of the principle of detailed balance, dictates that the rate of absorption and the rate of emission of photons have to be exactly equal. This condition implies that the rate of electron-hole pairs that are generated from absorbing photons emitted by the surrounding black-body at temperature T_c is equal to the rate of photons that are emitted from the cell as a result of electron-hole recombinations. Let this aforementioned rate that describes the thermal equilibrium state be F_{c_0}. Inside the cell, the rate of purely radiative recombinations is:

$$F_c(V) = F_{c_0} e^{V/Vc} \quad , \tag{1.7}$$

where V is the potential across the illuminated cell, equivalent to the difference between the quasi-Fermi levels of the holes and electrons, T_c is the solar cell temperature and $V_c = kT_c/q$ is the so-called "thermal voltage". In the SQ model, Planck's law is generalized such that the rate of radiative recombination current density is essentially dictated by the blackbody emitted photon flux of energy equal or higher than the band gap times the exponential factor containing the ratio V/V_c. Thus, the emitted photon flux Φ^e can be described as a function of the photon energy E and the voltage V:

$$\Phi^e(E, V) = \frac{2\pi E^2}{h^3c^2} e^{\frac{qV}{kT_c}} \frac{1}{e^{\frac{E}{kT_c}} - 1} \quad , \tag{1.8}$$

where h is Planck's constant, c is the speed of light and k is Boltzmann's constant. However, it was shown by the groups of De Vos et al. [62] and Ruppel et al. [63] that a more accurate expression for the blackbody emitted radiation is:

$$\Phi^e(E, V) = \frac{2\pi E^2}{h^3c^2} \frac{1}{e^{\frac{E-qV}{kT_c}} - 1} \quad . \tag{1.9}$$

Integrating the emitted flux expressed in Eq. (1.9) over the energy range gives the radiative recombination current density J_r:

$$J_r(E_g, V) = f_g \cdot q \int_{E_g}^{\infty} \frac{2\pi E^2}{h^3c^2} \frac{1}{e^{\frac{E-qV}{k_BT_c}} - 1} dE \quad , \tag{1.10}$$

where f_g is a geometrical factor. In the SQ model, $f_g = 2$ since the radiation is emitted from both sides of the cell, top and bottom. For simplicity, we will omit writing the current densities as functions of bandgap energies, *i.e.* $J_r(E_g, V) = J_r(V)$. At steady state the final external current density, J_{ext}, has to coincide with the sum of the individual current densities emerging in the cell [9] :

$$J_{ext} = J_{max} - J_r(V) + J_{nr}(0) - J_{nr}(V) \quad . \tag{1.11}$$

Here $J_{nr}(0)$ represents the current density that results for reasons different from the photogeneration. This is the nonradiative recombination current that is engendered by Auger or thermal effects that occur under a certain bias in the cell. Now one can rewrite this equation as:

$$J_{ext} = J_{max} - J_r(0) + [J_r(0) - J_r(V) + J_{nr}(0) - J_{nr}(V)] \quad . \tag{1.12}$$

Here the square bracket is the net current in a solar cell that is completely surrounded by a black body at temperature T_c. It shows that at zero bias there is radiative and non-radiative generation of electron-hole pairs and at a finite applied voltage there are losses in the form of radiative and nonradiative recombinations [9, 56].

The short circuit current density is defined as the illumination current due to solar flux, J_{max}, from which the radiative recombination current at zero-bias is substracted:

$$J_{sc} = J_{max} - J_r(0) \quad . \tag{1.13}$$

Furthermore, an additional parameter, f, is introduced in the idealized case of the cell being in contact with a black body of the same temperature, T_c. It is defined as the fraction of current that is equal to the difference between the radiatively generated current and the radiatively lost one, respectively,

$$J_r(0) - J_r(V) = f[J_r(0) - J_r(V) + J_{nr}(0) - J_{nr}(V)] \quad . \tag{1.14}$$

In the Shockley-Queisser model, $f = 1$ since $J_{nr}(V)$ and $J_{nr}(0)$ are neglected. This implies that

$$J_{ext} = J_{max} - J_r(V) \quad . \tag{1.15}$$

For the case where $J_{ext} = 0$, the open-circuit voltage V_{oc} is given by the associated voltage:

$$V_{oc} = \min_{V}[J_{ext}(V)] \quad . \tag{1.16}$$

The power density is defined as the product of the the total external current density and the voltage:

$$P = V \cdot J_{ext}(V) \quad . \tag{1.17}$$

Having said that, we now introduce the maximum power point voltage as the voltage that maximizes the power density:

$$V_{mpp} = \max_{V}[J_{ext}(V) \cdot V] \quad . \tag{1.18}$$

The corresponding current density is then:

$$J_{mpp} = J_{max} - J_r(V_{mpp}) \quad . \tag{1.19}$$

The ratio between the maximum obtained power density and the product of the short circuit current density and the open circuit voltage gives the fill factor (FF). Its expression is:

$$FF = \frac{V_{mpp} \cdot J_{mpp}}{V_{oc} \cdot J_{sc}} \quad . \tag{1.20}$$

Finally, these quantities enable the calculation of the PCE, which is found to be the ratio between the maximum obtained power density and the total incident solar power density:

$$\eta = \frac{P_{max}}{P_{in}} = \frac{V_{mpp} \cdot J_{mpp}}{P_{in}} = \frac{FF \cdot V_{oc} \cdot J_{sc}}{P_{in}} \quad , \tag{1.21}$$

where P_{in} is the power density produced by integrating the solar flux ϕ_{sun} over the solar spectrum energy range. With all these considerations taken into account, it was shown that the maximum efficiency for a junction with an energy band gap of 1.1 eV is 30%. Note that the descriptors in this model are functions only of the band gap, which is in fact the only system-dependent employed variable. The strength of this canonical model lies in its potential to establish a theoretical upper limit for the photoconversion efficiency. This can serve as a further benchmark for more accurate theoretical and experimental efficiency estimations.

In the work of Sven Rühle [9], a comprehensive analysis of the SQ model was used to determine the key descriptors for a series of various PV materials with different band gaps under standard solar test conditions. The SQ model did not assume standard testing conditions as it considered a solar cell temperature of 300 K and a solar spectrum coinciding with the radiation emission spectrum of a black body at a temperature of 6000 K. Therefore, in this work, one of the main distinctions from the SQ model resides in employing the true solar ASTM G173-03 solar photon flux [8] instead of the theoretical black body emission radiation. Both of the two standard solar irradiance distributions are considered, namely at 'direct normal' and at 'hemispheral on 37° tilted surface', respectively. These spectral distributions are conventionally termed "$AM1.5D$" and "$AM1.5G$" [8]. Hence, in Eq. (1.6) which defines J_{max}, the spectral photon flux ϕ_{sun} is:

$$\phi_{sun} = \frac{q\lambda}{hc} AM1.5G \quad , \tag{1.22}$$

where λ is the photon wavelength. In Eq.(1.6), the integration range is between the band gap E_g and the highest solar photon energy reported in the ASTM G173-03 standard, which is in the UV range at 4.43 eV. The other distinction from the SQ model is that the cell is set at the standard testing temperature, *i.e.* $T_c = 298.15K$. Implementing a slightly modified version of the SQ model, the short circuit current density, the open circuit voltage and the efficiency values are predicted for a range of different solar devices, some of which were mentioned in our overview of existing solar cell technologies. The highest certified experimental values for J_{sc}, V_{oc} and η are identified for a series of lab solar cells by Green et al. [64] and are presented as percentages relative to the detailed balance limit ones in Fig.1.13a), b) and c). This enables a comparison between the state-of-the-art parameters and the theoretically predicted ones in the detailed balance limit. As can be seen, laboratory-tested thin film GaAs solar cells have the highest relative efficiency, reaching more than 80% of the detailed balance limit one. This makes them the best optimized solar cell. Relative to the theoretically predicted values, the J_{sc} and V_{oc} of GaAs calculated by Rühle are also very high, reaching values of approximately 90% and almost 100%, respectively. The second best optimized device is based on crystalline Si, an indirect band gap semiconductor. The short circuit current density and the open circuit voltage are also very close to their detailed balance limit values, *i.e.* reaching more

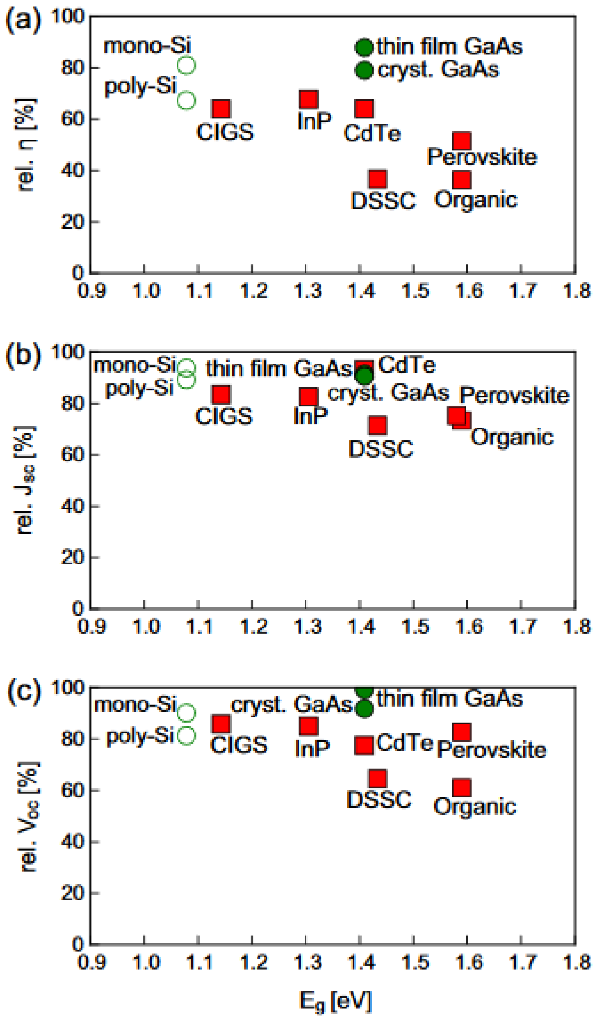

Figure 1.13: The ratios presented as percentages of the photoconversion efficiency a), the short circuit current density b) and the open circuit voltage c) parameters of solar cells with highest recorded empirical efficiencies [64] relative to the corresponding values calculated in the detailed balance limit in [9]. All the quantities are shown as a function of the band gap. The best performing devices are presented, namely homojunctions (circles), heterojunction devices (squares) with indirect band gap (empty symbols) and absorbers with direct optical transitions (full symbols). Image taken from the work of Rühle [9].

than 80% for both parameters. The fact that Si is an indirect gap semiconductor is not accounted for here although clearly this would influence its absorption spectrum [9].
Unlike in the case of highly optimized homojuctions, it is claimed that heterojunctions can currently reach only up to 68% of the efficiency obtained in the detailed balance limit. Their lower optimization levels are attributed to the voltage losses due to band edge discontinuities or non-optimized energy levels at the junction. Especially in dye sensitized solar cells and organic solar cells, the relatively low V_{oc}, reaching approximately 60% of is theoretical value, limits the photoconversion due to the non-optimized energy levels of the dye [9].

In contrast, organo-metal halide perovskite solar cells are highly optimized solar cells that present efficiencies above 80% of their theoretical limit. Of course, there are other factors unaccounted for that could substantially reduce the efficiency. Nevertheless, a more realistic treatment of the efficiency that accounts, for instance, for the stability of the pervoskite under fluctuating levels of humidity, is beyond the scope of the analysis of Rühle.

1.5.2 Multiple parameter model

The SQ assumed that all the photons with an energy higher than E_g are absorbed and then some are extracted as current, which is a clear simplification. To improve upon the limitation of the SQ model, Alharbi et al. [58] propose an efficient descriptor model that takes into account the inhomogeneity of the absorption spectrum. In addition, this model considers the charge carrier diffusion length, L_d, in order to account for the carrier transport ignored in the SQ model. L_d is the mean distance that an excited carrier travels through diffusion before recombining [58]. Since expensive calculations would be required to obtain this quantity, the model employs four different values for L_d, namely of 200 μm, 10 μm, 0.6 μm and 0.1 μm. Each of these values are chosen in this order as characteristic for indirect-gap semiconductors, direct-gap semiconductors, organometallic semiconductors such as hybrid perovkites and excitonic cells such as organic cells, based on empirical observations regarding the excitonic behaviour. The PCE is calculated as in the SQ model according to Eq.(1.21), employing J_{sc}, V_{oc} and FF. However, these quantities are obtained here by relying on experimental parameters of L_d and employing fittings. For example, the maximum obtained photocurrent density, defined in Eq.(1.6), is here approximated as a function of the band gap E_g through a fitting:

$$J_{max} = a \cdot e^{-b \cdot E_g} \quad , \tag{1.23}$$

with a=73.531, b=0.440 and c=1.862. The next descriptor that is defined is the short circuit current density:

$$J_{sc}(E, \alpha(E), \theta_{eff}) = q \int_{E_g}^{\infty} \phi_{sun}(E)[1 - e^{-\alpha(E)L_d/cos(\theta_{eff})}]dE \quad , \tag{1.24}$$

where θ_{eff} is a parameter that is chosen such that the ratio of J_{sc}/J_{max} is maximized for varying values of $1/cos(\theta_{eff})$. Unlike in the SQ model, the absorbance here is not necessarily taken to be 1 for energies higher than the band gap. It is governed by the absorption spectrum $\alpha(E)$ and it is obtained from the same first principles calculations that help determine E_g. Also, the solar AM1.5G solar photon flux and a cell temperature of 25°C are considered. The recombinations are accounted empirically by L_d. Fitting real experimental values of V_{oc} as a function of E_g yields:

$$q \cdot V_{oc} = E_g - (0.0114 E_g^{1.8617} + 0.057 E_g + q \cdot V_{L0}) \quad , \tag{1.25}$$

where V_{L0} is a constant fitting parameter. This parametrisation yields two fitting lines, one for excitonic cells, which result in V_{L0}=0.5 V and another one for non-excitonic cells with a corresponding V_{L0}=0.2 V. V_{L0} is meant to account for voltage losses. These are especially big for heterojunction excitonic cells due to their intrinsically larger band offsets that enable the dissociation of excitons [58]. The exciton binding energies in such cells are not negligible by comparison to those of excitons that form in non-excitonic cells [58].

A similar fit is repeated for the experimental fitting factor FF in terms of the empirical open circuit voltage V_{oc}. It is found that the parametrization can be expressed as:

$$FF = \frac{V_{oc}}{V_{oc} + akT} \tag{1.26}$$

where k is Boltzmann's constant, T is room temperature and $a = 6$ and $a = 12$ were found to best fit the upper limits of the empirical FF for non-excitonic cells and excitonic cells, respectively. The resulting values for all these descriptors, together with the experimentally collated ones are shown in Fig. 1.14 for non-excitonic cells. Similar to the descriptors obtained within the detailed balance limit, this model shows that state-of-the-art devices based on Si and GaAs have almost reached their optimization limits, whereas hybrid perovskite $MAPbI_3$, CIGS, CdTe, and InP solar cells still have room for improvements. It is shown that in the case of non-excitonic cells, the PCE is highly dependent on the absorber thickness up to a few μm, after which it fully saturates. The exception are Si devices which require thicknesses of at least two orders of magnitude larger to reach saturation.

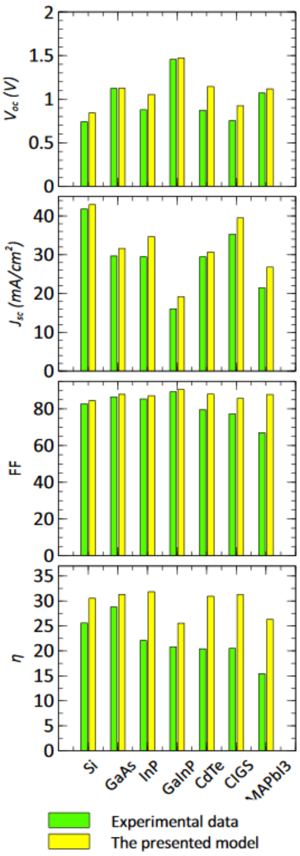

Figure 1.14: The values for the experimental photovoltaic descriptors of the best performing non-excitonic cells based on Si [51], GaAs [65], InP [66], GaInP [67], CdTe [68], CIGS [69] and the hybrid perovksite $MAPbI_3$ [70] are compared to the ones obtained in the model proposed by Alharbi et al. [58]. Image taken from Ref. [58].

1.5.3 SLME model

The following model proposed by Yu et al. [59] is called the “spectroscopic limited maximum efficiency" (SLME). It relies on the intrinsic properties of the materials by only considering the band gap, absorption spectra shape and recombination losses. At the same time, it also considers the cell thickness, which is an extrinsic property. This is set to L=0.5 μm, in order to account for the "material-dependent spectroscopic properties".

This model stands out, first of all, as it takes into account the existence of the lowest dipole-forbidden (DF) and dipole-allowed (DA) direct transitions, and it makes the distinctions between direct and indirect band gaps. Materials can be classified in four “optical types" as follows. If the DA direct gap, ${E_g}^{da}$, corresponds to the lowest allowed energy transition and the next one above it, ${E_g}^{df}$, corresponds to a direct-forbidden transition, *i.e.* (${E_g}^{da} \leq {E_g}^{df}$), then the material is defined as an OT1. Similarly, if the lowest direct transition is forbidden, *i.e.* ${E_g}^{df} < {E_g}^{da}$, then the material is defined is an OT2. The last two optical types (OT3) and (OT4) present both an indirect gap, E_g^i, and correspond to the cases where $E_g^i < {E_g}^{da} \leq {E_g}^{df}$ and $E_g^i < {E_g}^{df} < {E_g}^{da}$, respectively. An evaluation of the momentum matrix elements establishes whether a transition is allowed or forbidden. All the optical types can be visualized in Fig. 1.15. According to the SLME model, the SQ model approximates all materials to be OT1 and so their fraction of radiative recombination is $f_r = 1$. Based on the optical types classification, the SLME model extends the assumptions brought by the SQ model as it considers also nonradiative recombinations which can occur for an OT2 material, for example, where $f_r << 1$. The approximation that is made is that $f_r = e^{-\frac{\Delta}{kT}}$ where k_B is the Boltzmann constant, T is the temperature and $\Delta = {E_g}^{da} - E_g$.

Secondly, the SLME model improves the SQ model assumption regarding the nature of the absorbance. Instead of assuming it is a step-function, the absorbance is defined as:

$$a(E) = 1 - e^{-2\alpha(E)L} \quad , \tag{1.27}$$

where L is the thickness of the thin film with the front and back surfaces having zero and unity reflectivity, respectively. As in the Alharbi et al. model [58], $\alpha(E)$ is the absorption coefficient and it is obtained from first-principles calculations. Hence, the main ingredients of the SLME model are the band gap and the absorption spectrum which are calculated by applying the GW self-energy approximation [71] on top of the Kohn-Sham wavefunctions obtained with the hybrid functional HSE06 [72]. We shall give more details on the Kohn-Sham scheme and the hybrid functionals in Chapter 2. The solar photon flux is also considered here based on the AM1.5G standardized spectrum and the cell is at the standard temperature of 298 K.

The defining expression for the current density is

$$J = J_{sc} - J_0(e^{eV/kT} - 1) \quad , \tag{1.28}$$

where J_{sc} is defined as J_{max} in equation (1.6). Here J_0 is the reverse saturation current and it corresponds to the total electron-hole recombination (nonradiative J_{nr} and radiative J_r) current,

$$J_0 = J_{nr} + J_r = J_r/f_r \quad . \tag{1.29}$$

Since SLME closely follows the thermodynamic principle of the detailed balance introduced in the SQ model, J_r is calculated hereby in the same way, as shown in Eq. (1.10). The efficiency is obtained using the formula indicated in Eq.(1.21). This model is tested on 256 different compounds and the top resulting SLME values are found to correspond to materials that are established good photovoltaic compounds,

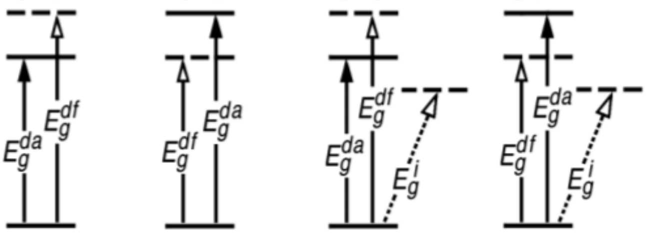

Figure 1.15: Schematic of four optical types. DA(DF) direct transitions are presented with an arrow pointing to a solid (dashed) line. Indirect states are depicted as dashed lines that are displaced laterally (not vertically). Image taken from the work of Yu et al. [59].

hence confirming the validity of this model. For instance, $CuInSe_2$ yields a SLME value of 28%, which slightly exceeds the highest experimentally measured one of 20% [73].

We conclude this section by reiterating that the SQ model is a strong starting point for assessing solar cell devices as it provides a set of descriptors such as J_{sc}, V_{oc}, FF and PCE that can guide the optimization process of a junction. The multi-parameter model proposed by Alharbi et al. considers the standard testing conditions by setting the cell temperature at room temperature and by employing the $AM1.5G$ solar photon flux. It also accounts for the material's specific absorbance spectrum, instead of overestimating it by assuming all photons with energies higher than the band gap are absorbed. This physical quantity requires a material-specific analysis which can be obtained from ab-initio calculations. Ab-initio or first-principle methods aim to describe electronic systems by solving approximately the Schrödinger equation without accessing empirical parameters. In order to account for recombinations, Alharbi et al. introduce the diffusion length which requires a treatment of the charge carriers transport properties. However, calculating the diffusion length is not feasible for a large set of materials. Therefore, these are introduced in the Alharbi model as external empirical parameters which characterize four different types of junctions. It is shown within this model that the efficiency is largely dependent on the absorption thickness. Hence, we note that the latter is also an important descriptor which is here set to approximately the size of the diffusion length. Moreover, this model relies on performing linear fittings between empirically known values of J_{sc}, V_{oc} and FF in terms of the band gap. The descriptors in this mode, therefore, are not obtained in an ab-initio way.

Taking a slightly more ab-initio approach, the spectroscopically limited maximum efficiency proposed by Yu et al. is essentially a more accurate treatment of the SQ model. Herein the descriptors have similar analytical expressions as in the SQ model that do not rely on prior knowledge of empirical parameters but they include the absorption spectrum of the PV compound, as well as the radiative and non-radiative recombinations which can be accounted for using ab-initio calculations. We note that it was possible in this model to assume a unique film thickness because a class of similar compounds was treated whose diffusion lengths were probably not very different. If a larger variety of compounds and junctions had been considered, a range of different film thicknesses would have been needed in the SLME model. These three models establish the band gap, the material-dependent absorption spectrum and the cell thickness as the most important variables that enable the theoretical determination of the PV descriptors and hence, of the best-performing solar cell devices achievable.

2 Theoretical background

The current chapter is devoted to the theories that lie at the core of all the electronic structure calculations conducted throughout this work. Firstly, there will be a brief introduction to the most important framework for treating single electrons in periodic crystals, *i.e.* Bloch theorem, followed by a number of significant consequences. Afterwards, we shall dedicate a slightly extended section to density functional theory. An overview of this widely-used theory will be provided together with an account of the most commonly implemented exchange-correlation functionals: the local density approximation (LDA) and the generalized gradient approximation (GGA). Since the problem of correctly estimating the true band gap of a system is highly relevant to our work, we concisely present the shortcoming that DFT poses on this front. We then go on to providing a description of a separate class of exchange-correlation functionals, namely of "hybrid functionals" that were specifically created to resolve the band gap underestimation of DFT. In view of our work involving two-dimensional materials, we also introduce the "Tkatchenko-Scheffler" method that was conceived in order to correct for the missing van der Waals effects within the standard DFT scheme. Moreover, we discuss the approaches with a special emphasis on the basis set implemented in the electronic structure code that we used throughout this work, namely the "Fritz Haber Institute ab initio molecular simulations" (FHI-AIMS) package. Lastly, we examine the dielectric function that arises from the random phase approximation and which we have heavily made use of throughout this work through its FHI-AIMS implementation.

2.1 Bloch Theorem

Bloch's theorem is central to studying independent electrons in a periodic potential. Such potentials obey the condition:

$$U(\boldsymbol{r}+\boldsymbol{R}) = U(\boldsymbol{r}) \quad , \tag{2.1}$$

for all $\boldsymbol{R}$ in a Bravais lattice. The eigenstate ψ of the one-electron Hamiltonian $H = -\hbar^2\boldsymbol{\nabla}^2/2m+U(\boldsymbol{r})$ will then be defined as a plane wave $e^{i\boldsymbol{k}\cdot\boldsymbol{r}}$, which is modulated by a function with the periodicity of the Bravais lattice, $u(\boldsymbol{r})$,

$$\psi_{\boldsymbol{k}}(\boldsymbol{r}) = e^{i\boldsymbol{k}\cdot\boldsymbol{r}}u_{\boldsymbol{k}}(\boldsymbol{r}) \quad . \tag{2.2}$$

This implies the canonical expression:

$$\psi_{\boldsymbol{k}}(\boldsymbol{r}+\boldsymbol{R}) = e^{i\boldsymbol{k}\cdot\boldsymbol{R}}\psi_{\boldsymbol{k}}(\boldsymbol{r}) \quad . \tag{2.3}$$

This important theorem is a consequence of the general observation which holds that the eigenstates of H can be chosen to be eigenstates of all the translation operators $T_{\boldsymbol{R}}$. The implications that Bloch's theorem gives rise to are:

1. The solution of H is no longer required to cover the entire crystal but can span only the unit cell. So the scale of the problem and, hence, the computational time, have been reduced by a factor of N, where $N = 10^{23}$ is the number of unit cells in a crystal structure. Bloch theorem can be considered, from this perspective, the bedrock of computational-based electronic structure for solids.

2. The number of distinct $\boldsymbol{k}$ states in a primitive cell is equal to the total number of lattice sites in the real space lattice, *i.e.* N. This fact follows from acknowledging that the vector $\boldsymbol{k}$ is a label for the Bloch state $\psi_{\boldsymbol{k}}(\boldsymbol{r})$, restricting the $\boldsymbol{k}$ vectors as a consequence of the periodic boundary conditions and by recalling that two $\boldsymbol{k}$ are identical if they differ by exactly an integer multiple of a reciprocal lattice vector $\boldsymbol{G}$.

3. The set of $\boldsymbol{k}$ vectors that make up the Bloch states fill up the first Brillouin zone (FBZ), the Wigner-Seitz cell in reciprocal space. FBZ is characterized by the crystal symmetry.

4. The free electron states have the form:

$$\langle \boldsymbol{r}|\boldsymbol{k}\rangle = e^{i\boldsymbol{k}\cdot\boldsymbol{r}} \quad , \tag{2.4}$$

where $\langle \boldsymbol{r}| \doteq (r_1^* \quad r_2^* \quad \ldots \quad r_N^*)$ and $|\boldsymbol{k}\rangle \doteq \begin{pmatrix} k_1 \\ k_2 \\ \vdots \\ k_N \end{pmatrix}$. In a periodic crystal these are not energy eigenstates. A linear combination of free electron waves, however, can be used to describe the energy eigenstates of the crystal:

$$|\psi\rangle = \sum_{\boldsymbol{k}} C_{\boldsymbol{k}} |\boldsymbol{k}\rangle \quad . \tag{2.5}$$

Bloch's theorem dictates that $|\psi\rangle$ is constituted only by $|\boldsymbol{k}\rangle$ states that differ by translations in the reciprocal lattice. In other words, each unit cell in the reciprocal lattice contributes with one $|\boldsymbol{k}\rangle$ state towards a Bloch state. That is why Bloch states are typically indexed with a particular $\boldsymbol{k}$-vector belonging to the FBZ:

$$|\psi_{n,\boldsymbol{k}}\rangle = \sum_{\boldsymbol{G}} C_n(\boldsymbol{k}+\boldsymbol{G}) |\boldsymbol{k}+\boldsymbol{G}\rangle \quad , \tag{2.6}$$

where the reciprocal lattice vectors $\boldsymbol{G}$ are expressed in terms of the reciprocal primitive vectors $\boldsymbol{b_1}, \boldsymbol{b_2}, \boldsymbol{b_3}$, namely $\boldsymbol{G} = n_1\boldsymbol{b_1} + n_2\boldsymbol{b_2} + n_3\boldsymbol{b_3}$. The index n serves as a band index which distinguishes between the various Bloch states that have the same $\boldsymbol{k}$-vector but different energies.

5. In the free-electron picture, all states are labelled solely by the index $\boldsymbol{k}$. On the other hand, Bloch states that characterize electrons in a periodic potential have the additional index n. However, this does not mean that the number of wavefunctions has multiplied. Note that $\psi_{n,\boldsymbol{k}+\boldsymbol{G}} = \psi_{n',\boldsymbol{k}}$ as they share the same eigenvalue $e^{i\boldsymbol{k}\cdot\boldsymbol{R}}$, when acted upon with a translation operator commensurate with the Bravais lattice vector $\boldsymbol{R}$. In order to build a set of complete and linearly independent wavefunctions $\psi_{n,\boldsymbol{k}}$, the $\boldsymbol{k}$ are limited to the first Brillouin zone so that $\boldsymbol{k}-\boldsymbol{k'} \neq \boldsymbol{G}$. This approach is called the *reduced zone scheme*. An equivalent approach involves considering all possible $\boldsymbol{k}$ vectors, hence, dropping the n index. This is known as the *extended zone scheme.* The state $\psi_{n,\boldsymbol{k}}$, labelled in the convention of the *reduced zone scheme* can, in fact, be written as $\psi_{n,\boldsymbol{k}+\boldsymbol{G}_n}$, in the *extended zone scheme* [74].

6. The density of states (DOS) describes the number of states that a system occupies at each level of energy. Its general form in d dimensions is:

$$D(E) = \int d\boldsymbol{k} \frac{2}{(2\pi)^d} \delta(E - E_{\boldsymbol{k}}) \quad . \tag{2.7}$$

In Eq.(2.7), $E_{\boldsymbol{k}}$ is the energy eigenvalue corresponding to the Bloch eigenstate $\psi_{n,\boldsymbol{k}}$ where we have suppressed the index n. Based on the proof presented in Marder [74], we shall demonstrate here how the density of states can be reformulated in terms of an integral over the energy surface $E = E_{\boldsymbol{k}}$. The respective expression will be used in Chapter 5 to describe the emergence of "band-nesting" in two-dimensional materials. We now consider the fact that the delta function is defined as the derivative of the Heaviside function, *i.e.*:

$$\delta(E - E_{\boldsymbol{k}}) = \frac{\theta(E - E_{\boldsymbol{k}}) - \theta(E - E_{\boldsymbol{k}} - dE)}{dE} \quad . \tag{2.8}$$

Let us now rewrite Eq. (2.7) so that we transform it from an integral over $\boldsymbol{k}$-space into an integral over energy surfaces $E_{\boldsymbol{k}}$. So for each $\boldsymbol{k}$-point, we fix $E = E_{\boldsymbol{k}}$ and vary E by dE, which is equivalent to increasing $\boldsymbol{k}$ by $d\boldsymbol{k}$. The variation in E by dE means we are moving from an energy surface $E = E_{\boldsymbol{k}}$ to $E = E_{\boldsymbol{k}+d\boldsymbol{k}}$, and there will be a change in the actual surface size by dS, which becomes the integral measure. The direction of the change that was previously provided by $d\boldsymbol{k}$ now becomes $d\boldsymbol{k} \cdot \hat{\boldsymbol{n}}$, where,

$$\hat{\boldsymbol{n}} = \frac{\nabla_{\boldsymbol{k}} E_{\boldsymbol{k}}}{|\nabla_{\boldsymbol{k}} E_{\boldsymbol{k}}|} \quad , \tag{2.9}$$

is the unit surface normal. Now, since the second energy surface has an additional $d\boldsymbol{k}$ to its associated $\boldsymbol{k}$ vector, one can apply Taylor expansion up to first order and get:

$$E_{\boldsymbol{k}+d\boldsymbol{k}} = E_{\boldsymbol{k}} + d\boldsymbol{k} \cdot \nabla_{\boldsymbol{k}} E_{\boldsymbol{k}} \quad . \tag{2.10}$$

As established previously, the variation in the energy is dE so it follows that $dE =$

$d\boldsymbol{k}\cdot\nabla_{\boldsymbol{k}}E_{\boldsymbol{k}}$. Since the numerator in the Heaviside is 1, Eq. (2.7) can thus be re-written in terms of an energy surface integral as:

$$D(E) = \frac{2}{(2\pi)^d}\int dS\cdot d\boldsymbol{k}\cdot\hat{\boldsymbol{n}}\frac{1}{dE} = \frac{2}{(2\pi)^d}\int\frac{dE}{|\nabla_{\boldsymbol{k}}E_{\boldsymbol{k}}|}\cdot\frac{dS}{dE} = \frac{2}{(2\pi)^d}\int\frac{dS}{|\nabla_{\boldsymbol{k}}E_{\boldsymbol{k}}|} \quad . \tag{2.11}$$

As it can be inferred from Eq.(2.11), the density of states has a singularity, where the electron velocity $\boldsymbol{v}_{n\boldsymbol{k}}$, *i.e.* $\frac{1}{\hbar}\nabla_{\boldsymbol{k}}E_{n\boldsymbol{k}}$ vanishes.

7. For certain systems such as metals, where the conduction electrons essentially behave as free electrons, it is convenient to express the Bloch states in terms of the plane waves defined in Eq.(2.6) [75]. However, in more covalent systems where the electronic density is largely situated around the ions, it is more straightforward to define basis functions that are localized at lattice points:

$$|\psi_{n,\boldsymbol{k}}\rangle = \sum_{\mu,\boldsymbol{R}} C_{\mu,n}(\boldsymbol{k},\boldsymbol{R})\,|\phi_{\mu,\boldsymbol{R}}\rangle \quad . \tag{2.12}$$

Here, $C_{\mu,n}(\boldsymbol{k},\boldsymbol{R})$ is a coefficient in the linear combination and $|\phi_{\mu,\boldsymbol{R}}\rangle$ is the μ-th orbital at lattice site $\boldsymbol{R}$. Using Bloch theorem, it can be shown fairly easily that the coefficients can be written as:

$$C_{\mu}(\boldsymbol{k},\boldsymbol{R}) = e^{i\boldsymbol{k}\cdot\boldsymbol{R}}C_{\mu}(\boldsymbol{k}) \quad . \tag{2.13}$$

This leads to rewriting the Bloch state in terms of a localized function as:

$$|\psi_{n,\boldsymbol{k}}\rangle = \sum_{\mu,\boldsymbol{R}} e^{i\boldsymbol{k}\cdot\boldsymbol{R}}C_{\mu,n}(\boldsymbol{k})\,|\phi_{\mu,\boldsymbol{R}}\rangle \quad . \tag{2.14}$$

Of course the Bloch state is the eigenket of a periodic Hamiltonian such that:

$$
\begin{aligned}
&\hat{H}\left|\psi_{n,\boldsymbol{k}}\right\rangle = E_n(\boldsymbol{k})\left|\psi_{n,\boldsymbol{k}}\right\rangle\\
&\sum_{\mu,\boldsymbol{R}} e^{i\boldsymbol{k}\cdot\boldsymbol{R}} C_{\mu,n}(\boldsymbol{k}) \left\langle\phi_{\nu,\boldsymbol{R_m}}\right|\hat{H}\left|\phi_{\mu,\boldsymbol{R}}\right\rangle = E_n(\boldsymbol{k}) \sum_{\mu',\boldsymbol{R'}} e^{i\boldsymbol{k}\cdot\boldsymbol{R'}} C_{\mu',n}(\boldsymbol{k}) \left\langle\phi_{\nu,\boldsymbol{R_m}}|\phi_{\mu',\boldsymbol{R'}}\right\rangle\\
&\sum_{\mu,\boldsymbol{R}} e^{i\boldsymbol{k}\cdot(\boldsymbol{R}-\boldsymbol{R_m})} C_{\mu,n}(\boldsymbol{k}) \left\langle\phi_{\nu,\boldsymbol{R_m}}\right|\hat{H}\left|\phi_{\mu,\boldsymbol{R}}\right\rangle = E_n(\boldsymbol{k}) \sum_{\mu',\boldsymbol{R'}} e^{i\boldsymbol{k}\cdot(\boldsymbol{R'}-\boldsymbol{R_m})} C_{\mu',n}(\boldsymbol{k}) \left\langle\phi_{\nu,\boldsymbol{R_m}}|\phi_{\mu',\boldsymbol{R'}}\right\rangle\\
&\sum_{\mu} C_{\mu,n}(\boldsymbol{k}) H_{\nu,\mu}(\boldsymbol{k}) = E_n(\boldsymbol{k}) \sum_{\mu'} C_{\mu',n}(\boldsymbol{k}) S_{\nu,\mu'}(\boldsymbol{k}) \quad .
\end{aligned}
$$

In these equations we made the substitutions:

$$H_{\nu,\mu}(\boldsymbol{k}) = \sum_{\boldsymbol{R}} e^{i\boldsymbol{k}\cdot(\boldsymbol{R}-\boldsymbol{R_m})} \left\langle\phi_{\nu,\boldsymbol{R_m}}\right|\hat{H}\left|\phi_{\mu,\boldsymbol{R}}\right\rangle \tag{2.15}$$

$$S_{\nu,\mu}(\boldsymbol{k}) = \sum_{\boldsymbol{R}} e^{i\boldsymbol{k}\cdot(\boldsymbol{R}-\boldsymbol{R_m})} \left\langle\phi_{\nu,\boldsymbol{R_m}}|\phi_{\mu,\boldsymbol{R}}\right\rangle \quad . \tag{2.16}$$

Knowing these matrices helps to solve the Schrödinger equation and obtain $E_n(\boldsymbol{k})$ and $C_{\mu',n}(\boldsymbol{k})$.

2.2 Density Functional Theory

The underlying principle of density functional theory is that the ground-state electron density contains all the information carried by the many-electron wave function. This surprising idea is somehow justified considering the fact that the two varying ingredients of many-electron systems are the external potential and the number of electrons. Now we will try and see how these two variables are directly correlated to the electronic density. Firstly, the correspondence between the electronic density and the number of electrons appears straightforwardly since the density is defined as:

$$n(\boldsymbol{r}) = N \int d\boldsymbol{r_2}...d\boldsymbol{r_N} \Psi^*(\boldsymbol{r},\boldsymbol{r_2}...\boldsymbol{r_N})\Psi(\boldsymbol{r},\boldsymbol{r_2}...\boldsymbol{r_N}) \quad , \tag{2.17}$$

where N is the number of electrons in the system. The second, less obvious observation that Hohenberg and Kohn made [76], was that knowing the density of a many-electron system in the ground state is sufficient to deduce the external potential up to a constant. To prove the validity of this statement, let us assume that for a system of N electrons there are two external potentials, $\hat{V}_{ext1}$ and $\hat{V}_{ext2}$, that differ by more than a constant, which result in the same ground-state density, $n_0(\boldsymbol{r})$. We then call the resulting Hamiltonians $\hat{H}_1$ and $\hat{H}_2$, E_1 and E_2 their associated energy eigenvalues and Ψ_1 and Ψ_2 their corresponding ground-state many-body wave functions. Assuming these two ground states to be non-degenerate, then we can write:

$$\begin{aligned} E_1 = \langle\Psi_1|\,\hat{H}_1\,|\Psi_1\rangle &< \langle\Psi_2|\,\hat{H}_1\,|\Psi_2\rangle && (2.18)\\ &= \langle\Psi_2|\,\hat{H}_2\,|\Psi_2\rangle + \langle\Psi_2|\,(\hat{H}_1 - \hat{H}_2)\,|\Psi_2\rangle && (2.19)\\ &= E_2 + \int d\boldsymbol{r}\, n_0(\boldsymbol{r})[V_{ext1}(\boldsymbol{r}) - V_{ext2}(\boldsymbol{r})] \quad . && (2.20) \end{aligned}$$

The last equality is valid since two Hamiltonians with the same number of electrons differ only in their external potential and since we assume that $\langle\boldsymbol{r}|\,\hat{V}_{ext}\,|\boldsymbol{r'}\rangle = V_{ext}(\boldsymbol{r})\delta(\boldsymbol{r}-\boldsymbol{r'})$. We can just as well switch the indices 1 and 2, leading to :

$$E_2 < E_1 + \int d\boldsymbol{r}\, n_0(\boldsymbol{r})[V_{ext1}(\boldsymbol{r}) - V_{ext2}(\boldsymbol{r})] \quad . \tag{2.21}$$

Adding Eq.(2.20) and (2.21), we arrive at the conclusion that $E_1 + E_2 < E_1 + E_2$, which is clearly a contradiction. Thus, V_{ext1} and V_{ext2} must be the same. So the ground-state density of a N-electron system uniquely defines the external potential up to an additive constant. This claim is known as the *first Hohenberg-Kohn theorem* [76]. As a result of this finding, knowing the charge density of a system allows for the ground state Ψ_0 and the ground-state energy E_0 to be written as functionals of the ground-state density $n_0(\boldsymbol{r})$ alone. Although DFT does not require the wave function, Kohn-Sham DFT refers to a noninteracting system whose ground state density matches that of the interacting one. As we shall show further, we can then use the quantum state $|\Psi_0\rangle$ of the noninteracting system to describe the interacting one. The ground state and its corresponding energy can be written as :

$$|\Psi_0\rangle = |\psi[n_0(\boldsymbol{r})]\rangle \quad , \tag{2.22}$$

and

$$E_0 = E[n_0(\boldsymbol{r}), V_{ext}(\boldsymbol{r})] = E[n_0(\boldsymbol{r})] \quad . \tag{2.23}$$

This means that for any other density $n'(\boldsymbol{r})$ that is not the ground-state density of $\mathrm{V}_{ext}(\boldsymbol{r})$:

$$E_0 = E[n_0(\boldsymbol{r}), V_{ext}(\boldsymbol{r})] < E[n'(\boldsymbol{r}), V_{ext}(\boldsymbol{r})] \quad . \tag{2.24}$$

This implication is known as the *second Hohenberg-Kohn theorem* [76]. An interesting consequence of this view of the many-body problem is that one can in fact write the energy functional $E[n(\boldsymbol{r})]$ as:

$$E[n(\boldsymbol{r})] = \int d\boldsymbol{r}\, n(\boldsymbol{r}) V_{ext}(\boldsymbol{r}) + F[n(\boldsymbol{r})] \quad , \tag{2.25}$$

where $F[n(\boldsymbol{r})]$ is the sum of the kinetic energy of the interacting electrons and the Coulomb energy:

$$F[n(\boldsymbol{r})] = T[n(\boldsymbol{r})] + V_{ee}[n(\boldsymbol{r})] \quad . \tag{2.26}$$

Let us assume that an exact or approximate expression for the Coulomb energy $V_{ee}[n(\boldsymbol{r})]$, and hence of the functional $F[n(\boldsymbol{r})]$, is known. It must be noted that this functional is universal, which means that it does not depend on the external potential and thus, is the same for all systems. Minimizing $F[n(\boldsymbol{r})]$ over all wavefunctions producing the density $n(\boldsymbol{r})$ and then over all densities defines $E[n(\boldsymbol{r})]$. This, in turn, helps determine the ground-state energy E_0 even in the case where the non-degeneracy condition cannot be imposed as in the demonstration above [74]. Also, this procedure circumvents the issue that can arise from the ill-defined $E[n(\boldsymbol{r})]$ in the absence of a $V_{ext}(\boldsymbol{r})$ that yields the ground-state density $n_0(\boldsymbol{r})$ [74].

Thus, the search for the ground-state energy E_0 of a many-body system can be carried out as follows [74]:

$$\begin{aligned}
E_0 &= \min_{\Psi} \langle\Psi|\,\hat{T} + \hat{V}_{ext} + \hat{V}_{ee}\,|\Psi\rangle && (2.27)\\
&= \min_{n}[\min_{\Psi\to n} \langle\Psi|\,\hat{T} + \hat{V}_{ext} + \hat{V}_{ee}\,|\Psi\rangle] && (2.28)\\
&= \min_{n}\left[\min_{\Psi\to n}\Big(\langle\Psi|\,\hat{T} + \hat{V}_{ee}\,|\Psi\rangle + \langle\Psi|\,\hat{V}_{ext}\,|\Psi\rangle\Big)\right] && (2.29)\\
&= \min_{n}\left[\min_{\Psi\to n} F[n(\boldsymbol{r})] + \int V_{ext}(\boldsymbol{r})n(\boldsymbol{r})d\boldsymbol{r}\right] && (2.30)\\
&\equiv \min_{n} E_{LL}[n(\boldsymbol{r}), V_{ext}(\boldsymbol{r})] && (2.31)
\end{aligned}$$

The term in the third equation on the right hand side between square brackets is a unique functional of the density and the external potential called the Levy-Lieb energy functional, $E_{LL}[n(\boldsymbol{r}), V_{ext}(\boldsymbol{r})]$ [77, 78]. The formalism presented before can also be applied to a noninteracting N-electron system:

$$E_0^s = E_{LL}^s[n_0(\boldsymbol{r}), V_{ext}^s(\boldsymbol{r})] = \min_{\Psi\to n}\Big(\langle\Psi|\,\hat{T}^s\,|\Psi\rangle + \int V_{ext}^s(\boldsymbol{r})n_0(\boldsymbol{r})d\boldsymbol{r}\Big) \quad , \qquad (2.32)$$

where $\hat{T}^s$ is the kinetic energy operator acting on the single electron states and V_{ext}^s represents the external potential for the noninteracting N-electron system. In this case, the ground state wave function can be written as a Slater determinant of single particle wave functions:

$$\psi(\boldsymbol{r}_1\sigma_1, ..., \boldsymbol{r}_N\sigma_N) = \frac{1}{\sqrt{N!}}\begin{pmatrix} \phi_1(\boldsymbol{r}_1\sigma_1) & \dots & \phi_N(\boldsymbol{r}_1\sigma_1)\\ \vdots & \ddots & \vdots\\ \phi_1(\boldsymbol{r}_N\sigma_N) & \dots & \phi_N(\boldsymbol{r}_N\sigma_N)\end{pmatrix} \qquad (2.33)$$

where σ denotes the spin index. The single particle eigenstates $\phi_i(\boldsymbol{r_i}\sigma_i)$ and their associated eigenvalues ϵ_i are, of course, obtained by solving the Schrödinger equation for a non-interacting system:

$$\Big(-\frac{1}{2}\nabla^2 + V_{ext}^s(\boldsymbol{r})\Big)\phi_i(\boldsymbol{r}\sigma) = \epsilon_i\phi_i(\boldsymbol{r}\sigma) \quad . \qquad (2.34)$$

Similarly to the many-body wave function expressed in Eq. (2.22), the single particle wave functions are also uniquely determined by the ground state density and hence, can be written as functionals, *i.e.* $\phi_i(\boldsymbol{r_i}\sigma_i)[n_0(\boldsymbol{r})]$.

The E_{LL} functional is minimized under the condition that the total number of electrons, N, is conserved, by solving the following equation [77, 79]:

$$\frac{\delta}{\delta n(\boldsymbol{r})}\Bigg[E_{LL}[n(\boldsymbol{r}), V_{ext}(\boldsymbol{r})] - \mu\bigg(\int d^3\boldsymbol{r} n(\boldsymbol{r}) - N\bigg)\Bigg]_{n(\boldsymbol{r})=n_0(\boldsymbol{r})} = 0 \quad , \tag{2.35}$$

where μ is the Lagrange multiplier used to impose the charge conservation condition. For Eq. (2.35) to be valid, certain criteria have to be satisfied for the functional derivatives to exist. It is provable that all N-representable densities *i.e.* densities, which can be obtained from any anti-symmetric state, satisfy those criteria [79]. Thus, we extend the definition of E_{LL} of Eq.(2.31), such that it includes densities that correspond to fractional particle numbers:

$$\int d^3\boldsymbol{r} n(\boldsymbol{r}) = N + \eta \quad \text{where} \quad 0 < \eta < 1 \quad .$$

We do this by redefining $F[n(\boldsymbol{r})]$:

$$F[n(\boldsymbol{r})] = \min_{(|\psi_N\rangle, |\psi_{N+1}\rangle) \to n(\boldsymbol{r})} \left[(1-\eta)\langle\Psi_N|\hat{T} + \hat{V}_{ee}|\Psi_N\rangle + \eta\langle\Psi_{N+1}|\hat{T} + \hat{V}_{ee}|\Psi_{N+1}\rangle\right] \quad , \tag{2.36}$$

where the state of this system with non-integer particle numbers is in a superposition of two states, *i.e.* a state ψ_N with N particles and a state ψ_{N+1} with $N+1$ particles. The density of such a state is then $n(\boldsymbol{r}) = (1-\eta)\langle\Psi_N|\hat{n}(\boldsymbol{r})|\Psi_N\rangle + \eta\langle\Psi_{N+1}|\hat{n}(\boldsymbol{r})|\Psi_{N+1}\rangle$ [79].

The constraining equation, Eq.(2.35) can clearly be applied to a noninteracting system as well, yielding:

$$\frac{\delta T^s[n_0(\boldsymbol{r})]}{\delta n(\boldsymbol{r})} + V^s_{ext}(\boldsymbol{r}) = \mu \quad . \tag{2.37}$$

So starting with the example of the noninteracting case, it appears that all densities for which we can build an associated energy functional E_{LL}, correspond to a Slater determinant made up of single particle eigenstates. This sets the foundation for the Kohn-Sham scheme [80]. Hence, densities in the KS scheme are of the type:

$n(\boldsymbol{r}) = \sum_i \sum_\sigma |\phi_i(\boldsymbol{r}\sigma)|^2$. Therefore, this allows one to express the Levy-Lieb energy functional for the interacting electrons as:

$$E_{LL}[n] = T^s[n] + E_H[n] + E_{ext}[n] + E_{xc}[n] \quad . \tag{2.38}$$

The first term on the right hand side is the kinetic energy of noninteracting electrons. The second term on the right hand side represents the classical Coulomb or Hartree energy $E_H[n]$, which accounts for the simple electrostatic potential arising from the charge distribution of N electrons and has the form $\frac{1}{2}\int d\boldsymbol{r} \int d\boldsymbol{r'} \frac{n(\boldsymbol{r})n(\boldsymbol{r'})}{|r-r'|}$. The third term corresponds to the energy due to the external potential $\int d\boldsymbol{r} V_{ext}(\boldsymbol{r})n(\boldsymbol{r})$. The last term, $E_{xc}[n]$, represents the exchange-correlation energy and it incorporates all the other electronic effects that cannot be classically accounted for, such as electron exchange and correlation. $E_{xc}[n]$ also contains the remaining interacting kinetic energy terms that are not captured by the noninteracting kinetic energy functional $T^s[n]$. Hence, knowing the exact expression of the $E_{xc}[n]$ functional would solve all the many-body problems for any external potential $V_{ext}(\boldsymbol{r})$. For this interacting system, the variational equation becomes:

$$\begin{aligned} \mu =& \frac{\delta E[n_0(\boldsymbol{r})]}{\delta n(\boldsymbol{r})} \quad , & (2.39) \\ =& \frac{\delta T^s[n_0(\boldsymbol{r})]}{\delta n(\boldsymbol{r})} + \int d\boldsymbol{r'} \frac{n(\boldsymbol{r'})}{|\boldsymbol{r}-\boldsymbol{r'}|} + V_{ext}(\boldsymbol{r'}) + \frac{\delta E_{xc}[n_0(\boldsymbol{r})]}{\delta n(\boldsymbol{r})} \quad . & (2.40) \end{aligned}$$

We define the sum of thee last three terms as the Kohn-Sham potential $v_{KS}(\boldsymbol{r})$. Now comparing Eq.(2.37) with Eq.(2.40), it is clear that they are the same for $V^s_{ext}(\boldsymbol{r}) = v_{KS}(\boldsymbol{r})$. Therefore, the interacting system has the same ground state density as that of a noninteracting system in an external potential $v_{KS}(\boldsymbol{r})$. This is called a Kohn-Sham system [80]. Knowing $v_{KS}(\boldsymbol{r})$ for the interacting system is equivalent to knowing the quadratic Hamiltonian of the noninteracting Kohn-Sham system. Hence for $V^s_{ext}(\boldsymbol{r}) = v_{KS}(\boldsymbol{r})$, the single-particle equations in Eq.(2.34) become the famous Kohn-Sham equations corresponding to the interacting system [80]:

$$\Big(-\frac{1}{2}\nabla^2 + v_{KS}(\boldsymbol{r})\Big)\phi_i(\boldsymbol{r}\sigma) = \epsilon_i \phi_i(\boldsymbol{r}\sigma) \quad . \tag{2.41}$$

Here, the $\phi_i(\boldsymbol{r_i}\sigma_i)$ eigenstates are called Kohn-Sham orbitals and are also a unique functional of $n(\boldsymbol{r})$, since they are uniquely determined by $v_{KS}(\boldsymbol{r})$. Now we can summarize the Kohn-Sham self-consistent-field (SCF) method that yields the ground-state density:

1. An initial guess for the density $n(\boldsymbol{r})$ is made based on the external potential $v_{ext}(\boldsymbol{r})$. Then the $v_{KS}(\boldsymbol{r})$ is calculated.
2. The density of the KS system is calculated by diagonalizing its Hamiltonian or by directly minimizing its energy functional.
3. The $v_{KS}(\boldsymbol{r})$ is reconstructed with the obtained density and the procedure is repeated until the density and the total energy are converged.

2.2.1 Semi-local exchange-correlation functionals

Density functional theory is an exact theory since knowing the exact exchange-correlation (XC) functional implies obtaining precisely the ground-state energy of the system. However, in practice this functional is only known within some approximations. We will review two main flavours of XC functionals: the local density approximation (LDA) and the generalized gradient approximation (GGA). The latter has been used throughout this work.

In the LDA, at a point in space $\boldsymbol{r}$, of density $n(\boldsymbol{r})$, $E_{xc}[n(\boldsymbol{r})]$ is the XC energy of an interacting uniform electron gas (jellium) with density $n(\boldsymbol{r})$. In other words, this approximation assumes that the charge density is not uniform, but varies slowly. So then $E_{xc}[n(\boldsymbol{r})]$ will be given by a known expression obtained in jellium, but evaluated locally and integrated over all space:

$$E_{xc}[n(\boldsymbol{r})] = \int d^3\boldsymbol{r} n(\boldsymbol{r})\epsilon(n) \quad , \tag{2.42}$$

where ϵ is the exact XC energy per electron in a uniform gas of constant density n. For metals, where the electron density is close to homogeneous, the LDA is expected to work well. If, however, the density is highly inhomogeneous, the LDA is not expected to work well [81]. The great advantage of the LDA consists in its fortuitous error cancellation, whereby the underestimation of the exchange term is compensated by the overestimation of the correlation term [82].

The generalized gradient approximation (GGA) is an improved version of LDA, where besides the density at point $\boldsymbol{r}$, one includes the gradient of the density at point $\boldsymbol{r}$, *i.e.* $\nabla n(\boldsymbol{r})$. Here we use the specific flavour of GGA called PBE, which was proposed by Perdew, Burke and Ernzerhof [83]. The general expression is:

$$E_{xc}^{PBE} = \int d^3\boldsymbol{r} n(\boldsymbol{r}) \epsilon_{xc}^{PBE}(r_S(\boldsymbol{r}), s(\boldsymbol{r}), \zeta(\boldsymbol{r})) \quad , \tag{2.43}$$

where $r_S = (4\pi n/3)^{-1/3}$ is the Weigner-Seitz radius, $\zeta = (n_\downarrow - n_\uparrow)/n$ is the relative spin-polarization and $s = |\nabla n|/(2k_F n)$, with $k_F = (3\pi^2 n)^{1/3}$ is the reduced density gradient. The exact expression of ϵ_{xc}^{PBE} is constructed to satisfy a number of conditions of the exact XC DFT functional, which are discussed in detail in Ref. [83].

2.2.2 The band gap problem

Kohn-Sham DFT is notorious for its incorrect prediction of the electronic gap of extended systems and molecules [84, 85]. The band gap is an essential quantity that determines the absorption of light in a system. Therefore, the inherent band gap underestimation in KS has to be addressed. In the following section we will discuss this limitation in more detail and then present a class of functionals that were designed to circumvent the band gap underestimation among other molecular properties.

To start understanding the problem of the band gap underestimation in Kohn-Sham DFT, let us start by considering again the system with a non-integer number of particles. As discussed in Eq. (2.36), such a system is expressed as a superposition of a state with N particles and one with $N+1$ particles [79, 86]. So the Levy-Lieb functional E_{LL} is minimized such that both $|\psi_N\rangle$ and $|\psi_{N+1}\rangle$ are ground states for the same $V_{ext}(\boldsymbol{r})$ [79, 86] . It follows then that:

$$E_0^{N+\eta} = (1-\eta)E_0^N + \eta E_0^{N+1} \quad , \tag{2.44}$$

where E_0^Q is the ground state energy of a system with Q interacting electrons.

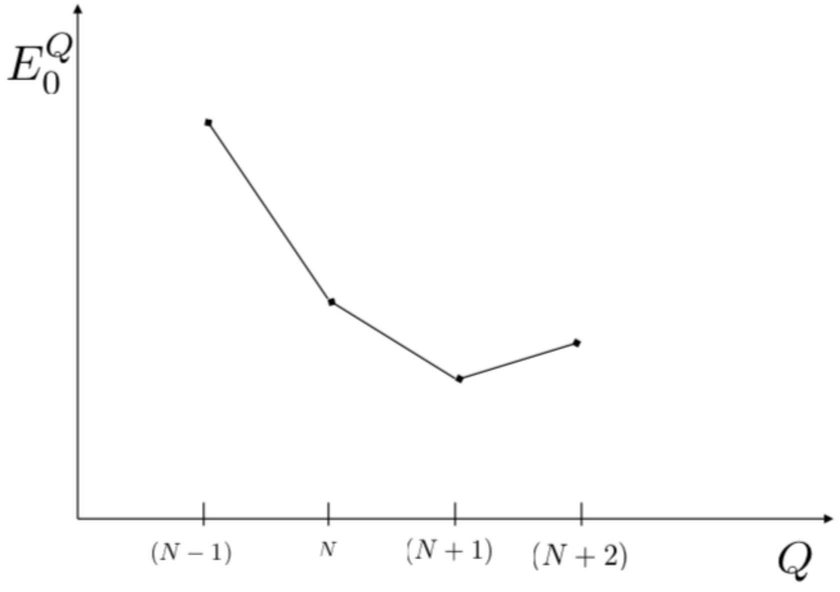

Figure 2.1: Ground-state energy corresponding to a system of interacting electrons as a function of number of particles. The plot E_0^Q against Q is linear between any two integer points. This yields E_Q non-differentiable at integral values of particle numbers. Image taken from [79] courtesy of Subhayan Roychoudhury.

As seen in Fig. 2.1, E_0^Q is not differentiable and there is clearly a linear behaviour between the integer values of Q. The fundamental gap of any N-particle system is the difference between the ionization potential and the electron affinity which, in turn, are calculated as total energy differences [87]:

$$E_{FG} = (E_0^{N+1} - E_0^{N}) - (E_0^{N} - E_0^{N-1}) \quad . \tag{2.45}$$

For a noninteracting N-particle system such as the KS system, the fundamental gap E_{FG} is the difference between the $(N+1)$-th and the N-th eigenvalue, *i.e.* :

$$\epsilon_{FG} = \epsilon_0^{N+1} - \epsilon_0^{N} \quad . \tag{2.46}$$

More specifically for a KS system, it is

$$\Delta_{KS} = \epsilon_{KS}^{N+1} - \epsilon_{KS}^{N} \quad . \tag{2.47}$$

Now for the interacting system, the total energy of a system with Q electrons, E_0^Q, is a linear function of Q between any two integer points, as can be seen from Fig. 2.1. Therefore E_{FG} is in fact equal to the derivative gap E_{DG}:

$$E_{DG} = \left.\frac{\partial E_0^N}{\partial N}\right|_{N^+} - \left.\frac{\partial E_0^N}{\partial N}\right|_{N^-} \quad , \tag{2.48}$$

where N^+ and N^- are the positive and the negative sides approaching N. Noting that $E_{LL}[n_Q(\boldsymbol{r}), V_{ext}(\boldsymbol{r})] = E_0^Q$ for the Q-particle system with ground-state density n_Q, it follows that: $\frac{\partial E_0^N}{\partial N} = \mu$ [79]. Looking at Eq. (2.35), we see that the Lagrange multiplier is $\mu = \left.\frac{\partial E_{LL}[n]}{\partial n}\right|_{n=n_N}$. One more thing to consider is that the Hartree potential and the external potential have continuous density derivatives.
Hence we can rewrite E_{DG} as:

$$\begin{aligned} E_{DG} &= \left.\frac{\delta E_{LL}[n]}{\delta n}\right|_{N^+} - \left.\frac{\delta E_{LL}[n]}{\delta n}\right|_{N^-} \\ &= \left[\left.\frac{\delta T[n]}{\delta n}\right|_{N^+} - \left.\frac{\delta T[n]}{\delta n}\right|_{N^-}\right] + \left[\left.\frac{\delta E_{xc}[n]}{\delta n}\right|_{N^+} - \left.\frac{\delta E_{xc}[n]}{\delta n}\right|_{N^-}\right] \\ &= \Delta_{KS} + \Delta_{XC} \quad . \end{aligned}$$

Δ_{XC} is called the derivative discontinuity [87]. For local and semi-local DFT XC functionals, this quantity is 0, and hence for standard DFT XC-functional: $E_{DG} = \Delta_{KS}$. In the case of a finite system, E_{xc} in LDA is a continuous, non-linear function of density, which is completely differentiable in N. However, in the limit of a bulk system consisting of an infinite number of unit cells, the plot of the total LDA energy becomes linear between integer points. This is due to the fact that the added charge is delocalized, resulting in infinitesimally small fractional charges per unit cell [85]. Therefore the so-called "delocalization error" defines the incorrect linear behaviour whereby the energies at integer values of Q are wrong in the limit of infinite number of cells [85]. The delocalization error is thought to be related to the self-interaction error (SIE) which arises in semilocal XC-functionals [84]. In the Levy-Lieb energy functional corresponding to a one-electron system, the electron Coulomb repulsion must cancel exactly the exchange-correlation [88]. Since semilocal approximations of the XC functionals do not provide this cancellation [88], the SIE refers to the electrons being allowed to interact with themselves which, naturally, leads to non-negligible errors in many-electron systems [89]. Reducing SIE has been correlated with improved values of the band gap [84, 88].

2.2.3 Hybrid functionals

One of the most useful classes of density functionals that alleviates the band-gap underestimation are "hybrid functionals", which incorporate a fraction of exact nonlocal Hartree-Fock-type exchange, $i.e$ HF exchange. HF exchange is defined by

$$E_X^{HF} = -\frac{1}{2}\sum_{\sigma}\sum_{i,j}\int d^3\mathbf{r}_1\int d^3\mathbf{r}_2\frac{\phi_{i\sigma}(\mathbf{r}_1)\phi^*_{i\sigma}(\mathbf{r}_2)\phi_{j\sigma}(\mathbf{r}_2)\phi^*_{j\sigma}(\mathbf{r}_1)}{|\mathbf{r}_1-\mathbf{r}_2|} \quad , \tag{2.49}$$

where σ denotes the spin and $\phi_{i\sigma}(\mathbf{r})$ is the orbital of the noninteracting Kohn-Sham system. Introducing SIE-free HF exchange to the semilocal XC functionals leads to a significant reduction in the unwanted SIE-induced effects and hence, to an improvement of many properties compared to semilocal functionals [88]. However, hybrid functionals pose difficulties in terms of computation. The integral introduced in Eq.(2.49) decays slowly with distance [90]. Also, the fact that there are a total of K^4 such integrals explains why E_X^{HF} is expensive to compute in extended systems, where K is the total number of basis functions over which the wave functions are expanded [74]. To overcome the problem of large computational cost, the two suggested solutions are to artificially truncate the exchange interactions and to accelerate the spatial decay [90]. The former method is more applicable to localized systems where the HF exchange decays rapidly with increasing charge separation [90]. In delocalized systems, it is claimed that this method leads to problems in the SCF calculation and inaccurate total energy prediction. These problems are avoided through the second approach in which the spatial decay is accelerated [90].

This method proposed by Heyd, Scuseria, and Ernzerhof [72] is based on screened hybrid functional and it essentially partitions the Coulomb operator in Eq.(2.49) into a short and a long- range component based on some empirically selected screening parameter ω. The HF exchange is then only applied to the short range part [88].

HSE is implemented based on one of the flavours of the Perdew-Burke-Ernzerhof

GGA [83], namely in the global hybrid PBEh [91, 92]. It is defined as:

$$E_{xc}^{\omega HSE} = aE_x^{HF,SR}(\omega) + (1-a)E_x^{PBE,SR}(\omega) + E_x^{PBE,LR}(\omega) + E_c^{PBE} \quad , \tag{2.50}$$

where $E_x^{HF,SR}$ is the short-range HF exchange, $E_x^{PBE,SR}$ and $E_x^{PBE,LR}$ are short-range and long-range components of the PBE exchange functional obtained from the model PBE exchange hole [93] and E_c^{PBE} is the PBE correlation energy. The fraction a=25% of HF exchange is derived from perturbation theory [94]. Therefore, HSE includes 25% short-range HF exchange and no long-range HF exchange. The inclusion of a fraction of HF exact exchange in HSE has the overall effect of decreasing the many-electron SIE inherent to semilocal functionals [95], hence reducing the error associated with the band gap estimation from band energy differences. That is due to the cancellation of error between HF, which induces unphysical localization [96] and semilocal XC, which induces unphysical delocalization [95, 97, 98]. The empirical range-separation parameter ω is set to 0.11 Bohr^{-1} in the latest version of the HSE functional, namely in HSE06 [93].

Another special feature of hybrids like HSE is that they include an approximate derivative discontinuity, *i.e.* $\Delta_{XC} \neq 0$ [99]. Thus, Δ_{XC} can be incorporated into the band energy differences of Eq. (2.47) by replacing the noninteracting Kohn-Sham reference system with a system containing some fraction of the electron-electron exchange interaction in a so-called generalized Kohn-Sham (GKS) scheme [100, 101].

2.2.4 van der Waals correction: Tkatchenko-Scheffler method

An important class of forces that semi-local XC functionals do not treat by default are the Van der Waals forces. These occur due to the weak attraction and repulsion interactions between instantaneous fluctuating dipoles even without electron densities overlapping. [102].

Implementing these long range van der Waals (vdW) interactions is a challenge in DFT. With no vdW correction added, GGA yields strictly repulsive potentials with no minimum and LDA drastically overbinds for certain diatomic molecules

[102]. Several attempts have been made to correctly incorporate the vdW interactions. Some proposed schemes are applicable only to systems with no density overlap [103, 104], others can be implemented for systems separated by any distance but are computationally demanding [105]. In our work, we consider the accurate nonempirical method proposed by Tkatchenko and Scheffler, whereby both short- and long- range screening effects are taken into account when computing the vdW energy.

The Tkatchenko-Scheffler (TS) method combines the Tkatchenko-Scheffler van der Waals (TS-vdW) scheme with the self-consistent screening equation of classical electrodynamics. Typically the vdW interaction that is added to standard DFT, i.e. E_{vdW}, takes the form of a pairwise interatomic term $C_6 R^{-6}$:

$$E_{vdW} = -\frac{1}{2} \sum_{A,B} f_{damp}(R_{AB}, R_A^0, R_B^0) C_{6AB} R_{AB}^{-6} \quad , \tag{2.51}$$

where R_{AB} is the distance between atoms A and B, C_{6AB} is the associated C_6 dispersion coefficient, R_A^0 and R_B^0 are the vdW radii. A short-ranged damping function $f_{damp}(R_{AB}, R_A^0, R_B^0)$ eliminates the singularity R_{AB}^{-6} that arises at small distances. The free-atom reference values for the C_6 coefficients are taken from a database and are used to define the effective coefficients for an atom inside a solid or a molecule via the Hirshfeld partitioning of the electron density [106].

Therefore, TS-vdW describes very well pointwise atomic polarizabilities and short range interactions and it determines them by calculating the effective vdW radii and C_6 coefficients of atoms in molecules or solids from the ground-state electron density obtained via DFT. Fortunately, the TS-vdW scheme does not depend on the chosen DFT exchange correlation-functional, be it LDA, PBE or BLYP (a flavour of hybrid functional). When tested on a dataset of more than 1000 complexes, it achieves a mean absolute error of only 5.5% in the C_6 intermolecular coefficients relative to the experimentally deduced ones [106].

For an atom that is part of a large molecule or of a solid, the dipolar fluctuations differ from the case of the free atom also due to the electrostatic interaction between a fluctuating dipole and other more distant ones. However, the TS-vdW scheme does not account for electrostatic screening beyond the range of the exponentially decaying atomic densities, thus considering only the local environment of a dipole starting from the free atom polarizability [107]. Therefore TS, an improved method, was conceived to tackle this problem [107]. By representing the N atoms in a certain molecular system as a set of quantum harmonic oscillators, one can solve a self-consistent screening equation and obtain the molecular and atomic polarizability tensors, which include both the short-range and the long-range electrostatic screening [107].

2.3 FHI-AIMS

The current section will describe the main features of the FHI-AIMS code and it will be largely based on its foundational paper [108].

The form of the basis set that defines the Hilbert space of the electrons, $\{\langle\phi_i|, i = 1, ..., N_b\}$ plays a crucial role in the efficiency and accuracy of electronic structure calculations. The FHI-AIMS ("Fritz Haber Institute ab initio molecular simulations”) package implements a very practical form of basis functions called numeric atom-centered orbitals (NAO) expressed as:

$$\varphi_i(r) = \frac{u_i(r)}{r} Y_{lm}(\Omega) \quad , \tag{2.52}$$

where Y_{lm} are spherical harmonics, whose indices are implicitly dependent on the basis function index i, Ω represents the angular degrees of freedom and $u_i(r)$ are numerically tabulated radial functions.

Most physical properties emerge due to the valence electrons. Therefore it is accurate to substitute the influence of the core electrons on the valence ones with an effective screening potential. The overall resulting potential acting on the valence electrons is smoother than the original ionic potential and it is coined "pseudopotential". Many electronic structure codes rely on this efficient replacement of the core electrons with a pseudopotential, hence requiring to only explicitly consider the valence electrons.

FHI AIMS, however, is an all-electron code with similar efficiency to the fast existing plane-wave pseudopotential schemes as implemented in codes such as VASP

("Vienna Ab initio Simulation Package") [109, 110]. It exhibits good scaling with system size for up to thousands of atoms, as well as good scaling on individual and parallel computers with many CPUs [108].

As indicated in section 2.2, all the observables such as energies, forces, polarizabilities, etc. of a cluster or periodic geometry require the solutions of the KS single particle Schrödinger equations. We can rewrite Eq. (2.41) in its explicit form:

$$\hat{H}^{KS} \left|\Psi_l\right\rangle = E_l \left|\Psi_l\right\rangle , \tag{2.53}$$

where the Hamiltonian $\hat{H}^{KS}$ incorporates the KS effective single-particle kinetic energy $\hat{T}_S$, the external potential $\hat{V}_{ext}$, the electrostatic potential $\hat{V}_H$ and the exchange-correlation potential $\hat{V}_{xc}$. Within each iteration performed in the SCF, the single-particle wave function is introduced as an expansion of the basis functions $\varphi_i(\boldsymbol{r})$, *i.e.* $\psi_l(\boldsymbol{r}) = \sum_{i=1}^{N_b} c_{il}\varphi_i(\boldsymbol{r})$. The discretized generalized eigenvalue problem to be solved becomes:

$$\sum_j h_{ij} c_{jl} = E_l \sum_j s_{ij} c_{jl} \tag{2.54}$$

where the Hamiltonian and overlap matrix elements h_{ij} and s_{ij} are obtained by numerical integration:

$$\begin{aligned} h_{ij} &= \int d^3\boldsymbol{r} \varphi_i(\boldsymbol{r}) \hat{H}^{KS} \varphi_j(\boldsymbol{r}) \\ s_{ij} &= \int d^3\boldsymbol{r} \varphi_i(\boldsymbol{r}) \varphi_j(\boldsymbol{r}) \quad . \end{aligned} \tag{2.55}$$

These matrices are essentially the real-space analogues of those defined in Eq.(2.15) and (2.16). The complex conjugate notation is omitted since only real-valued basis functions are used. The total number of Kohn-Sham states, N_{states}, is at most equal to the total number of basis functions, N_b. Now, the total energy of the KS system has the following expression:

$$E_{tot} = \sum_{l=1}^{N_{states}} f_l \varepsilon_l - \int d^3\boldsymbol{r}[n(\boldsymbol{r})V_{xc}(\boldsymbol{r})] + E_{xc}[n] - \frac{1}{2}\int d^3\boldsymbol{r}[n(\boldsymbol{r})V_H(\boldsymbol{r})] + E_{nuc-nuc} \quad . \tag{2.56}$$

Here the KS single-particle eigenvalues were summed up and their corresponding contribution to the exchange-correlation potential was subtracted in order to be replaced by the exchange-correlation energy functional $E_{xc}[n]$, which is needed to calculate the total energy. Moreover, the double-counting carried by the eigenvalues is removed and replaced with the nuclear-nuclear repulsion term. An essential principle of the FHI-AIMS code is that in order to ensure a wide range of total energy accuracies for rough or highly accurate calculations, the basis sets need to be preconstructed. The aim of this is to ensure the accuracy of the basis set and the convergence to a separately converged basis set limit. The numerical radial basis function $u_i(\boldsymbol{r})$ are chosen to satisfy the Schrödinger equation:

$$\left[-\frac{1}{2}\frac{d^2}{dr^2} + \frac{l(l+1)}{r^2} + v_i(r) + v_{cut}(r)\right] u_i(r) = \varepsilon_i u_i(r) \quad . \tag{2.57}$$

Two parts define the radial function: the potential $v_i(r)$, which describes the main shape of $u_i(r)$, and a fast increasing confining potential $v_{cut}(r)$, that ensures the smooth decay of each radial function such that they are strictly zero outside a confining radius r_{cut}.

Also, for different atomic structures, the basis sets should be transferable and should be as small as possible given a certain accuracy. The basis set construction procedure should be fully automated and objective, requiring no human assistance. To fulfil these goals, the construction assumes the following iterative workflow:

1. A large set of radial function shapes $u_i(r)$ (hydrogen-like and cation-like functions or valence and excited-states of single atoms) with a variable confinement potential is selected.

2. Starting from a given basis set (in the first iteration, the minimal free-atom basis set), run through the pool of candidate functions and add each separately to the given basis set. The radial function that yields the largest improvement in the total energy is added to the given basis set.

3. The same procedure is repeated iteratively until the total energy is converged.

It is worth noting that each radial function, $u_i(r)$, is associated to an angular momentum l according to the definition of NAOs in Eq. (2.52). Thus adding $u_i(r)$ to the given basis set implies in fact that all the $2l{+}1$ functions $\frac{u_i(r)}{r}Y_{lm}$ become part of the basis set. Also, the minimal basis set comprises core and valence functions of spherically symmetric free atoms and it is functional-dependent as it is obtained by setting $v_i(r)$ to the KS self-consistent free-atom radial potential.

For the optimization target, the simplest possible chemical bonds formed by a given element are chosen. Therefore the goal is to minimize the total energy error of a set of non-spinpolarized symmetric dimers constructed at $N_d \approx$ 4-5 different bond distances. The total energy error associated with each given basis set is evaluated as:

$$\Delta_{basis} = \frac{1}{N_d} \sum_{i=1}^{N_d} [\epsilon_{basis}(d_i) - \epsilon_{cb}(d_i)] \tag{2.58}$$

In the above expression, $\epsilon_{basis}(d_i)$ denotes the total energy per atom associated to the dimer with bond distance d_i for a given basis set. It is obtained non-selfconsistently in order to avoid potential systematic errors linked to the self-consistency cycle. It is then compared against the non-selfconsistent reference energy $\varepsilon_{cb}(d_i)$ for a converged basis set.

The different total energy accuracy levels (from qualitative tight-binding to sub-meV accuracies) correspond to increasingly larger sets of basis functions. These are organized as different, functional-independent, *tiers* or levels of different angular momenta such as spd-spdf-spdfg... . It is interesting how the automated basis construction process implemented here yields basis function groups similar to the more standard and human-devised Gaussian basis sets [111, 112].

One conclusion of this construction process is that valence functions of cations are really good additions to the minimal free atom basis set. Nevertheless, the main finding of the FHI-AIMS developers was that hydrogen-like functions perform better than all the initially considered radial functions, even better than the well-performing valence functions of cations. For Hartree Fock (HF) calculations, it would be desirable for the minimal basis set to be generated with a HF atomic solver that would essentially go beyond the standard DFT semilocal functional-based method. Such a solver is, however, not implemented so the starting minimal basis for HF calculations is the same as for conventional DFT ones. The only disadvantage is that additional tier basis functions are needed to achieve a target level of basis convergence.

2.4 Linear optical properties in RPA

DFT is highly accurate in determining ground-state properties for atoms, molecules and solids. As is known, the simplest approximation for E_{xc}, the LDA, employs the homogenous electron gas exchange-correlation energy density [81]. However, the success of LDA is not limited only to the correct prediction of ground-state properties of metals, but also of highly inhomogeneous system ones [113]. Due to the single-particle nature of the Kohn-Sham wavefunctions, their associated eigenvalues are quite often treated as quasiparticle energies [114, 115]. Since the Kohn-Sham single-particle states pertain to a fully noninteracting system, there is no particular theoretical rationale for identifying the Kohn-Sham eigenvalues as electron and removal energies [114]. Also, the LDA band gap and the transition energies in nonmetals are largely underestimated, causing a redshift of 30-50% in the absorption, photoemission and inverse photoemission spectra when compared to the experimental spectra [116]. Neverthless, using the Kohn-Sham equations as a starting point for perturbative calculations of quasiparticle energies for various systems is well founded, at least partially, in the resemblance between the Kohn-Sham and the quasiparticle equations where, in the latter case, the hole and the screened exchange caused by the addition of an electron are accounted for [114]. Another possible argument for this is the almost perfect overlap between the LDA and the quasiparticle wavefunctions, as it is claimed in the work of Hybertsen et al. [117] where systems with a large range of band gap sizes were investigated [114]. In order to discuss the absorption of light by an electronic system, one needs to go beyond the band structure and describe the response of the system to an external potential, which is reflected by the redistribution of its charge and their corresponding wave functions [114]. The response of the system to the external perturbation is quantified through the dielectric function which is found from Hedin's equations [71] to be:

$$\varepsilon(\boldsymbol{r},t;\boldsymbol{r'},t') = \delta(\boldsymbol{r}-\boldsymbol{r'})\delta(t-t') - \int P(\boldsymbol{r},t;\boldsymbol{r''},t')v(\boldsymbol{r''}-\boldsymbol{r'})d\boldsymbol{r''} \quad , \tag{2.59}$$

where v is the bare unscreened Coulomb interaction and P is the polarizability. The simplest approximation for P corresponds to the independent particle form that can be written in the random phase approximation (RPA) [118, 119] and it is expressed as [114]:

$$P_{RPA}(\boldsymbol{r},\boldsymbol{r}',E)=\sum_{ij}(f_i-f_j)\frac{\psi_i(\boldsymbol{r})\psi_j^*(\boldsymbol{r})\psi_j(\boldsymbol{r}')\psi_i^*(\boldsymbol{r}')}{E-\epsilon_{ij}+i\eta} \quad , \tag{2.60}$$

where f_i are Fermi occupation numbers and i and j are labels corresponding to the one-particle states of energy ϵ_i and ϵ_j. ϵ_{ij} represents the difference between energy ϵ_i and ϵ_j, respectively. The small imaginary term iη gives rise to an imaginary term in P, which is proportional to $\delta(E-\epsilon_{ij}+i\eta)$. This indicates that the photon energy E is conserved as an electron gets promoted from state i to state j [114].

In a nutshell, RPA describes a calculation where P has the expression found in Eq. (2.60) whereby the ψ_i wavefunctions and E_i energies can be DFT or GW eigenstates and eigenvalues. Also known as the Lindhard approximation [120], it was conceived to describe a calculation based on a linearized Hartree approach for the homogeneous electron gas [114]. Basically, the Hartree calculation is simplified by assuming that the induced charge is required only to first order in the total potential [75]. The presence of the hole is taken into account through the self consistent Hartree field [75]. In a nutshell, in this approximation, the electron-hole pair is noninteracting and thus, unscreened [114]. Since the neglect of exchange-correlation effects in the RPA electron-hole screening can lead to an underestimation of the dielectric constant, this approximation might overestimate exciton binding energies [114]. This is reflected, for instance, by the poor agreement between the RPA and experimental absorption spectrum of bulk Si [114].

Despite the mentioned issues regarding the use of DFT+RPA to obtain absorption spectra, we shall rely on this method to calculate the dielectric function of the systems discussed in this work. The good scaling with number of atoms renders DFT as a practical method to determine band structures for a large set of materials. As discussed, hybrid functionals enable a reasonably good determination of the band gap and hence, of the absorption edge. The advantage of using RPA for the calculation of the dielectric function of solids lies in the fact that it is more numerically practical compared to more precise methods that calculate effective two particle equations iteratively. In this work, the accurate determination of absorption spectra is not as relevant as understanding the relative differences in the absorption spectra of materials. Ultimately, we are interested to rank materials based on their absorption capabilities. Under these circumstances, we consider DFT+RPA to be a sufficiently valid approach.

In Ref. [115], a formalism for treating optical properties in the random phase approximation (RPA) is proposed. In the following, we shall reiterate the main steps and expressions required to derive the RPA dielectric function according to Ambrosch et al. [115].

For the case of a solid with translational symmetry, the states in Eq. (2.60) can be replaced by a sum over states and k-points, with $\boldsymbol{k}$ lying in the first Brillouin zone. It is also assumed here that the photon energy can be written as $E = \tilde{E} + i\eta$. Having said this, one can Fourier transform the polarization propagator P in Eq. (2.60) and obtain:

$$P_{\boldsymbol{G},\boldsymbol{G}'}(\boldsymbol{q}, E) = \frac{1}{\Omega_c} \sum_{n',n,\boldsymbol{k}} \frac{f(\epsilon_{n,\boldsymbol{k}+\boldsymbol{q}}) - f(\epsilon_{n',\boldsymbol{k}})}{\epsilon_{n,\boldsymbol{k}+\boldsymbol{q}} - \epsilon_{n',\boldsymbol{k}} - E} [M^{\boldsymbol{G}}_{n',n}(\boldsymbol{k}, \boldsymbol{q})]^* M^{\boldsymbol{G}'}_{n',n}(\boldsymbol{k}, \boldsymbol{q}) \quad , \tag{2.61}$$

where Ω_c is the unit cell volume, $\epsilon_{n,\boldsymbol{k}}$ are the eigenvalues corresponding to the k-point $\boldsymbol{k}$ and the band index n and M are the matrix elements defined as:

$$M^{\boldsymbol{G}}_{n,n'}(\boldsymbol{k}, \boldsymbol{q}) = \langle n', \boldsymbol{k}| \, e^{-i(\boldsymbol{q}+\boldsymbol{G})\cdot \boldsymbol{r}} \, |n, \boldsymbol{k} + \boldsymbol{q}\rangle \quad , \tag{2.62}$$

with $\boldsymbol{G}$ a reciprocal lattice vector and $\boldsymbol{q}$ belonging to the first Brillouin zone. Here the incoming photon of wavevector $\boldsymbol{q}$ excites an electron from state $|n', \boldsymbol{k}\rangle$ to state $|n, \boldsymbol{k} + \boldsymbol{q}\rangle$. By Fourier transforming Eq.(2.59), it follows that the polarization in Eq.(2.61) is related to the dielectric tensor as:

$$\varepsilon_{\boldsymbol{G},\boldsymbol{G}'}(\boldsymbol{q}, E) = \delta_{\boldsymbol{G},\boldsymbol{G}'} - v(\boldsymbol{q} + \boldsymbol{G}) P_{\boldsymbol{G},\boldsymbol{G}'}(\boldsymbol{q}, E) \quad . \tag{2.63}$$

The dielectric tensor establishes a connection between the total electrostatic potential V and the external potential, V^{ext}:

$$V^{ext}_{\boldsymbol{G}}(\boldsymbol{q}, E) = \sum_{\boldsymbol{G}'} \varepsilon_{\boldsymbol{G},\boldsymbol{G}'}(\boldsymbol{q}, E) V_{\boldsymbol{G}'}(\boldsymbol{q}, E) \quad . \tag{2.64}$$

Let us invert the dielectric tensor and denote it by $\overline{\varepsilon}$. It is reasonable to assume that the wavelength of the external perturbation potential resulted from the incoming light are much larger than the lattice size of the cell. In that case the assumptions made are that $\boldsymbol{q} \ll \boldsymbol{G_{min}}$ and that only the $\boldsymbol{G'} = 0$ component of $V^{ext}_{\boldsymbol{G'}}$, *i.e.* V^{ext}_0 would be non-zero and should be considered:

$$V_{\boldsymbol{G}}(\boldsymbol{q}, E) = \overline{\varepsilon}_{\boldsymbol{G},0}(\boldsymbol{q}, E) V^{ext}_0(\boldsymbol{q}, E) \quad . \tag{2.65}$$

As can be seen, even in the case of an external potential with long wavelengths in real space ($\boldsymbol{G'} = 0$), the response of the system has shorter wavelength components ($\overline{\varepsilon}_{\boldsymbol{G}\neq 0,0}$), which translate into microscopic changes in the local potential produced by particles or dipoles. These are referred to as local field effects. If we look at the previous equation and identify the average of the total potential in one unit cell as $V_0(\boldsymbol{q}, E)$, we can relate it to V^0_{ext} as:

$$V_0(\boldsymbol{q}, E) = \overline{\varepsilon}_{mac}(\boldsymbol{q}, E) V^{ext}_0(\boldsymbol{q}, E) \quad . \tag{2.66}$$

This gives us that the macroscopic dielectric constant ε_{mac} is essentially one over the (0,0) element of the inverse dielectric tensor:

$$\varepsilon_{mac}(\boldsymbol{q}, E) = \frac{1}{\overline{\varepsilon}_{0,0}(\boldsymbol{q}, E)} \quad . \tag{2.67}$$

Evaluating the dielectric tensor with components $\boldsymbol{G}, \boldsymbol{G'}$ and subsequently inverting it to obtain the (0,0) component of the inverse tensor is rather expensive. However, if we neglect the local field effect and substitute the (0,0) component of the inverse by the inverse of the (0,0) component, it follows that:

$$\varepsilon^{nlf}_{mac}(\boldsymbol{q}, E) = \varepsilon_{0,0}(\boldsymbol{q}, E) = 1 - v(\boldsymbol{q}) P^0_{0,0}(\boldsymbol{q}, E) \quad . \tag{2.68}$$

Local field effects will be further neglected in the derivation of the dielectric function expressed in terms of the KS eigenvalues. We expect their effect to be negligible, at least for the in-plane component of the dielectric function of our studied systems.
As argued before, it is assumed that light has a wavevector $\boldsymbol{q}$ that is much smaller than that of the electrons in the system. Hence the matrix elements in the expression for P will be studied in the limit of small $\boldsymbol{q}$ through perturbation theory in the

Appendix. There, in Eq. (A.13), it is indicated that the intraband matrix elements ($n' = n$) and the interband matrix elements have distinct limits. This motivates one to split the dielectric tensor into terms corresponding to intraband and interband transitions, respectively:

$$\varepsilon^{nlf}_{mac}(\boldsymbol{q}, E) = 1 + \varepsilon^{intra}(\boldsymbol{q} \to 0, E) + \varepsilon^{inter}(\boldsymbol{q} \to 0, E) \quad . \tag{2.69}$$

The minimum macroscopic dielectric tensor is 1 and it corresponds to the case where the system is unpolarizable. Considering that the Coulomb interaction in reciprocal space is $v(\boldsymbol{q}) = \dfrac{4\pi e^2}{|\boldsymbol{q}|^2}$ and using Eq.(2.63), it follows that the intraband term constituting the dielectric tensor is:

$$\varepsilon^{intra}(\boldsymbol{q} \to 0, E) = -\lim_{\boldsymbol{q}\to 0} \frac{4\pi e^2}{\Omega_c |\boldsymbol{q}|^2} \sum_{n,\boldsymbol{k}} \frac{f_0(\epsilon_{n,\boldsymbol{k}+\boldsymbol{q}}) - f_0(\epsilon_{n,\boldsymbol{k}})}{\epsilon_{n,\boldsymbol{k}+\boldsymbol{q}} - \epsilon_{n,\boldsymbol{k}} - E} |M^0_{n,n}(\boldsymbol{k}, \boldsymbol{q})|^2 \quad , \tag{2.70}$$

and the interband term is given by:

$$\varepsilon^{inter}(\boldsymbol{q} \to 0, E) = -\lim_{\boldsymbol{q}\to 0} \frac{4\pi e^2}{\Omega_c |\boldsymbol{q}|^2} \sum_{n',n\neq n',\boldsymbol{k}} \frac{f_0(\epsilon_{n',\boldsymbol{k}+\boldsymbol{q}}) - f_0(\epsilon_{n,\boldsymbol{k}})}{\epsilon_{n',\boldsymbol{k}+\boldsymbol{q}} - \epsilon_{n,\boldsymbol{k}} - E} |M^0_{n,n'}(\boldsymbol{k}, \boldsymbol{q})|^2 \quad . \tag{2.71}$$

Notice that in the case of the intraband term, in the limit of $\boldsymbol{q} \to 0$, $\epsilon_{\boldsymbol{k}+\boldsymbol{q}} - \epsilon_{\boldsymbol{k}} \approx E \approx 0$. Therefore, it is justified to transform the fraction into a derivative with respect to the energy eigenvalues. Using the expressions Eq.(A.11) and Eq.(A.13) for the expanded band energies and for the matrix elements, which were both derived in the Appendix, one obtains the following expression for the intraband term:

$$\varepsilon^{intra}(\boldsymbol{q} \to 0, E) = -\lim_{\boldsymbol{q}\to 0} \frac{4\pi \hbar^2 e^2}{\Omega_c m^2 E^2} \sum_{n,\boldsymbol{k}} \Big(-\frac{\partial f}{\partial \epsilon} \Big)_{\epsilon_{n,\boldsymbol{k}}} \Big(p_{n,n,\boldsymbol{k}} \cdot \frac{\boldsymbol{q}}{|\boldsymbol{q}|} \Big)^2 \quad , \tag{2.72}$$

where $p_{n,n,\boldsymbol{k}} = \langle \psi_{n\boldsymbol{k}} | - i\hbar\nabla | \psi_{n\boldsymbol{k}} \rangle$ are the momentum matrix elements corresponding to the intraband transitions. The derivative of the Fermi function with respect to the energy imposes the restriction to sum only over states at the Fermi level. The interband term is expressed as:

$$\varepsilon^{inter}(\boldsymbol{q} \to 0, E) = -\lim_{\boldsymbol{q}\to 0} \frac{4\pi \hbar^2 e^2}{\Omega_c m^2} \sum_{\boldsymbol{k},c,v} \frac{(p_{c,v,\boldsymbol{k}} \cdot \boldsymbol{q}/|\boldsymbol{q}|)^2}{(\epsilon_{c,\boldsymbol{k}} - \epsilon_{v,\boldsymbol{k}} - E)(\epsilon_{c,\boldsymbol{k}} - \epsilon_{v,\boldsymbol{k}})^2} \quad , \tag{2.73}$$

where c runs over the empty conductions states, v over the occupied valence ones and $p_{c,v,\boldsymbol{k}} = \langle\psi_{c\boldsymbol{k}}| - i\hbar\nabla |\psi_{v\boldsymbol{k}}\rangle$ are the momentum matrix elements corresponding to the interband transitions. Even in the limit $\boldsymbol{q} \to 0$, the direction of the vector $\boldsymbol{q}$ leads to defining the dielectric constant as a three dimensional tensor given by:

$$\begin{aligned}\varepsilon_{i,j}(E) =&\delta_{i,j}\\ &-\frac{4\pi\hbar^2e^2}{\Omega_c m^2E^2}\sum_{n,\boldsymbol{k}}\Big(-\frac{\partial f}{\partial\epsilon}\Big)_{\epsilon_{n,\boldsymbol{k}}}p_{i,n,n,\boldsymbol{k}}p^*_{j,n,n,\boldsymbol{k}}\\ &-\frac{4\pi\hbar^2e^2}{\Omega_c m^2}\sum_{\boldsymbol{k},c,v}\frac{p_{i,c,v,\boldsymbol{k}}p^*_{j,c,v,\boldsymbol{k}}}{(\epsilon_{c,\boldsymbol{k}}-\epsilon_{v,\boldsymbol{k}}-E)(\epsilon_{c,\boldsymbol{k}}-\epsilon_{v,\boldsymbol{k}})^2}\quad .\end{aligned} \tag{2.74}$$

The i and j indices correspond to the Cartesian directions along which the gradient are applied in $p_{i,c,v,\boldsymbol{k}}$ and $p_{j,c,v,\boldsymbol{k}}$, where $p_{j,c,v,\boldsymbol{k}}= \langle\psi_{c\boldsymbol{k}}|-i\hbar\nabla_j |\psi_{v\boldsymbol{k}}\rangle$. The obtained RPA expression for the dielectric constant will be computed using the KS orbitals and the associated single particle eigenvalues. In the case of a 2D material, we consider a large unit cell volume. Since we only sample one k-point in the third direction at Γ, we set the same large constant c axis for all 2D materials. The fact that each volume cell can be scaled by a common scaling factor allows for the dielectric functions to be comparable relative to one another.

In the remaining part we shall elaborate further the expression of the interband term of the dielectric function as implemented in FHI-AIMS. This decision is motivated by the fact that intraband transitions are dominant in metallic systems, where the free electrons respond to the incoming radiation by oscillating at a common plasma frequency, ω_{pl}. However, intraband transitions are negligible in the case of semiconductors and insulators. In the case of photovoltaic systems, semiconductors are the preferred absorbers due to their band gap. This ensures the presence of an energy barrier for the valence electrons to overcome when excited by the incoming photons, leading to the free flowing of the electrical current. Setting m=e=$\hbar$=1 and assuming that $\boldsymbol{q} \to 0$ and that the photon energy E satisfies $E \approx \epsilon_{c,\boldsymbol{k}} - \epsilon_{v,\boldsymbol{k}}$, the interband term of the dielectric constant derived in Eq.(2.73) is equivalent to:

$$\varepsilon^{inter}_{ij}(E) = \frac{4\pi}{\Omega_c\cdot(E+\eta)}\sum_{c,v,\boldsymbol{k}}\frac{2}{\epsilon_{cv}+\eta}\cdot\Big(\frac{p_{i,c,v,\boldsymbol{k}}p^*_{j,c,v,\boldsymbol{k}}}{E-\epsilon_{cv}-i\eta}-\frac{p^*_{i,c,v,\boldsymbol{k}}p_{j,c,v,\boldsymbol{k}}}{E+\epsilon_{cv}+i\eta}\Big)\quad , \tag{2.75}$$

where $\epsilon_{cv} = \epsilon_{c,\boldsymbol{k}} - \epsilon_{v,\boldsymbol{k}}$. The constant 2 stands for the occupation number in the case of spin degenerate states. Here $i\eta$ represents an infinitesimal energy that is added explicitly in the denominator to avoid singularities. This expression is equivalent to Eq.(A.38) in the Appendix, where we derive the dielectric function following the Kubo-Greenwood formula for optical conductivity as indicated in Marder et al. [74]. So in fact it follows that the imaginary part of the interband term of the dielectric function along a certain Cartesian direction is

$$Im[\varepsilon_{ii}(E)] = \frac{8\pi}{\Omega_c \cdot (E+\eta)} \sum_{c,v,\boldsymbol{k}} \frac{\eta \cdot |p_{i,c,v,\boldsymbol{k}}|^2}{\epsilon_{cv} + \eta} \cdot \Big(\frac{1}{[E-\epsilon_{cv}]^2 - \eta^2} - \frac{1}{[E+\epsilon_{cv}]^2 + \eta^2} \Big) \quad . \tag{2.76}$$

$Re[\varepsilon_{ii}(E)]$ can be obtained similarly, by taking the real part of the interband dielectric function defined in Eq. (2.75). Now let us consider the electric field $\boldsymbol{E}$ associated with the incident radiation. It propagates as a damped wave:

$$\boldsymbol{E}(x,t) = E_0(x)\hat{\boldsymbol{e}}e^{i\frac{\omega}{c}(nx-ct)} \quad , \tag{2.77}$$

where ω is the angular frequency, $\hat{\boldsymbol{e}}$ is the polarization vector, c is the speed of light, and n is the complex refractive index. The intensity of the field is proportional to $|E(x)|^2$, *i.e.*:

$$I(x) = E_0^2 e^{-2\frac{\omega}{c}n_2 x} \quad . \tag{2.78}$$

The absorption coefficient is defined as the inverse of the distance at which I_0 is reduced by e, where $I_0 = E_0^2$ is the initial intensity. Therefore:

$$\alpha = \frac{2\omega n_2}{c} \quad , \tag{2.79}$$

where n_2 is the imaginary part of the refractive index n. Let us note that the macroscopic dielectric constant and the complex refractive are related as $\varepsilon_{mac} = \varepsilon_1 + i\varepsilon_2 = n^2$. An equivalent expression for the absorption coefficient that follows is:

$$\alpha = \frac{\omega\varepsilon_2}{cn_1} \quad , \tag{2.80}$$

where n_1 is the real part of the refractive index. In calculating the absorption coefficient through Eq.2.80, we use the real expression of n_1, namely

$$n_1 = \sqrt{\frac{\varepsilon_1 + \sqrt{\varepsilon_1^2 + \varepsilon_2^2}}{2}} \quad . \tag{2.81}$$

2.5 k-means clustering

In Chapter 5 we present our work on the classification of transitional metal dichalcogenides. For this exercise, we employ a statistical technique that identifies numerical patterns in our selected pool of compounds and yields groups of similar materials based on the variable of interest. In our case, this is represented by the absolute value of the gradient of the energy difference between the bottom conduction and top valence band. For this purpose, we make use of a statistical technique known as "k-means". This is a widely-used method for "optimal classification" [121]. The algorithm was first proposed in 1956 by Steinhaus [122] and then exemplified for data clustering applications by Lloyd et al. in the work referenced in Ref. [123]. The technique relies on partitioning a multi-dimensional set of points into k sets or clusters. A number of k cluster centers are initialized. For each point in the dataset, the closest cluster center is found and the point gets assigned to the respective cluster. The measure for proximity is given by the shortest Euclidean distance between that respective point and the cluster center. Afterwards, the means of all the positions of the points defining each cluster are computed and the cluster centers get updated. Hence, at each iteration there is a different set of k-means based on the specific composition of each group at each stage [121]. This iterative process continues until no new updates are made to any of the clusters [124]. The described steps in the algorithm are graphically illustrated in Fig. 2.2. One can synthetically reformulate the objective of the k-means procedure as the minimization of the squared Euclidean distances also termed as "within-cluster sum of squares" [125]:

$$WCSS^1 := \sum_{c_i} \sum_{j=1\ldots d} \sum_{x,y \in c_i} (x_{ij} - y_{ij})^2 \quad , \tag{2.82}$$

where c_i denotes the ith cluster, d are the total number of dimensions of the vector and x and y are the data points or observables belonging to cluster c_i. So, the

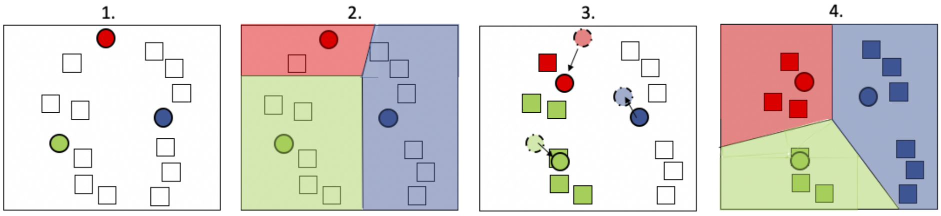

Figure 2.2: 1. Random generation of k-means 2. Closest points to the means form clusters 3. New means are calculated and updated 4. Previous two steps are repeated till convergence is reached.

Euclidean distance is calculated between the data points of all i clusters which are represented as d-dimensional vectors. Due to lower computational complexity, an equivalent definition of the WCSS is commonly used, namely as the sum of cluster variance weighted by the cluster size whereby the pairwise distances are in this case between the cluster points and their respective cluster centers [125]:

$$WCSS^2 := \sum_{c_i} \sum_{j=1...d} |2c_i| \sum_{x \in c_i} (x_{ij} - \mu_{ij})^2 \quad , \tag{2.83}$$

where μ_{ij} is the mean coordinate of cluster i in dimension j. It is worth noting that the overall sum of the Euclidean distances remains constant throughout each iteration and irrespective of the number of clusters. That implies that the total variance of the data set does not change, hence minimizing the WCSS is equivalent to maximizing the difference between points that are in different clusters [125]. The latter is also referred to as the "between-cluster sum of squares" (BCSS).

The presented statistical tool will be implemented in order to group 2D materials based on similarities identified in their electronic structure. The quantity that is selected for the classification is the absolute value of the gradient of the difference between the bottom conduction band and the highest valence band, $|\nabla_{\boldsymbol{k}}(E_{c1} - E_{v1})|$ across the irreducible Brillouin zone. We will show later how this quantity is related to band nesting, a process inherent to all transition metal dichalcogenides that gives rise to strong absorption peaks. Each compound will be characterized by a multidimensional vector representing the mentioned gradient calculated on a dense k-mesh. Compounds grouped together via k-means are expected to exhibit certain similar absorption features. Such a classification based on simple electronic structure analysis serves as a screening for suitable photovoltaic compounds.

3 Photoconversion efficiency study

3.1 Introduction

The following work consists of a study of the photoconversion efficiency of various well-established photovoltaic materials. The model used was conceived as a "hybrid" between the SQ and SLME models presented in sections 1.5.1 and 1.5.3, respectively. Here we describe the quantities relevant for the model. In order to account for the inhomogeneity of the absorption spectrum, we consider the SLME definition of the absorbance:

$$a(E) = 1 - e^{-\alpha(E)L} \quad , \tag{3.1}$$

where $\alpha(E)$ is the absorption coefficient obtained from the bandstructure postprocessing according to Eq.(2.80) and L is the thickness of the material considered. Note that we did not impose here the condition of reflectivity of the back surface for brevity. The short-circuit current density is essentially calculated as the maximum current extracted under solar radiation given the absorbance $a(E)$:

$$J_{sc} = q \int_0^\infty \Phi_{sun}(E) a(E) dE \quad , \tag{3.2}$$

where Φ_{sun} corresponds to the $AM1.5G$ solar photon flux according to the ASTM G173-03 standard [8] and q is the elementary charge. Note that we made the approximation $J_{sc} \approx J_{max}$, where the maximum photogenerated current density was defined in Eq.(1.6). This decision was motivated by the fact that the radiative current density at zero bias, which is the difference between J_{max} and J_{sc} in the

SQ model, is considered to be negligible according to Ref.[130]. According to the SLME model, an analysis of the momentum matrix elements would be required to determine whether a transition is forbidden or not. However, we did not follow this procedure in calculating the fraction of radiative recombination f_r due to technical difficulties. Instead, similarly to the SQ model, we assume that the only recombination losses are due to radiation, *i.e.* $f_r = 1$ so that $J_0 = J_r$, where J_0 is defined in Eq.(1.29). Then the total net current is found to be:

$$J = J_{sc} - J_r(e^{eV/k_BT} - 1) \quad , \tag{3.3}$$

where V is the voltage across the cell, k_B is Boltzmann constant and T is set to be at room temperature, *i.e.* 300 K. Here the radiative recombination current density is a function of the non-constant absorption coefficient:

$$J_r(V) = f_g \cdot q \int_0^\infty \frac{2\pi E^2}{h^3c^2} \cdot \frac{a(E)}{e^{\frac{E-qV}{k_BT_c}} - 1} dE \quad . \tag{3.4}$$

The maximum extracted power P_{max} is the maximum product between the voltage and the net current:

$$P_{max} = max(V \cdot J) \quad . \tag{3.5}$$

The photoconversion efficiency is the ratio between P_{max} and P_{in}, the latter being the total power of the irradiated solar flux, which is equal to 1000.22 A/m^2. Thus, the PCE can be expressed as:

$$PCE = \frac{P_{max}}{P_{in}} \tag{3.6}$$

We will start with a description of the workflow that was conducted in the initial phase in order to determine the photoconversion efficiency. As discussed in the Introduction chapter, amorphous and crystalline silicon have played a big role in establishing the first generation of PV technology. That is why we shall showcase silicon in this part.

3.2 Silicon

To start off, we perform convergence tests of the number of k-points with respect to two control quantities, namely to the total energy E and the direct band gap E_g. This is done through single-point calculations. This calculation runs multiple SCF cycles at the end of which the ground state density for the original unchanged geometrical structure is determined. This type of test is typical for the correct estimation of the number of k-points required for a subsequent geometrical optimization calculation. The total energy is chosen as an obvious control quantity because converging it towards its minimum essentially ensures a correct ground-state density estimation, which is critical for the calculation of further quantities. The band gap is a feature particularly of interest for the analysis of the absorption spectrum entailed in our study. These single-point calculations done with increasing number of k-points are performed with the "tight" basis set for each of the involved atom species, in this case Si only. The GGA semi-local functional as parametrized by PBE is employed in these calculations as well as for the relaxations, bandstructure and dielectric function ones.

As it can be seen from Fig. 3.1, the k-grid composed of 10x10x10 points is sufficient for obtaining an accurate band gap E_g and total energy E, respectively, *i.e.* within

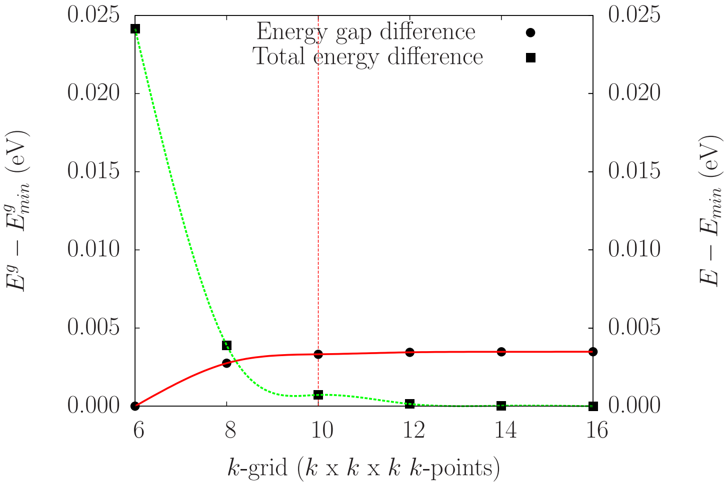

Figure 3.1: Convergence of the k-grid for single-point calculations of Si with respect to the total energy (squares and right-hand scale) and the direct band gap (circles and left-hand scale) values. The connecting lines are a guide to the eye obtained by interpolation.

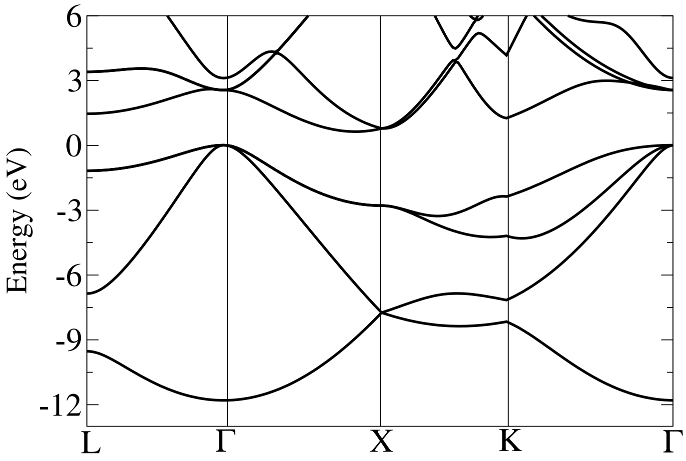

Figure 3.2: Silicon bandstructure plot using the GGA single-particle eigenvalues.

less than 5 meV from their corresponding minima. After the optimized geometry is calculated with a relaxation calculation performed with the converged k-grid, the band structure of Si is obtained. As expected, the bandstructure plot depicted in Fig.3.3, reveals that Si is an indirect gap semiconductor and the PBE energy gap value is approximately 0.63 eV. This value is in good agreement with the PBE band gap of 0.57 eV calculated in [131]. The valence band maximum is at Γ and the conduction band minimum is at Δ, where the latter symmetry point lies between Γ and X. As pointed out in Section 2.2.2, there is an inherent underestimation within DFT of the true band gap of any insulator.

In order to understand the severity of this effect, we compare the PBE-obtained band gap values with the experimental band gap values for Si [132]. These are tabulated below in Table 3.1.

The next step in our endeavour is to perform post-processing to the band structure according to Eq.(2.75). The three diagonal elements of the dielectric tensor $\underline{\underline{\varepsilon}}$, *i.e.* $\varepsilon_{xx}, \varepsilon_{yy}$ and ε_{zz} are identical since Si has a diamond lattice, and hence, it is an isotropic system. Therefore, in the case of Si, we will present only one of the components for simplicity. Before generating these quantities, it is worth noting from

	PBE	Exp.
E_g^i(eV)	0.63	1.14 [132]
E_g^d(eV)	2.55	3.40 [133]

Table 3.1: Silicon band gaps. The references for the experimental band gaps are also cited.

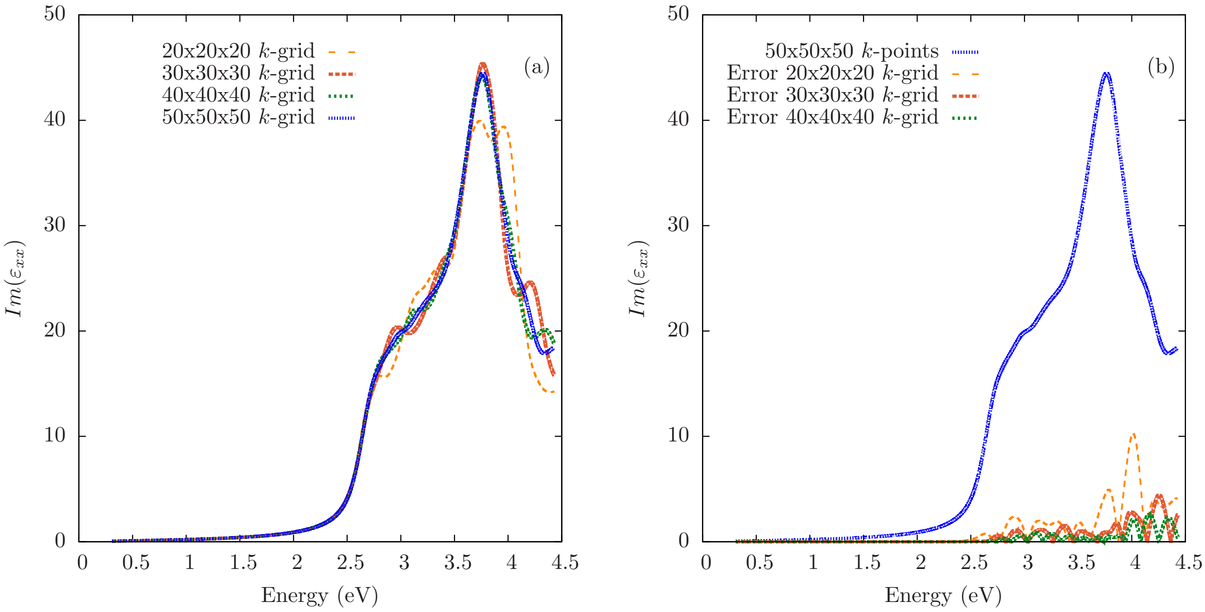

Figure 3.3: (a) The xx component of the imaginary part of the dielectric function of Si plotted for different k-grids. (b) The converged spectrum of Si with k-grid 50x50x50 along with the error functions.

Eq.(2.75) that a high number of k-points is crucial in order to capture a smooth, noise-free spectrum. To this end we conduct another k-grid test for the convergence of $Im(\varepsilon_{xx})$ which is defined in Eq.(2.76). We incrementally increase the size of the k-grid and quantify the gradual changes in the spectra by devising an error function equal to the absolute value of the difference between any two consecutive spectra. Once this error function reaches a critical value of approximately 10%, we consider that particular spectrum converged with respect to the number of k-points. Here, the grid consisting of 50x50x50 k-points was taken to be converged.

Let us now look at the imaginary part of the xx component of ε, Im(ε_{xx}) and its real counterpart Re(ε_{xx}). They can be seen in Fig. 3.4. These components are plotted in the same energy range, in which the visible spectrum lies as standardized by the American Society for Testing and Materials in Ref. [8]. The photon solar flux density rate reported in this source refers to photon energies between approximately 0.33 eV and 4.42 eV.

According to Eq.(2.76), only vertical transitions are considered in the calculation of the imaginary part of the dielectric function. These transitions are basically between single-particle states that are characterized by the same k-point. This implies that the onset of the spectrum of the imaginary part of the dielectric function (and also of

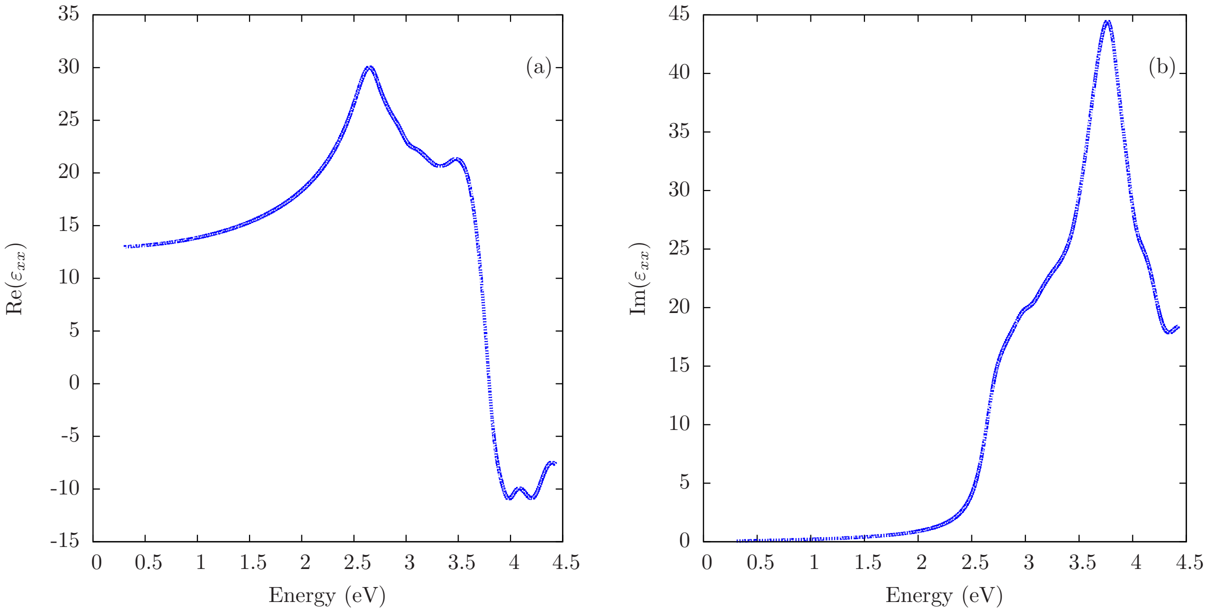

Figure 3.4: The real and imaginary parts of the xx-component of the dielectric tensor for Si obtained from FHI AIMS postprocessing of the bandstructure.

the absorption coefficient) lies at the direct band gap energy since that is essentially the energy of the lowest vertical transitions. In the case of Si, the onset of Im(ε) is at its PBE calculated direct band gap energy, namely at 2.55 eV. We proceed now to calculating the absorption coefficient in terms of the imaginary and real part of the dielectric functions. An obvious shortcoming of the resulting absorption spectrum is that its PBE determined onset is also drastically underestimated. In order to correctly describe the onset, we apply a band gap correction or what is also called a "scissors operator". This consists in rigidly shifting the energy range of the absorption coefficient spectrum by a quantity Δ equal to the difference between the empirical direct gap value and the calculated one, *i.e.* $\Delta = E^g_{exp} - E^g_{PBE}$.

The "corrected" and "uncorrected" absorption coefficients can be seen together with the spectrum of the solar flux in Fig. 3.5. Note the significant reduction in the overlap between the solar flux and the absorption spectrum of Si when applying the energy shift.

The next step involves calculating the efficiency for which we will follow the scheme described at the beginning of the chapter. The two relevant quantities, the short-circuit current density, J_{sc}, and the radiative recombination current density, $J_r(V)$, are functions of the absorbance, which in turn depends on the thickness L of a

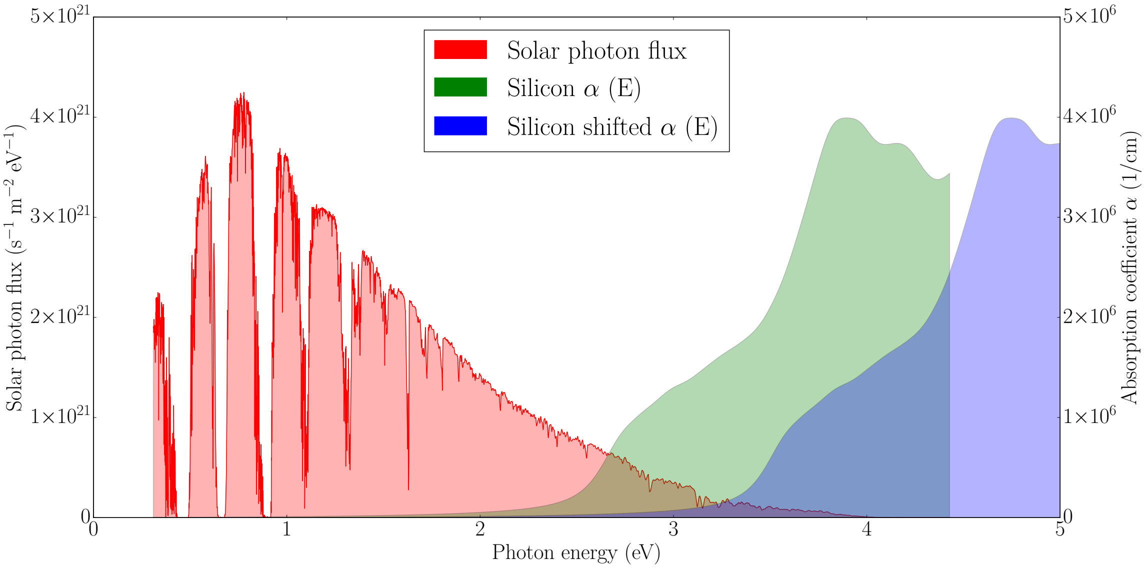

Figure 3.5: The shifted (blue) and unshifted (green) Si absorption coefficient obtained from the PBE bandstructure of Si along with the solar flux.

material. Obviously the thicker the material is, the larger is the absorbance. Hence, the PCE is also a thickness-dependent quantity. To explore J_{sc}, $J_r(V)$ and PCE for Si, we fix L to be equal to the experimental diffusion length, $L_d = 200\mu m$, which was reported in Ref. [51]. It is reasonable to assume that the cell thickness should coincide with the average length that carriers travel before recombining as, in principle, in this way the ratio between the fraction of the absorbance and that of the recombination, is maximized. We vary the voltage V between 0 and 5 V in steps of 0.1 V in the calculation of the net current density via Eq.(3.3). The efficiency obtained through Eq.(3.6) is 33.4%. This value is very close to the SQ maximum efficiency obtained by Rühle [9] for a material with a band gap $E_g = 1.34$ eV under $AM1.5G$ global solar spectrum. It is also worth noting that, since J_{sc} is calculated by integrating the corrected absorption spectrum from Fig. 3.5 over the solar spectrum, the amount of overlap between the two is essential. As mentioned before, the entire absorption spectrum is shifted so that the PBE direct band gap, 2.55 eV, would match with the real experimental one of 3.40 eV, thus ensuring that the onset of the calculated spectrum coincides with the one of the direct transitions occurring in a real Si system. Here, however, the entire shifted absorption spectrum including the portion below the direct band gap (for $E < 3.40$ eV) is considered. According to Eq. (2.75), only transitions between states described by the same k-

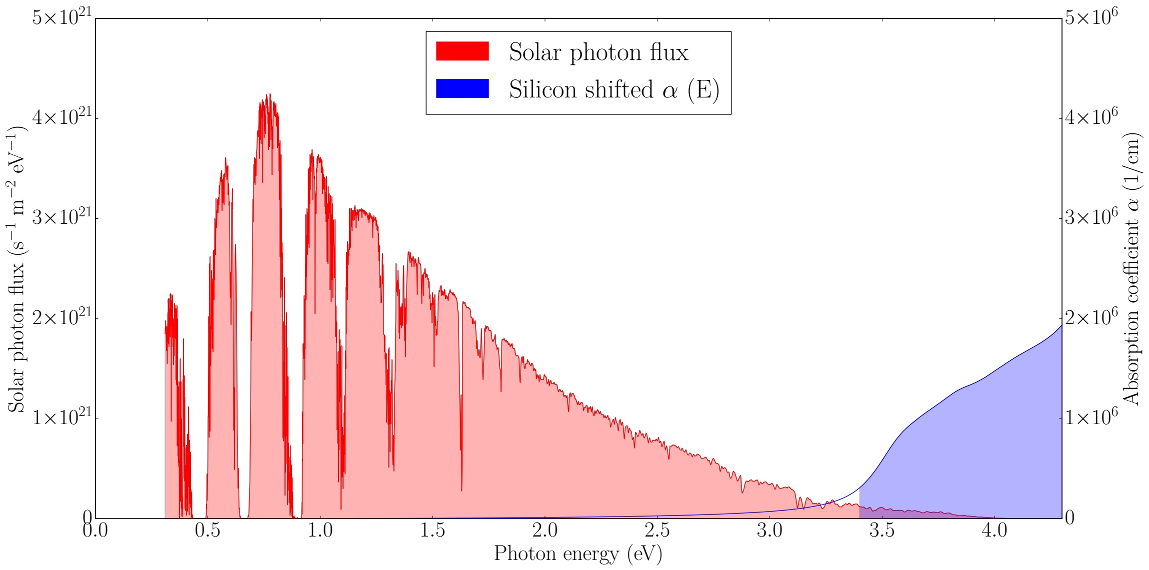

Figure 3.6: The Si shifted absorption coefficient (blue) and the solar flux (red) over the solar photon energy range. The portion below E_g=3.4 eV stems strictly from the artificially broadened absorption spectrum. The area below this region is not shaded in blue in order to emphasize how much of the overlap with the solar flux is lost when omitting it.

point contribute to the dielectric function. However, in order to account for the more realistic case where the system has a finite temperature and hence, the states have a limited lifetime, the imaginary part of the dielectric function are represented by Lorentzian functions that introduce an artificial broadening in the spectrum. This leads to a non-negligible amplitude in the spectrum at energies below the direct gap. Although this portion is up to three orders of magnitude lower than the one above direct gap, the fact that it lies in the energy region where the photon flux is the largest, leads to a high J_{sc} of 419.4 A/m^2, which is similar to the predicted value in Ref.[58]. If, in contrast, we completely neglect the artificially broadened region below 3.40 eV and rely only on the contribution that is derived strictly from the predicted direct transitions, the PCE drops to a value of 1.7%. The overlap of this truncated absorption spectrum with the solar flux spectrum can be seen in Fig. 3.6. This considerable reduction in the efficiency is not surprising as the photon flux is up to an order of magnitude weaker in the region of the direct band gap, hence leading to a much lower short-circuit current density of 5.6 A/m^2. Si devices are known to reach much higher efficiencies either due to the enhancement of the cell architecture, which leads to a reduction of recombination losses [134] or due to an enhanced absorption, made possible through a technique that exploits the wavelike nature of the light through "wave-interference-based light-trapping" [135]. Having said that, we conclude that in this model the treatment of the pre-gap artificial broadening is highly critical for indirect band gap materials. This is especially true for those materials like Si whose direct gap is very large. The portion of the absorption coefficient with the largest amplitude lies in the tail of the solar spectrum. However, this study aims to understand the effect of the absorption coefficient originating from the onset, namely the portion that is derived primarily from the band structure and not the pre-edge region. It is commonly considered that the pre-edge region is dominated by the amount of thermal and structural disorder present in the material, such as doping and defects [136, 137]. Therefore, we consider the strong impact of the artificial broadening on the PCE estimation for Si and other possible indirect materials to be an indication of the fact that this model would be better suited for direct band gap materials, or more generally, for systems whose direct band gaps matches the energies where the solar flux exhibits the highest amplitudes (at approximately at 0.8-1.1 eV). This condition could be more relevant than the shape of the absorption coefficient itself.

3.3 MAPI

We further investigate a different material, namely methylammonium lead iodide perovskite, in short MAPI. This hybrid perovskite has received increased attention due to its remarkably high photoconversion efficiency. Here we employ the exact same ground state orthorhombic phase structure that is investigated by the authors of Ref. [130]. In order to be able to compare our findings with those of the previously mentioned authors, we conduct the band structure and dielectric function calculations using LDA. Following the same convergence procedure described for Si, we obtained the necessary k-grid for performing the band structure and the dielectric function calculation in the case of MAPI, namely 20x20x20 k-points. As can be seen in Fig. 3.7, the structure has a direct gap of 1.55 eV at the Γ point. Along the Γ-Z line, the conduction band splits between a dispersed, parabolic band crossing 1.7 eV at Γ, and two flat bands above and below it. This splitting of the

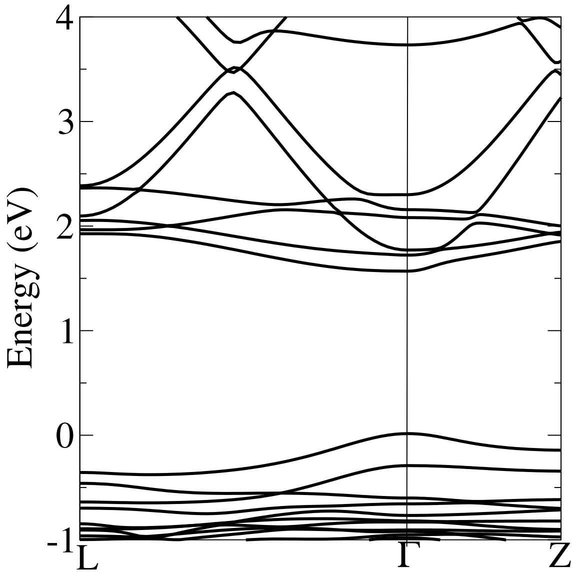

Figure 3.7: Band structure of MAPI in the orthorhombic phase calculated using LDA.

doublet of approximately 0.15 eV is due to the orthorhombic distortion [130]. One can see another doublet above 2 eV attributed to the folding of a band as a result of doubling the cell along the c-axis. Moving to the L-Γ direction, it appears that the lowest conduction band becomes dispersive, while the doublet splits into a flat band and a highly dispersive band, respectively. In contrast, the singlet band at the very top of the valence is significantly dispersive.

With this band structure at hand, we can now calculate the real and imaginary part of the dielectric function and compare them with those obtained by the previously mentioned authors. They employed a similar methodology to calculate the dielectric function, namely they omitted exciton effects and assumed a single-particle picture to calculate the dielectric function with the interaction accounted by the Hartree term via the RPA. The slight differences in amplitude of the various real and imaginary components in Fig. 3.8 that arise between our calculation and the one in Ref. [130], might be due to the use of different basis sets, pseudo-potentials and other possible slight variations in the determination of the imaginary part. Nevertheless, there is good agreement between the two dielectric functions.

Once again we proceed to calculating the *PCE*. Firstly, we look at how the *PCE* and the short-circuit current change with the omission of the pre-edge contribution. For clarity, we depict the resulting truncated spectrum along with the complete one

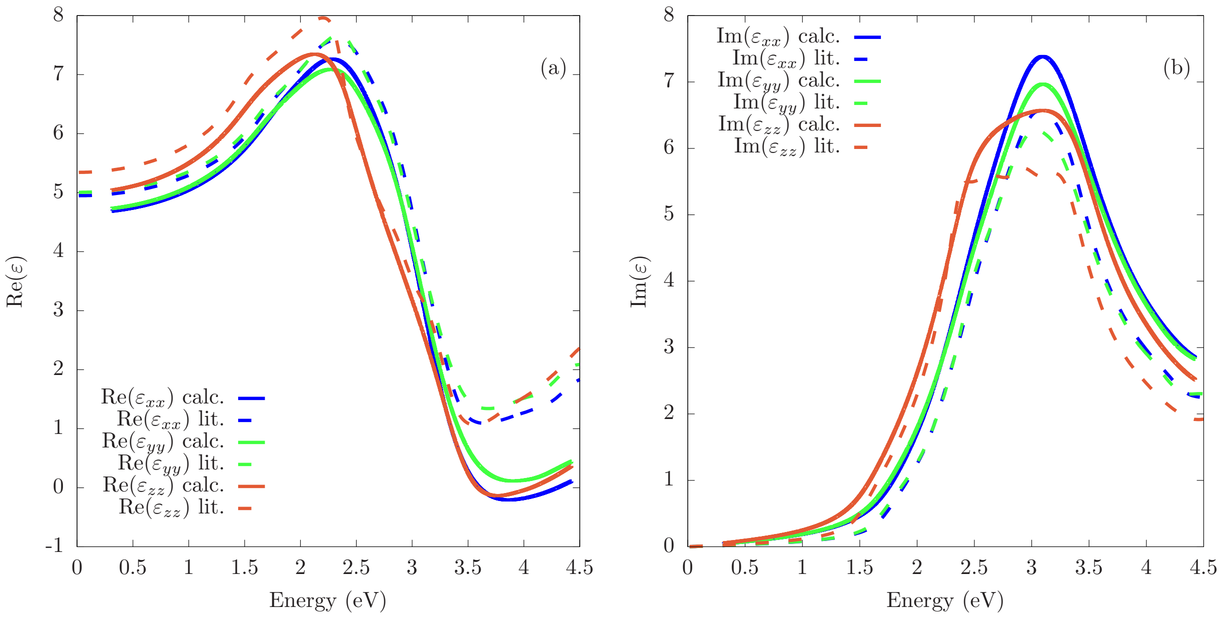

Figure 3.8: (a) The real parts of the xx, yy and zz components of the dielectric function of orthorhombic MAPI. The solid lines are our calculated functions while the dashed ones correspond to those of the authors of Ref. [130].(b) The imaginary parts of the xx, yy and zz components of the dielectric function. Same line convention applies.

in Fig. 3.9. Secondly, in order to understand how relevant the actual absorption spectrum is, we compare its corresponding PCE with the PCE obtained when the absorbance $a(E)$ is a step function that is unity at energies higher or equal to the band gap and zero below. Throughout this section we set the cell thickness L to 330 nm in order to match with that of the experimental work referenced in [138]. Similarly to our procedure implemented in the case of Si, we rigidly shift the LDA calculated band gap (E_g^{LDA}=1.55 eV) to the experimental one ($E_g^{exp.}$=1.57 eV) [139]. Therefore in the entire discussion that follows the direct band gap is assumed to be at 1.57 eV.

The PCE obtained when taking the entire absorption spectrum including the broadened region below the direct gap is 4.8% . The PCE becomes 27.2% when we consider only the spectrum above the direct gap. However, the short-circuit current densities do not change as drastically. They are 294.3 A/m^2 and 229.0 A/m^2, respectively. Hence, despite the reduction in the J_{sc} when omitting the spectrum below the gap, the PCE has an approximately six fold increase. This is due to the significant decrease of the reverse saturation current J_0 (which is equivalent here to

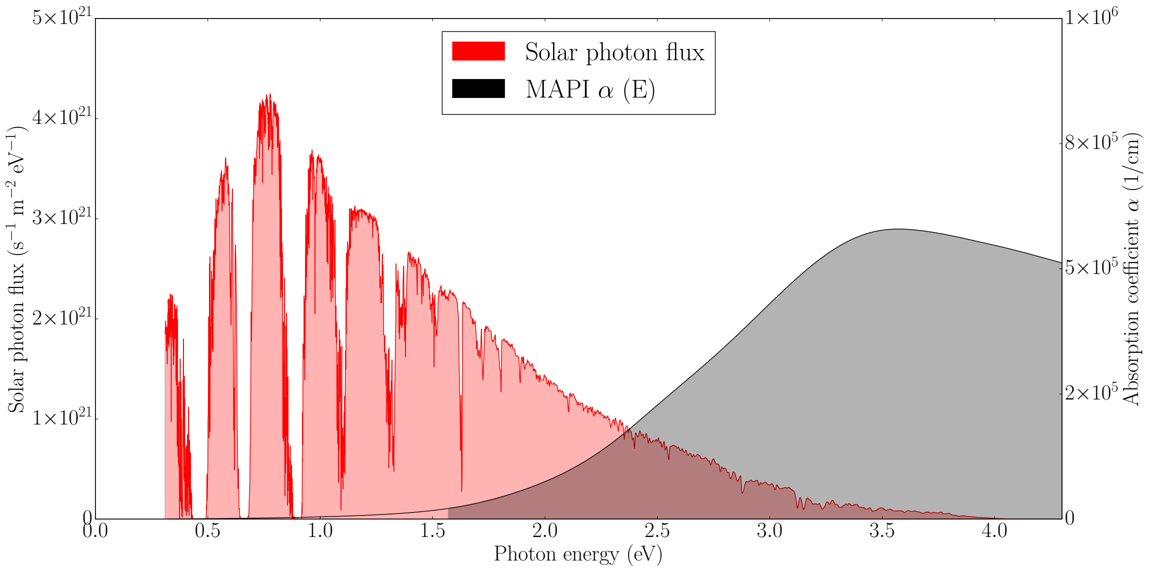

Figure 3.9: The absorption coefficient of MAPI and the solar flux over the AM1.5G solar photon energy range. The broadened tail of the absorption spectrum can be seen below E_g=1.57 eV.

the radiation recombination current J_r). As seen in Eq. (1.10), J_0 decays exponentially with energy, which implies that it only reaches values that are significantly higher than zero when the absolute value of the energy E is small, *i.e.* lower than the direct gap. Hence, J_0 calculated with the entire absorption spectrum is $2.3 \cdot 10^{-2}$ A/m^2, and only $2.3 \cdot 10^{-20}$ A/m^2 when the spectrum starts from the direct gap.

Furthermore, we do a similar test where we do not consider explicitly the absorption coefficient. Instead, we fix the absorbance to a maximum value of 1 starting from the band gap. Here we constrain the energy range to fully isolate the effect of the pre-edge broadening. The obtained PCE was 6.2% and the J_{sc} recorded a staggering value of 683 A/m^2. This result shows that even in the case of maximum absorbance above the band gap, the recombination current density dominates the photoconversion, rendering the cell at least 4 times less efficient than if one takes the DFT absorption. All the mentioned results are summarized in Table 3.2.

In order to correctly model the pre-edge region in MAPI, the authors of [130] applied an "Urbach exponential tail" to the absorption coefficient spectrum. This approximation is supposed to realistically account for the disorder caused by the localized states that emerge over certain temperatures ranges (at least between 200 K and

620 K) at the absorption edge [140]. Therefore an empirical expression is introduced to correct the absorption coefficient in the low spectral region *i.e.* below the direct gap,

$$\alpha = \alpha_0 e^{(E-E_g)/E_U} \quad , \tag{3.7}$$

where α_0 is the absorption coefficient at the direct band gap energy and E_U is the so-called Urbach energy. This denotes the slope of the exponential tail and it is, as mentioned before, dependent on temperature [137, 140]. This parameter is also very much system dependent and it roughly indicates the degree of structural disorder in the crystal. According to [137], MAPI has an E_U of approximately 15 meV. This rather small value indicates a low degree of structural disorder, as opposed to materials such as *a*-Si that have more localized states due to their indirect band gap and hence a larger broadening in the Urbach tail [137].

In Fig. 3.10 one can see our originally calculated absorption coefficients along the main Cartesian directions together with their corresponding pre-edge corrected ones. Since the orthorhombic MAPI is an anisotropic system [141], the xx, yy and zz components of the dielectric function and hence of the absorption coefficient, are not the same. As one can see, the slowly increasing tails of the absorption coefficients below the band gap are corrected into sharply increasing exponential tails that precede the band gap. We also show how the averaged absorption coefficient compares with the one in Ref. [130]. The latter has a slightly higher amplitude at higher energies possibly due to a small difference in the processing of the real and imaginary parts of the dielectric function.

With our corrected absorption spectrum, we obtain the following: $PCE = 27.0\%$

Table 3.2: The short-circuit current density J_{sc}, the reverse saturation current density J_0 and the photoconversion efficiency PCE are reported for the following cases: the absorption coefficient includes the pre-band-gap artificial broadening, the absorption coefficient only includes the post-band-gap artificial broadening, the absorbance is fixed to 1 starting from the direct band gap and the absorption coefficient is corrected below the direct gap with an Urbach exponential tail.

	$\alpha(E)$, $E \in [0.33, 4.42]$ eV	$\alpha(E)$, $E \geq E_g$	$a(E)$ step fct.	$a(E)$ Urbach tail
J_{sc} (A/m^2)	294.3	229.4	683.7	232.0
J_0 (A/m^2)	$2.3 \cdot 10^{-2}$	$2.3\cdot 10^{-20}$	1.5	$5.3\cdot 10^{-20}$
PCE (%)	4.8	27.2	6.2	27.0

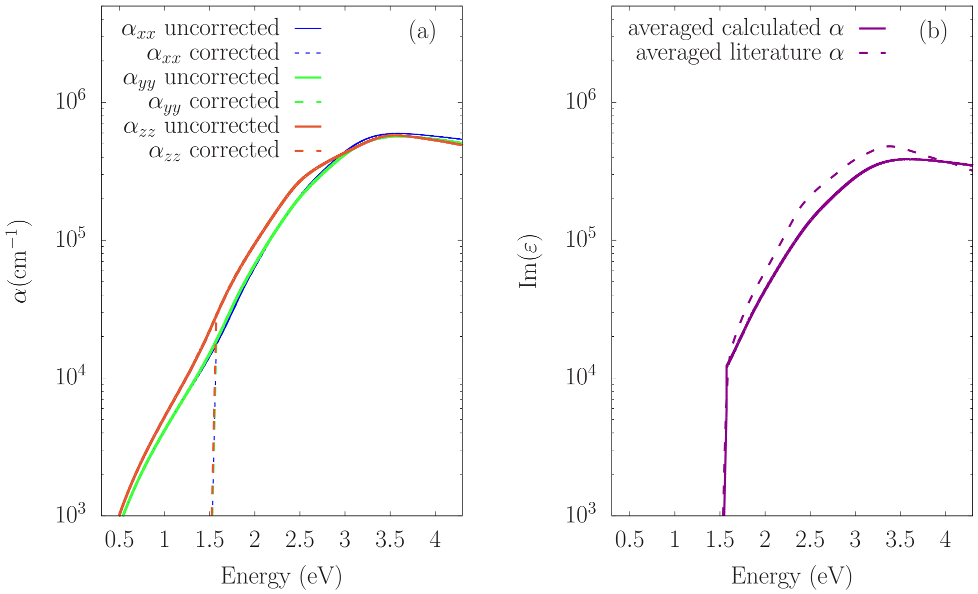

Figure 3.10: (a) xx, yy, zz components of the real and imaginary parts of the dielectric function of orthorhombic MAPI. The solid lines depict the uncorrected absorption spectra while the dashed ones those corrected with a pre-gap Urbach exponential tail. (b) Our absorption coefficient averaged over the 3 corrected components (solid line) along with that of the authors of Ref.[130] (dashed line).

and $J_{sc} = 232$ A/m^2, respectively. Our value for the short-circuit current density slightly exceeds the experimentally obtained one of 211.5 A/m^2 [138]. However, considering the potentially different methods through which this experimental result was obtained, we find to be in good agreement with it. Also, the PCE that the authors of Ref.[130] obtain for $L>$ 300 nm is larger than 23% and for L=300 nm they compute J_{sc}=230 A/m^2. Both these quantities seem to match well with ours. Compared to the case where the artificial broadening in the absorption is omitted, there is no significant improvement in J_{sc}, since the additional tail stemming from the Urbach correction is very sharply increasing and hence, its integral is very small . Perhaps more surprising is the fact that J_0 remains quite similar as well (here J_0=5.3·10^{-20} A/m^2) despite the fact that, as noted earlier in this section, it is extremely sensitive to any changes made to the pre-edge region. It seems that due to the very small empirical Urbach energy, E_U, the Urbach tail is significantly larger than zero within a very short energy range. The J_0 is a function of the absorption coefficient integrated over the entire energy range of the $AM1.5G$ spectrum and it is set to be equal to the radiative current density defined in Eq.(3.4).

Fig. 3.11 illustrates the black-body flux that is emitted during recombination with

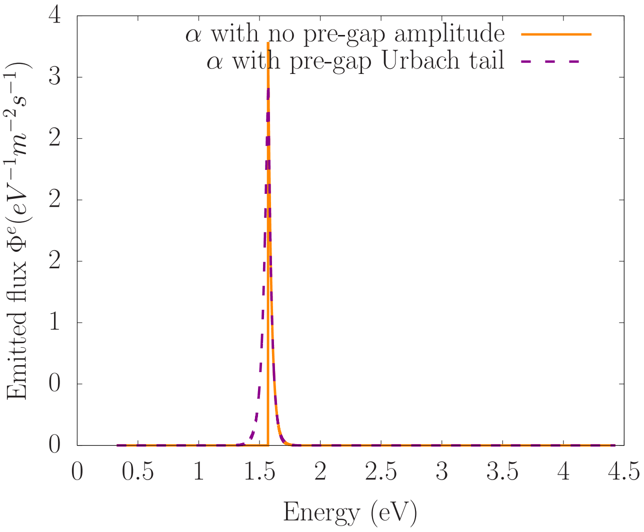

Figure 3.11: Black body emitted flux due to electron-hole recombinations when the absorption coefficient of MAPI does not include any amplitude below the direct gap (orange solid line) and when the absorption coefficient is corrected below the gap with the Urbach exponential tail (purple dashed line).

the addition of the Urbach tail. Due to the exponential function describing the pre-edge absorption coefficient, the emitted flux now correctly depicts a very narrow black body flux curve. As expected, the flux peaks close to the band gap energy and then dramatically drops to zero at larger energy values. The drop is due to the dominating exponential $e^{E/kT}$ in the denominator, which decays fast for energies larger than the band gap. So overall, the change in the recombination current density was roughly doubled. However, the PCE and the short-circuit current densities are very close when considering the absorption coefficient only from the band gap onwards compared to the case where the absorption coefficient includes the Urbach pre-gap correction.

Hence, it is tempting to assume that the correction is not very relevant when determining these quantities. However, it must be noted that the very slight improvement was highly dependent on the value of E_U which is an empirical and material-dependent quantity. Here it is quite circumstantial that E_U for MAPI matches the room temperature energy, hence rendering J_0 insignificant. This might be highly different for other systems, where the pre-gap absorption coefficient might either require a substantially larger E_U or might not even be correctly modeled below the gap with an Urbach tail. It would not be reasonable to rely on the similar PCE obtained for MAPI with an Urbach corrected absorption (27.0%) and with a pre-gap truncated one (27.2%), respectively, to justify calculating the PCE for other materials just by considering the latter modified absorption.

Let us look at J_{sc} instead. As seen in Table 3.2, the short-circuit current density did not change as dramatically as the PCE did when considering the entire pre-gap artificially broadened absorption coefficient spectrum. This fact leads us to conclude that the short-circuit current density is, in this model, a more meaningful quantity than the PCE, despite the fact that it only describes the absorption performance of a material, while ignoring the losses derived from recombination.

3.4 J^*_{sc} and L^*

In the light of the previous section, we introduce J^*_{sc}, an absorption descriptor that quantifies 95% of the saturated short-circuit current density of a material and L^*, the required thickness to achieve that value of the short-circuit current density. Obviously when comparing the J_{sc} obtained with the pre-edge truncated absorption coefficient and the J_{sc} calculated with the artificial broadening in the absorption coefficient, the former is closer to the most accurate J_{sc} obtained with the pre-edge correction. Hence, we will simply consider the truncated absorption for the next materials.

The next results are all obtained from DFT-post processing calculations obtained with the PBE functional for MAPI, Si, CdTe, InP and GaAs. A visual representation of the short-circuit current density as a function of the absorption thickness can be seen in Fig. 3.12. In Tables 3.3 and 3.4, we report the values of the employed lattice parameters and of the PBE calculated and experimentally determined band gaps, as well as those of the calculated J^*_{sc} and L^* along with the corresponding empirical values.

Firstly, let us point out that Si has a significantly small short-circuit current density J^*_{sc} due to the complete omission of the absorption coefficient below the direct band gap of 3.4 eV. Accounting only for the very weak solar flux excitation spanning the energy window 3.4 eV-4.4 eV, J^*_{sc} and L^* derived from this model are highly underestimated for Si. Studies that have proven record efficiencies and short-circuit current densities for Si have relied on sub-band gap absorption using the Urbach exponential tail [135], among other optimizations such as geometrical ones. These lead to so-called "wave-interference-based light-trapping" [135] and to very low power loss of the generated carriers [134]. Moreover, we would like to stress that the experimental references are based on measurements of systems that are not pristine but have defects that can lead to carrier trappings and account for sub-band absorption too.

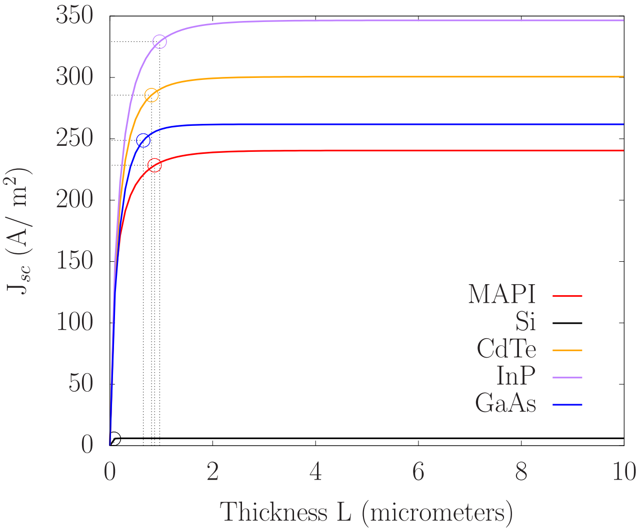

Figure 3.12: The short-circuit current density of five materials as a function of the absorption thickness. The value, at which 95% of the maximum is reached, is illustrated with a circle.

Table 3.3: Lattice parameters and direct PBE and experimental band gaps from literature for the five materials.

	a_0(Å), b_0(Å), c_0(Å)	$E_g(eV)$, $E_g^{exp}(eV)$
MAPI	8.83, 8.55, 12.58	1.55, 1.57 [139]
Si	5.40, - , -	2.55, 3.40 [133]
CdTe	6.62, - , -	0.59, 1.47 [132]
InP	5.94, - , -	0.46, 1.35 [132]
GaAs	5.60, - , -	0.15, 1.42 [132]

Table 3.4: J_{sc}^* and L^* for the five materials along with the experimentally measured J_{sc} and L from literature.

	J_{sc}^*(A/m^2), L^*(μm)	J_{sc}^{exp}(A/m^2), L^{exp}(μm)
MAPI	228.4, 0.87	211.5, 0.33 [138]
Si	5.6, 0.08	395, 100 [134]
CdTe	285.5, 0.81	385, 1.64 [142]
InP	329.2 , 0.97	397, 10 [143]
GaAs	248.7, 0.65	265, 1.57 [144]

In the case of GaAs based cells, for instance, the architecture of the device is complex, containing a GaP/Si template on which several layers of n- or p-doped GaAs, GaInP as a back surface field layer, n-AlInP as a window are grown. Hence, the measured short-circuit current density and the absorbing thickness are only roughly comparable to our calculated values. Si essentially is an indirect gap material that overall follows a different absorption mechanism whereby electrons transitions are phonon-assisted [133]. Therefore if we somewhat justifiably omit it from the list, the general ranking in terms of J_{sc} is preserved, yielding InP and CdTe as the most absorbent materials, followed by GaAs and MAPI. However, it is worth noting that the absorption thickness of the real MAPI and GaAs cells, namely of 0.33 μm [138] and 1.57 μm [144], respectively, are incredibly small due to the low degree of structural disorder which basically results in almost no recombination loss due to deep states trapping [137].

3.5 Conclusion

In conclusion, this part of our work has revealed that the absorption coefficient derived from postprocessing the band structure can, in principle, reveal the theoretical efficiency of photoconversion. We also found that the treatment of the pre-edge absorption spectrum, which is entirely governed by the degree of disorder characteristic to the system and cannot realistically be accounted for in an $ab-initio$ description, is particularly important for a large set of materials. In the case of Si, the PCE drops drastically, namely from 33.4% to 1.7% when we omit the pre-edge absorption. Our analysis hence showed that indirect-gap materials are more susceptible to the inclusion of the pre-edge absorption contribution to the spectrum. We further emphasize the importance of correctly treating the very narrow pre-edge for a direct gap material such as methyl ammonium lead iodide. In fact, due to this particular material's structural characteristics, the complete omission of the edge better described the absorption process, yielding a realistic short-circuit current density and efficiency. We recognize, though, that a slightly more disordered material with a direct gap could have a broader pre-edge absorption relative to MAPI. This, in turn, could lead to a significantly larger recombination current density and hence, to a reduction in the PCE, compared to the case where the pre-edge absorption is omitted. Nevertheless, even in such a case, the short-circuit current should not significantly change upon the complete omission of the pre-edge absorption. Since this outlook on efficiency prediction proved to be slightly incomplete within our model, we resorted to describe materials in terms of their absorption characteristics instead. As there is a rough threshold thickness for each system beyond which the J_{sc} is essentially saturated, we decided to define the 95% of the maximum saturated value of the J_{sc}, *i.e.* J^*_{sc}, as the characteristic parameter describing the near maximum short-circuit current density. The corresponding thickness yielding J^*_{sc} was termed L^* and it indicates the minimum necessary thickness to reach maximal values of the short-circuit current density. These descriptors were tested for three other direct gap materials and were proven to be fairly well in agreement, in particular the short-circuit current density, with experimental works.

4 Interlayer dielectric function of a type-II van der Waals semiconductor: the HfS/PtS heterobilayer

4.1 Introduction

In the previous chapter we have shown that within an ab-initio framework based on DFT band structure, we employed the short-circuit current density as a benchmark to make reliable predictions regarding the absorption capabilities of compounds. However, another process that requires fine-tuning in a PV system consists in minimizing the recombinations of the photogenerated free carriers. This can be achieved, if they are spatially separated. For this purpose, heterostructures composed of two-dimensional materials are ideal candidates.

Two-dimensional transition metal dichalcogenides are a very suitable materials class for PV applications, because of their well-developed production techniques and generally attractive electronic properties [41, 145]. Many of the known 2D TMDs have a semiconductor bandstructure and possess similar band gaps in the visible to near infrared range, high carrier mobility, strong photoluminescence and exciton binding energies that can be tuned with the number of layers that are stacked on top of each other. These are all features that make them strong candidates for various optoelectronic devices such as solar cells, photo-detectors and light-emitting diodes [146]. In general, 2D materials are layered compounds characterised by a crystalline planar structure held together by strong in-plane covalent bonds and weak out-of-plane van der Waals (vdW) forces [147]. This peculiar configuration allows them to be exfoliated into thin planes or monolayers (MLs) by either mechanical or chemical means, and to be re-assembled on top of each other to build a multitude of different vdW heterostructures. Such heterostructures can be designed layer by layer without being constrained by the lattice mismatch [146, 148, 149], a manufacturing flexibility that enables the practical realization of novel properties otherwise difficult to obtain.

For instance one can engineer heterogeneous bilayers (HBLs) having the so-called type-II band alignment, where the conduction band minimum (CBM) resides on one layer type, while the valence band maximum (VBM) is on the other (see Fig. 4.1). In this case spatial separation of the electron-hole pairs (excitons) is possible, such that the ground state of the exciton (the thermalised exciton) ends up having the charge carriers of different polarity located on the two different layer types. Such inter-layer excitons may form either already during the light absorption, or afterwards as the product of scattering. If they form during absorption, some inter-layer transitions might appear as additional features in the absorption spectra, overall increasing the absorption efficiency. In type-II HBLs, inter-layer transitions could occur at an energy below the absorption or emission edges of the individual layers (intra-layer transitions). This is the most favourable situation for detection as no other

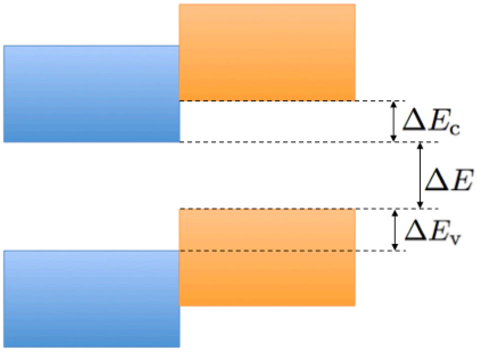

Figure 4.1: Type-II band alignment. The differently coloured blocks represent the valence and conduction bands of the two monolayers making up the bilayer. The bi-layer bandgap, ΔE, is between the valence band maximum of one layer type and the conduction band minimum of the other. The conduction and valence band offsets between the individual layers are denoted as ΔE_{c} and ΔE_{v}, respectively.

transitions are available in that spectral range. Inter-layer excitons recombine more slowly compared to intra-layer ones, a feature that can be detected experimentally. Such long-living inter-layer excitons have indeed been previously identified in TMDs HBLs in photoluminescence experiments [48, 150, 151, 152].

The formation process of inter-layer excitons in vdW materials is still debated. Some studies point to the existence of inter-layer excitations in the absorption spectra. For instance in Ref. [41] Bernardi *et al.* state that the absorption onset of the MoS_2/WS_2 bilayer, as calculated with highly-accurate many-body perturbation theory, is shifted to a lower energy as compared to that of monolayers. This feature is taken as a signature of an interlayer charge-transfer excitation. In contrast, other works report the absence of inter-layer effects in the HBLs absorption spectra [48, 153, 154].

Andersen *et al.* [155] proposed a model for computing the dielectric function of multi-layer systems based on *ab initio* calculations for monolayers combined with a classical electrostatic model for dielectric screening. Interlayer hybridization such as the creation of bonds between layers is not included in the model, which nonetheless yields a remarkably good agreement with full *ab initio* calculations of the dielectric function. This confirms that interlayer coupling is largely a screening effect meaning that it is due to the long-range electrostatic interaction between layers and that electronic inter-layer transitions are only weak. Komsa *et al.* performed first-principles calculations of the dielectric function of MoS_2/WS_2 heterostructures with many-body perturbation theory in order to accurately capture excitonic effects [156]. They found that electronic interlayer excitations are very weak, and that the absorption spectrum of the HBL resembles a superposition of those of the constituent MLs [156].

In general, screening effects are hard to distinguish from inter-layer excitons in absorption spectra of type II heterostructures. This is because they can both lead to a bandgap reduction and hence to a red-shift in the absorption spectra. In order to separate screening effects from interlayer transitions, here we decompose the dielectric function, as calculated with *ab initio* density functional theory (DFT), into inter-layer and intra-layer components. Our heterostructure of choice is HfS_2/PtS_2, a decision motivated by two main reasons. On the one hand, GW calculations for the constituent monolayers exist [157] and suggest that the HBL is indeed of type II. On the other hand, HfS_2 and PtS_2 have an almost identical in-plane lattice parameter so that a commensurate bi-layer unit cell can be constructed without the need for large supercells.

4.2 Methods and Computational Details

All the calculations have been performed with DFT [158, 159]. We have chosen the specific numerical DFT implementation contained in the FHI-AIMS all-electron package [108, 160] that adopts a numerically tabulated atom-centered orbitals basis set [161]. In order to ensure sufficient accuracy we have used the “tight" basis set constructed using the first tier numerical orbitals for the metal atoms and a modified version of the first tier for the sulphur atoms. Geometry relaxations have been performed with an all-electron potential and the GGA of the exchange and correlation energy, as parametrised by PBE [83]. A convergence threshold of 10^{-6} eV based on the total energy is used for the Kohn-Sham self-consistency cycle. The van der Waals interaction between layers has been taken into account by using the Tkatchenko-Scheffler van der Waals correction scheme [106]. A force convergence threshold of 10^{-5} eV/Å and a $10\times10\times1$ k-mesh have been used for the structural optimization of the HfS_2 and PtS_2 MLs.

Ground-state bandstructure calculations have been carried out with PBE and also with the hybrid HSE06 [72] exchange-correlation functional. Since the absorption spectrum is highly sensitive to the size of the direct bandgap, we have also employed HSE06 for the calculation of the dielectric function. In fact, HSE06 typically corrects for the bandgap underestimation produced by semilocal functionals such as PBE. We have obtained the layer-projected bandstructure of the HfS_2/PtS_2 HBL with VASP, the Vienna Ab initio Simulation Package [110]. VASP uses pseudopotentials and it is based on the projector augmented wave method. In this case the number of valence electrons for each distinct species is as follows: 12 for hafnium, 16 for platinum and 6 for sulphur. We have employed a $10\times10\times1$ Monkhorst-pack mesh and a plane-wave cutoff energy of 400 eV.

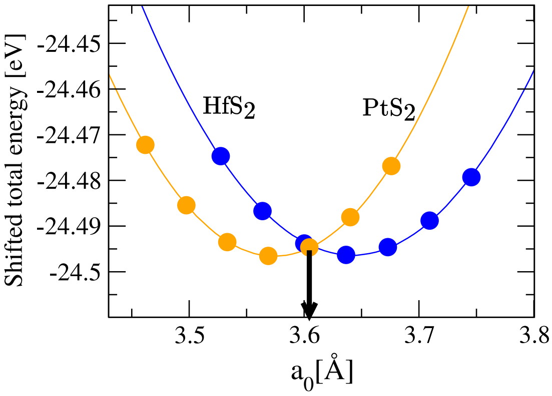

Figure 4.2: Total energy as a function of compressive/tensile strain for monolayers of HfS_2 (blue) and PtS_2 (yellow). The optimal lattice constant, $a_0^{HfS_2/PtS_2}$, minimizing the total strain energy is shown by an arrow.

Since the in-plane lattice parameters of the relaxed HfS_2 and PtS_2 monolayer are not identical ($a_0^{HfS_2}$= 3.64 Å and $a_0^{PtS_2}$ = 3.57 Å), constructing the primitive cell for the HfS_2/PtS_2 HBL imposes a small strain on the two layers. We have computed the HBL in-plane lattice parameters as follows. Firstly, the total energy of the two MLs, HfS_2 and PtS_2, has been calculated as a function of the in-plane strain, and fitted to a quadratic equation. We have then minimised the sum of such quadratic functions in order to find the optimal in-plane lattice constant of the HBL. This is the one that minimises the total strain energy and it is found to be $a_0^{HfS_2/PtS_2}$ = 3.60 Å (see arrow in Fig. 4.2). Throughout this work, in the case of the homogeneous (HfS_2/HfS_2 and PtS_2/PtS_2) and heterogeneous (HfS_2/PtS_2) bilayers, we have shifted the second layer relative to the first one by a distance d equal to the average of the relaxed bulk HfS_2 and PtS_2 out-of-plane lattice parameter, namely d=5.24 Å. All the fractional in-plane atomic coordinates of the MLs, homogeneous bilayers (BLs) and of the HBL are kept fixed, namely they are identical to the in-plane coordinates of the relaxed MLs relative to the HfS_2/PtS_2 HBL lattice constant $a_0^{HfS_2/PtS_2}$. This is done in order to compare results for the homogeneous ML and BL systems to those for the HBL, and to single out electronic effects from those arising from structural relaxation.

For monolayers and bilayers calculations choosing an appropriate out-of-plane lattice parameter, c, is equivalent to choosing the size of the vacuum gap between the periodic replicas of the cell. This needs to be optimised carefully in order to obtain the correct 2D limit of the various quantities to calculate. In our case we have used the imaginary part of the dielectric function, $Im(\varepsilon)$, as the control quantity and chose the value of c for which there was less than 1% variation in the amplitude of $Im(\varepsilon)$. The resulting c was found to be 22.62 Å. Note that the absolute scale of the dielectric function depends on the volume of the unit cell used for the calculation [see Eq. (2.75) in Chapter 2]. As such our calculated dielectric functions are not directly comparable with experiments. However, since for all the structures investigated we have maintained the same in-plane and out-of-plane lattice parameters, respectively $a_0^{\mathrm{HfS_2/PtS_2}}$ and c, they can be compared directly with each other. A k-grid of 30×30×1 points was found to converge the dielectric function reasonably well. The converged k-grid was established once the maximum value of the difference between two spectra of different k-grids was less than 10%, as discussed in Chapter 3. A Lorentzian function of width 0.1 eV was employed to construct smooth dielectric function spectra. Since the investigated systems have a finite band gap, the intraband term of the dielectric function is neglected and thus, $\varepsilon_{ij}^{inter} = \varepsilon_{ij}$. Thus, throughout this work, the entries of the part of the dielectric tensor, ε_{ij}, have been calculated through expression (2.75) defined in Chapter 2.

In order to single out quantitatively the contributions to the dielectric function originating from the intra- and inter-layer transitions we have applied the following procedure. We denote with α and β two distinct subsets of the basis functions placed respectively on the α and β layer, namely we partition the Kohn-Sham wave functions as

$$|\psi_{n\mathbf{k}}\rangle = |\psi_{n\mathbf{k}}^{\alpha}\rangle + |\psi_{n\mathbf{k}}^{\beta}\rangle \ . \tag{4.1}$$

The momentum matrix elements defined in Chapter 2 can be then decomposed as

$$p_{j,n',n,\mathbf{k}} = p_{j,n',n,\mathbf{k}}^{\alpha\alpha} + p_{j,n',n,\mathbf{k}}^{\alpha\beta} + p_{j,n',n,\mathbf{k}}^{\beta\alpha} + p_{j,n',n,\mathbf{k}}^{\beta\beta} \ , \tag{4.2}$$

with $p_{j,n',n,\mathbf{k}}^{\alpha\beta} = \langle\psi_{n'\mathbf{k}}^{\alpha}| - i\hbar\nabla_j \, |\psi_{n\mathbf{k}}^{\beta}\rangle$. This allows us to separate the dielectric function of Eq.(2.74) into three distinct components

$$\varepsilon_{ij}(\omega) = \varepsilon_{ij}^{\mathrm{inter}}(\omega) + \varepsilon_{ij}^{\mathrm{intra}}(\omega) + \varepsilon_{ij}^{\mathrm{mixed}}(\omega) \ , \tag{4.3}$$

where the inter-layer component, $\varepsilon_{ij}^{\text{inter}}(\omega)$, is restricted to products of inter-layer matrix elements of the form $p^{\alpha\beta}_{i,n',n,\mathbf{k}}p^{\alpha\beta*}_{j,n',n,\mathbf{k}}$ and $p^{\alpha\beta}_{i,n',n,\mathbf{k}}p^{\beta\alpha*}_{j,n',n,\mathbf{k}}$, the intra-layer component, $\varepsilon_{ij}^{\text{intra}}(\omega)$, contains only products between the intra-layer matrix elements of the form $p^{\alpha\alpha}_{i,n',n,\mathbf{k}}p^{\alpha\alpha*}_{j,n',n,\mathbf{k}}$ and $p^{\alpha\alpha}_{i,n',n,\mathbf{k}}p^{\beta\beta*}_{j,n',n,\mathbf{k}}$, and the "mixed" component, $\varepsilon_{ij}^{\text{mixed}}(\omega)$, is made up of all the remaining products between intra-layer and inter-layer matrix elements, $p^{\alpha\alpha}_{i,n',n,\mathbf{k}}p^{\alpha\beta*}_{j,n',n,\mathbf{k}}$, $p^{\alpha\alpha}_{i,n',n,\mathbf{k}}p^{\beta\alpha*}_{j,n',n,\mathbf{k}}$, $p^{\alpha\beta}_{i,n',n,\mathbf{k}}p^{\alpha\alpha*}_{j,n',n,\mathbf{k}}$, and $p^{\beta\alpha}_{i,n',n,\mathbf{k}}p^{\alpha\alpha*}_{j,n',n,\mathbf{k}}$.

Note that the three contributions to the dielectric function introduced by our procedure do not correspond, as those of any other partition, to any physical observables. However, they enable us to single out transitions between conduction and valence states localised on the different layers and to study how these contributions evolve when changing the structure, or the interaction between the layers. As such, the quantities introduced in Eq. (4.3) have to be considered in the same spirit as the orbital populations in the Mulliken analysis [162], namely as useful to understand trends. The mixed component of the dielectric function may be thought as the analogue to the overlap Mulliken population and it does not possess a transparent physical interpretation.

4.3 Results and Discussion

4.3.1 Bandstructure

We begin by discussing the calculated bandstructures of the fully relaxed MLs and of their corresponding BLs. These are presented in Fig. 4.3, where we report results for HfS_2 [panel (a)] and PtS_2 [panel (b)], computed at both the PBE and HSE level.

HfS_2 ML crystallises in the 1T form (its bulk structure belongs to the trigonal system, space group $P\bar{3}m1$, No. 164) and it is an indirect gap semiconductor with the VBM at the Γ point and the CBM at M. The only substantial difference between the PBE and HSE results is the increased bandgap obtained with HSE, while the band curvatures (effective masses) remain essentially identical for the two functionals. The HSE-calculated bandgap is 1 eV smaller than that computed with G_0W_0 starting from a local-density-approximation bandstructure (G_0W_0@LDA) as reported in Ref. [157] (see Table 4.1 for a detailed comparison of the various bandgap energies). The bandgap of HfS_2 has been measured in the past with a combination of angle-resolved photoemission and inverse photoemission. Bulk HfS_2 shows the significant indirect gap of 2.85 eV between the Γ and the M points [163]. Unfortunately the same measurement is not available for the ML form. In contrast a direct bandgap has been measured at Γ for both bulk [163] and for few-layer HfS_2 [164] to be around 3.6 eV and rather independent of the number of layers. Such value, which can be extrapolated to the ML, lies in between our computed HSE result of 2.97 eV and the G_0W_0@LDA one of 3.97 eV reported in [157]. This gives us confidence that our HSE description of the material is quantitatively sound. When forming the bilayer there is a small reduction of the bandgap (in the region of 200/300 meV). This is due partly to the dielectric screening by the other layer, and partly to the small interlayer interaction, which splits the bands. Notably, the VBM now moves slightly away from the Γ point to locate along the Γ-M symmetry line (for both HSE and PBE).

PtS_2 ML also crystallises in the 1T form and presents a semiconducting bandstructure with the CBM sitting along the Γ-M line, a feature common to both PBE and HSE. The VBM is also along the Γ-M line, but the precise location is different for PBE and HSE. Notably, the VBM is almost degenerate, since there is another point along the Γ-K direction, which is extremely close to the valence top. Such band-

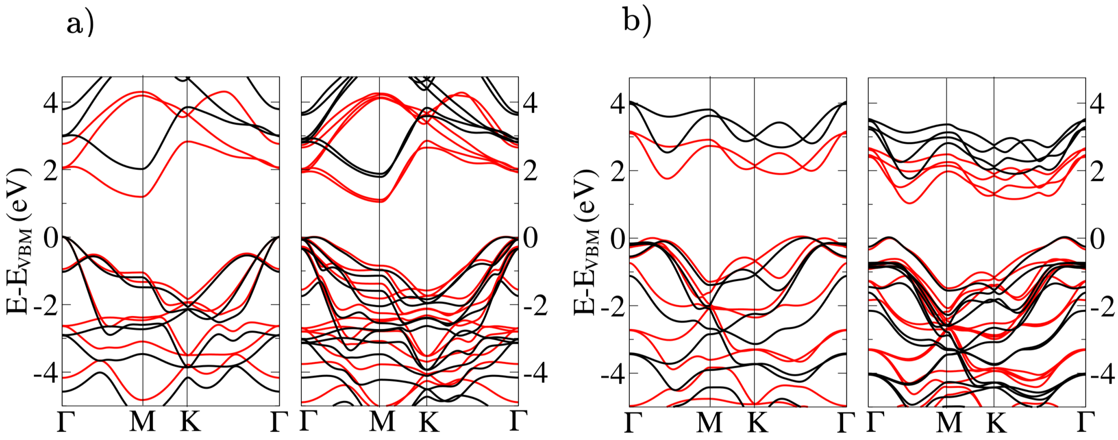

Figure 4.3: Bandstructure for (a) HfS_2 and (b) PtS_2 in their monolayer (left-hand side panels) and bilayer (right-hand panels) form. The red and black bands correspond to results obtained with the GGA and HSE functionals, respectively.

	$\Delta E_{\rm d}^{G_0W_0}$	$\Delta E_{\rm i}^{G_0W_0}$	$\Delta E_{\rm d}^{\rm HSE}$	$\Delta E_{\rm i}^{\rm HSE}$
HfS_2 ML	3.97 (Γ)	2.98 (Γ-M)	2.97 (Γ)	1.98 (Γ-M)
HfS_2 BL	-	-	2.67 (Σ)	1.77 (Σ-M)
PtS_2 ML	3.14 (T′)	2.95 (Σ-Σ)	2.61 (Σ)	2.49 (Σ-Σ)
PtS_2 BL	-	-	2.08 (Σ)	1.69 (Σ-Σ)
HfS_2/PtS_2 HBL	-	-	2.22 (Σ)	1.41 (Σ-M)

Table 4.1: Direct, $\Delta E_{\rm d}$, and indirect, $\Delta E_{\rm i}$, bandgaps (in eV) of HfS_2 and PtS_2 MLs and BLs as well as of the HfS_2/PtS_2 HBL. Results are presented for the HSE functional. We also report the results of reference [157] obtained with G_0W_0@LDA for the MLs. In that case the calculations were carried out at the relaxed geometry. In brackets we report the position in k-space for the direct bandgap and the position of both the VBM and CBM for the indirect ones. Note that here Σ/Σ' denotes a generic point along the Γ-M line and not the high-symmetry point at midway between Γ and M.

structure returns us PtS_2 ML as an indirect gap semiconductor, where the CBM and VBM are quite close in k-space. Furthermore, the direct gap is only about 150 meV larger than the indirect one, meaning that PtS_2 ML is almost a direct bandgap semiconductor. The same situation is found also in G_0W_0@LDA calculations [157], and now the HSE gap (either direct or indirect) is only about 0.5 eV smaller than that from G_0W_0@LDA. We are not aware of any photoemission and inverse-photoemission experiment for PtS_2, so an experimental determination of the quasi-particle gap is not available. However, the optical absorption edge of ML PtS_2 has been measured [165] in the region of 1.6 eV and found to be very sensitive to the number of layers. This is broadly consistent with our data, which returns a quasi-particle gap larger than such value, but does not provide the opportunity of establishing a full quantitative comparison.

When PtS_2 is taken in its BL form a few significant differences appear with respect to the ML case. The most striking one is a drastic reduction of the bandgap (by more than 0.5 eV) arising from substantial band-splitting. This is consistent with the strong absorption edge reduction as a function of the number of layers found in experiments [165], and points to an interlayer interaction much stronger than in the HfS_2 case. Such interaction produces large distortions of the valence band, which now presents two clear quasi-degenerate VBM near Γ along the Γ-M and Γ-K directions. In fact a closer inspection reveals that the VBM is formed by a set of k-points arranged arranged along a hexagon at the edge of the 2D Brillouin zone, a

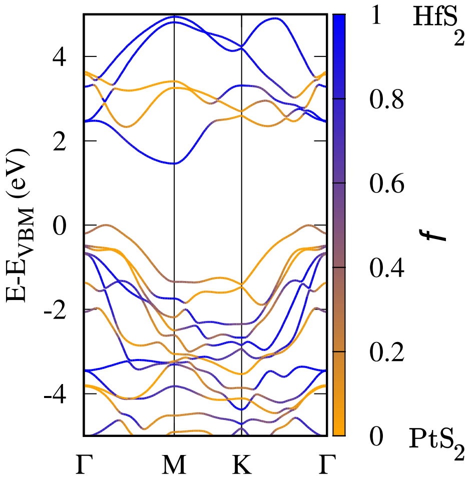

Figure 4.4: Bandstructure of the HfS$_2$/PtS$_2$ HBL calculated with HSE. The band colour encodes the quantity f =DOS$_{\mathrm{HfS}_2}$/(DOS$_{\mathrm{HfS}_2}$+DOS$_{\mathrm{PtS}_2}$), namely the projection of a particular eigenstate on the different layers. Blue bands are localised on the HfS$_2$ layer, orange ones on the PtS$_2$ layer.

fact already observed before [166].

Next we move to the bandstructure of the HfS$_2$/PtS$_2$ HBL, which is presented in Fig. 4.4. Since the electronic interaction across the van der Waals gap is typically weak, one expects the wave-functions to be rather localised on the individual layers. As such it is useful to attribute to each energy point, $\epsilon_{n\mathbf{k}}$, in the bandstructure a layer character. This is obtained by computing the following quantity, f =DOS$_{\mathrm{HfS}_2}$/(DOS$_{\mathrm{HfS}_2}$+DOS$_{\mathrm{PtS}_2}$), where DOS$_X$ is the density of states projected on layer X of the eigenfunction, $|\psi_{n\mathbf{k}}\rangle$. Thus, for $f = 1$ the state is entirely localised on the HfS$_2$ monolayer, while for $f = 0$ it is entirely localised on the PtS$_2$ layer. Such information is translated into a colour code in Fig. 4.4. Clearly the HfS$_2$/PtS$_2$ HBL presents a type-II band alignment since the CBM is almost completely localised on HfS$_2$, while the entire valence band is mostly on PtS$_2$. It is interesting to observe that, while the conduction band resembles closely that of the HfS$_2$ monolayer, the valence one is much more similar to that of the PtS$_2$ bilayer, with the k-degeneracy discussed before. This suggests that the interlayer interaction affects the two constituent materials differently, meaning that the two constituent monolayers have different susceptibility. The resulting hetero-bilayer is also an indirect semiconductor with an HSE bandgap of 1.41 eV between the M point (CBM) and a point along the Γ-M line (VBM). This is smaller than the indirect gaps of all the other structures investigated. In contrast, the direct gap is computed with HSE to be 2.22 eV,

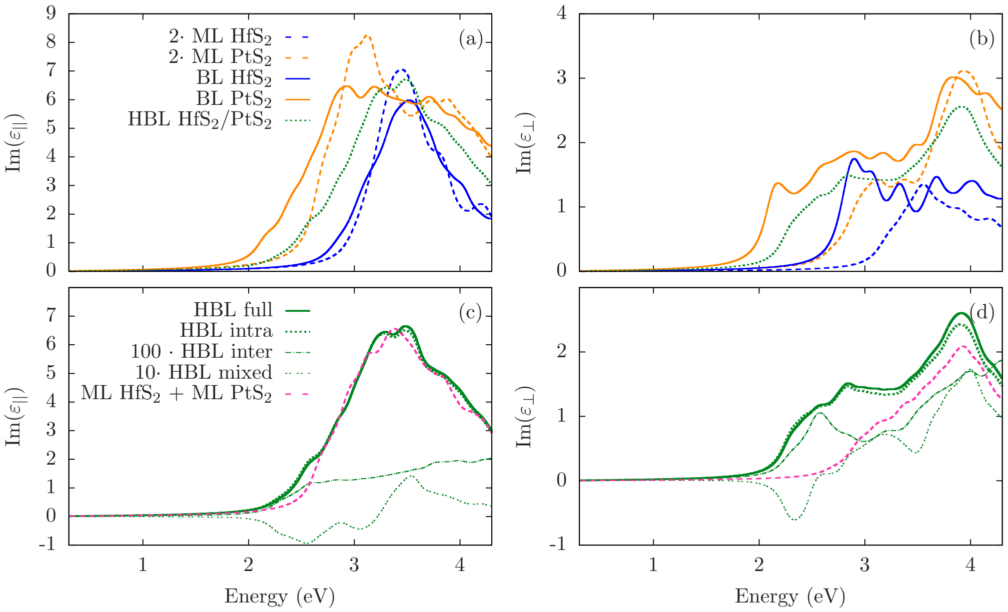

Figure 4.5: Imaginary part of the dielectric function for all the structures investigated. (a) in-plane and (b) out-of-plane components of the total dielectric function. Note that in the case of MLs we have scaled ε by a factor two for comparison. Panels (c) and (d) show the decomposition of the in-plane and out-of-plane dielectric function into intra-layer (“intra”), inter-layer (“inter”) and “mixed” components for the HfS$_2$/PtS$_2$ HBL (see Methods section for details). For comparison we also present the sum of the dielectric functions of the HfS$_2$ and PtS$_2$ MLs.

namely it is smaller than the corresponding one for HfS$_2$ BLs, but larger than that of the PtS$_2$ BLs. This means that the three bilayer structures investigated have all a different absorption edge.

4.3.2 Dielectric function

We now proceed to analyse the dielectric function and in particular its imaginary part, which is proportional to the absorption coefficient. In our discussion we separate the in-plane, $\varepsilon_{\|}$, and out-of-plane, $\varepsilon_{\perp}$, components and consider a spectral range between 0.3 eV and 4.3 eV, namely within the solar spectrum range as standardised by the American Society for Testing and Materials [8]. Our HSE results are presented in Fig. 4.5, where panels (a) and (b) show the total dielectric functions for all the structures investigated, while panels (c) and (d) focus on the decomposition of the dielectric function of the HfS$_2$/PtS$_2$ HBL into the inter-layer, intra-layer and mixed contributions.

Let us look first at $\varepsilon_{\parallel}$ for the MLs and the homogeneous BLs [Fig. 4.5 (a)]. In all cases the absorption edge, as expected, corresponds to the direct HSE bandgap (see Table 4.1). For HfS_2 there is little difference in the dielectric function when going from the ML to the BL, despite the change in direct bandgap by about 300 meV. In contrast, there is a significant red-shift in the case of PtS_2. Interestingly, while for HfS_2 the in-plane component of $\mathrm{Im}\,(\varepsilon)$ of the BL is essentially twice that of the ML (note that in Fig. 4.5 the ML plots have been rescaled by a factor 2), this is not the case for PtS_2, where the two functions are rather different. Such feature simply reflects the significant band distortion in PtS_2 introduced by the inter-layer interaction and it is in agreement with experimental evidence [165]. The situation for the out-of-plane component, $\varepsilon_{\perp}$, is somewhat different [Fig. 4.5(b)], mostly because now also HfS_2 displays an absorption-edge redshift when going from ML to BL, as expected from the corresponding reduction of the direct bandgap. Overall all perpendicular components of the dielectric function of the MLs are different from those of the corresponding BLs.

The dielectric function of the HfS_2/PtS_2 HBL, as expected, is different from all the others. Most importantly its absorption edge is always in between that of the homogeneous HfS_2 and PtS_2 bilayers, although it is lower than that of all the MLs (in particular for the perpendicular component). This reflects the relative magnitude of the direct gaps of the various structures. A distribution of absorption edges as the one described here, unfortunately, prevents the unique identification of HfS_2/PtS_2 HBLs in a mixture containing stacks with different numbers of layers, as those produced by liquid-phase exfoliation [167]. In fact, the most high-throughput means of producing 2D hetero-structures is by re-aggregating 2D materials previously exfoliated. In the process, however, one retains little control of the number of layers making the various structures, so that together with hetero-bilayers one will find in the mixture homo-bilayers, monolayers and a multitude of other structures comprising more than two layers [167, 168, 169]. As the lower part of the absorption is always dominated by structures consisting of PtS_2, the absorption edge of HfS_2/PtS_2 HBLs will never be spectrally separated, hence such structures will not be detectable by a single optical measurement.

The absorption edge of the HfS_2/PtS_2 HBL is just above 2 eV, where we find the first direct, inter-layer, transition. However, close to the two VBM there are several intra-layer transitions within PtS_2 available. These have an energy just above that of the direct gap (inter-layer), so that they can contribute close to the absorption edge. In order to identify the different types of transition, in panel (c) and (d) of Fig. 4.5 we decompose the dielectric function of HfS_2/PtS_2 HBL into its inter-layer, intra-layer and mixed contributions and these are compared with the sum of the dielectric functions of the individual isolated monolayers. Interestingly, while the in-plane component $\varepsilon_{\parallel}$ of the HBL is essentially the sum of those of the two monolayers (except for a small shoulder just below 2.5 eV), the out-of-plane part is significantly different, since its absorption edge is redshifted by about 0.5 eV with respect to the sum of the monolayers. This is a similar behaviour to that found when going from monolayers to homogeneous bilayers.

When looking at the different layer-resolved components the most striking feature concerns their relative amplitude. In fact the spectrum is dominated by the intra-layer component with the inter-layer one accounting for only about 1% of the total spectrum (note that the inter-layer ε has been multiplied by a factor 100 in Fig. 4.5). The mixed component instead contributes to about 10% and can also take negative values. This essentially means that inter-layer excitons indeed are available but they produce an absorption signal about 100 times smaller than their intra-layer counterparts. This is the same order of magnitude as the factor 200 found in resonant photocurrent measurements of the $MoSe_2$/WSe_2 HBL [170]. It has to be said that the spectra calculated here do not take into account the exciton binding energy. In bilayers both intra- and inter-layer excitons can have binding energies that are some fraction of an eV. However, the latter energy is generally significantly smaller than the former [171, 172, 173]. Thus, the actual relative positions of the excitations can be different from those calculated here, with the PtS_2 intra-layer excitations being at a lower energy than the inter-layer excitations. The main reason for such a small amplitude of inter-layer transitions has to be associated with the large spatial separation of the electron and hole wave-functions, which reside on different layers and make the dipole matrix elements small.

In order to enhance the amplitude of the interlayer transition, we explore the effect of compressing the stack. This is obtained by incrementally decreasing the interlayer

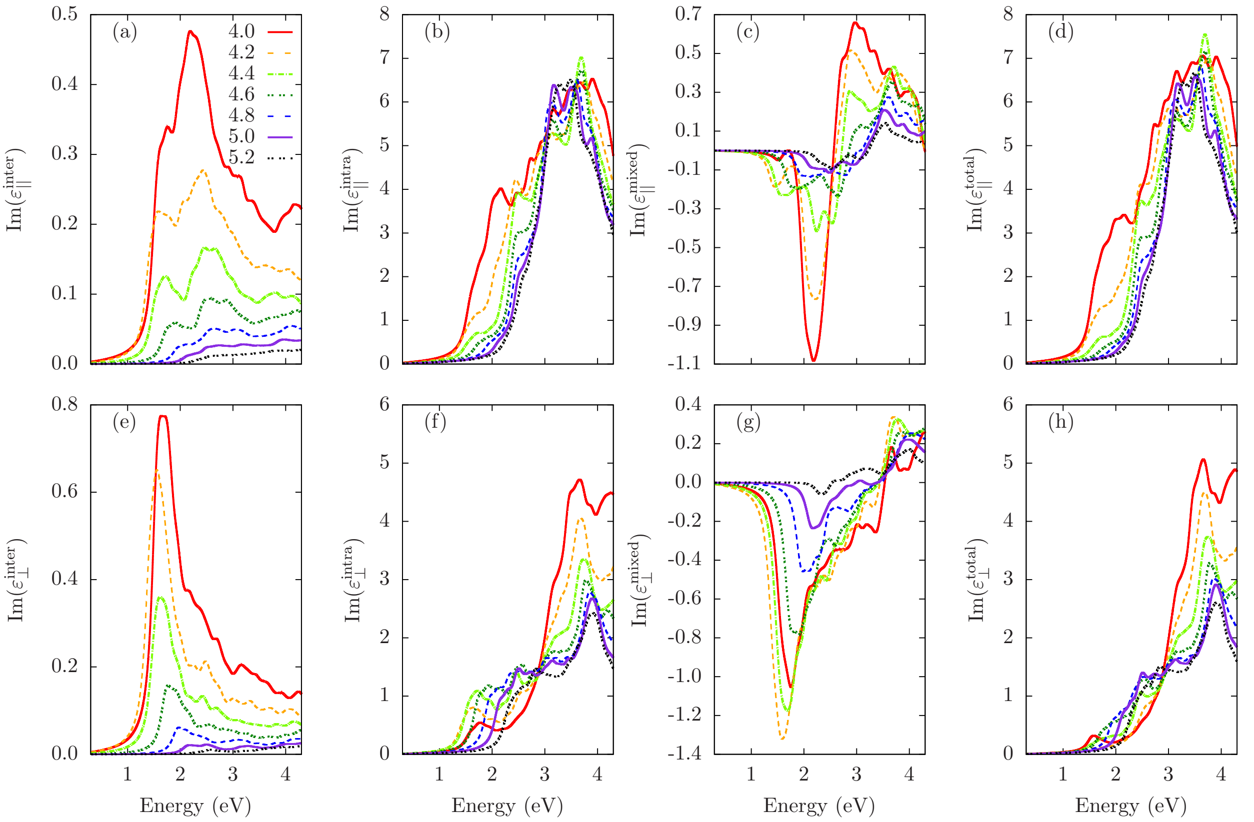

Figure 4.6: Imaginary part of the dielectric function as function of the interlayer distance d. In panel (a) through (d) we show the inter-layer, intra-layer and mixed parts together with the total spectrum for the in-plane component of ε. Panels (e) through (h) report the same quantities for the out-out-of-plane component.

distance of the HBL from the equilibrium value of $d = 5.2\,\text{Å}$ to $d = 4.0\,\text{Å}$. The corresponding spectra are depicted in Fig. 4.6. There are two clear features appearing as the inter-layer distance is reduced, common to both the in-plane and out-of-plane component of the dielectric function. On the one hand, there is a continuous red-shift of the absorption edge, which is sharper for the in-plane component than for that out of plane. This is as large as 1 eV for an inter-layer distance reduction of 1 Å. On the other hand, we can observe the formation of a well-isolated absorption peak just at the absorption edge, in particular for small interlayer distances. Thus, we observe that reducing d has profound effects on the dielectric function, which is significantly modified. Such modifications are more pronounced for the out-of-plane component, for which the formation of the new peak at the absorption edge is counterbalanced by a significant increase in amplitude in the spectral region $E > 3$ eV.

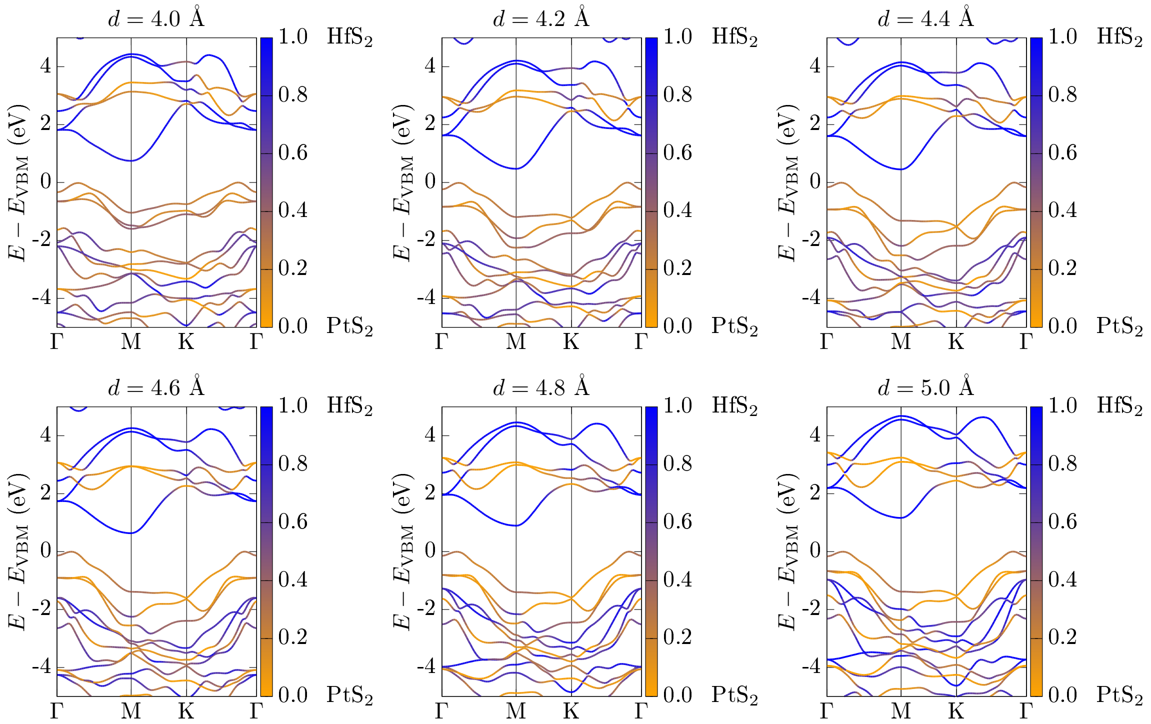

Figure 4.7: Bandstructure of the HfS_2/PtS_2 HBL calculated with HSE as a function of the interlayer distance d. The band colour encodes the quantity $f = \mathrm{DOS}_{HfS_2}/(\mathrm{DOS}_{HfS_2}+\mathrm{DOS}_{PtS_2})$, namely the projection of a particular eigenstate on the different layers. Blue bands are localised on the HfS_2 layer, orange ones on PtS_2. Note the formation of a split-off band upon compression.

These new features of the dielectric function can be understood by looking at the evolution of the bandstructure upon compression, presented in Fig. 4.7. We observe that, while the conduction bands are little affected by the change in interlayer distance, the valence bands are significantly altered. In particular at small d the top of the valence band splits from the rest of the manifold and already for $d > 4.8$ Å there is the formation of an impurity band. This contributes to closing the bandgap, which remains indirect but it is reduced by approximately 0.5 eV. Interestingly, despite the formation of the impurity band, the dispersion around the VBM is not significantly modified and the VBM degeneracy is preserved. Even more interesting is the fact that the VBM and CBM are localised on the PtS_2 and HfS_2 layer, respectively, thus the HBL has still a type-II bandstructure. This is in contrast with the rest of the valence bands, which are now formed by hybrid states with almost equal contributions of the two layers.

Thus, we can clearly attribute the peak in the dielectric function at the absorption edge to transitions between the impurity valence band and the lowest conduction band. These are inter-layer in nature, and in fact we observe a significant increase of the inter-layer absorption with compression [see Fig. 4.6(a) and Fig. 4.6(e)]. Such features suggest an overall enhanced charge separation, which is promoted both by the presence of layer-separated excitons and by the fact that these form at transitions across an indirect band-gap. For the smallest interlayer distance investigated, 4.0 Å, the intra-layer, inter-layer and mixed component of the dielectric function have comparable magnitudes at the absorption edge, while for energies larger than 3 eV the intra-layer component dominates again. This is because in such high energy range the available transitions now involve the lower part of the valence manifold. As a final observation we remark that in all cases the out-of-plane component of the inter-layer dielectric function is significantly larger than the in-plane component.

In order to estimate the pressure needed to yield the layer distances investigated, and hence to monitor the evolution of the inter-layer dielectric function, we compute the pressure, p, as a function of the layer distance, d. This is simply given by

$$p = -\frac{\partial E}{\partial V} , \tag{4.4}$$

where E is the total energy and V is the cell volume, given by the in-plane cell area times the interlayer distance d. Our results are plotted in Fig. 4.8, where we can observe that one needs a pressure of $\simeq$ 38 GPa to compress the $\mathrm{HfS_2/PtS_2}$ HBL to an interlayer distance of $d = 4.4\,\text{Å}$. Although this is a rather significant pressure, which exceeds what is possible in standard experimental investigations, it is still lower than the metallisation pressure predicted for other 2D systems, e.g. 68 GPa for $\mathrm{MoS_2}$ [174].

4.4 Summary and Outlook

Our rationale behind vertically stacking TMDs in a LEGO fashion was to explore whether one could find unique and experimentally distinguishable peaks in the dielectric function, which could be unequivocally attributed to inter-layer transitions. Ideally these should be present at energies where no other transitions are available so that they can be uniquely identified, a condition met by heterostructures with type-II band alignment. Furthermore, ideally one wishes to find these features at an energy where other homogeneous structures (multi-layers of the same TMD) have no absorption. This situation may enable one to identify inter-layer transitions in heterostructure mixtures produced by liquid-phase processing. Based on these criteria we have used previously published *GW* data to identify HfS_2/PtS_2 hetero-bilayer as a possible candidate.

We have then quantitatively studied the in-plane and out-of-plane components of the dielectric function for HfS_2 and PtS_2 mono-layers and bilayers, and for a HfS_2/PtS_2 hetero-bilayer. In particular we have decomposed the dielectric function into intra-layer, inter-layer and mixed components, so that the specific nature of the transitions can be distinguished. This is obtained by projecting the dipole matrix elements on the relevant layers. We find that the intra-layer component of the dielectric function exceeds the inter-layer component by a factor 100. Furthermore, the mixed component, which does not bear a transparent physical interpretation, is also larger than the inter-layer component and may be negative. Thus, it appears that, although inter-layer transitions are located predominantly at the absorption edge, they cannot be unequivocally separated from the intra-layer transitions. In addition we find that, although the absorption edge of the HfS_2/PtS_2 hetero-bilayer is at lower energy than that of the homogeneous HfS_2 bilayers, it is at higher energy than that

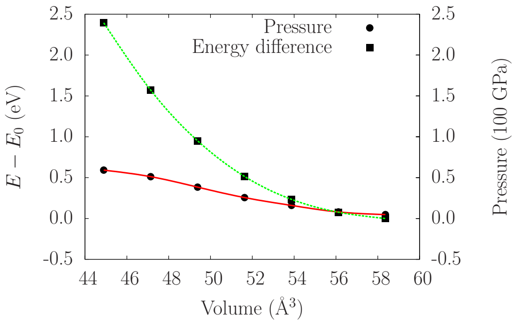

Figure 4.8: Energy curve as a function of volume for each interlayer distance d (squares) and its derivative corresponding to the pressure (circles). The energy was shifted by E_0, the total energy at the equilibrium distance $d = 5.2\,\text{Å}$. The lines (splines) are a guide for the eye.

of the PtS_2 bilayers. This is because the PtS_2 bandstructure is very sensitive to the layer interaction and hence to the number of layers in the stack, as reported before [165].

Since the small inter-layer transition amplitude originates from the large spatial separation between the electron and its hole (residing on different layers), we have investigated the changes in the dielectric function as the layer distance is reduced. Indeed, this promotes an increase in the inter-layer dielectric function, together with a significant red-shift of the absorption edge, mostly driven by the formation of a well separated peak. By following the evolution of the bandstructure upon decreasing the interlayer distance we can attribute such behaviour to the formation of a valence impurity band, well separated from the rest of the valence manifold. Most interestingly, the type-II band alignment is maintained even under severe compression, so that the split-off peak at the absorption edge is mostly composed of inter-layer transitions.

In conclusion, we have shown that TMD hetero-structures under severe compression present bandstructures and dielectric properties different from those of the constituent layers and different from those expected from simple electrostatic models. Here we have discussed one example in which the type-II band alignment can be preserved under pressure and where pressure can be used to uniquely isolate the inter-layer excitations from the rest of the spectrum. This work was published together with Dr. Sabine Körber, Dr. Carlo Motta, Prof. Fadwa El-Mellouhi and Prof. Stefano Sanvito in Physical Review Materials and it is referenced in Ref. [175].

5 2D material clustering and their joint density of states

5.1 Introduction to band nesting and JDOS

As discussed in the previous chapters, transition metal dichalcogenides (TMDs) are a family of crystals with the chemical formula MX_2, where M=W, Mo, Ti, Zr, Hf, Pd, Pt, etc. and X=S, Se, Te. TMDs typically form a two-dimensional (2D) structure that is constituted by two layers of chalcogens with a layer of transition metal atoms in between[176]. These three distinct atomic layers are embedded in hexagonal sublattices and together form a three-atom-thick sheet [176]. The metal-chalcogen bond is typically covalent in nature. The sheets are then held together by weak van der Waals forces, namely the attractive London dispersion interaction [28]. Given the environment of the metal centre, the two most common structural polytypes of TMDs are trigonal prismatic (2H=hexagonal or 3R=rhombohedral) and octahedral (1T=trigonal prismatic) [28]. These two polytypes are illustrated in Fig. 5.1. In this chapter, we shall also investigate transition metal halides (TMHs), which crystallise in layers [177]. The stoichiometry encountered in this study is MY_2 where M is a transition metal and Y is a halogen element. Like in the case of TMDs, the metal centre is in a trigonal prismatic or octohedral environment and the 2D TMH sheets, which are composed of the two halides and one metal layer, are stacked on top of each other and held together through the London dispersion forces [28]. Despite the fact that TMHs are ionic insulators [177], we shall consider in this study those whose band gap lies within the visible solar energy range, both in their bulk and monolayer form.

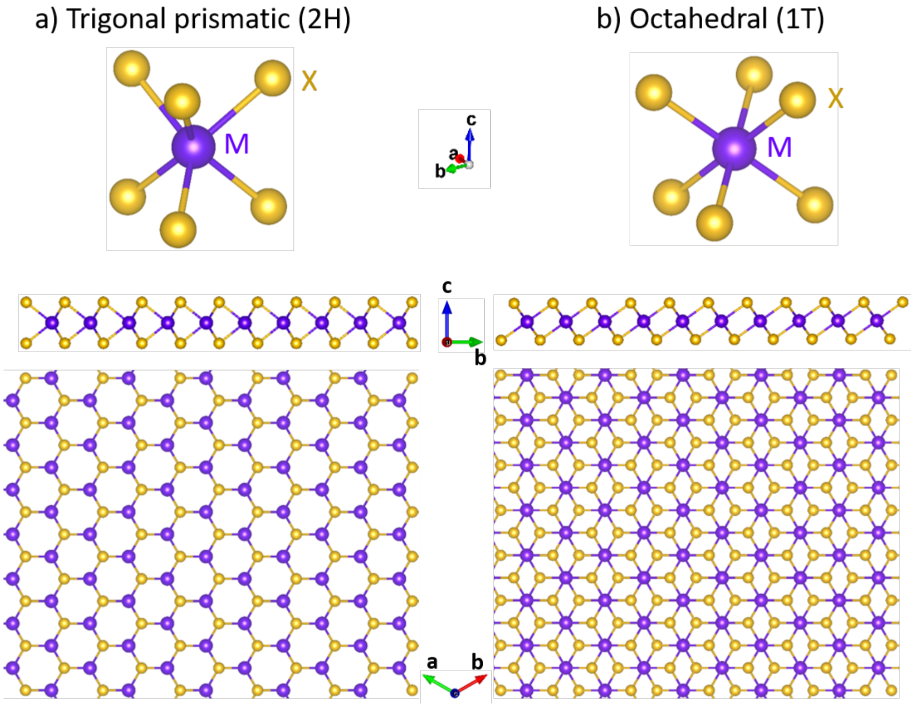
a) Trigonal prismatic (2H)

b) Octahedral (1T)

Figure 5.1: a) Trigonal prismatic (2H) and b) Octahedral (1T) configurations depicted for one metal atom (purple spheres) bonded to six chalcogens or halides (yellow spheres). The side and the top view of the extended hexagonal lattice is also shown.

With the advent of liquid phase exfoliation, the isolation of two-dimensional (2D) materials followed by the creation of various vertical stacks has become increasingly fruitful in the area of flexible and ultrathin devices. This newly emerged field of building heterostructures based on 2D crystals has also been geared towards the expansion of the conventional set of photoactive materials and device architectures. Creating a new generation of PV materials using 2D TMD is motivated by their band gaps, which lie in the visible range between 1 and 3 eV [178, 179]. Moreover, the optically generated excitons have large binding energies due to reduced screening and many-body interactions [180]. However, their strong absorption is a remarkable counter-intuitive feature despite being only three atoms thin [41]. Their unusually large optical response is associated with the existence of van Hove singularities in the electronic density of states (DOS) of TMDs and TMHs [177], which are usually not at the band-gap edge [176]. Such singularities in the DOS both in the conduction and the valence bands guarantee enhanced light-matter interactions, which lead to strong photon absorption and electron-hole creation through the process of "band-nesting" [176]. In this process, the conduction and valence bands have similar curvatures in certain k-space regions, which are determined by the points in the Brillouin zone where there are van Hove singularities [45]. These peaks in the DOS are thought to be the signature of the localized nature of the wave function [45]. The valence bands are mainly composed of localized d orbitals derived from the transition metal (TM) and the conduction bands are made of a linear superposition of the d and p orbitals coming from the TM and the chalcogen atom, respectively [45]. The consequence of such band-nesting is that the photo-generated electrons and holes propagate with exactly the same, but opposite, velocities [45, 176]. It is claimed that this phenomenon occurs for all TMDs [41, 176]. We will show in the following that band nesting results in the large optical conductivity characteristic of TMDs as noted earlier in the works cited in Ref.[41, 45, 176, 181]. The optical conductivity of a material can be expressed as

$$\sigma_1(\omega) = \varepsilon_2(\omega)\omega\varepsilon_0 \quad , \tag{5.1}$$

where $\varepsilon_2(\omega)$ is the imaginary part of the dielectric function, ω is the frequency of the incoming radiation and ε_0 is the vacuum permittivity [176]. Assuming that the wavevector of the perturbation is significantly smaller than that of the electrons in the material, *i.e.* $\mathbf{q} \to 0$ we can write [176]:

$$\varepsilon_2(\omega) = A(\omega) \sum_{v,c} \int_{BZ} \frac{d^2\mathbf{k}}{(2\pi)^2} |d_{vc}|^2 \delta(E_c - E_v - \hbar\omega) \quad , \tag{5.2}$$

where the integral is over the entire 2D Brillouin zone and the sum is over the occupied states in the valence band and the unoccupied states in the conduction band with energies E_c and E_v, respectively. The sum over spins is also included through $A(\omega) = 4\pi^2/(\Omega_c m^2 \omega^2)$ where e is the electric charge, m is the carrier mass and Ω_c is the volume of the unit cell. Here d_{vc} is the dipole matrix element. By writing the dipole matrix element in terms of the momentum matrix element, it can be shown that the imaginary part of the dielectric function in (5.2) is equivalent to the imaginary part of Eq.(2.73) derived in the RPA in Chapter 2. We note that the density of states is defined in 2D as $D(\omega) = \frac{2}{(2\pi)^2} \int_{S(\omega)} \frac{dS}{\nabla_k E_{\boldsymbol{k}}}$ as we have shown in Chapter 2. Then under the assumption that the dipole matrix element does not vary significantly in the regions of the spectrum where $|\nabla_{\boldsymbol{k}}(E_c - E_v)| \approx 0$, it follows that,

$$\varepsilon_2(\omega) \approx A(\omega) \sum_{v,c} |d_{vc}|^2 \rho_{vc}(\omega) \quad , \tag{5.3}$$

where

$$\rho_{vc}(\omega) = \frac{1}{(2\pi)^2} \int_{S(\omega)} \frac{dS}{\nabla_{\boldsymbol{k}}(E_c - E_v)} \quad , \tag{5.4}$$

is the joint density of states (JDOS) [176]. The points where $\nabla_k(E_c - E_v) = 0$ are called critical points (CP). If $\nabla_{\boldsymbol{k}} E_c = \nabla_k E_v = 0$, these singularities will either correspond to a maximum, a minimum, or a saddle point in each band and these usually occur at high-symmetry points [176]. These points are more easily identifiable through visual examinations of the regions in the band structure that are constant. The condition $\nabla_{\boldsymbol{k}}(E_c - E_v) = 0$ is also met when $|\nabla_{\boldsymbol{k}} E_c| \approx |\nabla_{\boldsymbol{k}} E_v| > 0$, which describes band nesting and hence the emergence of singularities of the JDOS [176].

After having said that, we would like to state that the work cited in Ref.[176] has systematically investigated band nesting in vast regions of the Brillouin zone for a number of 2D TMDs. They found that the octahedral compounds 1T-TiS$_2$ and 1T-ZrS$_2$ were among the materials with largest band-nesting regions. As a proof of concept, we aim to explore the band-nesting characteristics of a widely studied TMD, namely 2H-WS$_2$. We shall consider the results from the cited paper as a reference, against which we will compare our own findings. Then we will extend our analysis to a wide range of TMDs and TMHs.

In this chapter, we will focus on several related questions: 1) is it possible to classify the TMD and TMH family of materials in terms of the characteristic regions in the BZ, where band nesting occurs? 2) can one make the approximation that the imaginary part of the dielectric function and the JDOS are related by a semi-constant momentum matrix element squared? 3) if so, does this hypothesis hold over the entire visible solar spectrum? In that case, is it possible to reliably rank materials in terms of their absorption coefficient and short-circuit current density based on the JDOS scaled by the momentum matrix element squared instead of using the dielectric function?

The workflow is devised as follows: firstly, a series of HSE relaxations and then band structure calculations were performed on 36 different exfoliable TMD and TMH

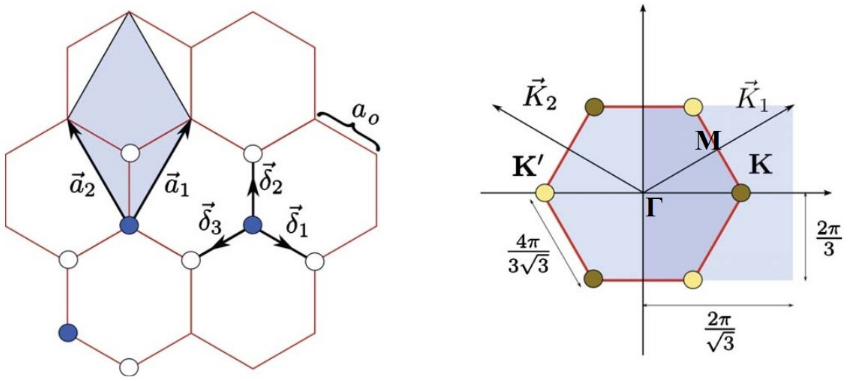

Figure 5.2: a) Bravais lattice of the hexagonal lattice where $\boldsymbol{a_i}$ are the primitive vectors, $\boldsymbol{\delta_i}$ are the nearest neighbors vectors and a_0 is the lattice constant. (b) The Brillouin zone of the hexagonal lattice, with the high symmetry points Γ, M, K indicated. K' and K are equivalent points hence the triangle delineated by Γ-M-K is the irreducible Brillouin zone. Image reproduced from Ref.[182]

.

compounds. Following a similar procedure as described in our previous chapter, we construct a unit cell with a sufficient amount of vacuum along the z-direction such as to avoid the spurious interactions between two neighbouring periodic unit cells. The number of k-points was also converged with respect to the total energy. From this analysis 29 distinct semiconducting TMD and TMH monolayers with direct band gaps in the optimal 0.33 to 4.42 eV visible solar energy range were identified. This set was further considered for spin-unpolarized band structure calculations with the FHI-AIMS all-electron DFT package. These were performed on a highly dense k-mesh consisting of 43x44x1 k-points in the $x-y$ plane by my colleague, Postdoctoral researcher Rui Dong, as part of a collaborative project on 2D materials. The discretized grid was chosen such that it would cover the irreducible Brillouin zone (IRBZ). The IRBZ of a hexagonal lattice is illustrated in Fig. 5.2 and is given by one of the equivalent 12 triangles making up the hexagonal Wigner Seitz cell, namely that along Γ-M-K. We then computed the gradient of the difference between the lowest conduction band and the highest valence band at each k-point in the IRBZ grid using finite differences.

The authors of [176] looked at the energy difference between the lowest unoccupied band and the highest occupied band, E_{c1}-E_{v1}, together with the absolute value of its gradient, $|\nabla_{\boldsymbol{k}}(E_{c1}-E_{v1})|$, along the Γ-M-K-Γ high-symmetry line of the Brillouin zone. The regions where band nesting occurs were established to be those where the condition $|\nabla_{\boldsymbol{k}}(E_{c1} - E_{v1})| \ll 1eV/(2\pi/a)$ was satisfied, where $2\pi/a$ is the modulus of the reciprocal lattice vector. Although the authors have used the GGA approximation and pseudopotentials to obtain their band structure, we shall compare our HSE-based results to theirs in order to gain a better understanding of how the energy difference and their gradient change with different employed methods.

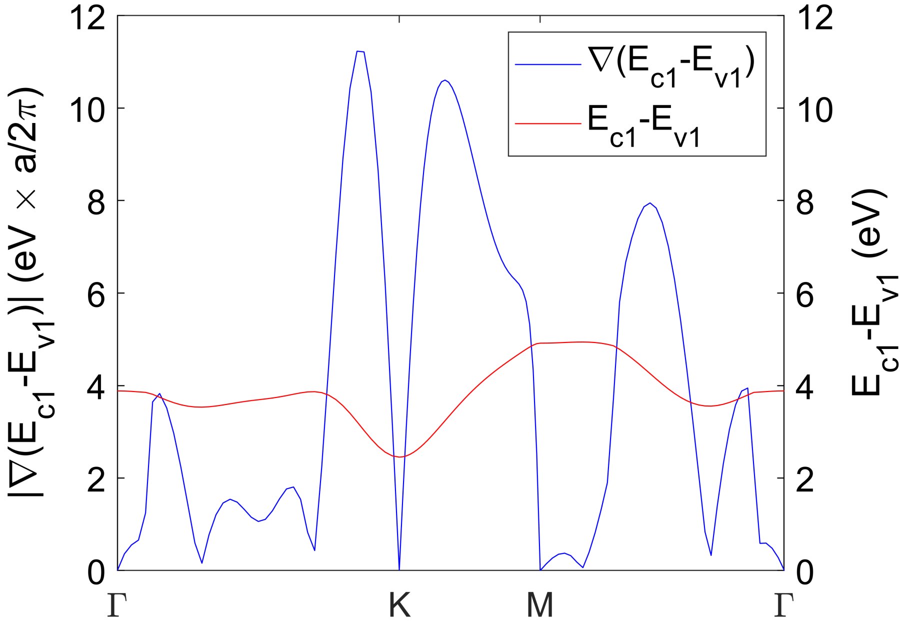

Figure 5.3: Our results for the monolayer 2H-WS$_2$ indicating the difference E_{c1}-E_{v1} together with the modulus of its gradient along the corresponding high symmetry path. The lowest unoccupied conduction band is denoted by E_{c1} and the highest occupied valence band by E_{v1}.

As can be seen from Fig. 5.3 and Fig. 5.4, our obtained energy difference, E_{c1}-E_{v1}, is very similar to the one presented by Carvalho et al. [176]. This is due to the fact that the shape of the bands seems to be well preserved when changing the exchange-correlation functional. The main difference resides in the fact that the HSE energy difference is almost rigidly shifted to higher values by approximately 1 eV due to the role the hybrid functional plays in widening the band gap. Also, our calculated $|\nabla_{\boldsymbol{k}}(E_{c1} - E_{v1})|$ and that of Carvalho et al. [176] have very similar trends if we do not consider the exact amplitude. It must be noted, though, that since we performed the band structure calculation without spin-orbit coupling, our calculated highest valence band is in fact nonequivalent to either of the two highest valence band obtained by Carvalho et al. [176].

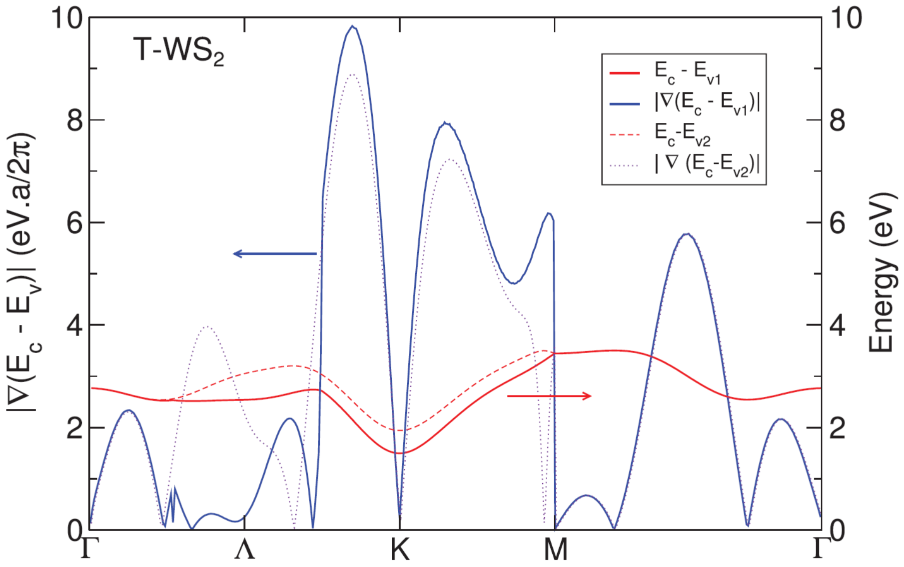

Figure 5.4: The results for 2H-WS$_2$ obtained by Carvalho et al. [176] present the same quantities as in Fig. 5.3. The authors also considered the energy difference E_{c1}-E_{v2} and $|\nabla_{\boldsymbol{k}}(E_{c1}E_{v2})|$, where E_{v2} denotes the the second highest occupied occupied valence band.

We further examine the entire IRBZ to obtain a better view of the extent of band nesting. Figure 5.5 shows $|\nabla_{\boldsymbol{k}}(E_c - E_{v1})|$ for WS$_2$ that was calculated based on the HSE band structure and without spin-orbit coupling. The white areas represent the regions where band nesting occurs and they are located at Λ, an intermediate point between Γ and K. This is found for both bands, namely for our HSE ones and for the PBE highest valence band and lowest conduction band [176]. Nevertheless, these white areas around Λ are more pronounced in the PBE case. The same observation can also be made when considering only the high-symmetry line Γ − Λ−K shown in

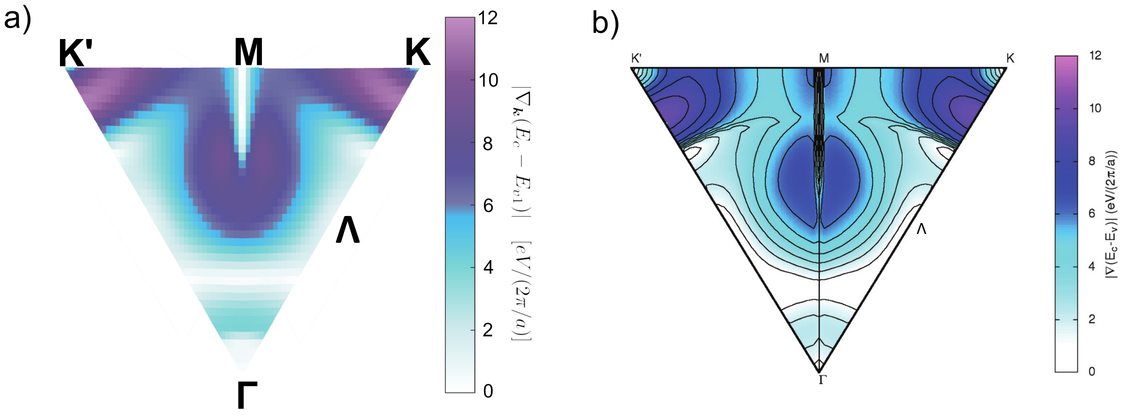

Figure 5.5: Map of $|\nabla_{\boldsymbol{k}}(E_{c1} - E_{v1})|$ over the Brillouin zone calculated for 2H-WS$_2$ with HSE by us in panel a) and with GGA by Carvalho et al. [176] in panel b), respectively.

Fig. 5.4 and Fig. 5.3, where $|\nabla_{\boldsymbol{k}}(E_{c1} - E_{v1})|$ reaches values close to zero near Λ. Moreover, due to the band splitting considered in the band structure calculations, Carvalho et al. [176] obtained an extra shoulder in $|\nabla_{\boldsymbol{k}}(E_{c1} - E_{v1})|$ along the K-M direction as depicted in Fig. 5.4. In Fig. 5.5)b one can see that along the K-M line, $|\nabla_{\boldsymbol{k}}(E_{c1} - E_{v1})|$ reaches high values of about 10 eV·nm after which it decreases to around 4 eV·nm and then steadily rises again to about 6 eV·nm as it aproaches M. This fluctuating trend is absent for our bands calculated without considering spin-orbit coupling, as it can be seen in Fig. 5.5)a.

5.2 TMD and TMH clustering

5.2.1 Monolayer analysis

Our initial exploratory work prompts us to tackle the first question that we raised at the beginning of this chapter regarding the classification of TMDs and TMHs based on their band-nesting features. To this end, we devise a plan of action in which we perform the following: first we consider the band structures of the 29 monolayers and compute the gradient of the difference between the bottom conduction band and the highest valence band $|\nabla_{\boldsymbol{k}}(E_{c1} - E_{v1})|$ across the entire IRBZ, for which we have the DFT band structure eigenvalues. In order to classify compounds based on common numerical patterns in their respective $|\nabla_{\boldsymbol{k}}(E_{c1} - E_{v1})|$ mapped on the IRBZ, we make use of a statistical technique known as "k-means" whose working principles were presented in Chapter 1. We begin by vectorizing, for all the 29 monolayer TMD and TMH compounds, their respective $|\nabla_{\boldsymbol{k}}(E_{c1} - E_{v1})|$ grids. We employ the statistical software R that has in-built packages that run the k-means algorithm. In order to overcome the tricky problem of visualizing high-dimensional data, we employ the t-SNE ("t-distributed Stochastic Neighbor Embedding") technique that is also implemented in R, whereby each datapoint is associated with a position in a two or three-dimensional map [126]. The most notable feature of this dimensionality reduction method is that it preserves both the local and the global structure of the high-dimensional data, as it produces well-separated clusters through a nonlinear dimensionality reduction technique [126, 127]. Unfortunately, large distances between points belonging to the same cluster are not accounted for, which renders both the relative and absolute positions of the clusters meaningless [127, 128]. In a nutshell, t-SNE works as follows: it calculates the probability of similarity of points in high-dimensional space and in the corresponding low-dimensional space. The similarity of points is taken as the conditional probability that a point X would choose point Y as its neighbour under the assumption that neighbours are chosen in proportion to their probability density under a normal distribution centered at X [126]. Then, the algorithms attempts to minimize the difference between the distribution of pairwise similarities in the high- and low- dimensional space such that the data points are accurately represented in the low-dimensional space [126]. This difference is quantified as the sum of the Kullback-Leibler divergence of all data points [129] and it is minimized using gradient descent. Since the resulting low-dimensional coordinates of the datapoints are no longer correlated to any identifiable quantity, the data should only be explored visually [126].

A non-trivial issue in implementing k-means is that of deciding the optimal number of clusters such that the similarities among same cluster members and the differences among different cluster members, respectively, are best captured. A common method employed for this purpose is the so-called "elbow method" discussed in Ref.[183]. The underlying idea is to plot the quantity that needs to be converged against the number of clusters. In our case, we consider this quantity to be the WCSS/BCSS ratio. If there is a noticeable flattening of this curve, this is an indication that a "good enough" threshold of minimization is reached. Hence, it is reasonable to assume that the appropriate number of clusters with sufficiently similar members is found, where the curve changes its slope most, forming an elbow-shape. In this case, four seem to be the optimum number of clusters, as it can be observed in Fig. 5.6.

A typical shortcoming of the k-means method is that it is highly dependent on the randomly chosen initial points that determine to a large extent the positions of the resultant cluster centers. The algorithm stops when it has reached a local optimum. Since in principle there is no guarantee of finding the global optimum cluster configurations, a common solution is to restart the algorithm with different initial conditions and keep only the configuration with the minimum final WCSS

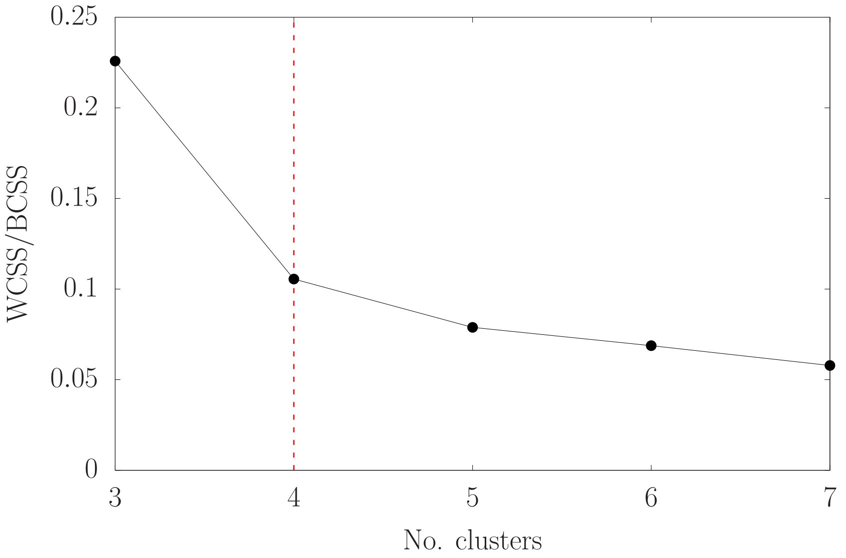

Figure 5.6: The total within-cluster sum of squares (TWCSS) divided by the between-cluster sum of squares (BCSS) against the preselected number of clusters. The curved elbow marks the appropriate threshold for the number of clusters (4 in this case).

[125]. Hence, we set k-means to initialize 100 distinct runs, each encompassing 1000 iterations, which should ensure a highly converged cluster configuration. Among the 100 runs, only the best configuration is kept and shown here. In Fig.5.7, we illustrate the resulting clusters projected in two-dimensional space. Each cluster is described in terms of its most representative data points, *i.e.* we show the $|\nabla_{\boldsymbol{k}}(E_{c1} - E_{v1})|$ mapped on IRBZ for only certain compounds from each group. Note that the compounds denoted by the * symbol refer to 2H polytypes and the rest are 1T polytypes. Throughout our entire analysis, band nesting will correspond to the regions in k-space where $|\nabla_{\boldsymbol{k}}(E_c - E_{v1})| \approx 0$.

The groups obtained after applying k-means with 4 clusters to our 29 TMD and TMH monolayers are the following:

Group 1 is constituted by the compounds 1T-CdI_2, 1T-GeI_2, 1T-PbI_2, 1T-PtO_2, 1T-SnS_2, 1T-$SnSe_2$, 1T-ZnI_2, 2H-GeI_2. One common feature of all these compounds is that the band nesting condition occurs at the Γ and more noticeably, at the M point. Moreover, almost invariably, there seem to be two other regions, where band nesting is present: one that is very close to the symmetry path Γ-K, closer to K and one that is along the Γ-M path, closer to Γ. Let us look at the details of the compounds with the transition metal belonging to the same group. Zinc

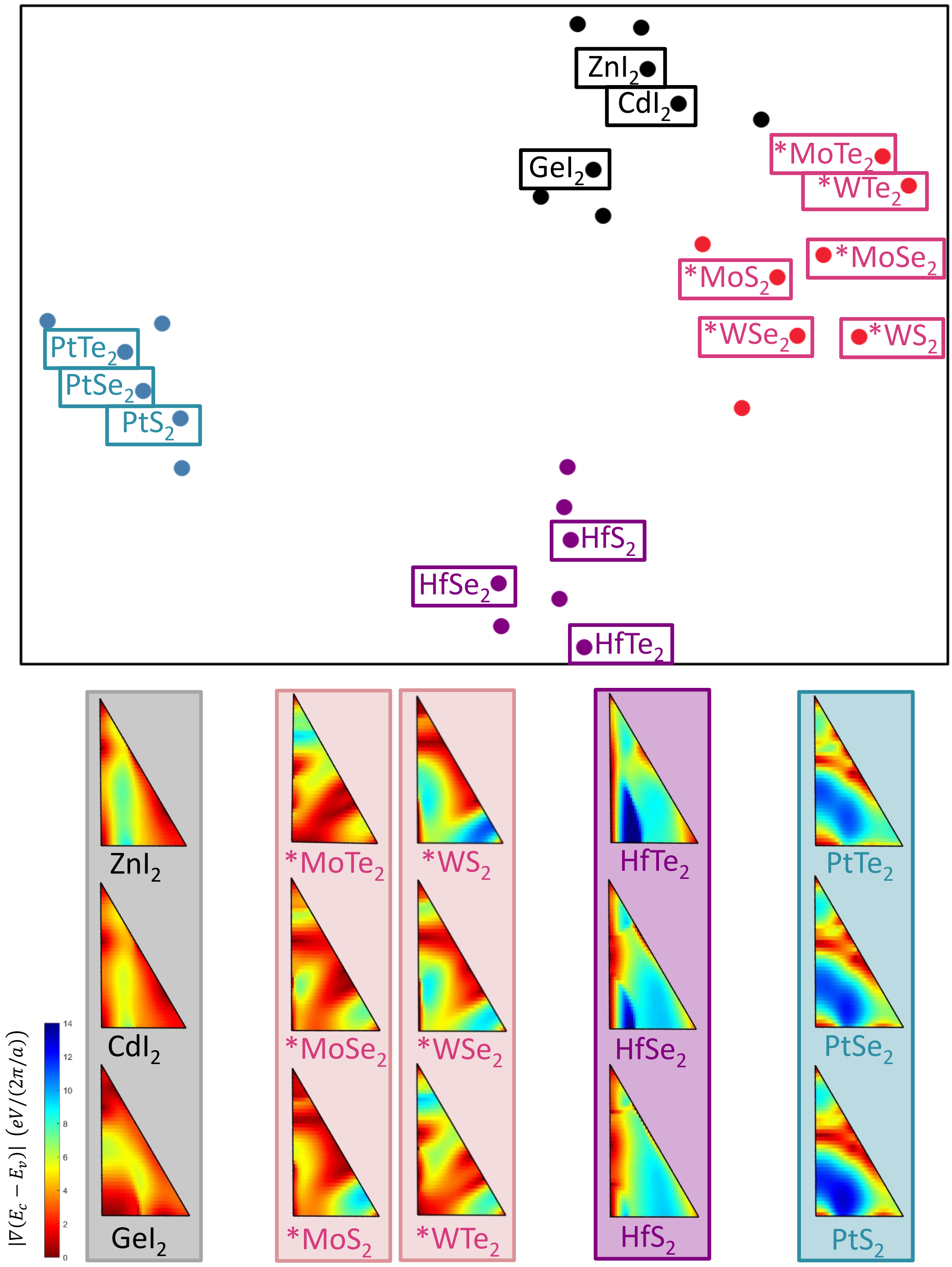

Figure 5.7: (Top panel) Two-dimensional representation of the relative distances between the 29 studied monolayer compounds. The different colors of the data points indicate the k-means determined clusters. (Bottom panel) $|\nabla_{\boldsymbol{k}}(E_{c1} - E_{v1})|$ mapped over the IRBZ of all the compounds that exhibit the most defining features of the group they belong to.

and Cadmium belong to group 12 having the valence d and s states fully occupied. Therefore, ZnI_2 and CdI_2 have very similar features *i.e.* $|\nabla_{\boldsymbol{k}}(E_c - E_{v1})|$ and the band nesting regions are virtually identical. However, because cadmium is heavier than zinc, its bands tend to be less dispersive as shown in Fig. 5.8. Moreover, the broadly flatter valence bands, stemming from iodide, which participates in a more ionic bond with cadmium than with zinc, can, in principle, lead to less variation between the slopes of the conduction and of the valence bands. This could explain the overall smaller values of $|\nabla_{\boldsymbol{k}}(E_c - E_{v1})|$ for CdI_2 than for ZnI_2. A similar argument can be employed to justify the strong resemblance between SnS_2 and $SnSe_2$, two compounds that have qualitatively similar bands to those of CdI_2 and ZnI_2. However we will not present here their band structure. Germanium is in group 14, making 1T-GeI_2 a compound with a slightly more covalent bond. One can take note of the significantly more dispersive valence bands along the Γ-M and M-K symmetry lines compared to those of 1T-CdI_2 and 1T-ZnI_2. The similarly dispersive bottom conduction and top valence bands in 1T-GeI_2 along M-K imply very small variation between $\nabla_{\boldsymbol{k}}(E_{c1})$ and $\nabla_{\boldsymbol{k}}(E_{v1})$ and lead, hence, to very small overall values of $|\nabla_{\boldsymbol{k}}(E_{c1} - E_{v1})|$ along M-K. This justifies the strong band nesting region that characterize this system around M with a noticeable spread towards K.

Group 2 contains 2H-MoS_2, 2H-$MoSe_2$, 2H-$MoTe_2$, 2H-WS_2, 2H-WSe_2, 2H-WTe_2, 2H-$HfTe_2$ and 1T-STl_2. These compounds are dominated by regions with $|\nabla_{\boldsymbol{k}}(E_{c1} - E_{v1})|$ ranging between 0 and 2 eV·nm. The band nesting regions generally cover larger areas of the BZ, e.g. between the Γ-M and the Γ-K symmetry paths in close proximity to Γ. Another significant band nesting region can be observed along the Γ-K path with a varyingly wide spread towards M. Band nesting is also localized strictly around Γ and M. The noticeable similarity between the tungsten- and molybdenum-based compounds, *i.e.* 2H-WS_2, 2H-WSe_2 and 2H-WTe_2 and 2H-MoS_2, 2H-$MoSe_2$ and 2H-$MoTe_2$, is striking. This can be justified on the basis of their very similar band structures, since the two transition metals belong to the same group and hence, have similar electronic behaviours when bonded with the three chalcogens. The band structures of 2H-WTe_2, 2H-WSe_2 and 2H-WS_2 and their corresponding $|\nabla_{\boldsymbol{k}}(E_{c1} - E_{v1})|$ maps are shown in Fig. 5.9. Since sulfur, selenium and tellurium increase in ionic radius size in this order, the valence bands of the corresponding transition metal chalcogenides become increasingly flatter while the conduction bands do not change much. The increasing offset between the slope of the top valence bands and that of the bottom conduction bands might then explain the gradual reduction in band nesting areas when going from sulfur- to selenium- and, finally, to tellurium-based compounds.

Group 3 is made of 1T-HfS_2, 1T-HfSe_2, 1T-HfTe_2, 1T-ZrS_2, 1T-ZrSe_2, 1T-YbI_2 and 1T-TiS_2. The common feature of all these compounds is that there is a large region of high gradient values, which exceeds 7 eV · nm and it is invariably located between M and K with a wide spread in the direction of Γ. For all the members of this group, the band nesting regions are situated sparsely along the Γ-M symmetry path. In the following order, 1T-HfS_2, 1T-HfSe_2, 1T-HfTe_2 gradually exhibit larger gradient areas although it is not immediately obvious from their band structure why that is the case. However, the band nesting regions seem to be largest for 1T-HfTe_2, extending significantly along Γ-M. From the band structure depicted in Fig. 5.10, one can see that between these two points, the top valence and bottom conduction bands of 1T-HfTe_2 are overall more similar that those of 1T-HfS_2.

Group 4 is made of 1T-PtS_2, 1T-PtSe_2, 1T-PtTe_2, 1T-PdTe_2, 1T-OTl_2 and 2H-ZrCl_2. The common feature that stands out is the wide-spread regions throughout the IRBZ characterized by large values of $|\nabla_{\boldsymbol{k}}(E_{c1} - E_{v1})|$, namely ranging between 11 and 14 eV·nm. However, there are isolated band nesting regions close to the Γ-K and Γ-M symmetry lines. In the case of the 1T-PtS_2, 1T-PtSe_2, 1T-PtTe_2 trio, both the band nesting and the high gradient regions decrease in this order as seen in Fig. 5.11. Also, since palladium and platinum belong to the same group, the band structure of 1T-PtTe_2 and 1T-PdTe_2 and hence their $|\nabla_{\boldsymbol{k}}(E_{c1} - E_{v1})|$ mapped over their respective IRBZ, are almost identical.

So far we have carried out an exploration of the way TMD and TMH materials can be grouped and classified in terms of their intrinsic band nesting features. We have found that the k-means clustering algorithm does indeed capture the regions in the BZ that are numerically closest and hence, helps quantitatively to shed some light on the subsets of TMD and TMH materials that go through band nesting at

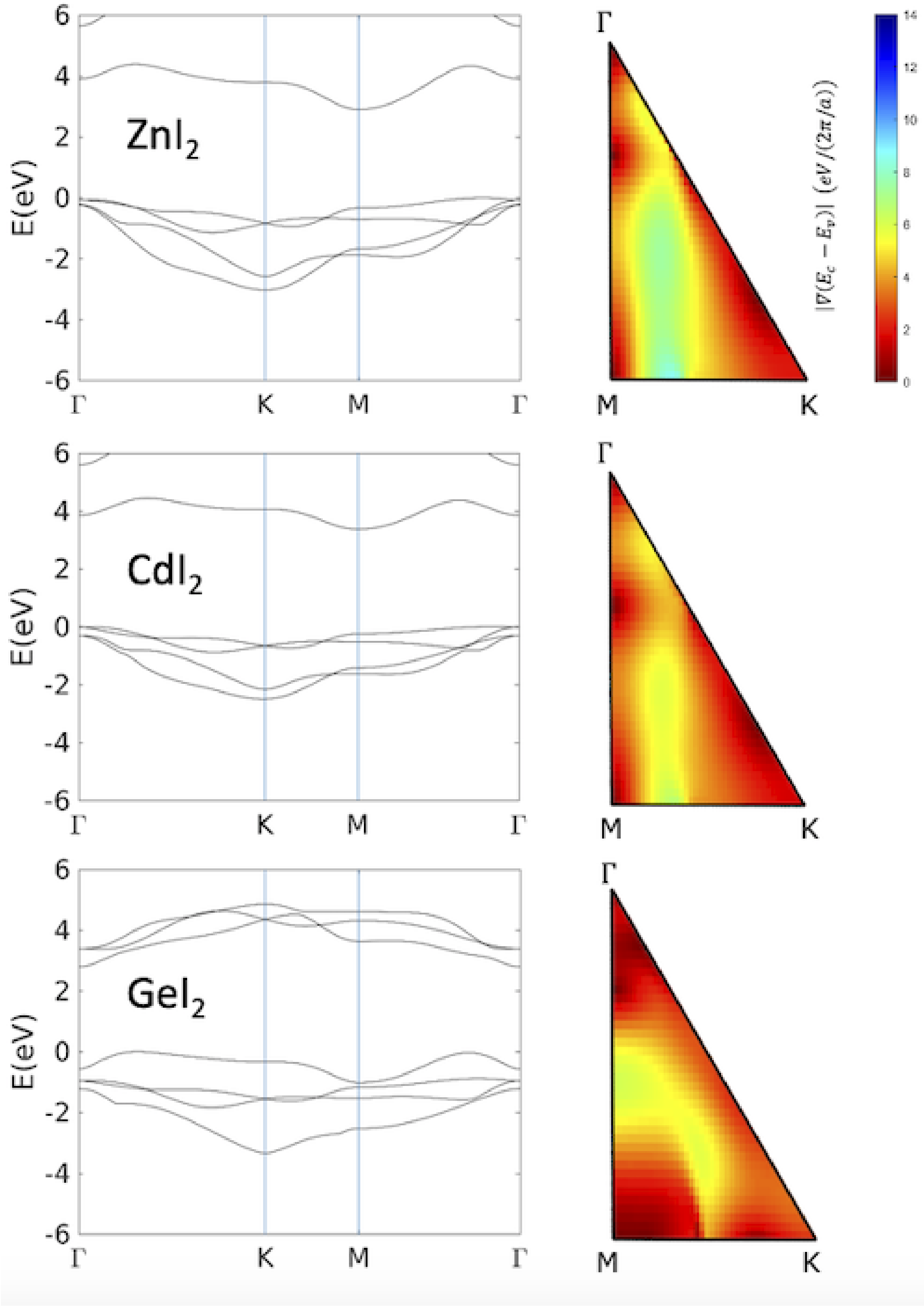

Figure 5.8: Group 1: Band structure of 1T-CdI$_2$, 1T-ZnI$_2$ and 1T-GeI$_2$ in monolayer form together with their characteristic $|\nabla_{\boldsymbol{k}}(E_{c1} - E_{v1})|$ map.

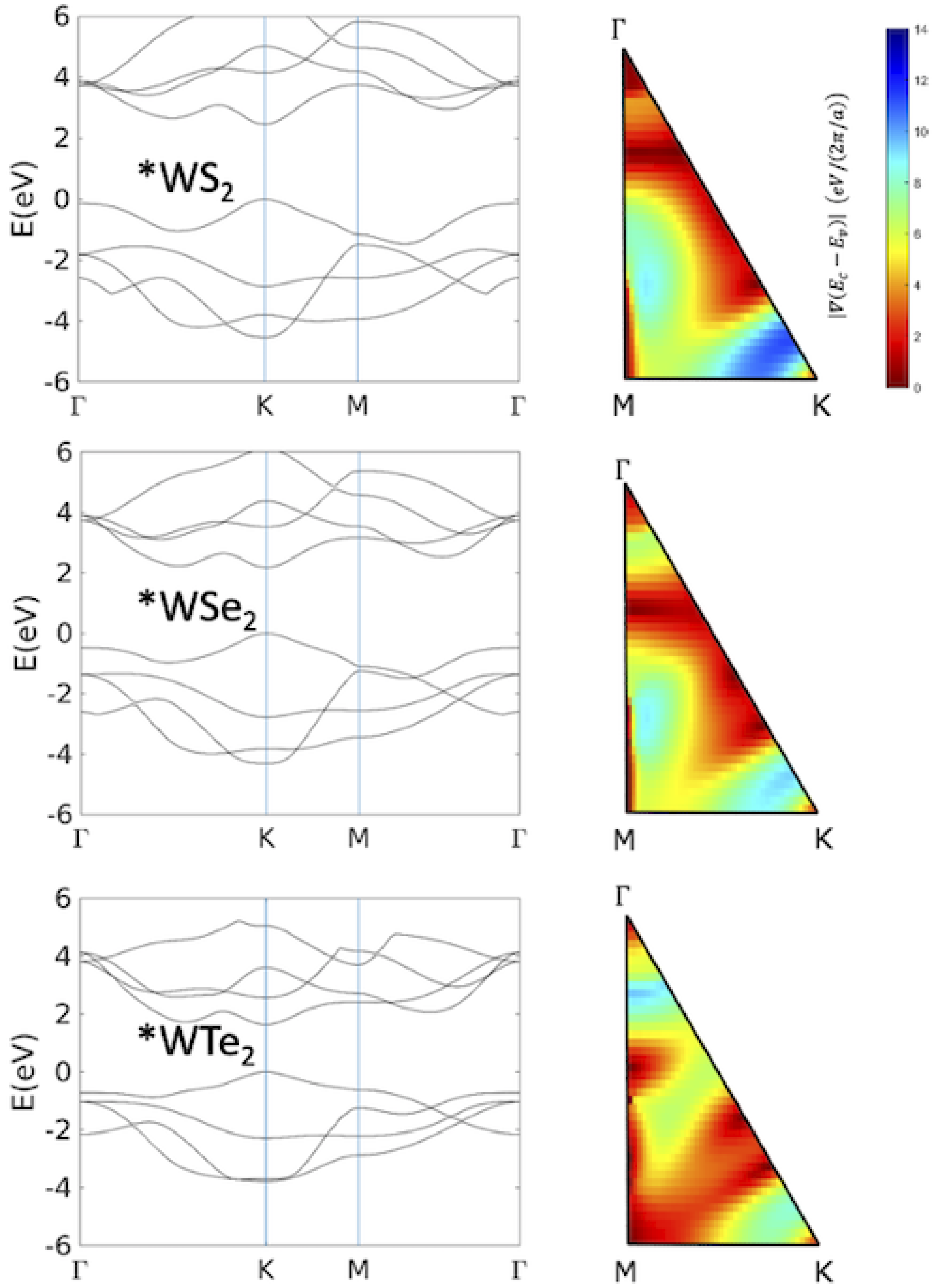

Figure 5.9: Group 2: Band structure of 2H-WS$_2$, 2H-WSe$_2$ and 2H-WTe$_2$ in monolayer form together with their characteristic $|\nabla_{\boldsymbol{k}}(E_{c1} - E_{v1})|$ map.

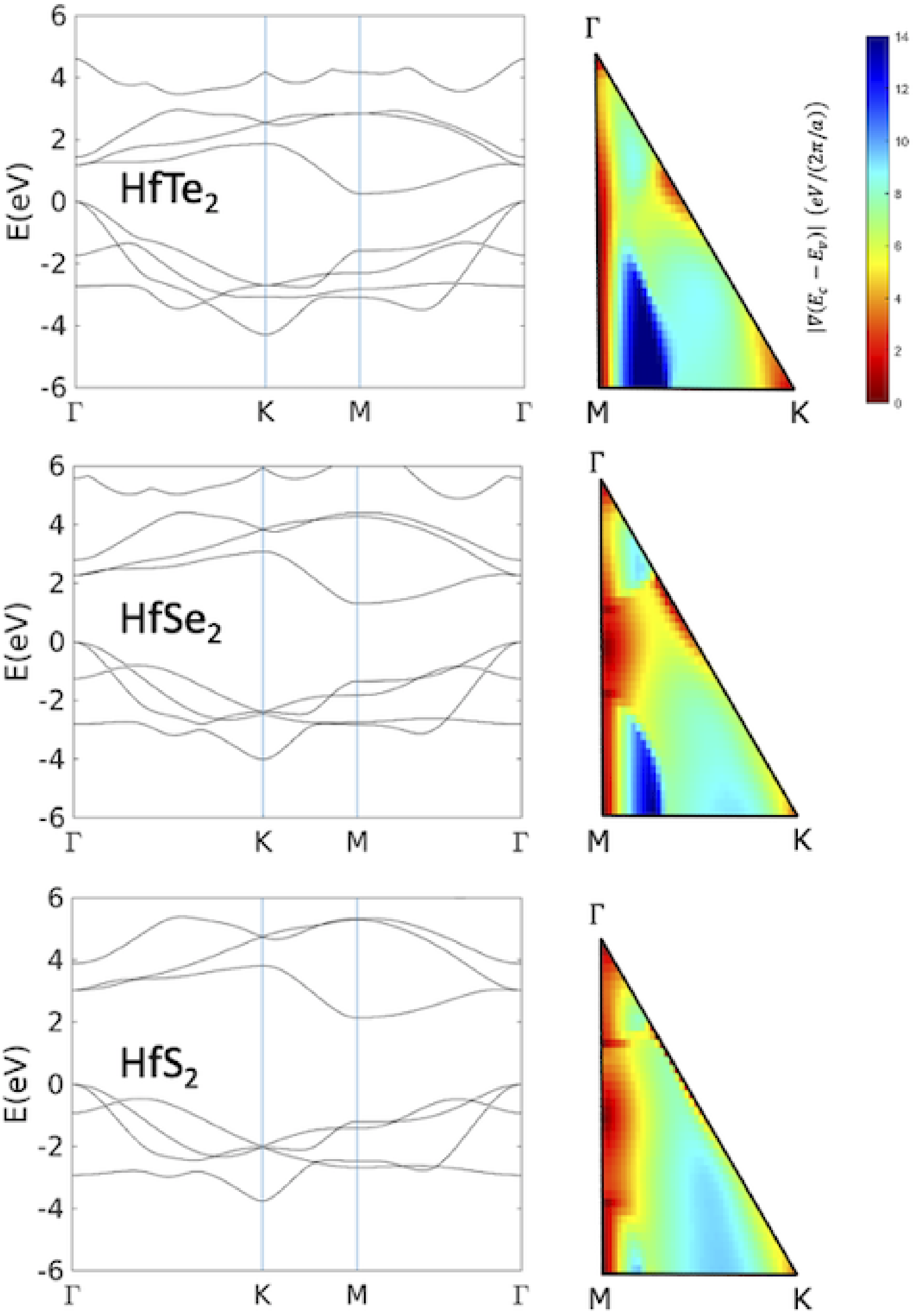

Figure 5.10: Group 3: Band structure of 1T-HfTe$_2$, 1T-HfSe$_2$ and 1T-HfS$_2$ in monolayer form together with their characteristic $|\nabla_{\boldsymbol{k}}(E_{c1} - E_{v1})|$ map.

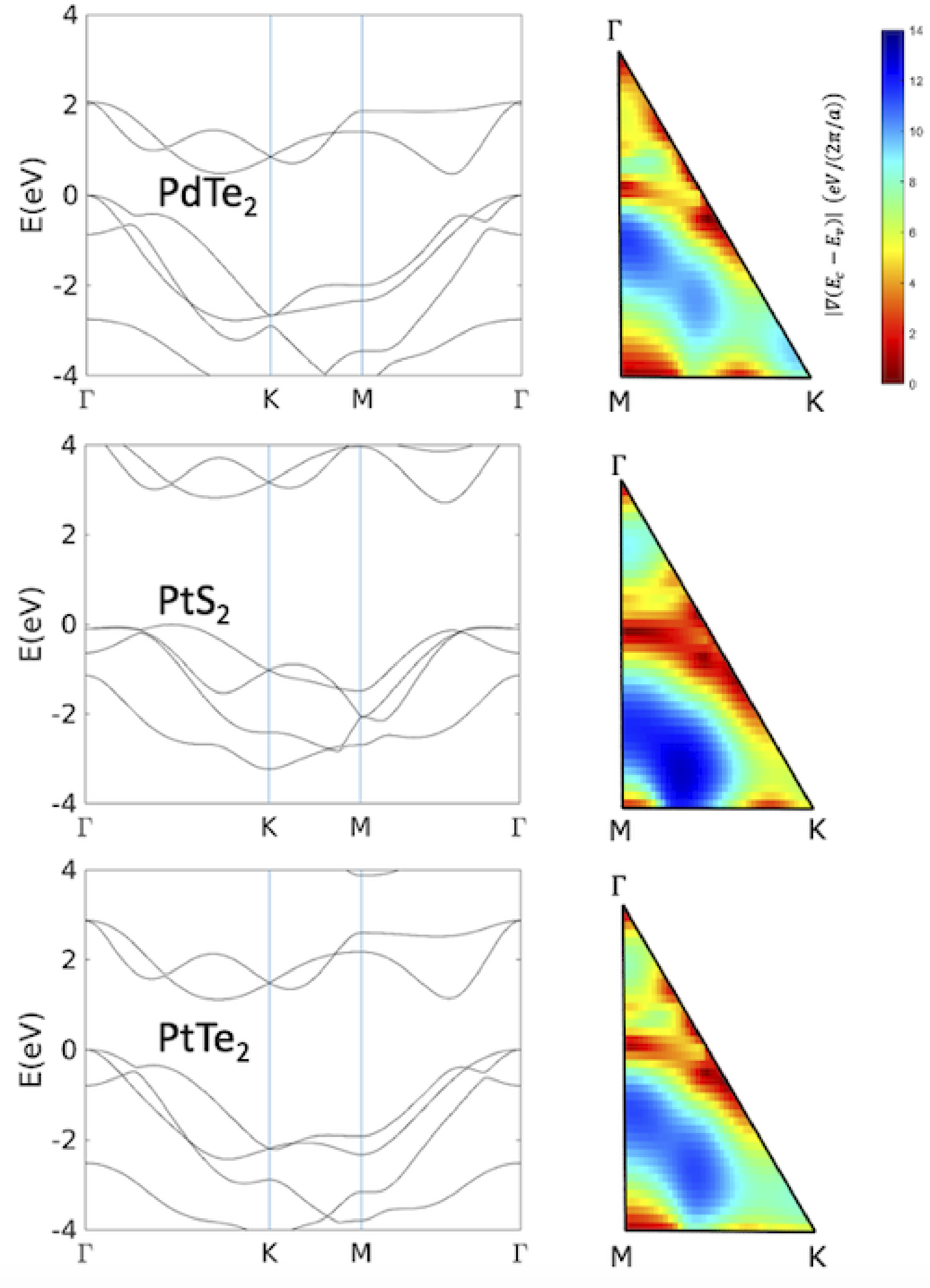

Figure 5.11: Group 4: Band structure of 1T-PdTe$_2$, 1T-PtS$_2$ and 1T-PtTe$_2$ in monolayer form together with their characteristic $|\nabla_{\boldsymbol{k}}(E_{c1} - E_{v1})|$ map.

similar places in the reciprocal space. This insightful band nesting classification can prove to be helpful in determining the regions in k-space where excitonic transitions occur. Also, as shown in the work of Kozawa et al. [184], photocarriers generated through band nesting relax towards the closest band extrema with opposite momentum. Therefore, band nesting is an important process that suppresses the radiative recombination of the photocarriers and hence, determines their relaxation pathways [184].

A further analysis that we undertake involves the classification of band nesting convoluted with the solar flux ϕ_{sol}. In other words, after studying the characteristic profile of the band nesting for each material and grouping them accordingly, we intend to introduce the solar flux ϕ_{sol} as another parameter in the IRBZ map of each compound. Essentially, we shall consider the solar flux ϕ_{sol} amplitude at the energy $E_{c1,\boldsymbol{k}} - E_{v1,\boldsymbol{k}}$ for each k-point in the IRBZ multiplied by the inverse $|\nabla_{\boldsymbol{k}}(E_{c1} - E_{v1})|$. In this way we obtain a better view of the absorption profile of TMDs and TMHs, since we also take into account the inhomogeneity of the solar spectrum.

This decision is motivated by the following observation: in Eq (5.3) the imaginary part of the dielectric function can be written in terms of the joint density of states, which is defined as an integral over the inverse $|\nabla_{\boldsymbol{k}}(E_c - E_v)|$. We have checked and most transitions that correspond to the same energy range as the visible solar radiation range are predominantly between the lowest conduction band and the top valence band. Therefore we believe it is a reasonably good assumption to make that these two bands denoted by c_1 and v_1 are sufficient in describing the absorption in TMDs and TMHs.

In Fig. 5.12, one can see that the solar flux ϕ_{sol} has a magnitude of the order of 10^{21} s^{-1}m^{-2}eV^{-1} throughout most of the spectrum. In the band nesting regions, where it is expected that $|\nabla_{\boldsymbol{k}}(E_{c,\boldsymbol{k}} - E_{v,\boldsymbol{k}})| \approx 0$, the resulting product between the inverse of the gradient $|\nabla_{\boldsymbol{k}}(E_c - E_v)|$ and the solar photon flux at the respective energy $E_{c1} - E_{v1}$ should have a magnitude order of at least 10^{22} s^{-1}m^{-3}eV^{-2}. We then loosely define the "regions of interest" to be those regions that facilitate band nesting in transitions that match energetically with the largest regions of the solar spectrum. Therefore, we shall analyze the resulting clusters by plotting their constituting compounds on a log scale and consider the "regions of interest" to be

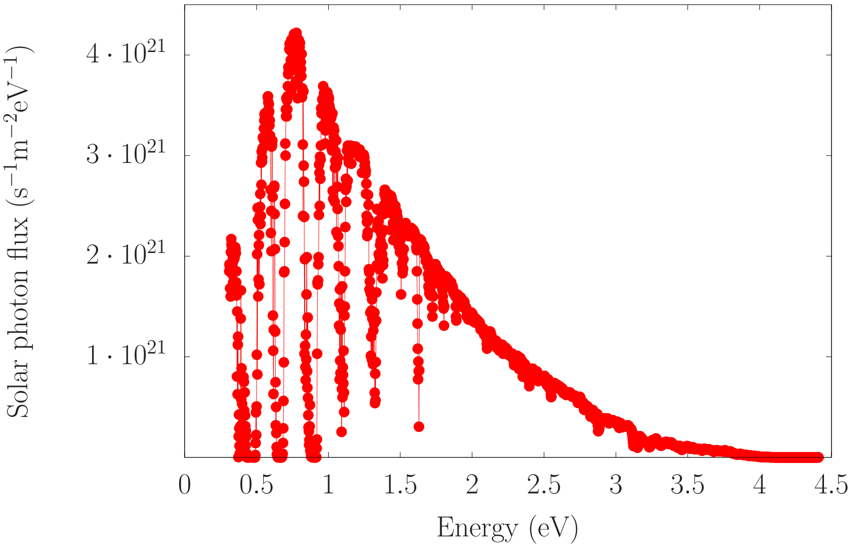

Figure 5.12: The solar photon flux as a function of the energy.

wherever $\phi_{sol}/|\nabla_{\boldsymbol{k}}(E_c - E_v)|$ is of the order 10^{22} s^{-1}m^{-3}eV^{-2}. Similar to the band nesting clustering section presented previously, we present in Fig. 5.13 the different clusters and their most defining compounds.

Group 1 (black) in Fig. 5.13 is composed of 1T-SnS_2, 1T-HfS_2, 1T-ZrS_2, 1T-ZnI_2, 1T-YbI_2, 1T-CdI_2 and 1T-PtO_2. The first three are the compounds with the smaller direct gaps that coincide energetically with the portions of the solar flux that are strongest. The other iodide and oxygen based systems have larger band gaps possibly due to their more ionic nature. This, in fact, leads to very limited "regions of interest" mostly due to the very weak solar spectrum at the $E = E_{c1} - E_{v1}$ energy transitions.

Group 2 (red) in Fig. 5.13 is made of 1T-$PdTe_2$, 1T-PtS_2, 1T-$PtSe_2$, 1T-$PtTe_2$, 2H-GeI_2, 2H-MoS_2, 2H-WS_2 and 2H-WSe_2. We indicated in the previous section that the extent of band nesting decreases from 1T-PtS_2, 1T-$PtSe_2$ to 1T-$PtTe_2$. But once we consider the solar flux ϕ_{sol}, the trend changes. Now 1T-$PtTe_2$ displays the largest "regions of interest". This is due to the decreasing direct band gap going from 1T-PtS_2, to 1T-$PtSe_2$, to 1T-$PtTe_2$. In all these compounds, the "regions of interest" match with the regions of inherent band nesting depicted in the previous section. Moreover, it seems that the intrinsically strong band nesting regions of 2H-MoS_2, 2H-WS_2 and 2H-WSe_2 cannot be exploited under solar radiation. This is simply because their band-nesting assisted transitions are energetically unfavourable since

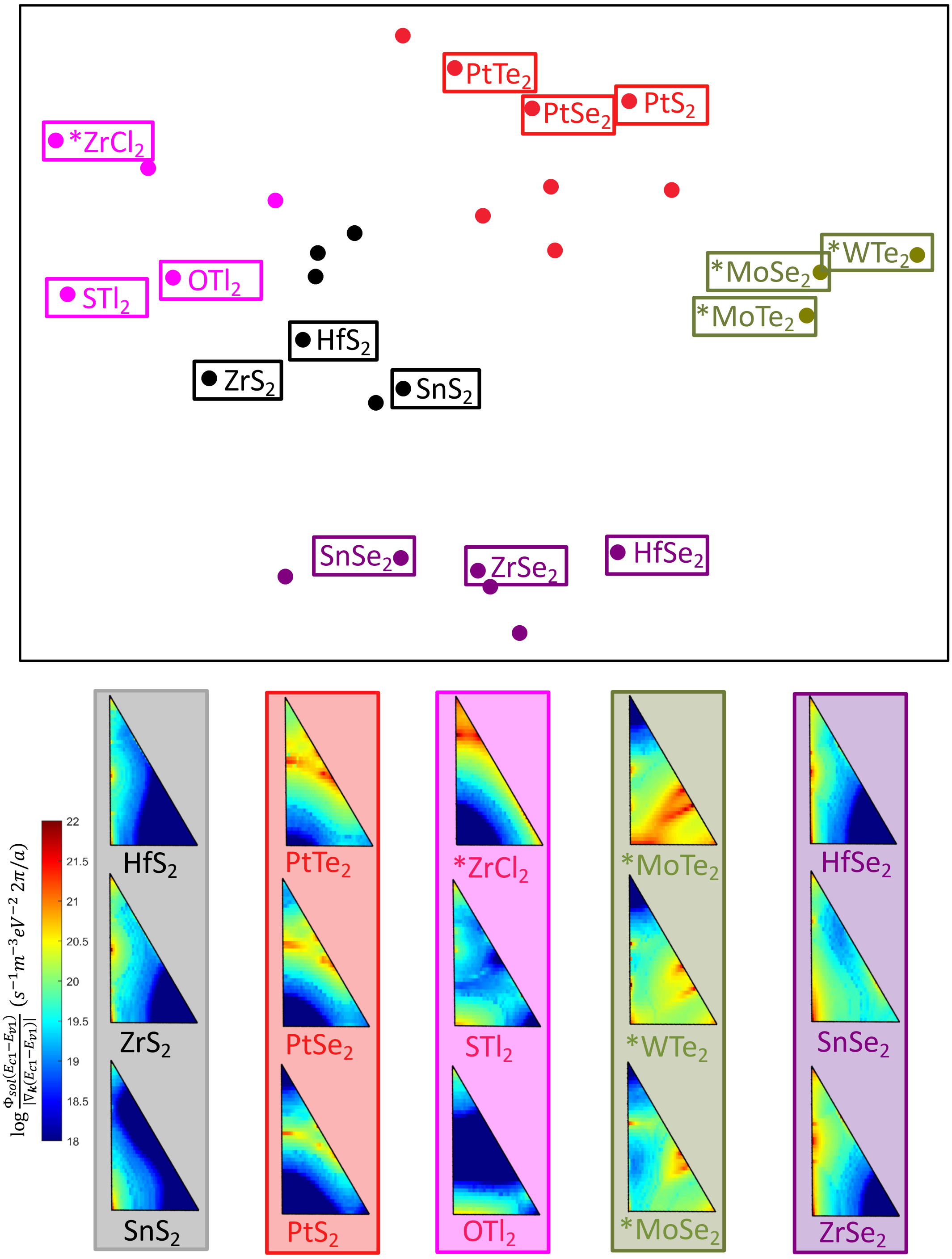

Figure 5.13: (Top panel) Two-dimensional representation of the relative distances between the 29 studied monolayer compounds. The different colors of the data points indicate the k-means determined clusters. (Bottom panel) $\log[\phi_{sol}(E_{c1} - E_{v1})/|\nabla_{\boldsymbol{k}}(E_{c1} - E_{v1})|]$ mapped over the IRBZ for the monolayer compounds that illustrate the most defining features of the group they belong to.

they have energies reaching $E = E_{c1} - E_{v1} > 3.5$ eV. According to Fig. 5.12, these are energies where the solar spectrum is strongly reduced.

Group 3 (pink) in Fig. 5.13 contains compounds 1T-GeI$_2$, 1T-PbI$_2$, 1T-STl$_2$, 1T-OTl$_2$, 2H-ZrCl$_2$. All exhibit values of $\phi_{sol}(E_{c1} - E_{v1})/|\nabla_{\boldsymbol{k}}(E_{c1} - E_{v1})|$ with a magnitude of the order of 10^{19} s^{-1}m^{-2} eV^{-1} around Γ. However there is an abrupt decrease towards the second half of the IRBZ, towards the M-K direction.

Group 4 (green) in Fig. 5.13 is made of three compounds, namely of 2H-MoTe$_2$, 2H-WTe$_2$, 2H-MoSe$_2$ due to their low band gaps. For all three, a significant fraction of the inherent band nesting regions along the Γ-K symmetry line, observed in Fig. 5.7, coincides with the "regions of interest" where $\phi(E_{c1} - E_{v1})/|\nabla_{\boldsymbol{k}}(E_{c1} - E_{v1})|$ is around 10^{22}s^{-1}m^{-2} eV^{-1}. However, these regions correspond to transitions of at least 2 eV, hence they do not fall in the solar spectrum energy range with high flux as can be noted from Fig. 5.12. The band nesting region between Γ-K is large for 2H-MoTe$_2$ as seen in Fig. 5.13. Nevertheless, since the "region of interest" are very similar to the regions of band nesting along Γ-K, they shrink gradually going from 2H-MoTe$_2$ to 2H-MoSe$_2$.

Group 5 (purple) in Fig. 5.13 consists of the low gap compounds, *i.e.* 1T-TiS$_2$ (1.15 eV), 1T-HfTe$_2$ (1.17 eV), 2H-HfTe$_2$ (1.44 eV), 1T-SnSe$_2$ (1.84 eV), 1T-ZrSe$_2$ (1.85 eV) and 1T-HfSe$_2$ (2.28 eV). This group is formed by roughly the same compounds as those of group 3 of the previous classification. The "regions of interest" are sparsely located in the very close vicinity of the Γ-M symmetry line. In all the 6 systems, the lowest values of $\phi_{sol}(E_{c1} - E_{v1})/|\nabla_{\boldsymbol{k}}(E_c - E_v)|$ are near the K point.

Once this analysis is concluded, we would like to point out, which are the compounds whose inherent band nesting regions best match the "regions of interest". We defined the "regions of interest" as the band nesting regions that also match energetically the high-flux portion of the solar spectrum. These are: 1T-PdTe$_2$ (group 2), 1T-PtTe$_2$ (group 2), 2H-HfTe$_2$ (group 3), 2H-ZrCl$_2$, 2H-MoSe$_2$ (group 4), 2H-MoTe$_2$ (group 4), 2H-WTe$_2$ (group 4) and 1T-TiS$_2$ (group 5).

5.2.2 Bulk analysis

A similar exercise based on the t-SNE and the k-means algorithms was done for a set of bulk 29 semiconductor TMD and TMH materials. Similarly to the monolayers, the structures were relaxed and then their HSE band structure was computed on a dense 43x44x1 k-grid. Only one k-point is sampled in the perpendicular z direction since we will classify the gradients of the difference between E_{c1} and E_{v1} mapped on the same Brillouin zone region as for the monolayers, namely within the Γ-M-K-Γ symmetry path in the $x - y$ plane. Unlike the monolayers, the unit cells of the bulk compounds have a small lattice parameter c_0 so that there is no need to omit the interlayer interaction in the z-direction by adding large amounts of vacuum as necessary in the case of monolayers. The number of clusters was determined by investigating once more the WCSS/BCSS ratio. This is depicted in Fig. 5.14 and as can be seen from the position of the 'elbow', the optimal number of clusters is again four. Despite the weak change in the WCSS/BCSS ratio corresponding to four clusters, the reduction is, nevertheless, strongest compared to the cases where larger number of clusters are considered.

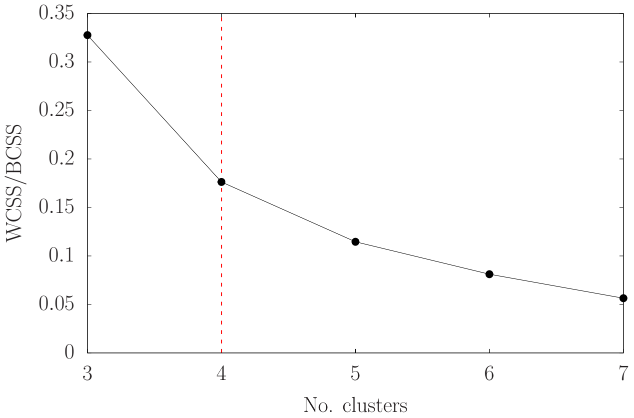

Figure 5.14: Four clusters are found to be 'good enough' to classify bulk 2D materials in terms of $|\nabla_{\boldsymbol{k}}(E_{c1} - E_{v1})|$. Their number is computed using the elbow method.

The obtained groups can be seen in Fig. 5.15 where we have arranged the members of the four resulting groups into four columns. For simplicity, we only show the $|\nabla_{\boldsymbol{k}}(E_{c1} - E_{v1})|$ maps over the IRBZ for all the studied materials. Let us look at the four groups.

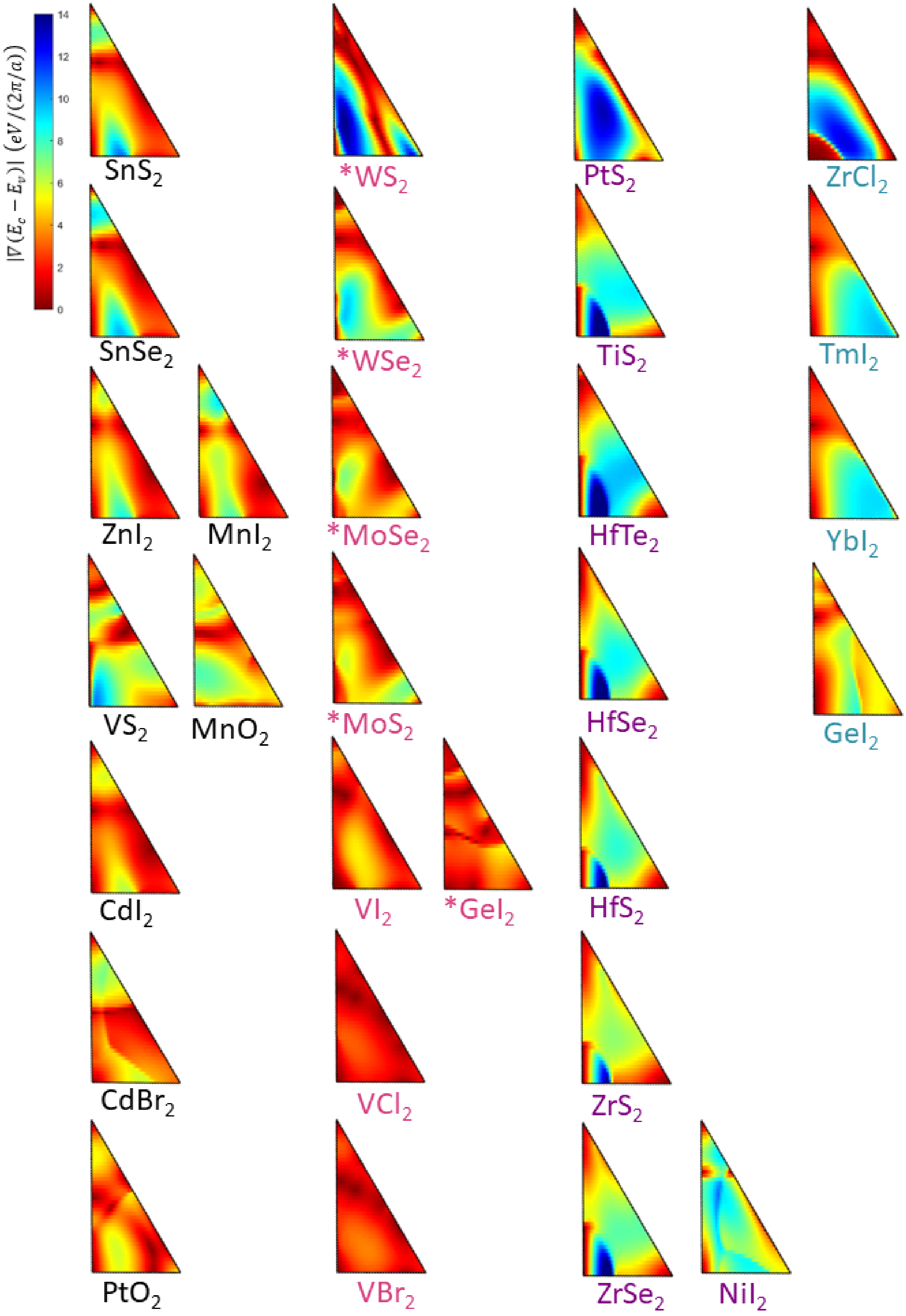

Figure 5.15: $|\nabla_{\boldsymbol{k}}(E_{c1} - E_{v1})|$ maps over the IRBZ for all the bulk compounds investigated. The four columns representing the four distinct groups depict the compounds and their characteristic maps.

Group 1 consists of 1T-ZnI_2, 1T-CdI_2, 1T-SnS_2, 1T-$SnSe_2$, 1T-$CdBr_2$, 1T-MnO_2, 1T-MnI_2, 1T-PtO_2 and 1T-VS_2. We first note that the first four compounds were also clustered together in group 1 during the monolayer band nesting analysis done in the previous section. This fact indicates that the band structure characteristics do not change significantly when considering the bulk instead of the monolayer geometries. The common features of all the members of this group are the emerging band nesting regions along the Γ-M and Γ-K symmetry lines and those tightly localized around the M point. Another common element is the existence of a region between M-K that spreads internally with high values of $|\nabla_{\boldsymbol{k}}(E_c - E_v)|$, exceeding 5 eV·nm. The band structures of 1T-CdI_2 and 1T-$SnSe_2$ are depicted in Fig. 5.16. Their band nesting regions along the Γ-K and along the Γ-M symmetry-lines can be traced back to the comparably similar top valence bands and bottom conduction bands, respectively. In both cases, the bands are quite parallel starting half-way between the Γ-K line going all the way up to K. This behaviour is even more pronounced for CdI_2, possibly because the valence bands stemming from iodide are slightly flatter due to iodide being a larger ion. This leads to a less dispersive top valence band, which matches appropriately with that of the conduction band above. In Fig. 5.16 we also show the band structure of 1T-VS_2, which is qualitatively different from the ones of 1T-CdI_2 and 1T-$SnSe_2$. Between Γ and M, the top valence and bottom conduction bands, have identical dispersions, hence the band-nesting region that between M and Γ.

Group 2 is composed of 1T-VBr_2, 1T-VCl_2, 1T-VI_2, 2H-GeI_2, 2H-MoS_2, 2H-$MoSe_2$, 2H-WS_2 and 2H-WSe_2. For all of these compounds, the profile of $|\nabla_{\boldsymbol{k}}(E_{c1} - E_v)|$ has the same broad features. On the one hand, the highest gradient $|\nabla_{\boldsymbol{k}}(E_{c1} - E_{v1})|$ values of at least 4 eV·nm are associated roughly with the center of the IRBZ and stretch along the Γ-M line. On the other hand, there are several pronounced band nesting regions, namely along the Γ-K line and between the Γ-M and Γ-K lines. In Fig. 5.17 we present the band structures of 2H-$MoSe_2$ and 2H-MoS_2, which display very similar top valence and bottom conduction bands. These bands are roughly parallel along the Γ-K line and along the Γ-M one in the close proximity of Γ. Once again, the fact that sulfur is lighter than selenium leads to a slightly more dispersive top valence band. Along the Γ-K line, this translates into a stronger resemblance with the bottom conduction above, hence yielding the stronger band nesting region for 2H-MoS$_2$ along the Γ-K line.

Group 3 consists of 1T-HfS$_2$, 1T-HfSe$_2$, 1T-HfTe$_2$, 1T-TiS$_2$, 1T-ZrS$_2$, 1T-ZrSe$_2$, 1T-PtS$_2$ and 1T-NiI$_2$. The first six compounds were also clustered together in the monolayer band nesting analysis of the previous section, proving once again the similarity between the overall features of the monolayer and bulk band structures. All the members of this group have band nesting regions along the Γ-M points and extremely high gradient values $|\nabla_{\boldsymbol{k}}(E_{c1}-E_{v1})|$ in a region between M-K. The latter regions spreads inside the IRBZ and reaches up to 14 eV·nm. We choose to represent here the band structures of 1T-TiS$_2$, 1T-HfS$_2$ and 1T-ZrS$_2$ in Fig. 5.18. Titanium, zirconium and hafnium belong to group 4 and have increasing atom size. As one can see from Fig. 5.18, aside from the increasing band gap going from 1T-TiS$_2$ to 1T-HfS$_2$, the overall features of the band structures are very similar. The top valence and conduction bands are roughly parallel along the Γ-M line and close to Γ on the Γ-K symmetry path. Since the electronegativity decreases from titanium to hafnium, the ionicity of the bond between the metal and the sulfur increases. As a consequence, the top conduction band pertaining to the metal becomes increasingly dispersive going from 1T-TiS$_2$ to 1T-HfS$_2$. This leads 1T-HfS$_2$ to have almost identical slopes along Γ-M in the conduction and valence bands and so, very low gradient values mostly along the entire Γ-M line.

Group 4 is made of 1T-GeI$_2$, 1T-TmI$_2$, 1T-YbI$_2$ and 2H-ZrCl$_2$. The common feature of all these materials is that one of the band nesting regions is invariably located at roughly the same position along the Γ-M line, closer to Γ than to M. The band structures of two of the compounds, namely of 1T-YbI$_2$ and 1T-TmI$_2$ are illustrated in Fig. 5.19. It has been claimed that the valence electrons of compounds containing lanthanide metals are quite inert [185], which could explain the flat bands stemming from the metal in 1T-YbI$_2$ and 1T-TmI$_2$. Their corresponding $|\nabla_{\boldsymbol{k}}(E_{c1}-E_{v1})|$ maps are virtually the same due to the complete lack of dispersion in the top valence bands.

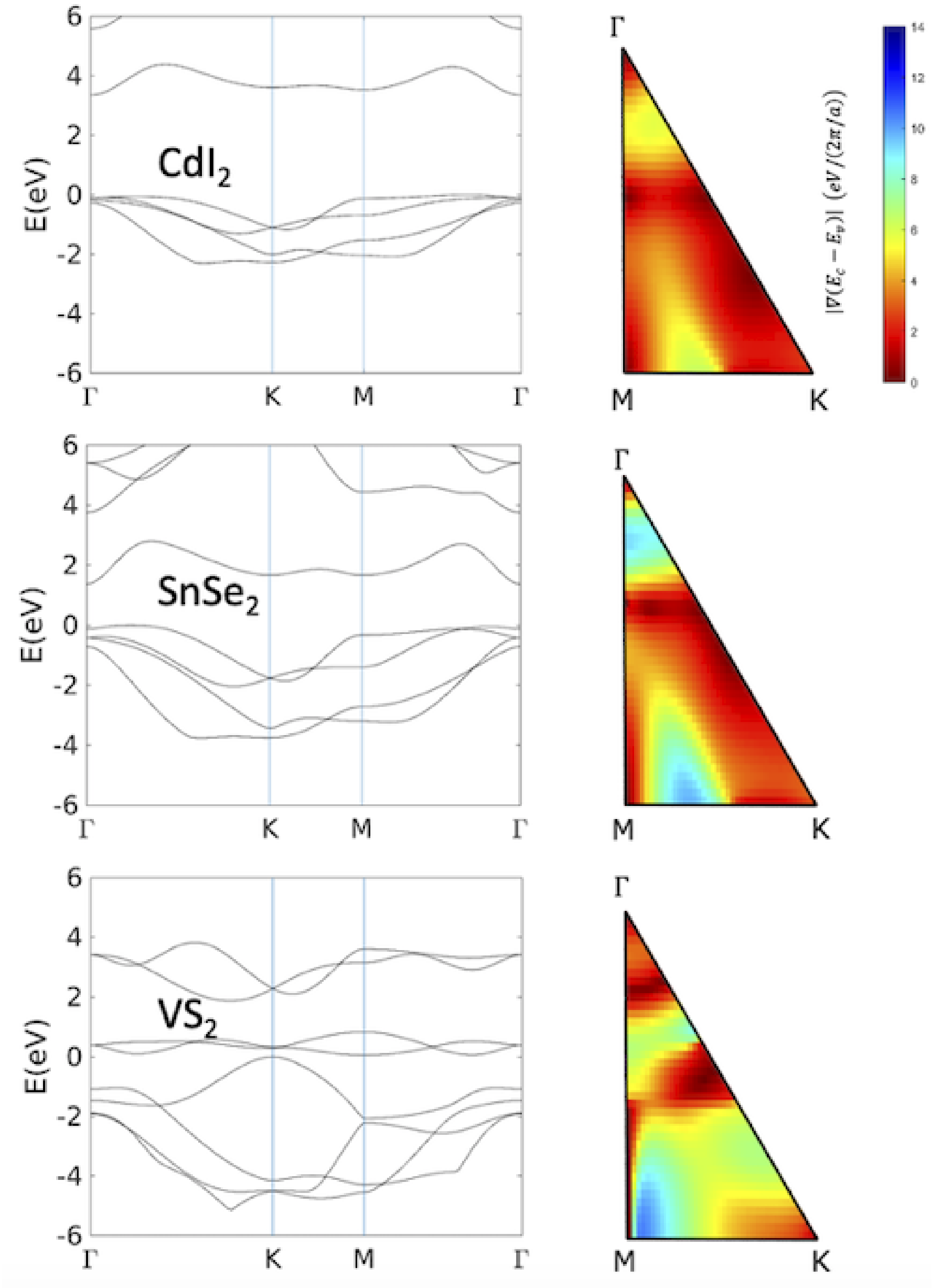

Figure 5.16: Group 1: Band structure of the bulk form of 1T-$\mathrm{CdI_2}$, 1T-$\mathrm{SnSe_2}$ and 1T-$\mathrm{VS_2}$ together with their characteristic $|\nabla_{\boldsymbol{k}}(E_{c1} - E_{v1})|$ map.

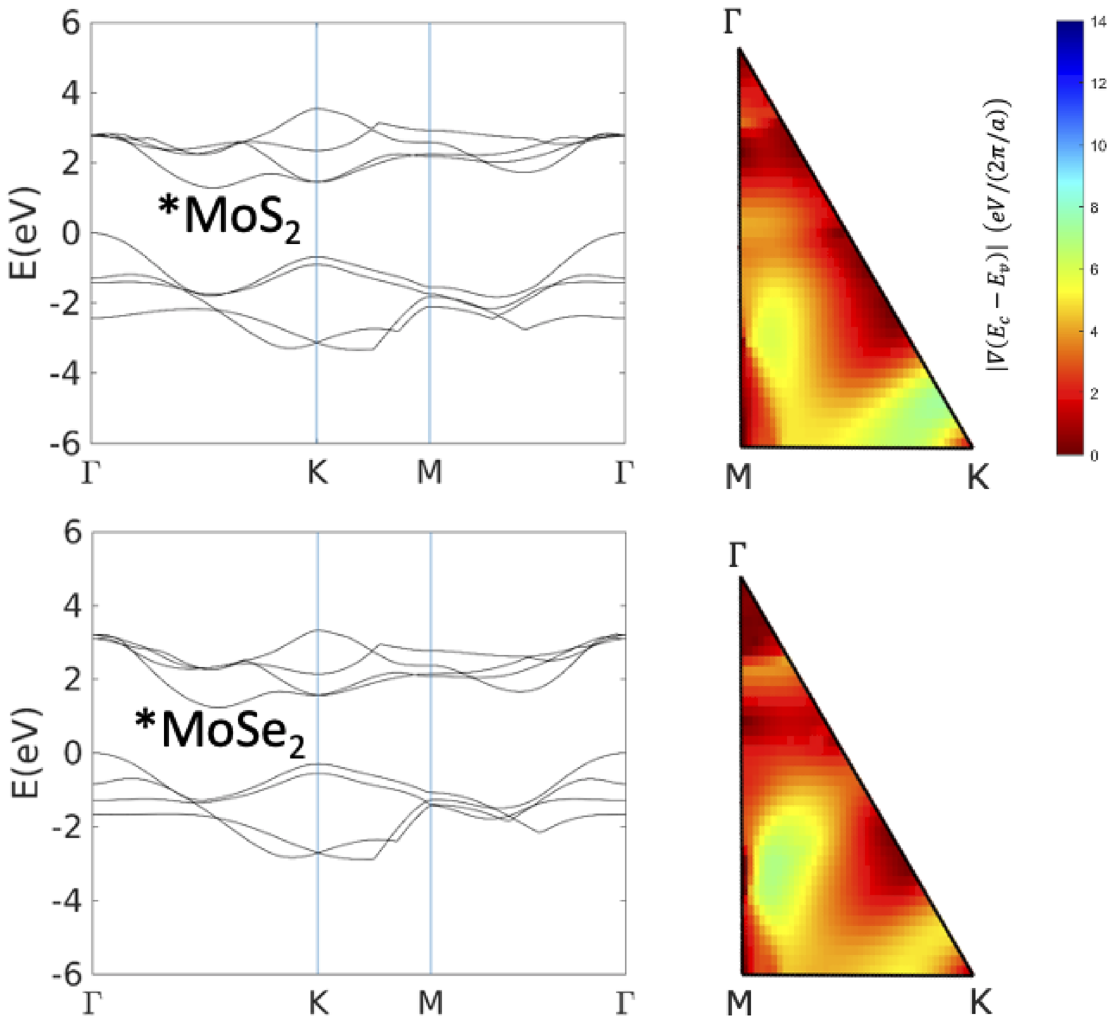

Figure 5.17: Group 2: Band structure of the bulk form of 2H-MoS$_2$ and 2H-MoSe$_2$ together with their characteristic $|\nabla_{\boldsymbol{k}}(E_{c1} - E_{v1})|$ map.

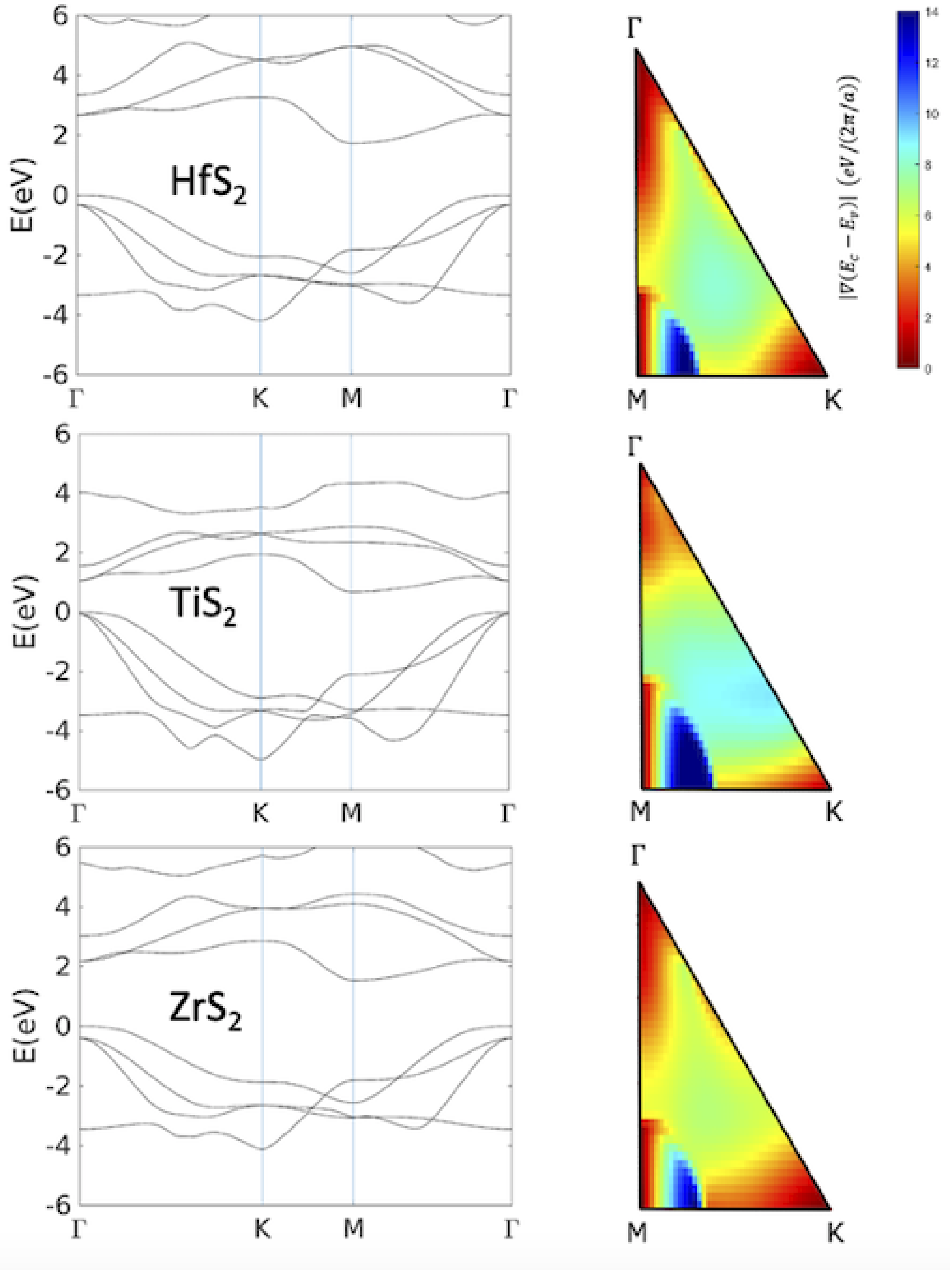

Figure 5.18: Group 3: Band structure of the bulk form of 1T-HfS$_2$, 1T-TiS$_2$ and 1T-ZrS$_2$ together with their characteristic $|\nabla_{\boldsymbol{k}}(E_{c1} - E_{v1})|$ map.

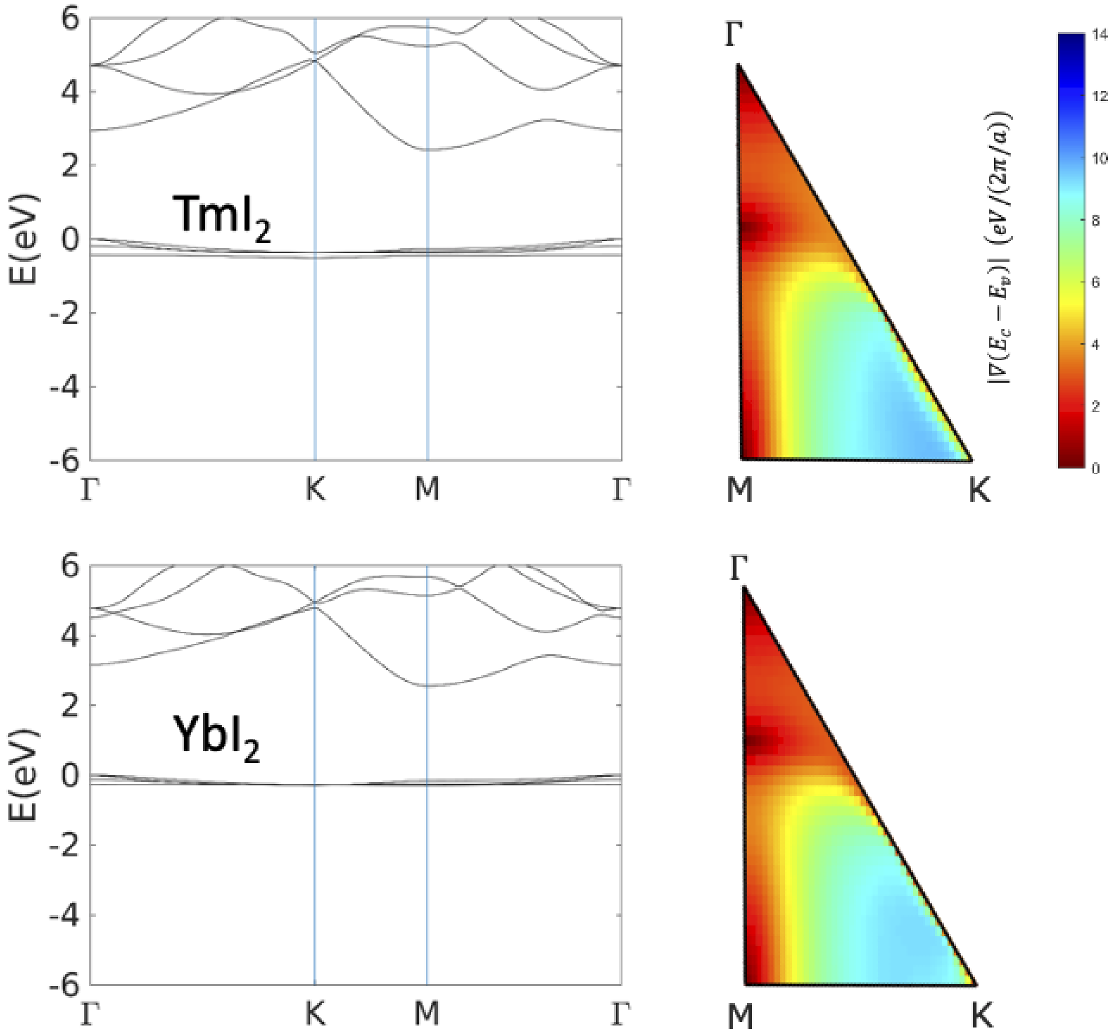

Figure 5.19: Group 4: Band structure of the bulk form of 1T-TmI$_2$ and 1T-YbI$_2$ together with their characteristic $|\nabla_{\boldsymbol{k}}(E_{c1} - E_{v1})|$ map.

We now proceed to cluster these materials in terms of their corresponding $\phi_{sol}(E_{c1} - E_{v1})/|\nabla_{\boldsymbol{k}}(E_{c1} - E_{v1})|$ product, which was also previously implemented for the monolayers. We start again by examining the optimal number of clusters and we find a rather weak minimization of the WCSS/BCSS ratio from three to four clusters. Nevertheless, since the magnitude of $\phi_{sol}(E_{c1} - E_{v1})/|\nabla_{\boldsymbol{k}}(E_{c1} - E_{v1})|$ is in the order of 10^{18} to 10^{22} $\mathrm{s^{-1}m^{-3}eV^{-2}}$, there will be considerably more variation between the corresponding maps over BZ and those of $|\nabla_{\boldsymbol{k}}(E_{c1} - E_{v1})|$. Therefore, we consider it reasonable to settle for a larger WCSS/BCSS ratio of 27% yielded in the case of four clusters. Moreover, by choosing four clusters, the comparison with the previous classification will also be more straightforward.

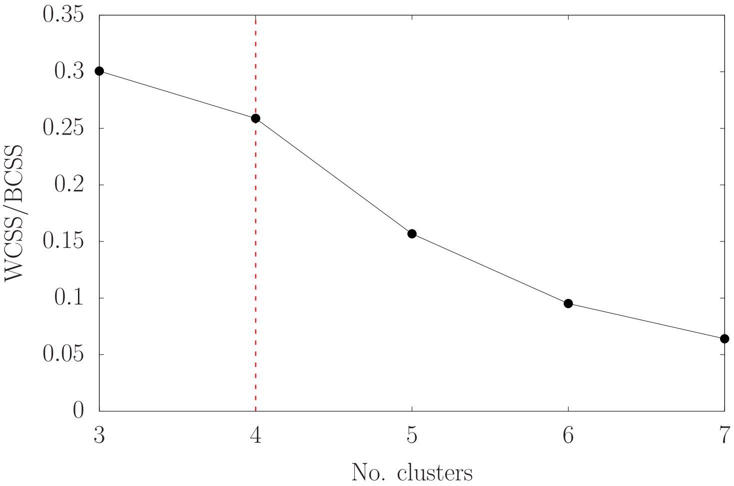

Figure 5.20: The appropriate number of clusters in terms of $\phi_{sol}(E_{c1} - E_{v1})/|\nabla_{\boldsymbol{k}}(E_{c1} - E_{v1})|$ is determined using the elbow method for the bulk TMD and TMH semiconductors.

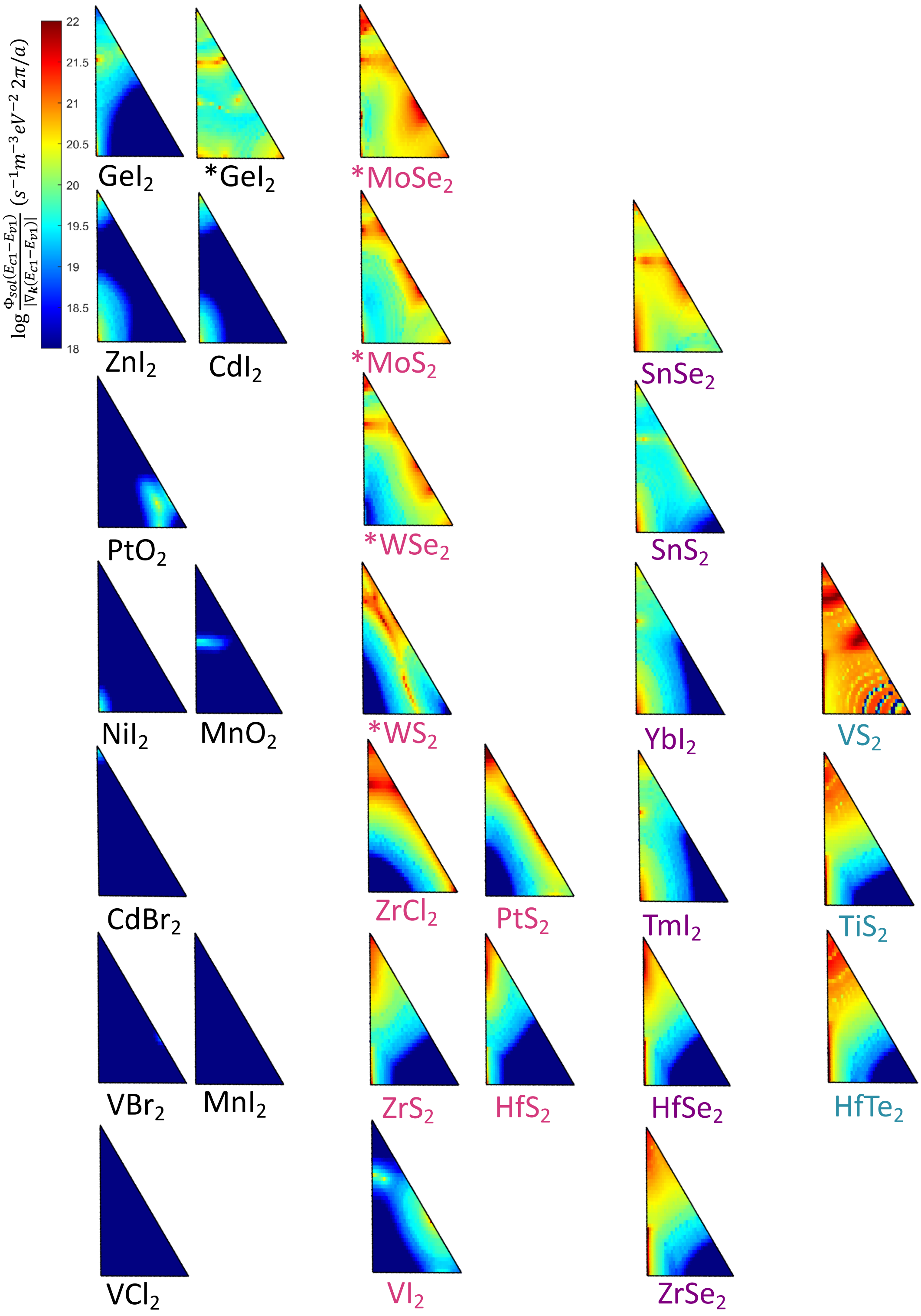

Figure 5.21: $\log[\phi_{sol}(E_{c1}-E_{v1})/|\nabla_{\boldsymbol{k}}(E_{c1}-E_{v1})|]$ mapped on the IRBZ for all the bulk compounds investigated. These illustrate the most defining features of the group they belong to.

Again let us describe the various groups.

Group 1 is composed of 1T-$CdBr_2$, 1T-CdI_2, 1T-GeI_2, 1T-MnI_2, 1T-MnO_2, 1T-NiI_2, 1T-PtO_2, 1T-VBr_2, 1T-VCl_2, 1T-ZnI_2 and 2H-GeI_2. All these materials exhibit very low values of $\phi_{sol}(E_{c1} - E_{v1})/|\nabla_{\boldsymbol{k}}(E_{c1} - E_{v1})|$ due to their large band gaps that exceed 3 eV. 2H-GeI_2 is an exception, since its HSE direct band gap only reaches 2.8 eV. When looking at the previous case, where only the intrinsic band nesting was investigated, 1T-CdI_2, 1T-$CdBr_2$, 1T-MnO_2, 1T-PtO_2 and 1T-ZnI2 exhibited significant band nesting regions between the Γ-K and Γ-M symmetry lines. Once we include the solar flux, the BZ map of $\phi_{sol}(E_{c1} - E_{v1})/|\nabla_{\boldsymbol{k}}(E_{c1} - E_{v1})|$ exhibits no "regions of interest". This can be due to the fact that the energy differences, $E_{c1} - E_{v1}$, exceed 3 eV . However, from Fig. 5.12, it is clear that the solar flux ϕ_{sol} is quite negligible at those energies. Hence group 1 is not appealing since its intrinsic band nesting features cannot be exploited for the absorption of solar radiation.

Group 2 is formed by 1T-HfS_2, 1T-PtS_2, 1T-VI_2, 1T-$ZrCl_2$, 1T-ZrS_2, 2H-MoS_2, 2H-$MoSe_2$, 2H-WS_2 and 2H-WSe_2. This is the most appealing group due to the existence of some "regions of interest". All compounds display large values of $\phi_{sol}(E_{c1} - E_{v1})/|\nabla_{\boldsymbol{k}}(E_{c1} - E_{v1})|$ of the order of 10^{21} $s^{-1}m^{-3}eV^{-2}$ along the Γ-K line with very low values in the M region. 1T-PtS_2, 1T-$ZrCl_2$, 2H-WS_2 and 2H-WSe_2 also exhibit "regions of interest". Once again, molybdenum- and tungsten-based compounds are grouped together due to their similar band structures.

Group 3 is composed of 1T-SnS_2, 1T-TmI_2, 1T-YbI_2, 1T-$SnSe_2$, 1T-$HfSe_2$ and 1T-$ZrSe_2$. The latter three display "regions of interest" along the Γ-M line. These are very narrow, short and mostly localized around M. All the compounds in this group have small values of the order of 10^{18} $^{-1}m^{-3}eV^{-2}$ in the corner of the IRBZ where the K-point is located. 1T-$SnSe_2$ also displays values that are overall around one order of magnitude higher than for the rest of the compounds.

Group 4 consists only of 1T-$HfTe_2$, 1T-TiS_2 and 1T-VS_2. All three compounds are characterized by a gradual increase of $\phi_{sol}(E_{c1} - E_{v1})/|\nabla_{\boldsymbol{k}}(E_{c1} - E_{v1})|$ as one traverses the IRBZ from K to Γ, with "regions of interest" in the proximity of M along the Γ-M line. 1T-VS_2 stands out because of its predominantly high $\phi_{sol}(E_{c1} - E_{v1})/|\nabla_{\boldsymbol{k}}(E_{c1} - E_{v1})|$, reaching values of the order of 10^{22} $s^{-1}m^{-3}eV^{-2}$ also across the Γ-K line and between the Γ-M and Γ-K lines. 1T-VS_2 exhibits also abrupt jumps in $\phi_{sol}(E_{c1} - E_{v1})/|\nabla_{\boldsymbol{k}}(E_{c1} - E_{v1})|$, oscillating between 10^{21} and 10^{18} $^{-1}$m^{-3}eV^{-2} approaching the K-point. A large fraction of the inherent band nesting regions, corresponding to these three compounds that were investigated previously, match with the "regions of interests" discussed here.

In conclusion, the materials that exhibited some match between the 'regions of interest' and those of intrinsic band nesting are 2H-GeI$_2$ from group 1, 1T-ZrCl$_2$, 1T-PtS$_2$, 2H-WS$_2$ and 2H-WSe$_2$ from group 2, 1T-SnSe$_2$, 1T-HfSe$_2$ and 1T-ZrSe$_2$ from group 3 and 1T-HfTe$_2$, 1T-TiS$_2$ and 1T-VS$_2$ from group 4.

5.3 JDOS operationally defined in terms of ε_2

At the beginning of the chapter, in Eq. (5.4), the joint density of states was described in terms of an integral over equal energy surfaces of the gradient difference between the conduction and the valence bands. Gradient values approaching zero define the regions in the Brillouin zone, where there is band nesting and hence high peaks in the imaginary part of the dielectric function. We sought to investigate in detail the band nesting features of 29 monolayers and 29 bulk TMD and TMH compounds and to classify them accordingly. Now we shall attempt to address the second question we raised at the beginning of the chapter. In practice, we shall test the hypothetically linear relation between the joint density of states and the imaginary part of the dielectric function, ε_2. Let us take another look at the expression used to calculate $Im(\varepsilon_{ii})$ in Chapter 2, namely at Eq. (2.76). Under the assumption made at the beginning of this chapter, namely that the momentum matrix elements do not vary significantly in the regions of band nesting and that any off-diagonal contributions in the dielectric tensor vanish, we can then re-write Eq. (2.76) as

$$Im[\varepsilon_{ii}(E)] \approx JDOS(E) \cdot \sum_{c,v,\boldsymbol{k}} |p_{i,c,v,\boldsymbol{k}}|^2 \quad , \tag{5.5}$$

where we define $JDOS(E)$ as

$$JDOS(E) = \frac{8\pi}{\Omega_c \cdot (E+\eta)} \sum_{c,v,\boldsymbol{k}} \frac{\eta}{\varepsilon_{cv}+\eta} \cdot \Big(\frac{1}{[E-\varepsilon_{cv}]^2+\eta^2} + \frac{1}{[E+\varepsilon_{cv}]^2+\eta^2} \Big) \quad , \tag{5.6}$$

with $\varepsilon_{cv} = \varepsilon_{c,\boldsymbol{k}} - \varepsilon_{v,\boldsymbol{k}}$. Another approximation that could, in principle, be made is to postulate that the sum over momentum matrix elements in Eq.(5.5) does not vary significantly across the solar energy range, namely between the direct gap and 4.42 eV. This hypothesis reads

$$\int_{E=E_g}^{E=4.42eV} Im[\varepsilon_{ii}(E)]dE \approx \mu_{ii} \cdot \int_{E=E_g}^{E=4.42eV} JDOS(E)dE \quad , \tag{5.7}$$

where μ_{ii} is a constant. Depending on the Cartesian direction i that defines $p_{i,c,v,\boldsymbol{k}}$, we expect different momentum matrix elements and hence, different scaling factors

μ_{ii}. In the following, we plan to test the extent to which this operational definition holds. So we set μ as the ratio between the two integrals defined in Eq.(5.7). We want to check how much variance there is between the JDOS scaled by μ and the imaginary part of the dielectric function that takes into account the total varying momentum matrix elements contribution. We take the difference at each energy in the energy spectrum considered and we integrate them all. We introduce δ to quantify this variance relative to the imaginary part of the dielectric function,

$$\delta = \int_{E=E_g}^{E=4.42eV} \frac{|Im[\varepsilon_{ii}(E)] - \mu_{ii} \cdot JDOS(E)|}{Im[\varepsilon_{ii}(E)]} dE \quad . \tag{5.8}$$

If δ is close to zero, one can conclude that the momentum matrix elements are not quite energy dependent and that their entire spectrum contribution could be replaced by the constant μ. This would imply that JDOS is accurate in capturing the behaviour of the imaginary part of the dielectric function. We employ the HSE band structure calculations done on a dense k-grid of 43x44x1 points, the same used to calculate $|\nabla_{\boldsymbol{k}}(E_{c1} - E_{v1})|$ in the previous section. We use it to calculate JDOS(E) according to Eq.(5.6), where we consider the first four conduction and the last four valence bands, respectively. We then integrate these contributions up over the energy range defined in Eq.(5.7). The HSE dielectric function was initially calculated on a dense k-grid of 40x40x1 points for six compounds, namely for the monolayers 2H-MoS$_2$, 2H-WS$_2$, 1T-PtS$_2$, 1T-HfS$_2$, 1T-ZrS$_2$ and 1T-TiS$_2$. For both this initial dielectric function calculation and for that of the JDOS, we set the Lorentzian broadening, η, to 0.025 eV. The dielectric function calculation was subsequently repeated for all the monolayers on a coarser k-grid of 20x20x1 k-points and with a larger broadening of 0.1 eV. We will compare both sets of dielectric function calculations against the JDOS, which is kept fixed.

In Tables 5.1 and 5.2 we present the μ obtained for the xx component of the dielectric function and the associated error δ. One first observation is that using a coarser k-mesh does not alter by more than 10% the value of μ. Let us take a look and see how the imaginary part of the xx component of the dielectric function, obtained with two distinct sets of k-meshes and broadening values compare to the JDOS. In Fig. 5.22, the three spectra are illustrated for 6 TMDs. Also note that the dielectric

Compound	μ_{xx}	δ
2H-WS_2	1.47	0.67
1T-HfS_2	1.14	0.44
1T-PtS_2	1.05	0.30
2H-MoS_2	0.90	0.82
1T-ZrS_2	0.84	0.44
1T-TiS_2	0.45	0.88

Table 5.1: μ_{xx} and δ for $Im(\varepsilon_{xx})$ calculated with 40x40x1 k-points and with η=0.025 eV.

Compound	μ_{xx}	δ
2H-WS_2	1.39	0.97
1T-HfS_2	1.05	0.35
1T-PtS_2	0.93	0.29
2H-MoS_2	0.86	1.00
1T-ZrS_2	0.77	0.44
1T-TiS_2	0.43	0.72

Table 5.2: μ_{xx} and δ for $Im(\varepsilon_{xx})$ calculated with 20x20x1 k-points and with η=0.1 eV.

function spectra have been scaled by a factor of $1/\mu$ in order be fully comparable to the JDOS. Employing a denser k-mesh with a small broadening of 0.025 eV yields two notable features in the dielectric function. On the one hand, the 2H polymorphs capture quite exactly the peaks in the JDOS, namely that at 3.5 eV for 2H-WS_2 and the one at 4.0 eV for 2H-MoS_2. For both compounds, the broader spectrum does not capture the individual peaks as they get smeared out into a wide peak, only exhibiting a faint shoulder. The dielectric function obtained with the denser k-mesh and smaller broadening is very accurate in describing the JDOS from 3.5 eV till about 4.0 eV. We thus speculate that the contribution of the momentum matrix elements to the dielectric function is to a large extent constant, namely that it is roughly equivalent to a constant scaling factor in the range 3.5 eV-4.0 eV. Analyzing the momentum matrix elements is still required to confirm this. Moreover, even when considering the entire energy range defined from the band gap to 4.4 eV, the error between the scaled JDOS and the imaginary part of the dielectric function is still smaller for the spectrum obtained with a narrower broadening and denser k-mesh. This can be noted from the values of δ reported in tables 5.1 and 5.2, namely 0.67 and 0.97 for 2H-WS_2 and 0.82 and 1.00 for 2H-MoS_2, respectively. On the other hand, for the 1T polymorphs, the broader and coarser spectra of the dielectric functions lead to slightly smaller values of δ. This is due to the fact that the peaks in the scaled JDOS are closer in amplitude to the coarser dielectric function spectra. Hence, the fluctuation in the momentum matrix elements might be higher for 1T than for 2H polytypes. This explains the disparity in amplitude between the highly accentuated noisy peaks of Im(ϵ_{xx}) calculated with 40x40x1 k-points and broadening η =0.025 eV and the broader and less strongly peaked JDOS obtained from the band structure calculated on a grid of 44x43x1 k-points and broadening η =0.025 eV.

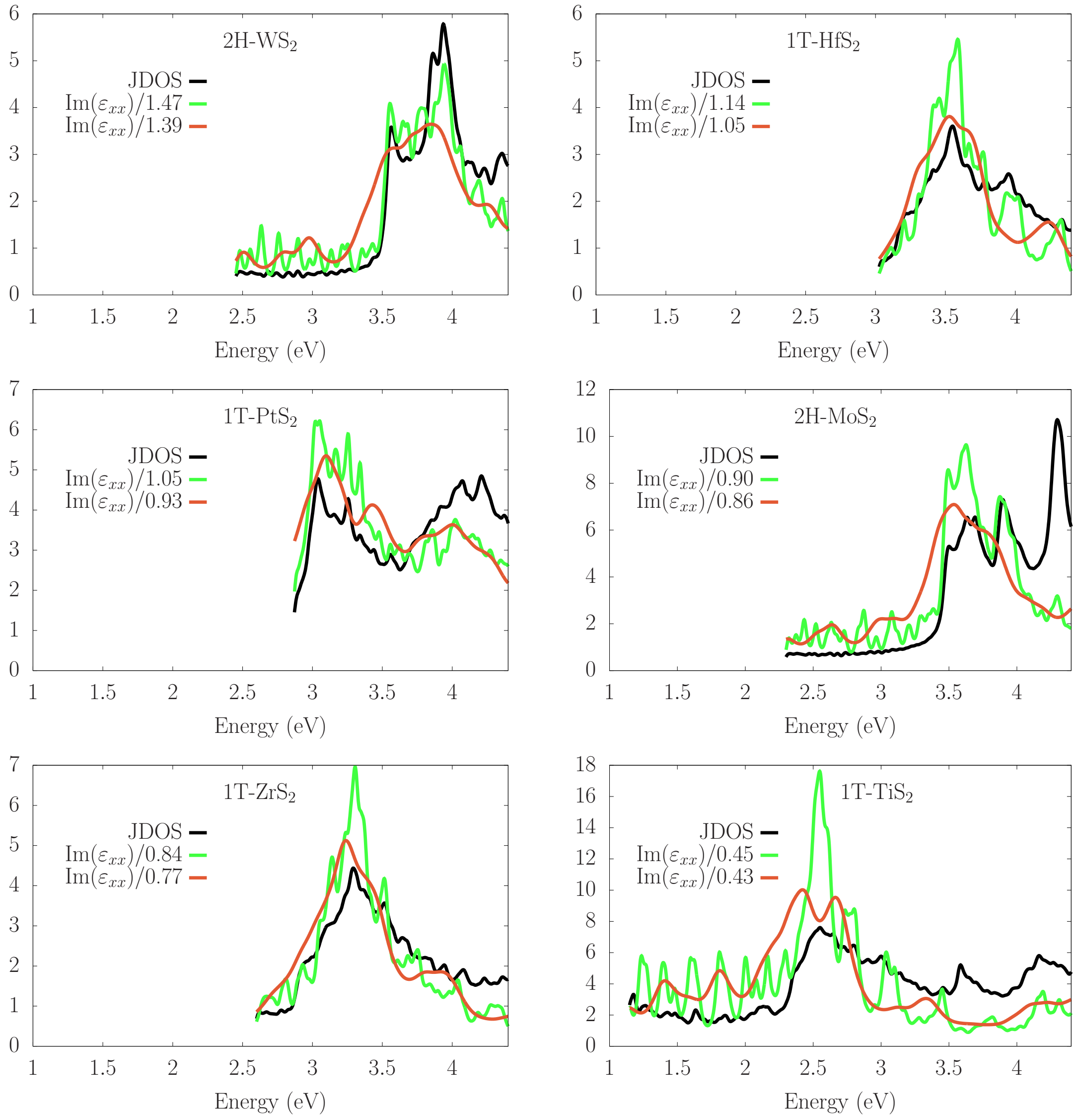

Figure 5.22: The joint density of states (black line) calculated on a dense k-mesh of 44x43x1 k-points and with a Lorentzian broadening $\eta = 0.025$ eV, the xx component of imaginary part of the dielectric function calculated on a dense k-mesh of 40x40x1 k-points and with a Lorentzian broadening $\eta = 0.025$ eV (green line) and on a coarse k-mesh of 20x20x1 k-points and with a Lorentzian broadening $\eta = 0.1$ eV (red line). The latter two quantities were divided by the corresponding scaling factor μ_{xx}.

We repeat the procedure for determining μ for the zz component of the imaginary part of the dielectric function. We expect the first two diagonal entries of the dielectric tensor, namely ε_{xx} and ε_{yy}, to be identical due to the in-plane isotropy of the 2D TMD and TMH compounds. Also, the obtained μ values are up to two orders of magnitude lower in the case of the zz-component compared to the xx one.

In fact, the momentum matrix elements are expected to be smaller in the out of plane direction. Also, the two dielectric function spectra obtained with different k-meshes and spectral broadening lead to roughly the same values of μ. By looking at Fig. 5.23, it becomes apparent that in the case of the 2H polymorphs, the roughly constant spectra ranging from the direct gap to about 3.5 eV is captured well by the constant JDOS. However, none of the higher energy peaks in the zz-dielectric spectra are equal in amplitude to the scaled JDOS. This suggests that an overall scaling factor cannot accurately substitute the momentum matrix elements along the zz direction for the entire considered energy interval. For the 1T polymorphs, we compare the amplitudes of the three sets of spectra. We observe that overall, the dielectric spectra with a coarser k-grid and larger broadening are closer in amplitude to the scaled JDOS. However, in the case of 1T-ZrS$_2$ and 1T-HfS$_2$ the dielectric spectra with a denser k-grid and narrower broadening preserves the general profile of the JDOS, displaying only some oscillations around the scaled JDOS. This translates into the small δ values computed for these compounds (Table 5.3), thus rendering the momentum matrix elements in the z direction slightly less fluctuating than for the 2H polymorphs.

Compound	μ_{zz}	δ
2H-WS$_2$	0.02	2.06
1T-HfS$_2$	0.23	0.35
1T-PtS$_2$	0.32	0.32
2H-MoS$_2$	0.03	3.03
1T-ZrS$_2$	0.21	0.71
1T-TiS$_2$	0.09	8.00

Table 5.3: μ_{zz} and δ for $Im(\varepsilon_{zz})$ calculated with 40x40x1 k-points and with η=0.025 eV.

Compound	μ_{zz}	δ
2H-WS$_2$	0.04	0.62
1T-HfS$_2$	0.23	0.13
1T-PtS$_2$	0.29	0.26
2H-MoS$_2$	0.04	0.60
1T-ZrS$_2$	0.21	0.20
1T-TiS$_2$	0.09	2.32

Table 5.4: μ_{zz} and δ for $Im(\varepsilon_{zz})$ calculated with 20x20x1 k-points and with η=0.1 eV.

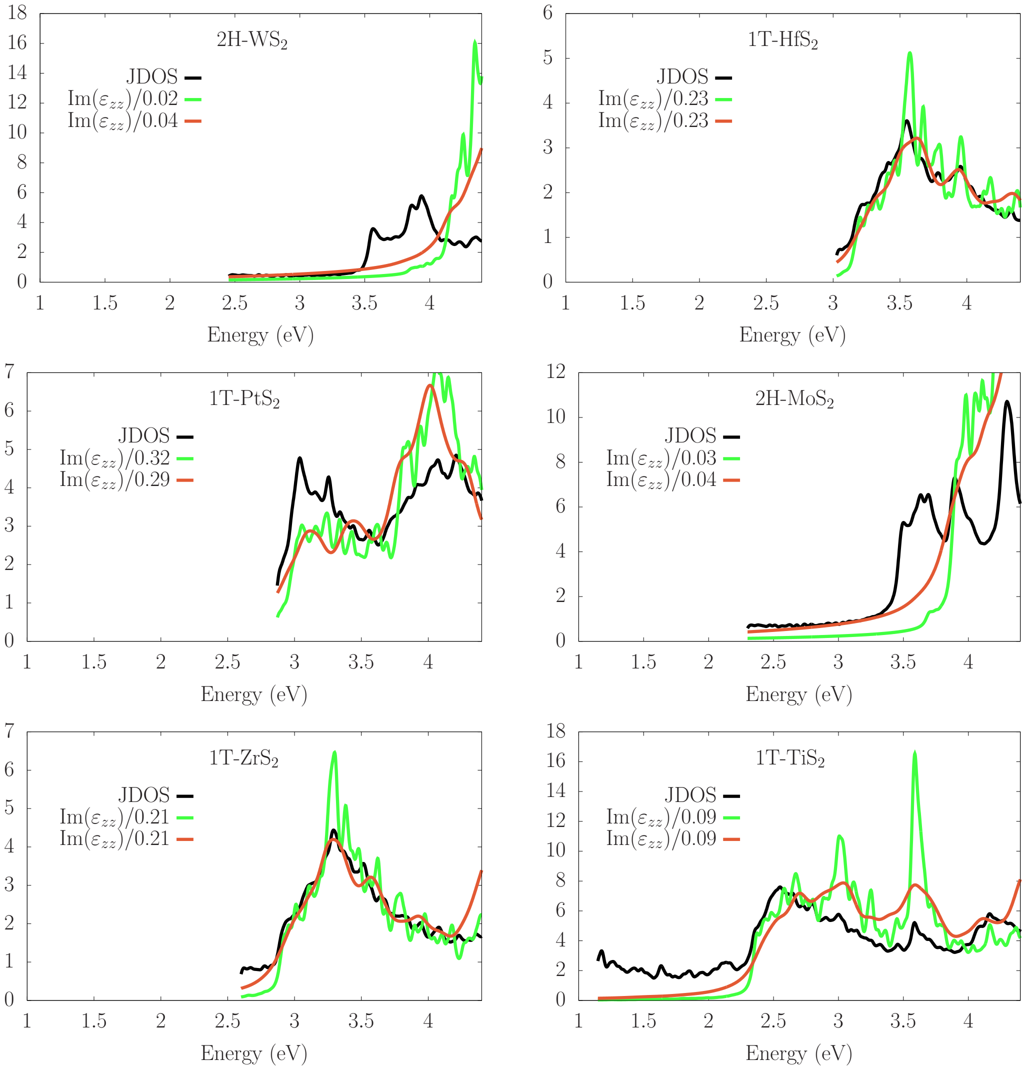

Figure 5.23: The joint density of states (black line) calculated on a dense k-mesh of 44x43x1 k-points and with a Lorentzian broadening $\eta = 0.025$ eV, the zz component of imaginary part of the dielectric function calculated on a dense k-mesh of 40x40x1 k-points and with a Lorentzian broadening $\eta = 0.025$ eV (green line) and on a coarse k-mesh of 20x20x1 k-points and with a Lorentzian broadening $\eta = 0.1$ eV (red line). The latter two were divided by the corresponding scaling factor μ_{zz}.

In order to test our speculation regarding the behaviour of the momentum matrix elements, we proceed to calculating them for 2H-WS$_2$ and 1T-ZrS$_2$ on a dense k-mesh of 400 points for 26 bands. For this purpose, we use VASP which enables technically straightforward access to the momentum matrix elements that are expected to be qualitatively comparable to those calculated through FHI-AIMS. Also, the Kohn-Sham single particle eigenstates needed to calculate the momentum matrix elements are obtained using PBE since such a calculation requires significantly less computational resources than an HSE-based one. Despite the known underestimation of the band gap, the PBE band structure is expected to display a similar curvature to the HSE one. Thus, we believe that the momentum matrix elements presented in Fig. 5.24 can offer a qualitative understanding of the HSE ones. For simplicity, we choose to plot the absolute value of the momentum matrix elements, namely $|\langle\psi_{c,\boldsymbol{k}}| - i\hbar\nabla_{\boldsymbol{k}} |\psi_{v,\boldsymbol{k}}\rangle|$ with $\hbar$ in atomic units. Fig. 5.24a) illustrates the momentrum matrix elements associated with the valence and conduction bands whose energy differences match the range of the solar spectrum, namely from approximately 0.3 eV to 4.4 eV. Each represented element is obtained by summing up over the contributing k-points. It can be seen that the 2H-WS$_2$ compound has a much smaller variance than 1T-ZrS$_2$. In other words, there is a larger fraction of semi-constant 2H-WS$_2$ momentum matrix elements spanning the transition energy range relative to 1T-ZrS$_2$, which clearly exhibits a more significant spread across the range. Fig. 5.24b)-g) displays $\langle\psi_{c,\boldsymbol{k}}| - i\hbar\nabla_{\boldsymbol{k}} |\psi_{v,\boldsymbol{k}}\rangle|$ mapped on a k-mesh for three selected optical transition energies in the first half of the solar spectrum, namely E=2.0, E=2.1 and E=2.2 eV. We chose these close transition values in order to observe the gradual changes across the k-mesh, which is represented in fractional coordinates along the x and y direction. The colored boxes indicate the value of $\langle\psi_{c,\boldsymbol{k}}| - i\hbar\nabla_{\boldsymbol{k}} |\psi_{v,\boldsymbol{k}}\rangle|$ associated with each contributing k-point for each selected energy transition. The outline of the irreducible Brillouin zone was included for reference in the k-mesh. We notice a larger variation across the k-mesh for 1T-ZrS$_2$ than for 2H-WS$_2$ at each chosen energy but also between meshes corresponding to different energies. Hence, this seems to indicate that the momentum matrix elements of 2H-WS$_2$ are significantly less varying with energy transition and also across the k-mesh. Due to the similar electronic structure of 2H-MoS$_2$ and 2H-WS$_2$, we infer that our initial speculation

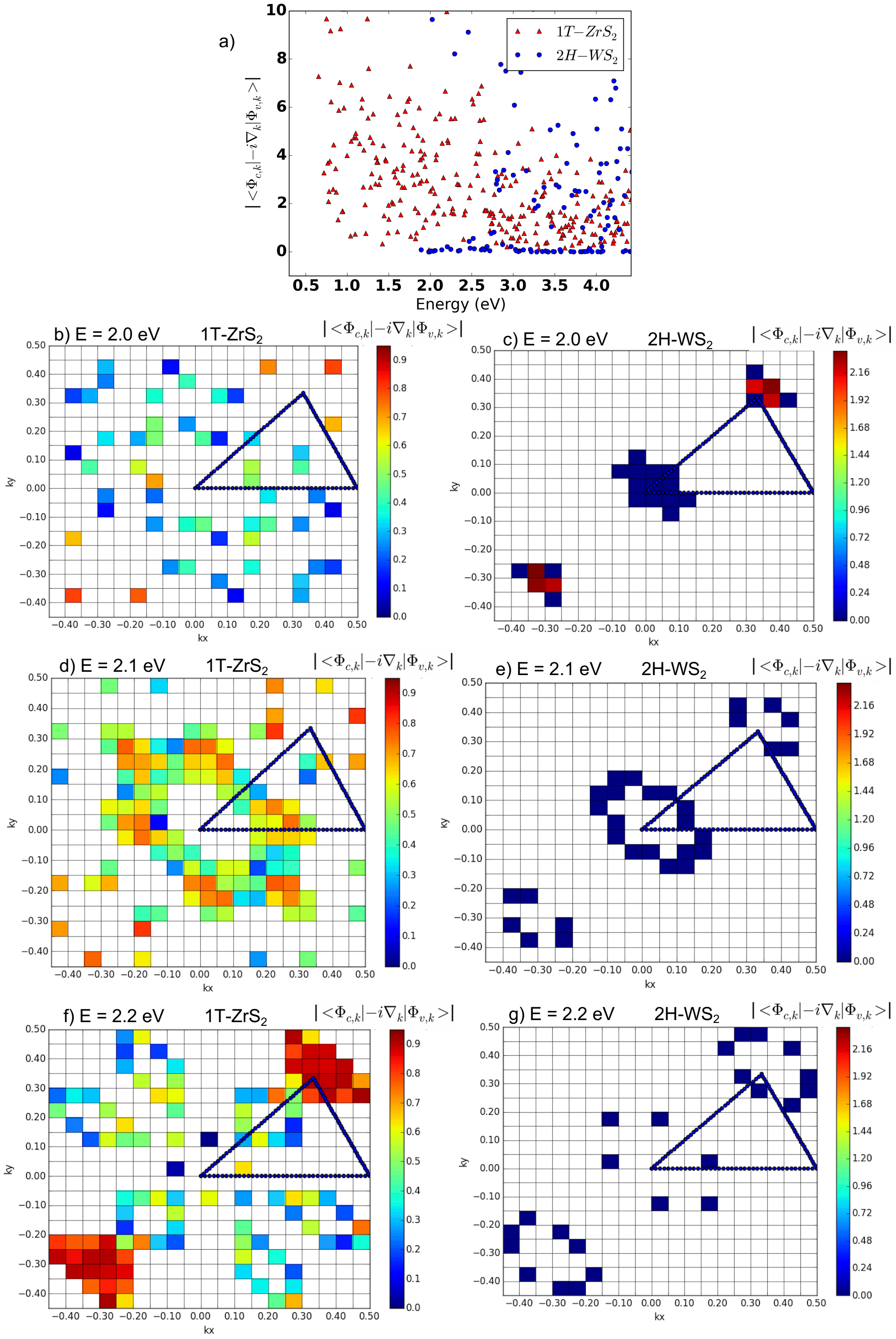

Figure 5.24: Absolute value of PBE momentum matrix elements a) for 2H-WS$_2$ (blue circles) and 1T-ZrS$_2$ (red triangles) represented along the solar energy range, *i.e.* from 0.3 eV to 4.4 eV and b)-g) mapped on the k-mesh of 1T-ZrS$_2$ and 2H-WS$_2$ for transition energies E=2.0 eV, E=2.1 eV and E=2.2 eV. The blue dots outline the irreducible Brillouin zone.

is indeed justified, namely that approximating the momentum matrix element by a global scaling factor μ is better suited for 2H polymorphs than for 1T ones.

In Fig. 5.25 we investigate the partial density of states of 2H-WS$_2$ and 1T-ZrS$_2$. The Fermi energy has been fixed at 0 eV. We notice that both the conduction and valence edge states of 2H-WS$_2$ are predominantly d states that originate from tungsten. In the case of 1T-ZrS$_2$, the entire valence manifold stems from the p orbitals of sulfur while the conduction manifold pertains to the d orbitals of zirconium. Thus, as opposed to 1T-ZrS$_2$, 2H-WS$_2$ is characterized by the same orbital character in conduction and valence states separated by energies between 2.4 and 4 eV. This might roughly explain why the momentum matrix elements of 2H-WS$_2$ corresponding to transitions equal to the band gap energy and up to 1.5 eV larger are less varying than those of 1T-ZrS$_2$. Also, the change in the dominant orbital character (from d- to p-like) at energies lower than -2.5 eV for 2H-WS$_2$ might explain the larger variation in the momentum matrix elements at E>4 eV and hence, the poor match between the JDOS and the scaled Im(ε_{xx}) at energies larger than 4 eV.

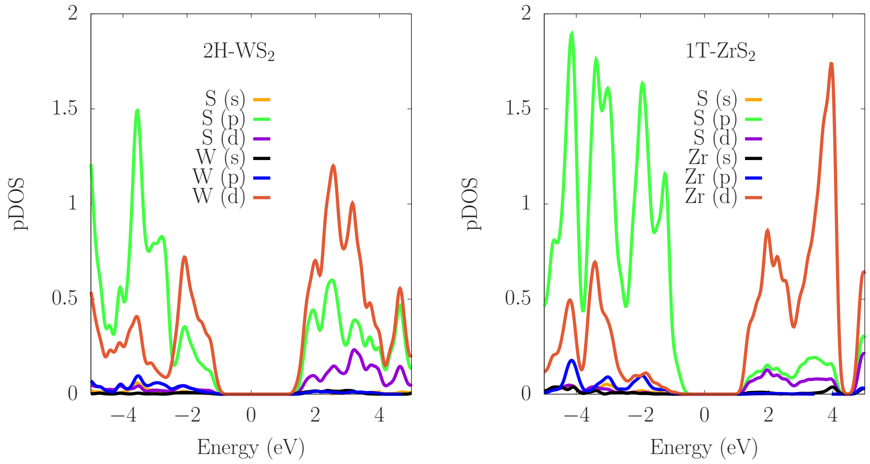

Figure 5.25: Partial density of states (pDOS) of 2H-WS$_2$ (right) and 1T-ZrS$_2$ (left) depicting the contribution of s, p, d orbitals coming from the TM and sulfur, respectively.

5.3.1 JDOS - a descriptor for ranking compounds

In the light of our previous section, we would now like to test the newly obtained sets of scaled JDOS and see whether it can be used as an accurate descriptor for the imaginary part of the dielectric function over the entire solar spectrum. In order to account for the inhomogeneity of the solar flux, we perform a numerical integration of the imaginary dielectric function multiplied by the solar flux ϕ_{sol}(E) over the energy range defined by the direct band gap energy and the uppermost solar radiation energy, namely 4.42 eV. We shall then compare this integral with the analogous one where the joint density of states spectrum is multiplied by ϕ_{sol}. These pairs of integrals will be sorted in descending order in order to check to what extent the ranking of one integral is preserved in the ranking of the other integral. Hence, the two studied quantities are

$$I_{\varepsilon_{ii}} = \int_{E=E_g}^{E=4.42eV} Im[\varepsilon_{ii}(E)] \cdot \phi_{sol}(E) dE \quad , \tag{5.9}$$

$$I_{JDOS} = \int_{E=E_g}^{E=4.42eV} \mu_{ii} \cdot JDOS(E) \cdot \phi_{sol}(E) dE \quad . \tag{5.10}$$

The subscripts ii denote the component of the dielectric function and consequently, of the scaling factor μ, for which we calculate the integrals. We choose to present here only the xx component. The dielectric functions calculations with a coarser k-grid of 20x20x1 k-points and a Lorentzian broadening of 0.1 eV were used for these integrations, since they were done for the entire set consisting of the 29 2D semiconducting monolayers. Firstly, by looking at Table 5.5, we note that the 29 compounds mostly occupy the same position in the two rank categories. The highest deviation is recorded by 2H-HfTe$_2$, occupying position number 8 in the rank based on $I_{\varepsilon_{xx}}$ and no. 4 in the rank based on I_{JDOS}. Since the band gap is 1.44 eV, the intense solar flux at that energy amplifies the inherent discrepancy between JDOS and Im(ε), caused by the omission of potentially highly contributing momentum matrix elements at the band edge. The first ten compounds with the highest values of $I_{\varepsilon_{xx}}$ and I_{JDOS} feature the lowest direct band gaps, none of which exceeds 2 eV. This has to be expected since the solar spectrum peaks between 0.7 and 1.3 eV. The next ten compounds have larger band gaps, ranging between 2 and 2.7 eV, which explains their relatively lower integral values. The last nine compounds can be split in two types: one containing materials with very large band gaps , namely exceeding 3.2 eV, thus overlapping with a very weak section of the solar spectrum; the other with compounds having direct gaps between 2.8 and 3.0 eV. These exhibit very low JDOS due to their predominantly flat valence bands. This is the case, for instance, of 1T-YbI_2.

Compound	$\text{I}_{\varepsilon_{xx}}(\text{s}^{-1}\text{m}^{-2})$	Rank $\text{I}_{\varepsilon_{xx}}$	μ_{xx}	$\text{I}_{JDOS}(\text{s}^{-1}\text{m}^{-2})$	Rank $\text{I}_{JDOS}(\text{s}^{-1}\text{m}^{-2})$
1T-PdTe_2	$1.84\cdot10^{22}$	1	1.02	$1.41\cdot10^{22}$	1
1T-HfTe_2	$9.85\cdot10^{21}$	2	0.85	$5.38\cdot10^{21}$	3
1T-PtTe_2	$8.03\cdot10^{22}$	3	1.24	$5.96\cdot10^{21}$	2
1T-TiS_2	$4.94\cdot10^{21}$	4	0.43	$3.26\cdot10^{21}$	7
1T-PtSe_2	$4.39\cdot10^{21}$	5	1.76	$3.38\cdot10^{21}$	6
2H-MoTe_2	$4.22\cdot10^{21}$	6	0.65	$3.61\cdot10^{21}$	5
2H-WTe_2	$3.52\cdot10^{21}$	7	0.81	$2.37\cdot10^{21}$	8
2H-HfTe_2	$3.23\cdot10^{21}$	8	0.38	$3.74\cdot10^{21}$	4
1T-ZrSe_2	$2.96\cdot10^{21}$	9	0.68	$1.70\cdot10^{21}$	10
1T-OTl_2	$2.61\cdot10^{21}$	10	1.19	$1.91\cdot10^{21}$	9
2H-ZrCl_2	$1.98\cdot10^{21}$	11	0.85	$1.54\cdot10^{21}$	12
2H-MoSe_2	$1.75\cdot10^{21}$	12	0.72	$1.04\cdot10^{21}$	13
1T-HfSe_2	$1.67\cdot10^{21}$	13	0.91	$9.84\cdot10^{20}$	14
2H-WSe_2	$1.19\cdot10^{21}$	14	0.93	$5.79\cdot10^{20}$	16
2H-MoS_2	$9.58\cdot10^{20}$	15	0.86	$5.02\cdot10^{20}$	18
1T-STl_2	$7.58\cdot10^{20}$	16	1.64	$7.26\cdot10^{20}$	15
1T-PtS_2	$6.31\cdot10^{20}$	17	0.93	$5.03\cdot10^{20}$	17
2H-WS_2	$6.19\cdot10^{20}$	18	1.39	$3.81\cdot10^{20}$	20
1T-SnSe_2	$5.92\cdot10^{20}$	19	0.83	$1.59\cdot10^{21}$	11
1T-ZrS_2	$5.60\cdot10^{20}$	20	0.77	$4.45\cdot10^{20}$	19
1T-HfS_2	$2.48\cdot10^{20}$	21	1.05	$2.08\cdot10^{20}$	21
2H-GeI_2	$1.45\cdot10^{20}$	22	0.96	$1.12\cdot10^{20}$	23
1T-GeI_2	$1.14\cdot10^{20}$	23	2.90	$1.37\cdot10^{20}$	22
1T-SnS_2	$4.69\cdot10^{19}$	24	0.38	$8.38\cdot10^{19}$	24
1T-YbI_2	$3.95\cdot10^{19}$	25	0.09	$2.85\cdot10^{19}$	25
1T-PbI_2	$1.01\cdot10^{19}$	26	3.09	$1.74\cdot10^{19}$	26
1T-ZnI_2	$7.67\cdot10^{18}$	27	0.49	$1.55\cdot10^{19}$	27
1T-CdI_2	$2.28\cdot10^{18}$	28	0.50	$3.77\cdot10^{18}$	28
1T-PtO_2	$1.33\cdot10^{17}$	29	0.32	$9.17\cdot10^{16}$	29

Table 5.5: Integrals of the xx component of the imaginary part of the dielectric function and of the JDOS scaled by μ_{xx}, and multiplied by the solar flux. The ranking is conceived in descending order. See definition in Eqs.(5.9) and (5.10).

So far we based our endeavor on the strong assumption conveyed by Eq.(5.7), namely that the imaginary part of the dielectric function integrated over the solar spectrum energy range can be approximated as the integral of the joint density of states scaled by a constant factor. This can be thought of as a constant momentum matrix element squared. It was shown that the approximation allows us to rank the compounds based on the overlap between the solar flux and $Im(\varepsilon_{xx})$. Another exercise worth trying now is to calculate the absorption coefficient to further test the robustness of this approximation. This will be based on the following method: let us introduce a quantity λ, which is equivalent to the dielectric function ε with the sole distinction that its momentum matrix elements are fully constant. Since ε=$Re(\varepsilon_{ii})$+$i\cdot$ $Im(\varepsilon_{ii})$, we analogously write λ=JDOS$_1^{ii}$+i$\cdot$JDOS$_2^{ii}$, where:

$$JDOS_2^{ii}(E) = \mu_{ii} \cdot JDOS(E) \quad , \tag{5.11}$$

and JDOS$_1^{ii}$ and JDOS$_2^{ii}$ are related through the Kramers-Kronig relation:

$$JDOS_1^{ii}(E') = \int_{-\infty}^{\infty} \frac{JDOS_2^{ii}(E)}{E - E'} dE \quad . \tag{5.12}$$

We will discuss in the Appendix how this integration was implemented numerically. Now we will employ the xx and zz components of the real and imaginary parts of the dielectric function to compute the absorption coefficients along the x and z direction, *i.e.* α_{xx} and α_{zz}, respectively, through the expression:

$$\alpha_{ii} = \frac{\omega \cdot Im(\varepsilon_{ii})}{c \cdot \sqrt{\frac{Re(\varepsilon_{ii}) + \sqrt{Re(\varepsilon_{ii})^2 + Im(\varepsilon_{ii})^2}}{2}}} \quad . \tag{5.13}$$

Moreover, we plan to construct the absorption coefficient by using λ instead of ε, namely we will substitute $Im(\varepsilon_{ii})$ with JDOS$_2^{ii}$ and $Re(\varepsilon_{ii})$ with JDOS$_1^{ii}$, respectively.

In Fig. 5.26, we illustrate all these quantities where $ii = xx$ for 2H-WS$_2$ plotted from the direct band gap up to 4.42 eV. In this case, μ_{xx}=1.39. The JDOS$_1^{xx}$ in the right plot is significantly higher in amplitude than $Re(\varepsilon_{xx})$. The JDOS and the dielectric function were calculated with spectra having a Lorentzian broadening of 0.025 eV and 0.1 eV, respectively, as mentioned previously. Hence, JDOS$_1^{xx}$ exhibits clearly defined peaks that match in position with the more smeared out peaks of $Re(\varepsilon_{xx})$ at approximately 3.4 and 3.8 eV, respectively. Interestingly, the absorption coefficient $\alpha^{\varepsilon}_{xx}$ calculated using $Im(\varepsilon_{xx})$ and $Re(\varepsilon_{xx})$ exceeds in amplitude the absorption coefficient α^{λ}_{xx} obtained using JDOS^{xx}_{1} and JDOS^{xx}_{2}. This is probably due to the larger denominator in Eq.(5.13) in the case of α^{λ}_{xx}.

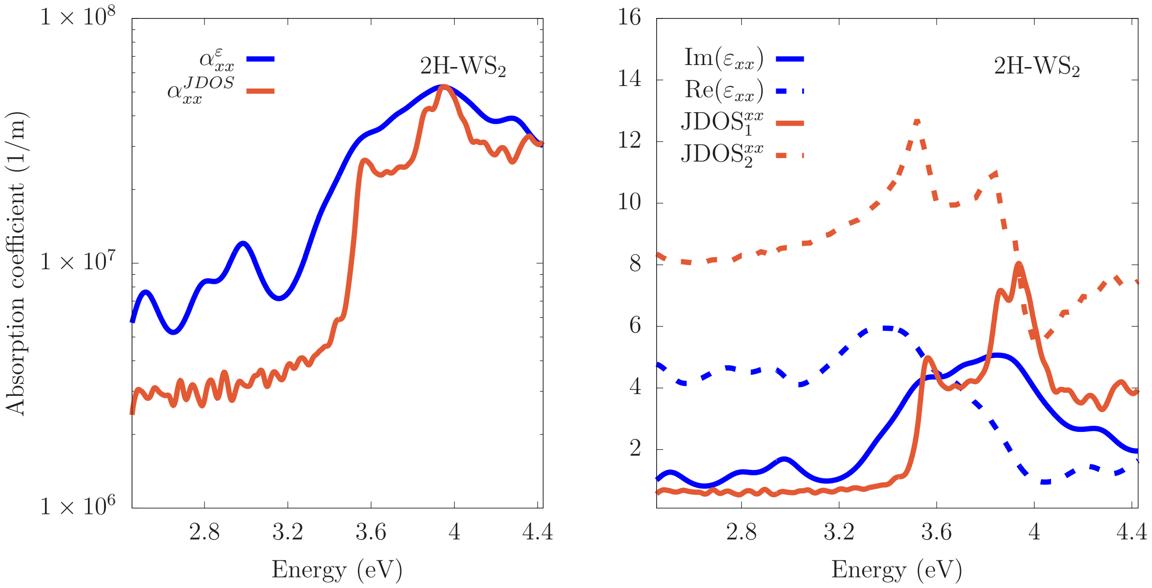

Figure 5.26: Left panel: The absorption coefficient $\alpha^{\varepsilon}_{xx}$ obtained with $Re(\varepsilon_{xx})$ and $Im(\varepsilon_{xx})$ together with the absorption coefficient α^{λ}_{xx} calculated with JDOS^{xx}_{1} and JDOS^{xx}_{2}. Right panel: $Re(\varepsilon_{xx})$ and $Im(\varepsilon_{xx})$, the JDOS scaled by μ_{xx} and JDOS^{1}_{xx}. For 2H-WS$_2$, μ_{xx}=1.39

In Tables 5.6 and 5.7 we look at the integrated absorption coefficients, $\alpha^{\varepsilon}_{ii}$ and α^{λ}_{ii}, over the energy defined by the direct band gap and the solar spectrum maximum energy of 4.42 eV:

$$I^{\varepsilon}_{\alpha_{ii}} = \int_{E=E_g}^{E=4.42eV} \alpha^{\varepsilon}_{ii}(E)dE \quad , \tag{5.14}$$

and

$$I^{\lambda}_{\alpha_{ii}} = \int_{E=E_g}^{E=4.42eV} \alpha^{\lambda}_{ii}(E)dE \quad . \tag{5.15}$$

Once again, we shall rank the materials from highest to lowest values according to these integrals. The main observation that we derive is that the ordering of the compounds is not preserved for the xx component, although it is fully preserved for the zz one. This is a surprising takeaway message and we do not fully understand why the discrepancy between $I^{\varepsilon}_{\alpha_{ii}}$ and $I^{\lambda}_{\alpha_{ii}}$ is reduced for $ii = zz$ with respect to $ii = xx$.

Compound	$I^{\varepsilon}_{\alpha_{xx}}$ (1/m)	Rank	$I^{\lambda}_{\alpha_{xx}}$ (1/m)	Rank
1T-PtSS$_2$	$2.86 \cdot 10^{10}$	1	$2.53 \cdot 10^{10}$	1
2H-MoS$_2$	$2.76 \cdot 10^{10}$	2	$2.09 \cdot 10^{10}$	3
2H-WS$_2$	$2.43 \cdot 10^{10}$	3	$1.64 \cdot 10^{10}$	5
1T-TiS$_2$	$2.29 \cdot 10^{10}$	4	$2.29 \cdot 10^{10}$	2
1T-HfS$_2$	$1.85 \cdot 10^{10}$	5	$1.59 \cdot 10^{10}$	6
1T-ZrS$_2$	$1.80 \cdot 10^{10}$	6	$1.70 \cdot 10^{10}$	4

Table 5.6: Integrals of the absorption coefficients $I^{\varepsilon}_{\alpha_{xx}}$ and $I^{\lambda}_{\alpha_{xx}}$, respectively. The rank of each integral is shown for all compounds.

Compound	$I^{\varepsilon}_{\alpha_{zz}}$(1/m)	Rank	$I^{\lambda}_{\alpha_{zz}}$ (1/m)	Rank
1T-PtS$_2$	$1.05 \cdot 10^{10}$	1	$1.43 \cdot 10^{10}$	1
1T-TiS$_2$	$6.38 \cdot 10^{10}$	2	$1.06 \cdot 10^{10}$	2
1T-ZrS$_2$	$5.38 \cdot 10^{10}$	3	$8.94 \cdot 10^{9}$	3
1T-HfS$_2$	$4.26 \cdot 10^{10}$	4	$7.41 \cdot 10^{9}$	4
2H-MoS$_2$	$1.76 \cdot 10^{9}$	5	$4.78 \cdot 10^{9}$	5
2H-WS$_2$	$8.61 \cdot 10^{8}$	6	$2.81 \cdot 10^{9}$	6

Table 5.7: Integrals of the absorption coefficients $I^{\varepsilon}_{\alpha_{zz}}$ and $I^{\lambda}_{\alpha_{zz}}$, respectively. The rank of each integral is shown for all compounds.

Having the absorption coefficient now enables us to calculate the short circuit current density as defined in Chapter 3, namely as

$$J^{ii}_{sc} = q \int_{E_g}^{4.42eV} \phi_{sol}(E)[1 - e^{-L \cdot \alpha_{ii}}(E)]dE \quad . \tag{5.16}$$

We shall employ the previously obtained absorption coefficients, α^{λ}_{ii} and $\alpha^{\varepsilon}_{ii}$ to determine their associated $J^{\varepsilon_{ii}}_{sc}$ and $J^{\lambda_{ii}}_{sc}$. For all compounds, we will consider a thickness L equal to 0.35 μm. This decision is based on the knowledge of the experimental carrier diffusion length observed in 2H-MoS$_2$ by P. Yuan et al. [186]. In Table 5.8 we record the short circuit current densities obtained in descending order for the xx component. An observation that can be first made is that the ordering of the first 8 and last 6 compounds, respectively, is perfectly preserved. For the top compounds, this is due to their low direct gaps that do not exceed 1.7 eV. This implies that inherent errors arising from the assumption $Im[\varepsilon(E)] \approx \mu \cdot JDOS(E)$ are blurred out, since the absorption coefficient appears as an exponent in Eq. (5.16). In other words, the short circuit current densities of small-gap materials are not sensitive to the shortcomings associated with the assumption made, rendering the joint density of states a solid absorption descriptor for low-gap materials. The next 14 materials have larger band gaps and thus the fluctuations in the momentum matrix elements are now made obvious since the solar flux diminishes rapidly at high energies. Nevertheless, the deviation is not larger than three positions from the $J_{sc}^{\varepsilon_{xx}}$ rank, which means the approximation is fairly robust even for the higher band gap materials. Interestingly, the last six compounds have the same ordering according to both $J_{sc}^{\varepsilon_{xx}}$ and $J_{sc}^{\lambda_{xx}}$. In conjunction with their very high band gaps, these systems have considerably low band dispersion, which might explain their low-valued JDOS spectra. Their respective δ values, which quantify the relative error associated with the constant momentum matrix elements assumption, are among the lowest, averaging 0.6. The JDOS and the imaginary part of the dielectric function with its components along xx and zz are plotted for two representative low-ranking compounds, 1T-ZnI$_2$ and 1T-CdI$_2$ and are shown in the Appendix together with all the values of μ_{xx} and associated δ.

By investigating the short circuit current densities along the zz component tabulated in Table 5.9, it is evident that the $J_{sc}^{\varepsilon_{zz}}$ values are considerably lower than those of $J_{sc}^{\varepsilon_{xx}}$ presented in Table 5.8. The monolayers in the study have an out-of-plane dispersion considerably lower than the in-plane one, leading to smaller zz momentum matrix elements and hence lower amplitude of the $Im(\varepsilon_{zz})$ spectra compared to the $Im(\varepsilon_{xx})$ one. It is also worth noting that due to the values of the scaling factors, μ_{zz}, being up to two orders of magnitude lower than those of μ_{xx}, the values of $J_{sc}^{\lambda_{zz}}$ are also overall lower than those of $J_{sc}^{\lambda_{xx}}$. Perhaps more striking is the fact that $J_{sc}^{\lambda_{zz}}$ is up to 5 times larger than $J_{sc}^{\varepsilon_{zz}}$ despite the relative order of compounds being conserved. This seems to suggest that omitting the fluctuations of the momentum matrix elements in the zz direction does overestimate the short circuit current densities. In terms of the compounds relative order, the ranking among the top ten compounds with the largest values of $J_{sc}^{\varepsilon_{zz}}$ is not fully conserved in the case of the $J_{sc}^{\lambda_{zz}}$. This shows that the high solar flux occurring at low energies cannot make up for the errors inherent in our approximation when determining the best out of plane absorbing monolayers. The highest rank deviation is found for 2H-WSe$_2$ which probably has a similar discrepancy between the scaled JDOS and the imaginary part of the dielectric function as illustrated for 2H-WS$_2$ in Fig. 5.23. The worst performing monolayers have matching rank positions due to their large

Compound	$J_{sc}^{\varepsilon_{xx}}$ (Am^{-2})	Rank	$J_{sc}^{\lambda_{xx}}$ (Am^{-2})	Rank
1T-PdTe$_2$	498.7	1	485.1	1
1T-HfTe$_2$	401.1	2	369.1	2
1T-TiS$_2$	375.6	3	326.4	3
2H-HfTe$_2$	291.3	4	298.4	4
1T-PtTe$_2$	265.1	5	259.4	5
1T-OTl$_2$	265.0	6	253.4	6
2H-MoTe$_2$	229.4	7	203.2	7
2H-WTe$_2$	226.5	8	184.0	8
1T-ZrSe$_2$	174.6	9	156.9	10
2H-MoSe$_2$	126.1	10	102.4	12
1T-SnSe$_2$	107.7	11	173.4	9
1T-STl$_2$	105.7	12	102.6	11
2H-WSe$_2$	103.0	13	75.6	16
1T-PtSe$_2$	98.9	14	98.6	13
1T-HfSe$_2$	90.5	15	83.4	15
2H-ZrCl$_2$	89.5	16	89.3	14
2H-MoS$_2$	83.9	17	62.8	17
2H-WS$_2$	63.1	18	46.8	18
1T-ZrS$_2$	47.9	19	45.2	19
1T-PtS$_2$	25.9	20	25.8	21
1T-HfS$_2$	16.8	21	16.43	23
1T-SnS$_2$	15.9	22	28.5	20
1T-YbI$_2$	15.6	23	18.5	22
1T-GeI$_2$	9.7	24	9.7	24
2H-GeI$_2$	8.70	25	8.6	25
1T-ZnI$_2$	3.50	26	7.5	26
1T-PbI$_2$	2.3	27	2.5	27
1T-CdI$_2$	1.1	28	2.1	28
1T-PtO$_2$	0.3	29	0.3	29

Table 5.8: Short circuit current density, J_{sc}, calculated using the xx components of the dielectric function and of the joint density of states, respectively. The compounds have been ranked according to their respective J_{sc}.

band gaps and small momentum matrix elements, which entails low fluctuations, hence rendering the scaling more appropriate.

Compound	$J_{sc}^{\varepsilon_{zz}}$ ($\mathrm{Am^{-2}}$)	Rank	$J_{sc}^{\lambda_{zz}}$ ($\mathrm{Am^{-2}}$)	Rank
1T-$PdTe_2$	260.7	1	459.2	1
2H-$HfTe_2$	208.8	2	283.9	2
1T-$PtTe_2$	151.4	3	247.4	5
1T-$HfTe_2$	123.0	4	304.7	3
1T-TiS_2	90.7	5	229.7	4
1T-$PtSe_2$	82.2	6	97.0	6
1T-$ZrSe_2$	76.8	7	128.8	8
2H-$MoTe_2$	61.6	8	149.5	10
2H-WTe_2	47.7	9	119.2	9
1T-OTl_2	45.7	10	195.0	15
1T-$HfSe_2$	41.6	11	69.3	7
1T-STl_2	36.9	12	86.5	12
1T-ZrS_2	28.9	13	38.2	17
1T-$SnSe_2$	26.5	14	15.0	11
1T-PtS_2	23.2	15	25.1	13
2H-$MoSe_2$	18.4	16	56.9	14
1T-HfS_2	11.9	17	14.4	19
2H-WSe_2	11.8	18	35.8	23
1T-GeI_2	7.9	19	8.9	16
2H-MoS_2	7.6	20	24.5	18
2H-$ZrCl_2$	7.0	21	67.6	22
1T-YbI_2	6.9	22	15.8	20
2H-GeI_2	5.8	23	8.6	21
1T-SnS_2	4.8	24	21.4	24
2H-WS_2	4.6	25	14.3	25
1T-PbI_2	2.2	26	2.1	26
1T-ZnI_2	1.5	27	5.0	27
1T-CdI_2	0.5	28	1.4	28
1T-SnS_2	0.2	29	0.2	29

Table 5.9: Short circuit current density, J_{sc}, calculated using the zz components of the dielectric function and of the joint density of states, respectively. The compounds have been ranked according to their respective J_{sc}.

In conclusion, we have attempted in this chapter to explore band nesting for a set of 29 transition metal dichalcogenides and halides. We first clustered the monolayers according to their characteristic $|\nabla_{\boldsymbol{k}}(E_{c1} - E_{v1})|$ mapped on their IRBZ, which was sampled using a dense grid of 43x44x1 k-points. We identified four groups exhibiting certain common patterns. The group displaying the largest intrinsic band nesting regions contain molybdenum- and tungsten- based compounds. We repeated the clustering procedure by introducing the solar flux, whereby each k-point in the IRBZ was associated to $\phi_{sol}(E_{c1}-E_{v1})/|\nabla_{\boldsymbol{k}}(E_{c1}-E_{v1})|$. We defined the regions in the IRBZ that yield band nesting transitions at energies where the solar flux is at its strongest "regions of interest". Materials with the largest "regions of interest" were identified as residing in a group and they consisted of platinum-based compounds and of the molybdenum and tungsten monolayers that exhibit lower band gaps, namely of 2H-$MoTe_2$, 2H-WTe_2 and 2H-$MoSe_2$. A very similar analysis was performed for a set of bulk TMD and TMH compounds. "Regions of interest" were identified in all the clusters although they were quite localized and narrowly spread. In the second part of the chapter we introduced an operational definition relating the imaginary part of the dielectric function to the joint density of states. We tested the hypothesis, under which the two have a linear relation, where the scaling factor is a constant quantifying the global effect of the momentum matrix elements. We compared two sets of dielectric function spectra with varying number of k-points and Lorentzian broadening. We found that these features of the dielectric spectrum do not have a significant effect on the size of the scaling factor, μ, and its corresponding relative error, δ. We also came to the conclusion that the hypothesis is better justified when considering the xx component of the spectrum than the zz one. We plotted $|p_{c,v,\boldsymbol{k}}|$ for 2H-WS_2 and 1T-ZrS_2 along the solar energy range and observed a smaller variance in the case of the former compound. This helped validate our assumption made from observing the good match between JDOS and the scaled $\mathrm{Im}(\varepsilon_{xx})$ spectra of 2H-WS_2 and 2H-MoS_2 in Fig.5.22. The pDOS of 2H-WS_2 indicates that there is a change in the orbital character in the lower lying valence bands, thus possibly justifying why the scaled JDOS does not describe well the xx component of the imaginary part of the dielectric function from 4 eV onwards. We went on to show that observables such as the absorption coefficient along both the xx and zz directions, together with the short circuit current density can very reliably be employed as ranking descriptors using interchangeably the dielectric function spectra or the joint density of states and its Kramers-Kronig derived counterpart. An important conclusion is that the values of the strong solar flux downplay the error that arise from ignoring the energy dependence of the in-plane momentum matrix elements, while this is not necessarily the case for the out-of-plane ones.

6 Conclusions

Throughout this PhD thesis we have explored different avenues for describing the absorption properties of semiconductors under direct solar radiation. We selected DFT as our theoretical framework to determine the states and the eigenvalues of the system, predominantly employing the hybrid functional HSE06 to correct for the inherent band gap underestimation of the LDA/GGA. The assumption that underlies this work is that the Kohn-Sham states can be interpreted to a certain level of accuracy as the ground and excited states of the system in question. Despite the lack of a formal theoretical justification to back up this approximation, the loose identification of the Kohn-Sham as the quasi-particle states of an electronic system have been made successfully before. Nevertheless, as stated in Chapter 1, the objective of this work was aimed at providing a qualitative, rather than a fully quantitative method of ranking and assessing the absorption characteristics of compounds, especially of two-dimensional layered ones. We consider that this goal is achieved by employing the DFT-derived Kohn-Sham states into the optical response expression formulated in the many-body RPA approximation.

Firstly, we found that the correct estimation of the pre-edge absorption spectrum is critical for a reliable theoretical assessment of a material's photoconversion efficiency. However, the shape and the amplitude of the pre-edge is largely affected by the level of disorder inherent to a system, which is a sample-specific property, rather than an intrinsic one. Surely enough, indirect gap systems are prime candidates that require an in-depth pre-edge absorption analysis. We have seen that this is the case even for direct gap materials such as the well-established hybrid perovskite, methyl ammonium lead iodide, whereby its efficiency was enhanced up to 5 times when the empirical pre-edge Urbach tail was added to the ab-initio absorption spectrum. In contrast, it was found that the shortcircuit current density, J_{sc}, did not change significantly with the inclusion of the sub-band absorption. However, a fully theoretical treatment of the pre-edge absorption coefficient and hence, of the PCE, would be impossible. This prompted us to focus fully on the property that appeared to be reliably determined with our model, namely the intrinsic absorption performance of materials. To this end, we designated as proxy the short circuit current density. We opted to quantify this quantity for six materials by taking 95% of their saturated J_{sc} and their corresponding characteristic material thickness. Both these descriptors were reasonably well in agreement with experimental measurements identified in the scientific literature.

We then moved on to investigate the dielectric function, a direct proxy of the absorption coefficient, in vertically stacked TMD monolayers. We looked at the HfS_2/PtS_2 heterostructure characterised by a type II band alignment in order to determine whether its imaginary part of the dielectric function spectrum exhibits any unique peaks that could be pinned down to inter-layer transitions. Essentially we decomposed the total dielectric function into its constituting intra-layer, inter-layer and mixed components by projecting the momentum matrix elements on the individual layers. The inter-layer component exhibited an amplitude that was a factor of 100 lower than the intra-layer one. Unfortunately, the mixed component displayed a non-zero contribution in the same energy region where the inter-layer component was present. Therefore, one cannot categorically separate the inter-layer transitions from the intra-layer ones. Nevertheless, gradually compressing the two layers led to the creation of a valence impurity band which, eventually, led to a well-isolated peak at the absorption edge. This was attributed to the inter-layer transitions alone.

Lastly, we attempted to bring together the two previous lines of work by quantifying absorption characteristics of 2D compounds. We investigated the concept of "band nesting" and its emergence due to van Hove singularities, which are a prevalent feature in the density of states of transition metal dichalcogenides. We set out to examine the specific regions in the Brillouin zone that are associated with these singularities, since they are attributed to the strong optical conductivity recorded in TMD systems. We first took a data-driven approach whereby we classified the compounds, first in their monolayer form and then, separately, in their bulk form, using statistical algorithms such as "k-means". The quantity used for the classification consisted of the individual gradients of the energy difference between the the top valence and bottom conduction bands, *i.e.* $|\nabla_{\boldsymbol{k}}(E_{c1} - E_{v1})|$ mapped onto their respective IRBZ. We found similar human-discernible patterns in the resulting groups that, to some extent, justified the emerging groups. We also introduced the solar flux to constrain the energy window on which the band nesting could have a substantial impact on the solar radiation-induced transitions. These restricted band nesting regions were defined as "regions of interest". A considerable number of compounds appeared to exhibit band-nesting features in the visible solar range, although they were a lot less wide-spread than the inherent ones, which were at energies exceeding the visible solar range. Furthermore, we delved into the study of the joint density of states and compared it to the imaginary part of the dielectric function. We noted that there was a roughly linear relation between the two spectra. Based on this coarse approximation, we attempted to calculate observable macroscopic quantities such as the absorption coefficient and the short circuit current density using a scaled $JDOS$ and its Kramers-Kronig analogue. In these the scaling factor was normalized to the energy range. We tested whether the compounds ranking in terms of these macroscopic quantities would be roughly unchanged when using the full dielectric function. This was indeed the case, especially for the in-plane component of the absorption coefficient. The first five compounds with the strongest in-plane short circuit current densities were found to be 1T-PdTe$_2$, 1T-HfTe$_2$, 1T-TiS$_2$, 2H-HfTe$_2$ and 1T-PtTe$_2$. Then 2H-MoTe$_2$, 2H-WTe$_2$ and 2H-MoSe$_2$ closely follow, being on the 7^{th}, 8^{th} and 10^{th} positions. In this work we have not taken into account the formation of excitons and their impact on the dielectric spectra. As excitons are known to have relatively large binding energies in lower dimensional systems, an idea for the future plan is to semi-classically model the exciton binding energies for our pool of 2D compounds. To this end, we will use the quantum-electrostatic heterostructure (QEH) model developed by Andersen et al. [155] that enables the calculation of dielectric properties and electronic excitations of realistic incommensurable systems at considerably lower computational costs than the full many-body approach. The workflow consists of performing ab-initio calculations to obtain the response functions of the freestanding layers. Within the dipole approximation, the induced density in the isolated layers is found. Afterwards, the full density response of the van der Waals heterostructure is obtained through a Dyson-like equation that couples the dielectric building blocks through Coulomb interaction. Then the inverse dielectric function in the monopole/dipole basis can be calculated knowing the full density response and the Coulomb matrices. The reason why this model works is because the hybridization of the band structure does not have a significant impact on the dielectric properties of a van der Waals heterostructur [155]. We plan to implement this model for our entire pool of 2D systems in order to study the change in the dielectric function from mono- to multi-layers. This model will also enable us to calculate the screened electron-hole interactions from the full response function and the Coulomb interaction matrix. Hence, the QEH model appears as a computationally cheap and accurate way to explore heterojunctions with varying number of layers that exhibit excitonic transitions at energies that are in the high-flux part of the solar spectrum, i.e. between 0.7-1.3 eV.

For the most promising systems that emerge from the QEH model and which have a maximum number of 5 layers, we plan to apply many-body perturbation theory in order to obtain the close-to-exact optical response. Therefore, we will perform some GW+Bethe Salpeter calculations [187] and we will compare the excitation energies obtained with those determined in the QEH model.

A Appendix

A.1 $k \cdot p$ perturbation theory

The following brief overview aims to provide supplementary details regarding section 2.4. Its content is based on the work of Ambrosch et al. [115]. The Schrödinger equation corresponding to a system of independent electrons in a periodic potential can be written as

$$\left[\frac{-\hbar^2\nabla^2}{2m} + V(\boldsymbol{r})\right]\psi_{n,\boldsymbol{k}}(\boldsymbol{r}) = \epsilon_{n,\boldsymbol{k}}\psi_{n,\boldsymbol{k}}(\boldsymbol{r}) \quad , \tag{A.1}$$

where m is the electron mass, $V(\boldsymbol{r})$ is the periodic crystal potential and $\epsilon_{n,\boldsymbol{k}}$ are the single-particle energy eigenvalues. The solution to this equation is the Bloch wavefunction $\langle \boldsymbol{r}|n, \boldsymbol{k}\rangle$ introduced in Chapter 2, Section 2.1. The periodic part of the Bloch state, $u_{n,\boldsymbol{k}}(\boldsymbol{r})$, is an eigenstate of the Hamiltonian $H_k = \dfrac{(\boldsymbol{p}+\boldsymbol{k})^2}{2m} + V(\boldsymbol{r})$. We will use perturbation theory under the assumption that the light wave vector $\boldsymbol{q}$ is negligible to derive $\epsilon_{n,\boldsymbol{k}+\boldsymbol{q}}$ and $M^0_{l,n}(\boldsymbol{k}, \boldsymbol{q})$, two quantities that are central to the calculation of the macroscopic dielectric constant introduced in Chapter 2, Section 2.4. The equation for $u_{n,\boldsymbol{k}+\boldsymbol{q}}(\boldsymbol{r})$ is

$$H_{\boldsymbol{k}+\boldsymbol{q}}u_{n,\boldsymbol{k}+\boldsymbol{q}}(\boldsymbol{r}) = \epsilon_{n,\boldsymbol{k}+\boldsymbol{q}}u_{n,\boldsymbol{k}+\boldsymbol{q}}(\boldsymbol{r}) \quad , \tag{A.2}$$

where the perturbed Hamiltonian is

$$H_{\boldsymbol{k}+\boldsymbol{q}} = H_{\boldsymbol{k}} + \frac{\hbar\boldsymbol{p}\cdot\boldsymbol{q}}{m} + \frac{\hbar^2\boldsymbol{k}\cdot\boldsymbol{q}}{m} + \frac{\hbar^2\boldsymbol{q}}{2m} \quad . \tag{A.3}$$

The last three terms are considered to be the perturbation. Let us introduce the notation convention

$$(\boldsymbol{r}|n,\boldsymbol{k}) = u_{n,\boldsymbol{k}}(\boldsymbol{r}) \quad . \tag{A.4}$$

The matrix element of an operator $\hat{O}$ are

$$(n',\boldsymbol{k'}|\hat{O}|n,\boldsymbol{k}) = \frac{1}{\Omega}\int_{\Omega} d\boldsymbol{r} u^{*}_{n',\boldsymbol{k'}}(\boldsymbol{r})\hat{O}u^{*}_{n,\boldsymbol{k}}(\boldsymbol{r}) \quad , \tag{A.5}$$

with the integral running over the unit cell volume, Ω. According to perturbation theory the wavefunction to first order in $\boldsymbol{q}$ is

$$|n,\boldsymbol{k}+\boldsymbol{q}) = |n,\boldsymbol{k}) + \sum_{n'\neq n} |n',\boldsymbol{k})\frac{(n',\boldsymbol{k}|H_{\boldsymbol{k}+\boldsymbol{q}} - H_{\boldsymbol{k}}|n,\boldsymbol{k})}{\epsilon_{n,\boldsymbol{k}} - \epsilon_{n',\boldsymbol{k}}} \quad . \tag{A.6}$$

Only one of the perturbation terms of Eq.(A.3) has a non-zero contribution to the first order correction of the wavefunction and hence the previous expression can be reformulated as

$$|n,\boldsymbol{k}+\boldsymbol{q}) = |n,\boldsymbol{k}) + \sum_{n'\neq n} |n',\boldsymbol{k})\frac{(n',\boldsymbol{k}|\frac{\hbar}{m}\boldsymbol{p}\cdot\boldsymbol{q}|n,\boldsymbol{k})}{\epsilon_{n,\boldsymbol{k}} - \epsilon_{n',\boldsymbol{k}}} \quad . \tag{A.7}$$

Since the states are normalized, the expression for energy to linear order in $\boldsymbol{q}$ is

$$\epsilon_{n,\boldsymbol{k}+\boldsymbol{q}} = \epsilon_{n,\boldsymbol{k}} + \frac{\hbar}{m}[(n,\boldsymbol{k}|\boldsymbol{p}|n,\boldsymbol{k}) + \hbar\boldsymbol{k}]\cdot\boldsymbol{q} \quad . \tag{A.8}$$

We shall now introduce the momentum matrix element, defined as

$$\boldsymbol{p}_{l,n,\boldsymbol{k}} \equiv \langle l,k|\,\boldsymbol{p}\,|n,\boldsymbol{k}\rangle = \delta_{l,n}\hbar\boldsymbol{k} + (l,\boldsymbol{k}|\boldsymbol{p}|n,\boldsymbol{k}) \quad , \tag{A.9}$$

where the right-hand side expression can be derived using Eq.(A.7) and the fact that the wavefunctions $\psi_{n,\boldsymbol{k}}$ are normalized and are Bloch states. The wavefunctions and energies to first order in $\boldsymbol{q}$ are then recasted in terms of the momentum matrix element as

$$|n,\boldsymbol{k}+\boldsymbol{q}) = |n,\boldsymbol{k}) + \frac{\hbar}{m}\sum_{n'\neq n} |n',\boldsymbol{k})\frac{\boldsymbol{p}_{l,n,\boldsymbol{k}}}{\epsilon_{n,\boldsymbol{k}} - \epsilon_{n',\boldsymbol{k}}}\cdot\boldsymbol{q} \quad , \tag{A.10}$$

and

$$\epsilon_{n,\boldsymbol{k}+\boldsymbol{q}} = \epsilon_{n,\boldsymbol{k}} + \frac{\hbar}{m}\boldsymbol{p}_{n,n,\boldsymbol{k}} \cdot \boldsymbol{q} \quad . \tag{A.11}$$

We continue applying a similar procedure whereby we use the periodic function, $u_{n,\boldsymbol{k}}$, to express the matrix element

$$M^0_{l,n}(\boldsymbol{k},\boldsymbol{q}) = \langle l,\boldsymbol{k}|\, e^{-i\boldsymbol{q}\boldsymbol{r}}\, |n,\boldsymbol{k}+\boldsymbol{q}\rangle = (l,\boldsymbol{k}|n,\boldsymbol{k}+\boldsymbol{q}) \quad . \tag{A.12}$$

Based once more on Eq.(A.7), the matrix element of the first order for small $\boldsymbol{q}$ becomes

$$M^0_{l,n}(\boldsymbol{k},\boldsymbol{q}\to 0) = \delta_{l,n} + (1-\delta_{l,n})\frac{\hbar}{m}\frac{\boldsymbol{p}_{l,n,\boldsymbol{k}}\cdot\boldsymbol{q}}{\epsilon_{n,\boldsymbol{k}} - \epsilon_{l,\boldsymbol{k}}} \quad . \tag{A.13}$$

A.2 Semi-classical derivation of the dielectric function

In this section we will derive the linear response theory for a set of electrons in an external electromagnetic field. This expression is relevant for obtaining the electrical conductivity of solids, and hence their dielectric function, in addition to a description of the interaction between electrons and light. We assume to have an independent electron approximation for a collection of electrons that occupy states of energy

$$\epsilon_l = \hbar\omega_l \quad , \tag{A.14}$$

with probability f_l. Generally f_l is a Fermi factor, meaning that states up to Fermi energy are occupied, while those above are empty. The first step in this calculation is to work out the response to the first order of an arbitrary time-evolved state to a potential $\hat{U}(t)$ with time dependence $e^{-i\omega t}$. The next step involves finding the expectation value of the current in this state. For this goal, we need to find $|l(t)\rangle$, which is the time-evolved eigenstate of $\hat{H}$, *i.e.* $|l\rangle$, under the combined action of $\hat{H}$ and $\hat{U}$.

We start off by considering a many-particle system with a time-independent Hamiltonian $\hat{H}$. The system is perturbed at $t = t_0$ by turning on an additional time-dependent Hamiltonian $\hat{U}(t)$. The new Schrödinger state vector now satisfies the equation:

$$i\hbar\frac{|\partial\psi_S(t)\rangle}{\partial t} = [\hat{H} + \hat{U}(t)]|\psi_S(t)\rangle \quad . \tag{A.15}$$

We seek for a solution of the form:

$$|\psi_S(t)\rangle = e^{-i\hat{H}t/\hbar}\hat{A}(t)\,|\psi_S(0)\rangle \quad , \tag{A.16}$$

where the operator $\hat{A}(t)$ obeys the causal boundary condition

$$\hat{A} = 1, \quad t \leq t_0 \quad . \tag{A.17}$$

Let us apply the time-derivative to the the Schrödinger state vector

$$\frac{\partial\psi_S(t)}{\partial t} = \frac{-i}{\hbar}\hat{H}|\psi_S(t)\rangle + e^{-i\hat{H}t/\hbar}\frac{\partial\hat{A}(t)}{\partial t}\,|\psi_S(t_0)\rangle \quad . \tag{A.18}$$

Considering Eq. (A.15), Eq. (A.16) and multiplying to the left by $e^{i\hat{H}t/\hbar}$, it follows that:

$$i\hbar\frac{\partial\hat{A}(t)}{\partial t}\,|\psi_S(t_0)\rangle = e^{i\hat{H}t/\hbar}\hat{U}e^{-i\hat{H}t/\hbar}\hat{A}(t)\,|\psi_S(0)\rangle \quad , \tag{A.19}$$

where $e^{i\hat{H}t/\hbar}\hat{U}e^{-i\hat{H}t/\hbar}$ is, in fact, $\hat{U}(t)$. Acknowledging that any smooth function could be expressed as

$$\hat{A}(t) = \hat{A}(t_0) + \int_{t_0}^{t}\frac{\partial\hat{A}(t')}{\partial t'}dt' \quad , \tag{A.20}$$

we can rewrite Eq. (A.15) iteratively to first order as:

$$\hat{A}(t) = \hat{A}(t_0) + \frac{1}{i\hbar}\int_{t_0}^{t}dt' e^{i\hat{H}t'/\hbar}\hat{U}e^{-i\hat{H}t'/\hbar}\hat{A}(t_0) \quad . \tag{A.21}$$

Similarly, the perturbed time-dependent Schrödinger state has the expression:

$$|\psi_S(t)\rangle = e^{-i\hat{H}t/\hbar}(|\psi_S(t_0)\rangle + \int_{-\infty}^{t}dt' e^{i\hat{H}t'/\hbar}\frac{\hat{U}}{i\hbar}e^{-i\hat{H}t'/\hbar}\,|\psi_S(t_0)\rangle). \tag{A.22}$$

For simplicity of notation, let us replace the eigenstate of the unperturbed Hamiltonian, $|\psi_S(t_0)\rangle$ with $|l\rangle$ and let us introduce in Eq. (A.22) a sum over all l' states of the unitary operator, *i.e.* $\sum_{l'} |l'\rangle \langle l'| = \mathbb{1}$,

$$|l(t)\rangle = e^{-i\hat{H}t/\hbar} |l\rangle + \sum_{l'} \int_{-\infty}^{t} dt' \, |l'\rangle \langle l'| \, e^{-i\hat{H}(t-t')/\hbar} \frac{\hat{U}}{i\hbar} e^{-i\hat{H}t')/\hbar} |l\rangle \tag{A.23}$$

Let us now consider the time-evolution operator as a Taylor series

$$e^{-i\hat{H}t/\hbar} = 1 - \frac{i\hat{H}t}{\hbar} + \frac{1}{2!}\Big(\frac{i\hat{H}t}{\hbar}\Big)^2 + O^3(\hat{H}) + ... \quad . \tag{A.24}$$

Now, if we approximate this operator to first order and acknowledge the fact that its eigenvalues are scalars, we obtain,

$$|l(t)\rangle = e^{-i\omega_l t} |l\rangle + \sum_{l'} \int_{-\infty}^{t} dt' e^{-i\omega_{l'}(t-t')} |l'\rangle \langle l'| \frac{\hat{U}}{i\hbar} |l\rangle \, e^{-i\omega_l t'} e^{-i\omega t'} \quad . \tag{A.25}$$

In Eq. (A.25), we assumed $\hat{U}(t')$ has time dependence $e^{-i\omega t'}$, which we added explicitly. Here ω_l and $\omega_{l'}$ are the eigenfrequencies of the hamiltonian, $\omega_l = \frac{\epsilon_l}{\hbar}$. We now separate the sum over the l' states from the integral over time

$$|l(t)\rangle = e^{-i\omega_l t} |l\rangle + \sum_{l'} |l'\rangle \langle l'| \frac{\hat{U}}{i\hbar} |l\rangle \, e^{-i\omega_{l'} t} \int_{-\infty}^{t} dt' e^{i\omega_{l'} t'} e^{-i\omega_l t'} e^{-i\omega t'} \quad . \tag{A.26}$$

In order for the time integral to converge, we add a small imaginary part η to ω. Also, we omit the l state from the sum over all l' states for normalization purposes. The final form of the time-dependent state is then

$$|l(t)\rangle = e^{-i\omega_l t} \left\{ |l\rangle + \sum_{l' \neq l} |l'\rangle \frac{\langle l'| \hat{U} |l\rangle \, e^{-i\omega t}}{\hbar(\omega_l - \omega_{l'} + \omega)} \right\} \quad . \tag{A.27}$$

It is worth mentioning that if the time-dependent potential has the complex conjugated form of $\hat{U} e^{-i\omega t}$, *i.e.* $\hat{U}^* e^{i\omega^* t}$, then the time-dependent state would be

$$|l(t)\rangle = e^{-i\omega_l t} \left\{ |l\rangle + \sum_{l' \neq l} |l'\rangle \frac{\langle l'| \hat{U}^* |l\rangle \, e^{i\omega^* t}}{\hbar(\omega_l - \omega_{l'} - \omega^*)} \right\} \quad . \tag{A.28}$$

The imaginary part η in ω alleviates convergence problems, but besides that it does not pose a real physical interest. It indicates that the interaction potential is turned on very slowly in the past such that the system can reach a steady state by adjusting itself adiabatically to the new potential.

We need now to describe how electrons interact with an electromagnetic field. An appropriate way of accounting for a uniform electrical field within the periodic boundary conditions is through a vector potential. According to Maxwell's equation, electric fields are generated by time-dependent vector potentials

$$\boldsymbol{E} = \frac{1}{c}\frac{\partial \boldsymbol{A}}{\partial t} - \nabla V \quad , \tag{A.29}$$

where $\boldsymbol{A}$ is the vector potential and V is a scalar potential. We also note that the wavelength of the light passing through a solid is approximately 100 Å in the visible spectrum, while the typical unit cell dimensions are significantly smaller. Hence it is justifiable to consider electric fields to be of the form

$$\boldsymbol{E}(\boldsymbol{r}, t) = \boldsymbol{E}e^{-i\omega t} \quad , \tag{A.30}$$

and to set $\boldsymbol{q} = 0$ in the dielectric and conductivity tensor, omitting $\boldsymbol{q}$ altogether. Based on Eq. (A.29), the vector potential describing the spatially uniform oscillating field is

$$\boldsymbol{A} = \frac{c\boldsymbol{E}}{i\omega}e^{-i\omega t} + \frac{c\boldsymbol{E}}{-i\omega^*}e^{i\omega^* t} \quad , \tag{A.31}$$

where we have included the complex conjugate in the second term. The next step allows us to determine the expectation value of the current in the state $|l(t)\rangle$. The canonical momentum that describes a charge in an electromagnetic field is known to be $\boldsymbol{p} = \boldsymbol{P} - \frac{e}{c}\boldsymbol{A}$. In addition, the kinetic term of the Hamiltonian is responsible for the emergence of the current and it can be shown that it is $\boldsymbol{j} = Re\{e\psi^* \boldsymbol{p}\psi\}$. The current operator is finally expressed as

$$\hat{j} = -\frac{e}{m}(\hat{P} + \frac{e}{c}\boldsymbol{A}) \quad , \tag{A.32}$$

Applying the chain rule and noting that $\boldsymbol{\nabla} \cdot \boldsymbol{A} = 0$, the kinetic term is hence to first order $\frac{\hat{P}^2}{2m} + \frac{e}{mc}\boldsymbol{A}\hat{P}$. Therefore, to linear order, the Hamiltonian is modified by the addition of

$$\hat{U}(t) = \frac{e}{mi\omega}\boldsymbol{E}\hat{P}e^{-i\omega t} - \frac{e}{mi\omega^*}\boldsymbol{E}\hat{P}e^{i\omega^* t} \quad . \tag{A.33}$$

To first order in the perturbative term, the current corresponding to the state $|l(t)\rangle$ is

$$\begin{aligned}\boldsymbol{J}_{|l(t)\rangle} = \Omega \boldsymbol{j}_{|l(t)\rangle} =& -\frac{e}{m}\langle l(t)|\, \hat{P} + \frac{e\boldsymbol{A}}{c}\, |l(t)\rangle = -\frac{e}{m}\langle l|\, \hat{P}\, |l\rangle - \frac{e^2}{mc}\langle l|\, \boldsymbol{A}\, |l\rangle \\ & -\sum_{l'\neq l}\frac{e}{m}\langle l|\, \hat{P} + \frac{\boldsymbol{A}}{c}\, |l'\rangle \langle l'|\, \frac{\hat{U}e^{-i\omega t}}{\hbar(\omega_l - \omega_{l'} + \omega)} + \frac{\hat{U}^* e^{i\omega^* t}}{\hbar(\omega_l - \omega_{l'} - \omega^*)}\, |l\rangle \\ & -\sum_{l'\neq l}\frac{e}{m}\langle l'|\, \hat{P} + \frac{e\boldsymbol{A}}{c}\, |l\rangle \langle l|\, \frac{\overline{\hat{U}e^{-i\omega t}}}{\hbar\overline{(\omega_l - \omega_{l'} + \omega)}} + \frac{\overline{\hat{U}^* e^{i\omega^* t}}}{\hbar\overline{(\omega_l - \omega_{l'} - \omega^*)}}\, |l'\rangle \quad .\end{aligned} \tag{A.34}$$

If we assume that the ground state has no net current and we sum up over all l states, we get:

$$\begin{aligned}\boldsymbol{J}_i = \Omega \sum_l f_l \boldsymbol{j}_i^l =& \frac{-e^2}{mi} E_i \sum_l f_l \langle l|\, \frac{e^{-i\omega t}}{\omega} - \frac{e^{i\omega^* t}}{\omega^*}\, |l\rangle \\ & -\sum_l \sum_{l'\neq l} \frac{e^2}{\hbar m^2} f_l \langle l|\, p_i\, |l'\rangle \sum_j \langle l'|\, \frac{p_j E_j e^{-i\omega t}}{i\omega(\omega_l - \omega_{l'} + \omega)} + \frac{p_j E_j e^{i\omega^* t}}{-i\omega^*(\omega_l - \omega_{l'} - \omega^*)}\, |l\rangle \\ & -\sum_l \sum_{l'\neq l} \frac{e^2}{\hbar m^2} f_l \langle l'|\, p_i\, |l\rangle \sum_j \langle l|\, \frac{p_j E_j e^{i\omega^* t}}{-i\omega^*(\omega_l^* - \omega_{l'}^* + \omega^*)} + \frac{p_j E_j e^{-i\omega t}}{i\omega(\omega_l^* - \omega_{l'}^* - \omega)}\, |l'\rangle \quad .\end{aligned} \tag{A.35}$$

Since the conductivity tensor $\sigma(\omega)$ is defined as the coefficient of $e^{-i\omega t}$ that relates the the applied electric field $\boldsymbol{E_i}$ to the current $\boldsymbol{j_i}$, we obtain

$$\sigma_{ij}(\boldsymbol{q} \to 0, \omega) = \frac{-e^2}{im\omega\Omega}\left[\sum_l f_l \delta_{ij} + \sum_l \sum_{l'\neq l} \frac{f_l}{\hbar m}\left\{\frac{\langle l|\, p_i\, |l'\rangle \langle l'|\, p_j\, |l\rangle}{\omega_l - \omega_{l'} + \omega} + \frac{\langle l'|\, p_i\, |l\rangle \langle l|\, p_j\, |l'\rangle}{\omega_l^* - \omega_{l'}^* - \omega}\right\}\right] \quad . \tag{A.36}$$

The dielectric constant and the conductivity are related as

$$\epsilon(\boldsymbol{q} \to 0, \omega) = 1 + \frac{4\pi i \sigma(\boldsymbol{q} \to 0, \omega)}{\omega} \quad . \tag{A.37}$$

Therefore, the part of the dielectric constant for which $l \neq l'$ has the form

$$\epsilon_{ij}(\boldsymbol{q} \to 0, \omega) = \frac{-4\pi e^2}{m\omega^2\Omega}\sum_l \sum_{l'\neq l} \frac{f_l}{\hbar m}\left\{\frac{\langle l|\, p_i\, |l'\rangle \langle l'|\, p_j\, |l\rangle}{\omega_l - \omega_{l'} + \omega} + \frac{\langle l'|\, p_i\, |l\rangle \langle l|\, p_j\, |l'\rangle}{\omega_l^* - \omega_{l'}^* - \omega}\right\} \quad . \tag{A.38}$$

Let us note that $\hbar\omega = E$. Moreover, let us assume that $\hbar = e = m = 1$, ω has a small imaginary part iη, all ω_l and $\omega_{l'}$ are real, $\omega \approx (\omega_l - \omega_{l'})$, the irradiated electronic system is a solid, which then imposes a summation over k-points to account for its periodicity, l states correspond to conduction states c and l' states correspond to valence states v and finally, the system is spin-degenerate, hence $f_l = 2$, we get that Eq.(A.38) is equivalent to Eq.(2.75) of Chapter 2, which defines the interband dielectric function in the RPA approximation.

A.3 Computational approach to Kramers-Kronig relations

The Kramers-Kronig relations for two real analytic functions χ_1 and χ_2 defined via $\chi(\omega) = \chi_1(\omega) + i\chi_2(\omega)$ are

$$\chi_1(\omega') = \frac{1}{\pi} p.v. \int_{-\infty}^{\infty} \frac{\chi_2(\omega)}{\omega' - \omega} d\omega \quad , \tag{A.39}$$

and

$$\chi_2(\omega') = \frac{-1}{\pi} p.v. \int_{-\infty}^{\infty} \frac{\chi_1(\omega)}{\omega' - \omega} d\omega \quad , \tag{A.40}$$

where p.v. denotes the "principal values" of a multivalued function. These refer to values along a certain branch of that function where it is single-valued. We will briefly describe below how we computationally implement the Kramers-Kronig relations to obtain the real part of the dielectric function from its imaginary part. In our case, we have access to the imaginary part of the dielectric function, ε_2, obtained from the DFT bandstructure. The energy range of our spectrum is limited between 0 and 10 eV. The goal is to find an accurate method to perform the integral in Eq. (A.39) in order to obtain the real part of the dielectric function. In our case, the integral in Eq.(A.39) can be broken down as

$$\begin{split} \varepsilon_1(E') = \frac{1}{\pi}\Bigg(p.v. \int_{-\infty}^{-10} \frac{\varepsilon_2(E)}{E' - E} dE + p.v. \int_{-10}^{a} \frac{\varepsilon_2(E)}{E' - E} dE + \\ p.v. \int_{a}^{b} \frac{\varepsilon_2(E)}{E' - E} dE + p.v. \int_{b}^{10} \frac{\varepsilon_2(E)}{E' - E} dE + p.v. \int_{10}^{\infty} \frac{\varepsilon_2(E)}{E' - E} dE \Bigg) \quad , \end{split} \tag{A.41}$$

with $-10\,eV < a < b < 10\,eV$. Now by invoking the fact that the imaginary part of the dielectric function is an odd function, it follows that $\varepsilon_2(-E) = -\varepsilon_2(E)$ with $E \in [0, 10]$ eV. Essentially, this means that the three middle integrals, that range from -10 eV to 10 eV, can be computed. For each value of E', let its corresponding a and b values be $E' - h$ and $E' + h$, respectively

$$\begin{aligned} a(E') &= E' - h \\ b(E') &= E' + h \quad , \end{aligned} \tag{A.42}$$

where h is an arbitrarily small overshooting positive constant. The reason why we introduce h is the following: E' can have any value between 0 and 10 eV. Now, the second and the fourth integral with energy E ranging from -10 eV to a and from b to 10 eV, respectively, pose no particular difficulty and so they can be easily estimated numerically using the trapezoidal rule. That is because there is no singularity in the second and fourth integrals since the denominator will always be non-zero, *i.e.* $|E' - E| > 0\,eV$. However, the third integral is defined over the energy range comprised between $E' - h$ and $E' + h$, meaning that it has a singularity for $E = E'$. To make the integral tractable, we shall need to apply the Cauchy principal value. To this end, we will have to transform $\varepsilon_2/(E' - E)$ into an analytic function. This can be done by expanding the function $\varepsilon_2/(E' - E)$ around the singularity $E = E'$ in terms of polynomial functions. After performing some basic complex calculus we arrive at the expression

$$p.v. \int_{E'-h}^{E'+h} \frac{\varepsilon_2(E)}{E' - E} dE = \sum_{i=0}^{i=m} a_{i+1} \cdot \frac{h^{i+1}}{i+1} \quad , \tag{A.43}$$

where m is the maximum order of the polynomial expansion of $\varepsilon_2/(E' - E)$ and a_i is the coefficient of the i-th order polynomium. The overshooting term ensures that the polynomial fit is done over a sufficiently large range around the singularity $E = E'$ so that the function is well-described at that point. However, choosing a value for h that is too large can lead to an erroneous polynomial expansion of the function in the close proximity of the singularity.

The only remaining integrals to solve are the first and the last. Since we cannot practically obtain them, we note that for $0 \ll |E'| \ll 10eV$, the error term which we define as

$$err(E') = \int_{-\infty}^{-10} \frac{\varepsilon_2(E)}{E'-E} dE + \int_{10}^{\infty} \frac{\varepsilon_2(E)}{E'-E} dE \quad , \tag{A.44}$$

is finite but independent of E'. This is somewhat expected due to the overall effect of ε_2 being a continuous function and that

$$\int_{-\infty}^{-10} \frac{1}{E'-E} dE + \int_{10}^{\infty} \frac{1}{E'-E} dE \approx \int_{-\infty}^{-10} \frac{1}{E'+\zeta-E} dE + \int_{10}^{\infty} \frac{1}{E'+\zeta-E} dE \quad , \tag{A.45}$$

where ζ is taken to satisfy $0 \ll |E'+\zeta| \ll 10eV$. Clearly this holds only because for the most part $|E| \gg 10$ eV.

By contrast, approximating $err(E')$ to a constant when $|E'| \approx 10$ eV or $|E'| \approx 0$ eV is not expected to hold anymore.

In Fig. A.1 we show the xx component of ε_2 for the 2H-MoS$_2$ monolayer, our calculated ε_1 and the FHI-AIMS calculated ε_1. Here, we found that the constant value by which we can approximate $err(E')$ when $0\ eV \ll |E'| \ll 10$ eV was the minimum value of $\varepsilon_1(E')$, where $E' \in [0, 10]$ eV. As it can be seen, the boundary regions are increasingly deviating from the correct spectrum due to the error effect we described.

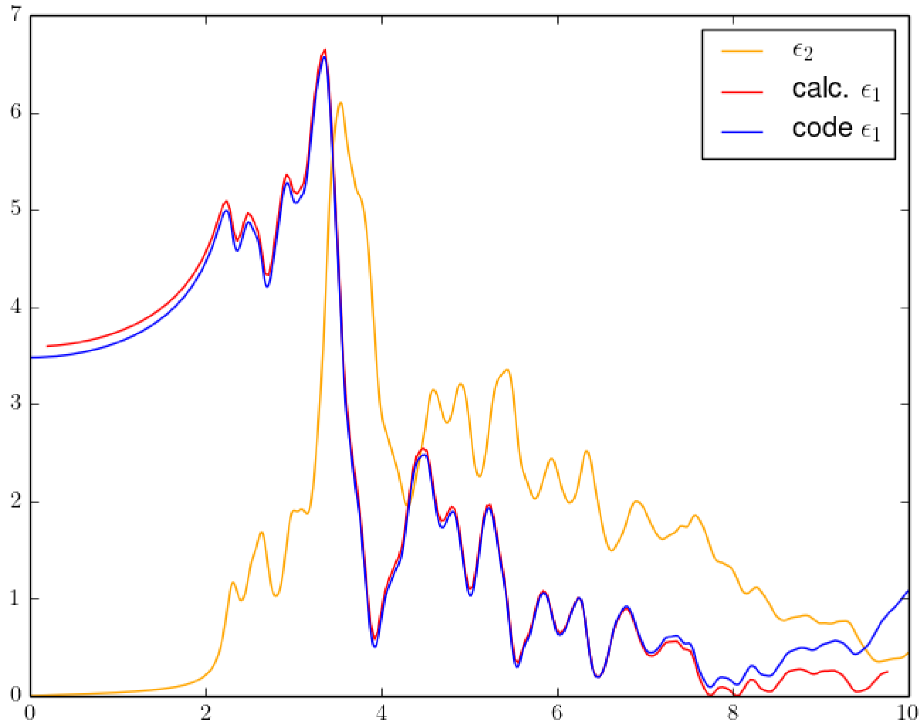

Figure A.1: The orange line designates the xx component of the imaginary part of the dielectric function as computed from DFT for 2H-MoS$_2$ monolayer, the red line is the calculated real part of the dielectric function using the approach described herein and the blue line is the real part of the dielectric function as obtained from DFT.

A.4 Additional information for Chapter 5

Below we present the complete list of the scaling factors μ_{xx}, μ_{zz} and their corresponding δ values.

Compound	μ_{xx}	δ
1T-PbI_2	3.09	0.71
1T-GeI_2	2.90	0.47
1T-$PtSe_2$	1.76	0.46
1T-STl_2	1.64	0.21
2H-WS_2	1.39	0.97
1T-$PtTe_2$	1.24	0.46
1T-OTl_2	1.19	0.80
1T-HfS_2	1.05	0.35
1T-$PdTe_2$	1.02	0.54
2H-GeI_2	0.96	0.35
1T-PtS_2	0.93	0.29
2H-WSe_2	0.93	0.99
1T-$HfSe_2$	0.91	1.27
2H-MoS_2	0.86	1.00
1T-$HfTe_2$	0.85	1.44
2H-$ZrCl_2$	0.85	0.92
1T-$SnSe_2$	0.83	1.59
2H-WTe_2	0.81	0.56
1T-ZrS_2	0.77	0.44
2H-$MoSe_2$	0.72	0.56
1T-$ZrSe_2$	0.67	1.22
2H-$MoTe_2$	0.65	0.33
1T-CdI_2	0.50	0.42
1T-ZnI_2	0.48	0.71
1T-TiS_2	0.43	0.72
2H-$HfTe_2$	0.38	0.68
1T-SnS_2	0.38	0.62
1T-PtO_2	0.32	0.19
1T-YbI_2	0.09	0.34

Table A.1: μ_{xx} and δ for $Im(\varepsilon_{xx})$ calculated with 20x20x1 k-points and with η=0.1 eV.

Compound	μ_{zz}	δ
1T-PbI_2	1.06	0.15
1T-GeI_2	0.81	0.27
1T-$PtSe_2$	0.63	0.54
1T-STl_2	0.68	1.33
2H-WS_2	0.04	0.62
1T-$PtTe_2$	0.46	1.30
1T-OTl_2	0.37	3.78
1T-HfS_2	0.23	0.13
1T-$PdTe_2$	0.39	2.49
2H-GeI_2	0.74	1.70
1T-PtS_2	0.29	0.26
2H-WSe_2	0.07	0.74
1T-$HfSe_2$	0.21	0.60
2H-MoS_2	0.04	0.60
1T-$HfTe_2$	0.22	2.43
2H-$ZrCl_2$	0.04	4.80
1T-$SnSe_2$	0.26	4.94
2H-WTe_2	0.10	0.87
1T-ZrS_2	0.21	0.20
2H-$MoSe_2$	0.07	0.97
1T-$ZrSe_2$	0.18	0.65
2H-$MoTe_2$	0.09	1.28
1T-CdI_2	0.12	0.13
1T-ZnI_2	0.10	0.27
1T-TiS_2	0.09	2.32
2H-$HfTe_2$	0.17	0.50
1T-SnS_2	0.10	1.07
1T-PtO_2	0.07	0.33
1T-YbI_2	0.04	0.28

Table A.2: μ_{zz} and δ for $Im(\varepsilon_{zz})$ calculated with 20x20x1 k-points and with η=0.1 eV.

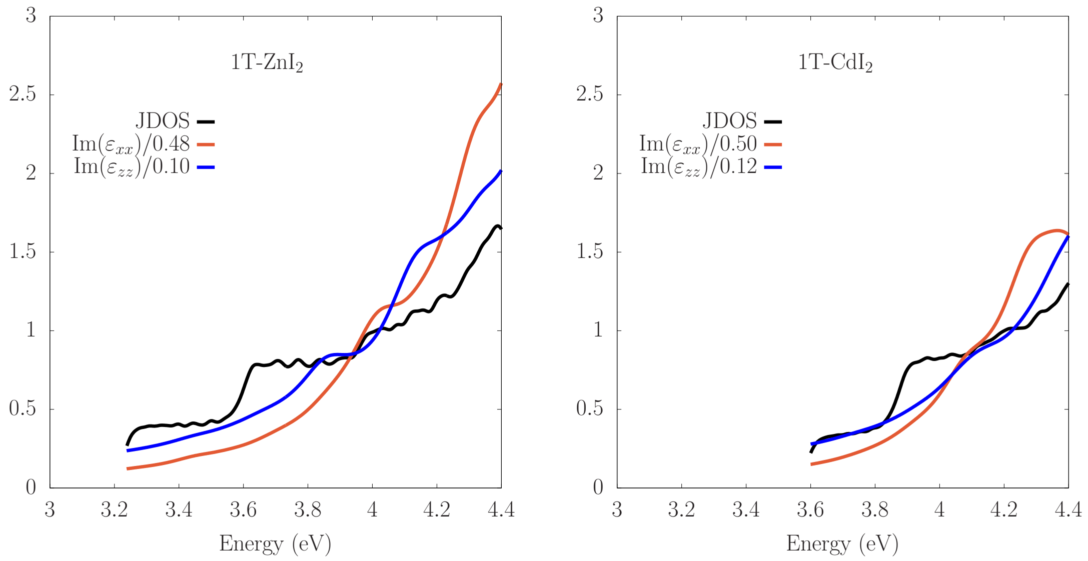

Figure A.2: a) JDOS spectrum, $Im(\varepsilon_{xx})$ and $Im(\varepsilon_{zz})$ for 1T-ZnI$_2$, where the latter two are scaled by μ_{xx} and μ_{zz}, respectively. b) Same as in a) but for the compound 1T-CdI$_2$. These two materials are shown here since they exhibit among the lowest values of J_{sc}. Their δ values corresponding to μ_{zz} are very low as seen in Table A.2.

Bibliography

[1] Elmar Kriegler, Keywan Riahi, Nico Bauer, Valeria Jana Schwanitz, Nils Petermann, Valentina Bosetti, Adriana Marcucci, Sander Otto, Leonidas Paroussos, Shilpa Rao, et al. Making or breaking climate targets: The ampere study on staged accession scenarios for climate policy. *Technological Forecasting and Social Change*, 90:24–44, 2015.

[2] Detlef P Vuuren, Andries Frido Hof, and Michael Gerardus Jacobus Elzen. *Meeting the 2 C Target: From Climate Objective to Emission Reduction Measures.* Netherlands Environmental Assessment Agency, 2009.

[3] Alexandre C Köberle, David EHJ Gernaat, and Detlef P van Vuuren. Assessing current and future techno-economic potential of concentrated solar power and photovoltaic electricity generation. *Energy*, 89:739–756, 2015.

[4] Michael Peters, Tobias S Schmidt, David Wiederkehr, and Malte Schneider. Shedding light on solar technologies—a techno-economic assessment and its policy implications. *Energy Policy*, 39(10):6422–6439, 2011.

[5] http://solargis.info.

[6] Tetsuo Soga. Fundamentals of solar cell. In *Nanostructured Materials for Solar Energy Conversion*, pages 3–43. Elsevier, 2006.

[7] Chaudhery Mustansar Hussain. *Handbook of nanomaterials for industrial applications.* Elsevier, 2018.

[8] Standard tables for reference solar spectral irradiances: direct normal and hemispherical on 37° tilted surface. *ASTM G173 - 03*, 14.04, 2012.

[9] Sven Rühle. Tabulated values of the Shockley–Queisser limit for single junction solar cells. *Solar Energy*, 130:139–147, 2016.

[10] Martin A. Green, Keith Emery, Yoshihiro Hishikawa, Wilhelm Warta, and Ewan D. Dunlop. Solar cell efficiency tables (version 42). *Prog. Photovolt*, 21: 827–837, 2013.

[11] Pabitra K Nayak, Suhas Mahesh, Henry J Snaith, and David Cahen. Photovoltaic solar cell technologies: analysing the state of the art. *Nature Reviews Materials*, 4(4):269, 2019.

[12] Mikio Taguchi, Ayumu Yano, Satoshi Tohoda, Kenta Matsuyama, Yuya Nakamura, Takeshi Nishiwaki, Kazunori Fujita, and Eiji Maruyama. 24.7% record efficiency hit solar cell on thin silicon wafer. *IEEE Journal of photovoltaics*, 4 (1):96–99, 2013.

[13] Armin Richter, Martin Hermle, and Stefan W Glunz. Reassessment of the limiting efficiency for crystalline silicon solar cells. *IEEE journal of photovoltaics*, 3(4):1184–1191, 2013.

[14] YM Yang, A Yu, B Hsu, WC Hsu, A Yang, and CW Lan. Development of high-performance multicrystalline silicon for photovoltaic industry. *Progress in Photovoltaics: Research and Applications*, 23(3):340–351, 2015.

[15] Daniel Macdonald and LJ Geerligs. Recombination activity of interstitial iron and other transition metal point defects in p-and n-type crystalline silicon. *Applied Physics Letters*, 85(18):4061–4063, 2004.

[16] Jan Benick, Armin Richter, Ralph Müller, Hubert Hauser, Frank Feldmann, Patricia Krenckel, Stephan Riepe, Florian Schindler, Martin C Schubert, Martin Hermle, et al. High-efficiency n-type hp mc silicon solar cells. *IEEE journal of photovoltaics*, 7(5):1171–1175, 2017.

[17] Martin A. Green, Keith Emery, Yoshihiro Hishikawa, Wilhelm Warta, and Ewan D. Dunlop. Solar efficiency tables (version 53). *Prog. Photovolt.*, 27: 3–12, 2019.

[18] K Shoori and G Kavei. " copper indium gallium diselenide–cigs photovoltiac solar cell technology a review". *Int.Mater.Phys*, 1:15–21, 2013.

[19] Michael Grätzel. Dye-sensitized solar cells. *Journal of photochemistry and photobiology C: Photochemistry Reviews*, 4(2):145–153, 2003.

[20] Sonali Das, Deepak Pandey, Jayan Thomas, and Tania Roy. The role of graphene and other 2d materials in solar photovoltaics. *Advanced Materials*, 31(1):1802722, 2019.

[21] Deji Akinwande, Nicholas Petrone, and James Hone. Two-dimensional flexible nanoelectronics. *Nature communications*, 5(1):1–12, 2014.

[22] Changgu Lee, Xiaoding Wei, Jeffrey W Kysar, and James Hone. Measurement of the elastic properties and intrinsic strength of monolayer graphene. *science*, 321(5887):385–388, 2008.

[23] Frank Schwierz. Graphene transistors: status, prospects, and problems. *Proceedings of the IEEE*, 101(7):1567–1584, 2013.

[24] Yanqing Wu, Keith A Jenkins, Alberto Valdes-Garcia, Damon B Farmer, Yu Zhu, Ageeth A Bol, Christos Dimitrakopoulos, Wenjuan Zhu, Fengnian Xia, Phaedon Avouris, et al. State-of-the-art graphene high-frequency electronics. *Nano letters*, 12(6):3062–3067, 2012.

[25] Kenji Watanabe, Takashi Taniguchi, and Hisao Kanda. Direct-bandgap properties and evidence for ultraviolet lasing of hexagonal boron nitride single crystal. *Nature materials*, 3(6):404–409, 2004.

[26] Saptarshi Das, Hong-Yan Chen, Ashish Verma Penumatcha, and Joerg Appenzeller. High performance multilayer mos2 transistors with scandium contacts. *Nano letters*, 13(1):100–105, 2013.

[27] Hui Fang, Steven Chuang, Ting Chia Chang, Kuniharu Takei, Toshitake Takahashi, and Ali Javey. High-performance single layered wse2 p-fets with chemically doped contacts. *Nano letters*, 12(7):3788–3792, 2012.

[28] Pere Miró, Martha Audiffred, and Thomas Heine. An atlas of two-dimensional materials. *Chemical Society Reviews*, 43(18):6537–6554, 2014.

[29] Arijit Bardhan Roy, Arup Dhar, Mrinmoyee Choudhuri, Sonali Das, S Minhaz Hossain, and Avra Kundu. Black silicon solar cell: analysis optimization and evolution towards a thinner and flexible future. *Nanotechnology*, 27(30): 305302, 2016.

[30] Arijit Bardhan Roy, Sonali Das, Avra Kundu, Chandan Banerjee, and Nillohit Mukherjee. c-si/n-zno-based flexible solar cells with silica nanoparticles as a light trapping metamaterial. *Physical Chemistry Chemical Physics*, 19(20): 12838–12844, 2017.

[31] Atse Louwen, Wilfried Van Sark, Ruud Schropp, and André Faaij. A cost roadmap for silicon heterojunction solar cells. *Solar Energy Materials and Solar Cells*, 147:295–314, 2016.

[32] Piotr Kowalczewski and Lucio Claudio Andreani. Towards the efficiency limits of silicon solar cells: How thin is too thin? *Solar Energy Materials and Solar Cells*, 143:260–268, 2015.

[33] A Metz, M Fischer, and J Trube. International technology roadmap for photovoltaics (itrpv): Crystalline silicon technology-current status and outlook. In *Proceedings of the PV Manufacturing in Europe Conference, Brussels, Belgium*, pages 18–19, 2017.

[34] Meng-Lin Tsai, Sheng-Han Su, Jan-Kai Chang, Dung-Sheng Tsai, Chang-Hsiao Chen, Chih-I Wu, Lain-Jong Li, Lih-Juann Chen, and Jr-Hau He. Monolayer mos2 heterojunction solar cells. *ACS nano*, 8(8):8317–8322, 2014.

[35] Michael Grätzel. The light and shade of perovskite solar cells. *Nature materials*, 13(9):838, 2014.

[36] Lei Zhai, Saiful I Khondaker, Jayan Thomas, Chen Shen, and Matthew McInnis. Ordered conjugated polymer nano-and microstructures: Structure control for improved performance of organic electronics. *Nano Today*, 9(6):705–721, 2014.

[37] Chao Li, Joseph Sleppy, Nitesh Dhasmana, Mikhael Soliman, Laurene Tetard, and Jayan Thomas. A pcbm-assisted perovskite growth process to fabricate high efficiency semitransparent solar cells. *Journal of Materials Chemistry A*, 4(30):11648–11655, 2016.

[38] Dian Wang, Matthew Wright, Naveen Kumar Elumalai, and Ashraf Uddin. Stability of perovskite solar cells. *Solar Energy Materials and Solar Cells*, 147: 255–275, 2016.

[39] Mohammed Aziz Ibrahem, Tian-wey Lan, Jing Kai Huang, Yang-Yuan Chen, Kung-Hwa Wei, Lain-Jong Li, and Chih Wei Chu. High quantity and quality few-layers transition metal disulfide nanosheets from wet-milling exfoliation. *RSC advances*, 3(32):13193–13202, 2013.

[40] Andres Castellanos-Gomez. Why all the fuss about 2d semiconductors? *Nature Photonics*, 10(4):202, 2016.

[41] Marco Bernardi, Maurizia Palummo, and Jeffrey C. Grossman. Extraordinary sunlight absorption and one nanometer thick photovoltaics using two-dimensional monolayer materials. *Nano Lett.*, 13(8):3664–3670, 2013.

[42] KS Novoselov, A Mishchenko, A Carvalho, and AH Castro Neto. 2d materials and van der waals heterostructures. *Science*, 353(6298):aac9439, 2016.

[43] Hye Yun Jeong, Un Jeong Kim, Hyun Kim, Gang Hee Han, Hyangsook Lee, Min Su Kim, Youngjo Jin, Thuc Hue Ly, Si Young Lee, Young-Geun Roh, et al. Optical gain in mos2 via coupling with nanostructured substrate: fabry–perot interference and plasmonic excitation. *ACS nano*, 10(9):8192–8198, 2016.

[44] Min Seok Jang, Victor W Brar, Michelle C Sherrott, Josue J Lopez, Laura Kim, Seyoon Kim, Mansoo Choi, Harry A Atwater, et al. Tunable large resonant absorption in a midinfrared graphene salisbury screen. *Physical Review B*, 90(16):165409, 2014.

[45] Liam Britnell, RM Ribeiro, A Eckmann, R Jalil, BD Belle, A Mishchenko, Y-J Kim, RV Gorbachev, T Georgiou, SV Morozov, et al. Strong light-matter

interactions in heterostructures of atomically thin films. *Science*, 340(6138): 1311–1314, 2013.

[46] Marco M Furchi, Armin A Zechmeister, Florian Hoeller, Stefan Wachter, Andreas Pospischil, and Thomas Mueller. Photovoltaics in van der waals heterostructures. *IEEE Journal of Selected Topics in Quantum Electronics*, 23 (1):106–116, 2016.

[47] Chul-Ho Lee, Gwan-Hyoung Lee, Arend M Van Der Zande, Wenchao Chen, Yilei Li, Minyong Han, Xu Cui, Ghidewon Arefe, Colin Nuckolls, Tony F Heinz, et al. Atomically thin p–n junctions with van der waals heterointerfaces. *Nature nanotechnology*, 9(9):676, 2014.

[48] Hui Fang, Corsin Battaglia, Carlo Carraro, Slavomir Nemsak, Burak Ozdol, Jeong Seuk Kang, Hans A Bechtel, Sujay B Desai, Florian Kronast, Ahmet A Unal, et al. Strong interlayer coupling in van der waals heterostructures built from single-layer chalcogenides. *Proceedings of the National Academy of Sciences*, 111(17):6198–6202, 2014.

[49] Tania Roy, Mahmut Tosun, Mark Hettick, Geun Ho Ahn, Chenming Hu, and Ali Javey. 2d-2d tunneling field-effect transistors using wse2/snse2 heterostructures. *Applied Physics Letters*, 108(8):083111, 2016.

[50] Rui Cheng, Dehui Li, Hailong Zhou, Chen Wang, Anxiang Yin, Shan Jiang, Yuan Liu, Yu Chen, Yu Huang, and Xiangfeng Duan. Electroluminescence and photocurrent generation from atomically sharp wse2/mos2 heterojunction p–n diodes. *Nano letters*, 14(10):5590–5597, 2014.

[51] Keiichiro Masuko, Masato Shigematsu, Taiki Hashiguchi, Daisuke Fujishima, Motohide Kai, Naoki Yoshimura, Tsutomu Yamaguchi, Yoshinari Ichihashi, Takahiro Mishima, Naoteru Matsubara, et al. Achievement of more than 25% conversion efficiency with crystalline silicon heterojunction solar cell. *IEEE Journal of Photovoltaics*, 4(6):1433–1435, 2014.

[52] Jian Ye, Xueliang Li, Jianjun Zhao, Xuelan Mei, and Qian Li. A facile way to fabricate high-performance solution-processed n-mos 2/p-mos 2 bilayer photodetectors. *Nanoscale research letters*, 10(1):1–7, 2015.

[53] Joeson Wong, Deep Jariwala, Giulia Tagliabue, Kevin Tat, Artur R Davoyan, Michelle C Sherrott, and Harry A Atwater. High photovoltaic quantum efficiency in ultrathin van der waals heterostructures. *ACS nano*, 11(7):7230–7240, 2017.

[54] KS Novoselov and AH Castro Neto. Two-dimensional crystals-based heterostructures: materials with tailored properties. *Physica Scripta*, 2012(T146):014006, 2012.

[55] Ming-Yang Li, Chang-Hsiao Chen, Yumeng Shi, and Lain-Jong Li. Heterostructures based on two-dimensional layered materials and their potential applications. *Materials Today*, 19(6):322–335, 2016.

[56] William Shockley and Hans J Queisser. Detailed balance limit of efficiency of p-n junction solar cells. *Journal of Applied Physics*, 32(3):510–519, 1961.

[57] Yunlu Xu, Tao Gong, and Jeremy N Munday. The generalized shockley-queisser limit for nanostructured solar cells. *Scientific reports*, 5:13536, 2015.

[58] Fahhad H Alharbi, Sergey N Rashkeev, Fedwa El-Mellouhi, Hans P Lüthi, Nouar Tabet, and Sabre Kais. An efficient descriptor model for designing materials for solar cells. *arXiv preprint arXiv:1706.01974*, 2017.

[59] Liping Yu and Alex Zunger. Identification of potential photovoltaic absorbers based on first-principles spectroscopic screening of materials. *Physical Review Letters*, 108(6):068701, 2012.

[60] M. Würfel. *Proc. I.R.E.*, (48):1246, 1960.

[61] Robert A Alberty. Principle of detailed balance in kinetics. *Journal of Chemical Education*, 81(8):1206, 2004.

[62] A De Vos and H Pauwels. On the thermodynamic limit of photovoltaic energy conversion. *Applied physics*, 25(2):119–125, 1981.

[63] WOLFGANG Ruppel and PETER Wurfel. Upper limit for the conversion of solar energy. *IEEE Transactions on Electron Devices*, 27(4):877–882, 1980.

[64] Martin A. Green, Keith Emery, Yoshihiro Hishikawa, Wilhelm Warta, and Ewan D. Dunlop. Solar cell efficiency tables (version 47). *Prog. Photovolt*, 24: 3–11, 2016.

[65] Brendan M Kayes, Hui Nie, Rose Twist, Sylvia G Spruytte, Frank Reinhardt, Isik C Kizilyalli, and Gregg S Higashi. 27.6% conversion efficiency, a new record for single-junction solar cells under 1 sun illumination. Photovoltaic Specialists Conference (PVSC), 2011 37th IEEE:4–8, 2011.

[66] CJ Keavney, VE Haven, and SM Vernon. Emitter structures in mocvd inp solar cells. In *IEEE Conference on Photovoltaic Specialists*, pages 141–144. IEEE, 1990.

[67] John F Geisz, Myles A Steiner, I Garcia, Sarah R Kurtz, and Daniel J Friedman. Enhanced external radiative efficiency for 20.8% efficient single-junction gainp solar cells. *Applied Physics Letters*, 103(4):041118, 2013.

[68] William H Huber and Anil R Duggal. The renaissance of cdte-based photovoltaics. In *Thin Films for Solar and Energy Technology VI*, volume 9177, page 917702. International Society for Optics and Photonics, 2014.

[69] M Osborne. Hanergys solibro has 20.5% cigs solar cell verified by nrel, 2014.

[70] Mingzhen Liu, Michael B Johnston, and Henry J Snaith. Efficient planar heterojunction perovskite solar cells by vapour deposition. *Nature*, 501(7467): 395–398, 2013.

[71] Lars Hedin. New method for calculating the one-particle green's function with application to the electron-gas problem. *Physical Review*, 139(3A):A796, 1965.

[72] Jochen Heyd, Gustavo E Scuseria, and Matthias Ernzerhof. Hybrid functionals based on a screened coulomb potential. *J. Chem. Phys.*, 118(18):8207–8215, 2003.

[73] Martin A. Green, Keith Emery, Yoshihiro Hishikawa, Wilhelm Warta, and Ewan D. Dunlop. Solar cell efficiency tables (version 42). *Prog. Photovolt*, 19: 565, 2011.

[74] Michael P Marder. *Condensed matter physics*. John Wiley & Sons, 2010.

[75] Neil W Ashcroft, N David Mermin, et al. Solid state physics [by] neil w. ashcroft [and] n. david mermin. 1976.

[76] Pierre Hohenberg and Walter Kohn. Inhomogeneous electron gas. *Physical review*, 136(3B):B864, 1964.

[77] Mel Levy. Universal variational functionals of electron densities, first-order density matrices, and natural spin-orbitals and solution of the v-representability problem. *Proceedings of the National Academy of Sciences*, 76(12):6062–6065, 1979.

[78] Mel Levy. Electron densities in search of hamiltonians. *Physical Review A*, 26 (3):1200, 1982.

[79] Subhayan Roychoudhury. Ab initio calculation of parameters for electron and spin transport in organic crystals. *PhD Thesis*, 2018.

[80] Walter Kohn and Lu Jeu Sham. Self-consistent equations including exchange and correlation effects. *Physical review*, 140(4A):A1133, 1965.

[81] Viraht Sahni, K-P Bohnen, and Manoj K Harbola. Analysis of the local-density approximation of density-functional theory. *Physical Review A*, 37(6): 1895, 1988.

[82] Abhirup Patra, Jefferson E Bates, Jianwei Sun, and John P Perdew. Properties of real metallic surfaces: Effects of density functional semilocality and van der waals nonlocality. *Proceedings of the National Academy of Sciences*, 114(44): E9188–E9196, 2017.

[83] John P Perdew, Kieron Burke, and Matthias Ernzerhof. Generalized gradient approximation made simple. *Phys. Rev. Lett.*, 77(18):3865, 1996.

[84] Aron J Cohen, Paula Mori-Sánchez, and Weitao Yang. Insights into current limitations of density functional theory. *Science*, 321(5890):792–794, 2008.

[85] Paula Mori-Sánchez, Aron J Cohen, and Weitao Yang. Localization and delocalization errors in density functional theory and implications for band-gap prediction. *Physical review letters*, 100(14):146401, 2008.

[86] Eberhard Engel and Reiner M Dreizler. *Density functional theory*. Springer, 2013.

[87] John P Perdew and Mel Levy. Physical content of the exact kohn-sham orbital energies: band gaps and derivative discontinuities. *Physical Review Letters*, 51(20):1884, 1983.

[88] Benjamin G Janesko, Thomas M Henderson, and Gustavo E Scuseria. Screened hybrid density functionals for solid-state chemistry and physics. *Physical Chemistry Chemical Physics*, 11(3):443–454, 2009.

[89] Stefano Sanvito. Self-interaction errors in density functional calculations of electronic transport. In *APS March Meeting Abstracts*, 2006.

[90] Jochen Heyd and Gustavo E Scuseria. Efficient hybrid density functional calculations in solids: Assessment of the heyd–scuseria–ernzerhof screened coulomb hybrid functional. *The Journal of chemical physics*, 121(3):1187–1192, 2004.

[91] Carlo Adamo and Vincenzo Barone. Toward reliable density functional methods without adjustable parameters: The pbe0 model. *The Journal of chemical physics*, 110(13):6158–6170, 1999.

[92] Matthias Ernzerhof and Gustavo E Scuseria. Assessment of the perdew–burke–ernzerhof exchange-correlation functional. *The Journal of chemical physics*, 110(11):5029–5036, 1999.

[93] Aliaksandr V Krukau, Oleg A Vydrov, Artur F Izmaylov, and Gustavo E Scuseria. Influence of the exchange screening parameter on the performance of screened hybrid functionals. *The Journal of Chemical Physics*, 125(22): 224106, 2006.

[94] John P Perdew, Matthias Ernzerhof, and Kieron Burke. Rationale for mixing exact exchange with density functional approximations. *The Journal of chemical physics*, 105(22):9982–9985, 1996.

[95] Oleg A Vydrov, Gustavo E Scuseria, and John P Perdew. Tests of functionals for systems with fractional electron number. *The Journal of chemical physics*, 126(15):154109, 2007.

[96] Thomas M Henderson, Joachim Paier, and Gustavo E Scuseria. Accurate treatment of solids with the hse screened hybrid. *physica status solidi (b)*, 248 (4):767–774, 2011.

[97] Adrienn Ruzsinszky, John P Perdew, Gábor I Csonka, Oleg A Vydrov, and Gustavo E Scuseria. Spurious fractional charge on dissociated atoms: Pervasive and resilient self-interaction error of common density functionals. *The Journal of chemical physics*, 125(19):194112, 2006.

[98] Paula Mori-Sánchez, Aron J Cohen, and Weitao Yang. Many-electron self-interaction error in approximate density functionals, 2006.

[99] Aron J Cohen, Paula Mori-Sánchez, and Weitao Yang. Fractional charge perspective on the band gap in density-functional theory. *Physical Review B*, 77(11):115123, 2008.

[100] A Seidl, A Görling, P Vogl, JA Majewski, and M Levy. Generalized kohn-sham schemes and the band-gap problem. *Physical Review B*, 53(7):3764, 1996.

[101] Ralf Neumann, Ross H Nobes, and Nicholas C Handy. Exchange functionals and potentials. *Molecular Physics*, 87(1):1–36, 1996.

[102] Qin Wu and Weitao Yang. Empirical correction to density functional theory for van der waals interactions. *The Journal of chemical physics*, 116(2):515–524, 2002.

[103] K Rapcewicz and NW Ashcroft. Fluctuation attraction in condensed matter: A nonlocal functional approach. *Physical Review B*, 44(8):4032, 1991.

[104] John F Dobson and Bradley P Dinte. Constraint satisfaction in local and gradient susceptibility approximations: Application to a van der waals density functional. *Physical review letters*, 76(11):1780, 1996.

[105] Walter Kohn, Yigal Meir, and Dmitrii E Makarov. van der waals energies in density functional theory. *Physical review letters*, 80(19):4153, 1998.

[106] Alexandre Tkatchenko and Matthias Scheffler. Accurate molecular van der Waals interactions from ground-state electron density and free-atom reference data. *Phys. Rev. Lett.*, 102(7):073005, 2009.

[107] Alexandre Tkatchenko, Robert A DiStasio Jr, Roberto Car, and Matthias Scheffler. Accurate and efficient method for many-body van der waals interactions. *Physical review letters*, 108(23):236402, 2012.

[108] Volker Blum, Ralf Gehrke, Felix Hanke, Paula Havu, Ville Havu, Xinguo Ren, Karsten Reuter, and Matthias Scheffler. Ab initio molecular simulations with numeric atom-centered orbitals. *Comp. Phys. Comm.*, 180(11):2175–2196, 2009.

[109] Georg Kresse and Jürgen Furthmüller. Efficiency of ab-initio total energy calculations for metals and semiconductors using a plane-wave basis set. *Computational materials science*, 6(1):15–50, 1996.

[110] Georg Kresse and Jürgen Furthmüller. Efficient iterative schemes for ab initio total-energy calculations using a plane-wave basis set. *Physical review B*, 54 (16):11169, 1996.

[111] F Weigend and RJPCCP Ahlrichs. 7, 3297-3305; b) f. weigend. *Phys. Chem. Chem. Phys*, 8:1057–1065, 2005.

[112] Michael J Frisch, John A Pople, and J Stephen Binkley. Self-consistent molecular orbital methods 25. supplementary functions for gaussian basis sets. *The Journal of chemical physics*, 80(7):3265–3269, 1984.

[113] Friedhelm Bechstedt. *Many-Body Approach to Electronic Excitations.* Springer, 2016.

[114] Giovanni Onida, Lucia Reining, and Angel Rubio. Electronic excitations: density-functional versus many-body green's-function approaches. *Reviews of Modern Physics*, 74(2):601, 2002.

[115] Claudia Ambrosch-Draxl and Jorge O Sofo. Linear optical properties of solids within the full-potential linearized augmented planewave method. *Comp. Phys. Comm.*, 175(1):1–14, 2006.

[116] Friedhelm Bechstedt. Quasiparticle corrections for energy gaps in semiconductors. *Advances in Solid State Physics*, 32, 1992.

[117] Mark S Hybertsen and Steven G Louie. Electron correlation in semiconductors and insulators: Band gaps and quasiparticle energies. *Physical Review B*, 34 (8):5390, 1986.

[118] Stephen L Adler. Quantum theory of the dielectric constant in real solids. *Physical Review*, 126(2):413, 1962.

[119] Nathan Wiser. Dielectric constant with local field effects included. *Physical Review*, 129(1):62, 1963.

[120] J Lindhard, M Scharff, and HE Schiøtt. Kgl. danske videnskab. selskab, mat. *Fys. Medd*, 28(8):l954, 1954.

[121] James MacQueen et al. Some methods for classification and analysis of multivariate observations. In *Proceedings of the fifth Berkeley symposium on mathematical statistics and probability*, volume 1, pages 281–297. Oakland, CA, USA, 1967.

[122] Hugo Steinhaus. Sur la division des corps materiels en parties. Bull. Acad. Polon. Sci., C1. III vol IV: 801-804. 1956.

[123] Stuart Lloyd. Least squares quantization in pcm. *IEEE transactions on information theory*, 28(2):129–137, 1982.

[124] John A Hartigan and Manchek A Wong. Algorithm AS 136: A k-means clustering algorithm. *Journal of the Royal Statistical Society. Series C (Applied Statistics)*, 28(1):100–108, 1979.

[125] Hans-Peter Kriegel, Erich Schubert, and Arthur Zimek. The (black) art of runtime evaluation: Are we comparing algorithms or implementations? *Knowledge and Information Systems*, 52(2):341–378, 2017.

[126] Laurens van der Maaten and Geoffrey Hinton. Visualizing data using t-sne. *Journal of machine learning research*, 9(Nov):2579–2605, 2008.

[127] Yuansheng Zhou and Tatyana Sharpee. Using global t-sne to preserve inter-cluster data structure. *bioRxiv*, page 331611, 2018.

[128] Martin Wattenberg, Fernanda Viégas, and Ian Johnson. How to use t-sne effectively. *Distill*, 1(10):e2, 2016.

[129] Solomon Kullback. Letter to the editor: The kullback–leibler distance. *The American Statistician*, 41(4):340–341, 1987.

[130] Alessio Filippetti, Pietro Delugas, and Alessandro Mattoni. Radiative recombination and photoconversion of methylammonium lead iodide perovskite by first principles: properties of an inorganic semiconductor within a hybrid body. *The Journal of Physical Chemistry C*, 118(43):24843–24853, 2014.

[131] Fabien Tran and Peter Blaha. Importance of the kinetic energy density for band gap calculations in solids with density functional theory. *The Journal of Physical Chemistry A*, 121(17):3318–3325, 2017.

[132] Otfried Madelung. *Semiconductors: data handbook*. Springer Science & Business Media, 2012.

[133] Yaguang Guo, Qian Wang, Yoshiyuki Kawazoe, and Puru Jena. A new silicon phase with direct band gap and novel optoelectronic properties. *Scientific Reports*, 5, 2015.

[134] Kunta Yoshikawa, Hayato Kawasaki, Wataru Yoshida, Toru Irie, Katsunori Konishi, Kunihiro Nakano, Toshihiko Uto, Daisuke Adachi, Masanori Kanematsu, Hisashi Uzu, et al. Silicon heterojunction solar cell with interdigitated back contacts for a photoconversion efficiency over 26%. *Nature Energy*, 2(5): 17032, 2017.

[135] Sayak Bhattacharya and Sajeev John. Beyond 30% conversion efficiency in silicon solar cells: A numerical demonstration. *Scientific reports*, 9(1):1–15, 2019.

[136] GD Cody, T Tiedje, B Abeles, B Brooks, and Y Goldstein. Disorder and the optical-absorption edge of hydrogenated amorphous silicon. *Physical Review Letters*, 47(20):1480, 1981.

[137] Stefaan De Wolf, Jakub Holovsky, Soo-Jin Moon, Philipp Loper, Bjoern Niesen, Martin Ledinsky, Franz-Josef Haug, Jun-Ho Yum, and Christophe Ballif. Organometallic halide perovskites: sharp optical absorption edge and its relation to photovoltaic performance. *The journal of physical chemistry letters*, 5(6):1035–1039, 2014.

[138] Dianyi Liu and Timothy L Kelly. Perovskite solar cells with a planar heterojunction structure prepared using room-temperature solution processing techniques. *Nature photonics*, 8(2):133, 2014.

[139] Tom Baikie, Yanan Fang, Jeannette M Kadro, Martin Schreyer, Fengxia Wei, Subodh G Mhaisalkar, Michael Graetzel, and Tim J White. Synthesis and crystal chemistry of the hybrid perovskite (ch 3 nh 3) pbi 3 for solid-state sensitised solar cell applications. *Journal of Materials Chemistry A*, 1(18): 5628–5641, 2013.

[140] Franz Urbach. The long-wavelength edge of photographic sensitivity and of the electronic absorption of solids. *Physical Review*, 92(5):1324, 1953.

[141] Mingchao Wang and Shangchao Lin. Anisotropic and ultralow phonon thermal transport in organic–inorganic hybrid perovskites: Atomistic insights into solar cell thermal management and thermoelectric energy conversion efficiency. *Advanced Functional Materials*, 26(29):5297–5306, 2016.

[142] OK Echendu, F Fauzi, AR Weerasinghe, and IM Dharmadasa. High short-circuit current density cdte solar cells using all-electrodeposited semiconductors. *Thin Solid Films*, 556:529–534, 2014.

[143] Louis C Kilmer and Allen M Barnett. A novel high open-circuit voltage p-n inp solar cell design. *Progress in Photovoltaics: Research and Applications*, 1 (3):181–192, 1993.

[144] Shizhao Fan, Daehwan Jung, Yukun Sun, Brian D Li, Diego Martín-Martín, and Minjoo L Lee. 16.8%-efficient n+/p gaas solar cells on si with high short-circuit current density. *IEEE Journal of Photovoltaics*, 9(3):660–665, 2019.

[145] Yinghui Sun, Rongming Wang, and Kai Liu. Substrate induced changes in atomically thin 2-dimensional semiconductors: Fundamentals, engineering, and applications. *Appl. Phys. Rev.*, 4(1):011301, 2017.

[146] Wonbong Choi, Nitin Choudhary, Gang Hee Han, Juhong Park, Deji Akinwande, and Young Hee Lee. Recent development of two-dimensional transition metal dichalcogenides and their applications. *Mater. Today*, 20(3):116–130, 2017.

[147] Pulickel Ajayan, Philip Kim, and Kaustav Banerjee. Two-dimensional van der waals materials. *Phys. Today*, 69(9):38–44, 2016.

[148] Andre K. Geim and Irina V. Grigorieva. Van der Waals heterostructures. *Nature*, 499(7459):419, 2013.

[149] Nitin Choudhary, Juhong Park, Jun Yeon Hwang, Hee-Suk Chung, Kenneth H. Dumas, Saiful I. Khondaker, Wonbong Choi, and Yeonwoong Jung. Centimeter scale patterned growth of vertically stacked few layer only 2D MoS_2/WS_2 van der Waals heterostructure. *Sci. Rep.*, 6:25456, 2016.

[150] Pasqual Rivera, Hongyi Yu, Kyle L. Seyler, Nathan P. Wilson, Wang Yao, and Xiaodong Xu. Interlayer valley excitons in heterobilayers of transition metal dichalcogenides. *Nature Nanotechnol.*, 13:1004, 2018.

[151] Jiahao Yan, Churong Ma, Yingcong Huang, and Guowei Yang. Tunable Control of Interlayer Excitons in WS_2/MoS_2 Heterostructures via Strong Coupling with Enhanced Mie Resonances. *Adv. Sci.*, 6:1802092, 2019.

[152] Hoseok Heo, Ji Ho Sung, Soonyoung Cha, Bo-Gyu Jang, Joo-Youn Kim, Gangtae Jin, Donghun Lee, Ji-Hoon Ahn, Myoung-Jae Lee, Ji Hoon Shim, et al. Interlayer orientation-dependent light absorption and emission in monolayer semiconductor stacks. *Nature Commun.*, 6:7372, 2015.

[153] Xiaoyang Zhu, Nicholas R Monahan, Zizhou Gong, Haiming Zhu, Kristopher W Williams, and Cory A Nelson. Charge transfer excitons at van der Waals interfaces. *J. Am. Chem. Soc.*, 137(26):8313–8320, 2015.

[154] Yifei Yu, Shi Hu, Liqin Su, Lujun Huang, Yi Liu, Zhenghe Jin, Alexander A Purezky, David B Geohegan, Ki Wook Kim, Yong Zhang, and Linyou Cao. Equally efficient interlayer exciton relaxation and improved absorption in epitaxial and nonepitaxial MoS_2/WS_2 heterostructures. *Nano Lett.*, 15(1):486–491, 2014.

[155] Kirsten Andersen, Simone Latini, and Kristian S Thygesen. Dielectric genome of van der Waals heterostructures. *Nano Lett.*, 15(7):4616–4621, 2015.

[156] Hannu-Pekka Komsa and Arkady V Krasheninnikov. Electronic structures and optical properties of realistic transition metal dichalcogenide heterostructures from first principles. *Phys. Rev. B*, 88(8):085318, 2013.

[157] Filip A Rasmussen and Kristian S Thygesen. Computational 2D materials database: electronic structure of transition-metal dichalcogenides and oxides. *J. Phys. Chem. C*, 119(23):13169–13183, 2015.

[158] Walter Kohn, Axel D Becke, and Robert G Parr. Density functional theory of electronic structure. *J. Phys. Chem.*, 100(31):12974–12980, 1996.

[159] Robert G Parr and Yang Weitao. *Density-Functional Theory of Atoms and Molecules*. Oxford University Press, 1994.

[160] Ville Havu, Volker Blum, Paula Havu, and Matthias Scheffler. Efficient O (N) integration for all-electron electronic structure calculation using numeric basis functions. *J. Comp. Phys.*, 228(22):8367–8379, 2009.

[161] Xinguo Ren, Patrick Rinke, Volker Blum, Jürgen Wieferink, Alexandre Tkatchenko, Andrea Sanfilippo, Karsten Reuter, and Matthias Scheffler. Resolution-of-identity approach to hartree–fock, hybrid density functionals, RPA, MP2 and GW with numeric atom-centered orbital basis functions. *New J. Phys.*, 14(5):053020, 2012.

[162] R. S. Mulliken. Electronic population analysis on LCAO-MO molecular wave functions. I. *J. Phys. Chem.*, 23:1833, 1955.

[163] M. Traving, T. Seydel, L. Kipp, M. Skibowski, F. Starrost, E. E. Krasovskii, A. Perlov, and W. Schattke. Combined photoemission and inverse photoemission study of HfS_2. *Phys. Rev. B*, 63:035107, 2001.

[164] C. Kreis, S. Werth, R. Adelung, L. Kipp, M. Skibowski, E. E. Krasovskii, and W. Schattke. Valence and conduction band states of HfS_2: From bulk to a single layer. *Phys. Rev. B*, 68:235331, 2003.

[165] Yuda Zhao, Jingsi Qiao, Peng Yu, Zhixin Hu, Ziyuan Lin, Shu Ping Lau, Zheng Liu, Wei Ji, and Yang Chai. Extraordinarily strong interlayer interaction in 2D layered PtS_2. *Adv. Mater.*, 28:2399, 2016.

[166] Rovi Angelo B. Villaos, Christian P. Crisostomo, Zhi-Quan Huang, Shin-Ming Huang, Allan Abraham B. Padama, Marvin A. Albao, Hsin Lin, and Feng-Chuan Chuang. Thickness dependent electronic properties of Pt dichalcogenides. *npj 2D Mater. App.*, 3:2, 2019.

[167] Samanta Witomska, Tim Leydecker, Artur Ciesielski, and Paolo Samorì. Production and patterning of liquid phase–exfoliated 2d sheets for applications in optoelectronics. *Advanced Functional Materials*, 29(22):1901126, 2019.

[168] Hong Wang, Fucai Liu, Wei Fu, Zheyu Fang, Wu Zhou, and Zheng Liu. Two-dimensional heterostructures: fabrication, characterization, and application. *Nanoscale*, 6(21):12250–12272, 2014.

[169] Xiumei Zhang, Haiyan Nan, Shaoqing Xiao, Xi Wan, Xiaofeng Gu, Aijun Du, Zhenhua Ni, and Kostya Ken Ostrikov. Transition metal dichalcogenides bilayer single crystals by reverse-flow chemical vapor epitaxy. *Nature communications*, 10(1):598, 2019.

[170] Jason S. Ross, Pasqual Rivera, John Schaibley, Eric Lee-Wong, Hongyi Yu, Takashi Taniguchi, Kenji Watanabe, Jiaqiang Yan, David Mandrus, David Cobden, Wang Yao, and Xiaodong Xu. Interlayer exciton optoelectronics in a 2d heterostructure p–n junction. *Nano Letters*, 17(2):638–643, 2017.

doi: 10.1021/acs.nanolett.6b03398. URL `https://doi.org/10.1021/acs.nanolett.6b03398`. PMID: 28006106.

[171] Simon Ovesen, Samuel Brem, Christopher Linderälv, Mikael Kuisma, Tobias Korn, Paul Erhart, Malte Selig, and Ermin Malic. Interlayer exciton dynamics in van der waals heterostructures. *Communications Physics*, 2(1):23, 2019.

[172] Simone Latini, Kirsten T Winther, Thomas Olsen, and Kristian S Thygesen. Interlayer excitons and band alignment in mos2/hbn/wse2 van der waals heterostructures. *Nano letters*, 17(2):938–945, 2017.

[173] Engin Torun, Henrique PC Miranda, Alejandro Molina-Sánchez, and Ludger Wirtz. Interlayer and intralayer excitons in mos 2/ws 2 and mose 2/wse 2 heterobilayers. *Physical Review B*, 97(24):245427, 2018.

[174] Avinash P Nayak, Tribhuwan Pandey, Damien Voiry, Jin Liu, Samuel T Moran, Ankit Sharma, Cheng Tan, Chang-Hsiao Chen, Lain-Jong Li, Manish Chhowalla, Jung-Fu Lin, Abhishek K. Singh, and Deji Akinwande. Pressure-dependent optical and vibrational properties of monolayer molybdenum disulfide. *Nano Lett.*, 15(1):346–353, 2014.

[175] Stefana Anais Colibaba, Sabine Körbel, Carlo Motta, Fedwa El-Mellouhi, and Stefano Sanvito. Interlayer dielectric function of a type-ii van der waals semiconductor: The HfS_2/PtS_2 heterobilayer. *Physical Review Materials*, 3(12): 124002, 2019.

[176] A Carvalho, RM Ribeiro, and AH Castro Neto. Band nesting and the optical response of two-dimensional semiconducting transition metal dichalcogenides. *Physical Review B*, 88(11):115205, 2013.

[177] J Thomas, G Jezequel, and I Pollini. Optical properties of layered transition-metal halides. *Journal of Physics: Condensed Matter*, 2(24):5439, 1990.

[178] Michael S Fuhrer and James Hone. Measurement of mobility in dual-gated MoS_2 transistors. *Nature nanotechnology*, 8(3):146–147, 2013.

[179] Kin Fai Mak, Changgu Lee, James Hone, Jie Shan, and Tony F Heinz. Atomically thin MoS_2: a new direct-gap semiconductor. *Physical review letters*, 105 (13):136805, 2010.

[180] Andreas Koitzsch, Anna-Sophie Pawlik, Carsten Habenicht, Tom Klaproth, Roman Schuster, Bernd Büchner, and Martin Knupfer. Nonlocal dielectric function and nested dark excitons in MoS_2. *npj 2D Materials and Applications*, 3(1):1–9, 2019.

[181] Bo Peng, Priscilla Kailian Ang, and Kian Ping Loh. Two-dimensional dichalcogenides for light-harvesting applications. *Nano Today*, 10(2):128–137, 2015.

[182] NMR Peres. Colloquium: The transport properties of graphene: An introduction. *Reviews of modern physics*, 82(3):2673, 2010.

[183] Robert L. Thorndike. Who belongs in the family? *Psychometrika*, 18(4): 267–276, 1953.

[184] Daichi Kozawa, Rajeev Kumar, Alexandra Carvalho, Kiran Kumar Amara, Weijie Zhao, Shunfeng Wang, Minglin Toh, Ricardo M Ribeiro, AH Castro Neto, Kazunari Matsuda, et al. Photocarrier relaxation pathway in two-dimensional semiconducting transition metal dichalcogenides. *Nature communications*, 5(1):1–7, 2014.

[185] Nevil Vincent Sidgwick. The electronic theory of valency. pages 178–181, 1927.

[186] Pengyu Yuan, Jing Liu, Ridong Wang, and Xinwei Wang. The hot carrier diffusion coefficient of sub-10 nm virgin MoS_2: uncovered by non-contact optical probing. *Nanoscale*, 9(20):6808–6820, 2017.

[187] Edwin E Salpeter and Hans Albrecht Bethe. A relativistic equation for bound-state problems. *Physical Review*, 84(6):1232, 1951.